ELECTRONIC AND KINETIC PROCESSES IN THE Cu/CuCl DOUBLE PULSE LASER

Thesis by

Mark Jay Kushner

In Partial Fulfillment of the Requirements

for the Degree of

Doctor of Philosophy

California Institute of Technology

Pasadena, California

1979

(Submitted May 1, 1979)

ACKNOWLEDGMENTS

I would like to thank my advisor and friend Professor F.E.C. Culick for his guidance and encouragement throughout my stay at Caltech. I would also like to thank Dr. A.A. Vetter for his suggestions and conversations during this work.

My parents, Len and Muriel, and my brother Michael were always there to help. Joseph and Donna Shepherd gave me the friendship and encouragement I needed, and Anita was there to make the closing months happier.

Vere Snell cheerfully and expertly typed the manuscript.

This work was supported in part by the Caltech President's Fund. Computing funds were generously provided by the Division of Engineering and Applied Science.

ABSTRACT

Kinetic and electronic processes in a Cu/CuCl double pulsed laser were investigated by measuring discharge and laser pulse characteristics, and by computer modeling. There are two time scales inherent to the operation of the Cu/CuCl laser. The first is during the interpulse afterglow (tens to hundreds of microseconds). The second is during the pumping pulse (tens of nanoseconds). It was found that the character of the pumping pulse is largely determined by the initial conditions provided by the interpulse afterglow. By tailoring the dissociation pulse to be long and low energy, and by conditioning the afterglow, one may select the desired initial conditions and thereby significantly improve laser performance. With a low energy dissociation pulse, the fraction of metastable copper obtained from a CuCl dissociation is low. By maintaining the afterglow, contributions to the metastable state from ion recombinations are prevented, and the plasma impedance remains low thereby increasing the rate of current rise during the pumping pulse. Computer models for the dissociation pulse, afterglow, pumping pulse and laser pulse reproduced experimentally observed behavior of laser pulse energy and power as a function of time delay, pumping pulse characteristics, and buffer gas pressure. The sensitivity of laser pulse properties on collisional processes (e.g., CuCl reassociation rates) was investigated.

TABLE OF CONTENTS

I. INTRODUCTION TO THE Cu/CuCl DOUBLE PULSE LASER

I.A. The Copper Laser

The copper laser has been the focus of much interest in recent years as a source of intense, nanosecond optical pulses. The copper laser oscillates on the green 5106Å and the yellow 5782Å transitions of neutral copper. Typical pulse energies are a few millijoules, and pulse widths are 10-50 nanoseconds. The green line is sufficiently more intense than the yellow line so that the laser spot appears green.

Metallic vapor lasers in general, and the copper laser in particular, are members of a class of lasers known as "cyclic" or "self terminating" lasers [I-1]. This terminology can be explained by referring to the energy level diagram of copper in Figure I-1. The upper laser levels ($^2P_{3/2,1/2}$) are resonant with the ground state ($^2S_{1/2}$) and hence have large cross sections for electron impact excitation [II-2]. The lower laser levels ($^2D_{5/2,3/2}$) are metastable and therefore have small electron impact excitation cross sections. The laser usually operates with a small partial pressure of copper vapor (.01-.1 Torr) in a buffer gas (e.g., Ne, He, Ar) of about 2-20 Torr pressure. When the gas mixture is subjected to a short rapidly rising current pulse (~2-15 GA/s), the upper laser level is quickly populated. Laser action occurs, with the atoms making the transition to the lower laser levels. Because these levels are metastable, a large population of copper builds up in the ^2D states. When the pumping rate to the upper level can no longer sustain the inversion, the gain turns negative, and the laser effectively turns itself off. Before the

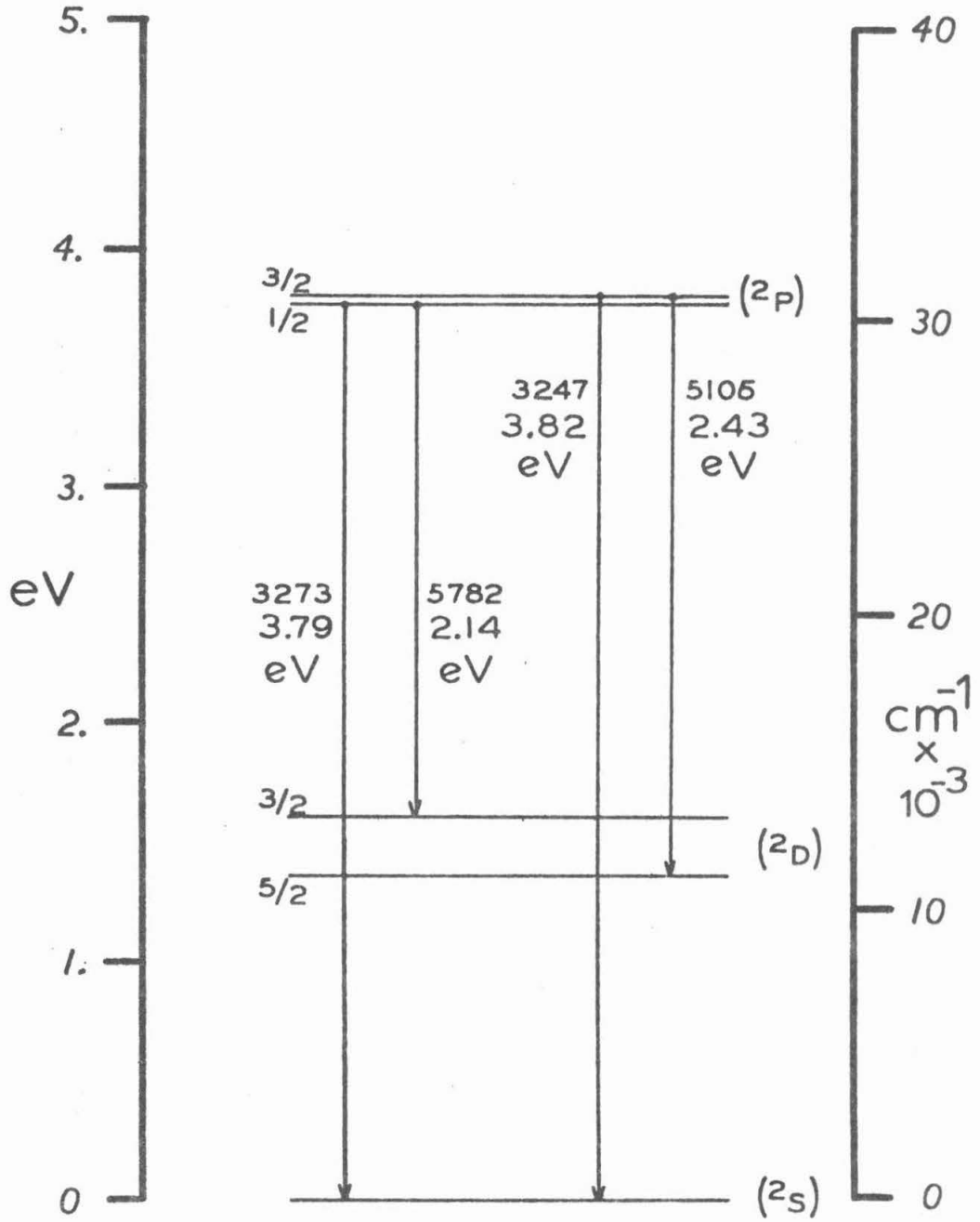

FIGURE II.- Energy Levels of Copper.

laser can be pulsed again, the lower laser levels must relax to the ground state by atom-atom or atom-wall collisions. This usually takes tens of microseconds, thereby setting an upper limit to the repetition rate.

The copper three-level system is especially attractive for efficiently obtaining an inversion in an electric discharge. The resonant excitation cross section is 10-100 times larger than the excitation cross section to the metastable level, and there are no other atomic levels less than 1 eV above the upper laser level. This contributes to high practical efficiencies by minimizing the number of competing parallel paths for energy loss.

I.B. The Copper/Copper Chloride Double Pulse Laser

In the conventional copper or metallic vapor laser, metal vapor is obtained by heating the pure metal, thereby requiring tube temperatures in excess of 1000^{o}C [I-1,3]. A low repetition rate laser requires an expensive external heater, while a high repetition rate laser may use discharge heating, with the disadvantage that repetition rate and metal density cannot be separately optimized. The metal-halide laser circumvents these problems by using a volatile metal bearing compound, such as copper chloride, as the source of metal. The metal density is determined by the vapor pressure of the compound. Sufficient vapor pressure with a metal halide is obtained at temperatures of about 400^{o}, as much as 1100^{o}C less than using the pure metal. Hence the density of metal atoms can be controlled independent of the

discharge and at a relatively low and easily maintained temperature. The density of copper atoms from saturated copper chloride vapor as a function of temperature is shown in Figure I-2.

To obtain laser action from copper chloride vapor, a minimum of two electrical discharge pulses are required. The first discharge pulse (12-20 kV,5-50 nF) dissociates the copper chloride into copper and chlorine. The second discharge pulse (12-20 kV, 1-15 nF) excites the copper. Due to the large fraction of copper atoms which emerge from the dissociation in the metastable lower laser level, there is a minimum time which must pass before the second or pumping pulse is applied, in order to allow enough copper atoms to collisionally relax to permit oscillation. This time (a few to tens of microseconds) is termed the "minimum time delay". Since copper and chlorine are continually reassociating to form the parent molecule, there is a maximum time after the "dissociation pulse" beyond which too much copper has reassociated to permit oscillation. This time,of the order of hundreds of microseconds,is termed the "maximum time delay". Laser pulse energy is optimum at an intermediate time called the "optimum delay" (tens of microseconds). For sufficiently high repetition rates, each discharge pulse excites the existing copper vapor, and dissociates copper chloride for the next discharge pulse. Hence laser action is obtained for every discharge pulse. A typical trace of laser energy as a function of time delay is shown in Figure I-3.

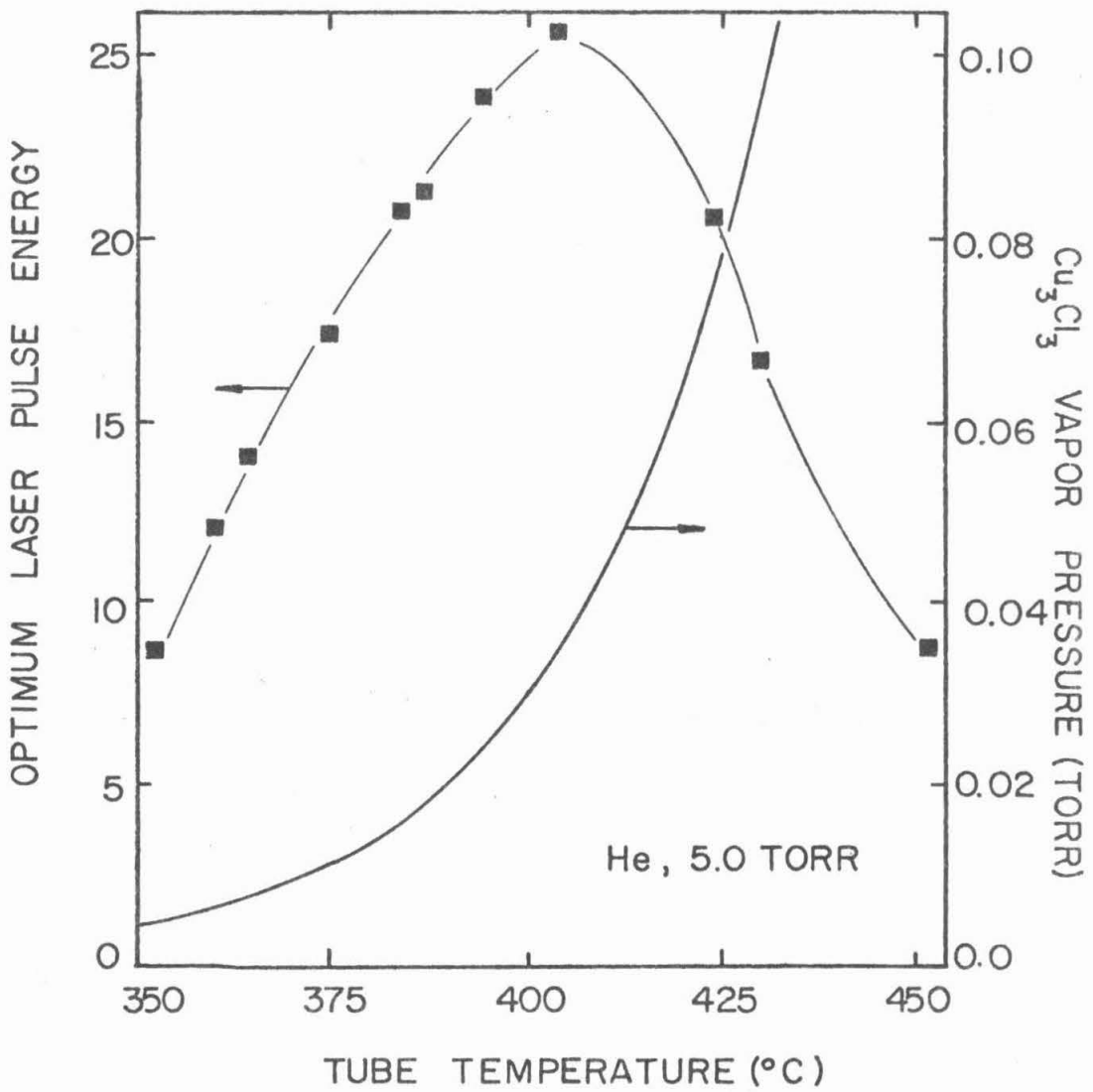

Figure I.2. The equilibrium vapor pressure of Cu_3Cl_3 and optimum laser energy (in arbitrary units) as a function of tube temperature.

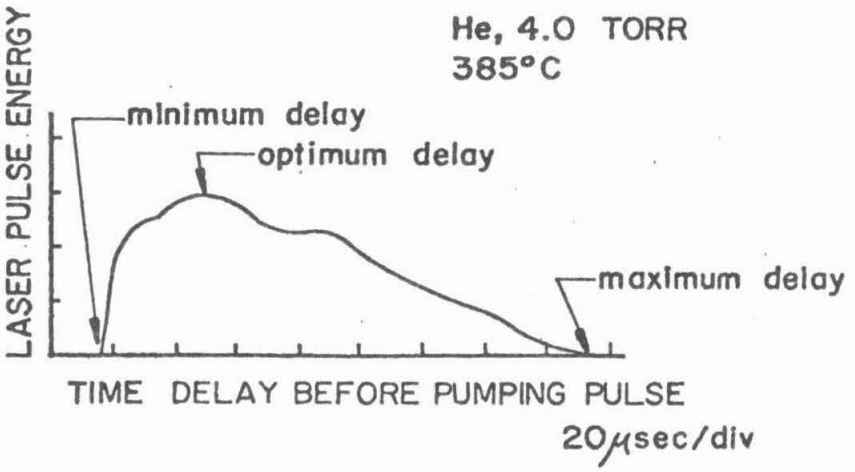

Figure I.3. Laser pulse energy as a function of time delay between discharge pulses.

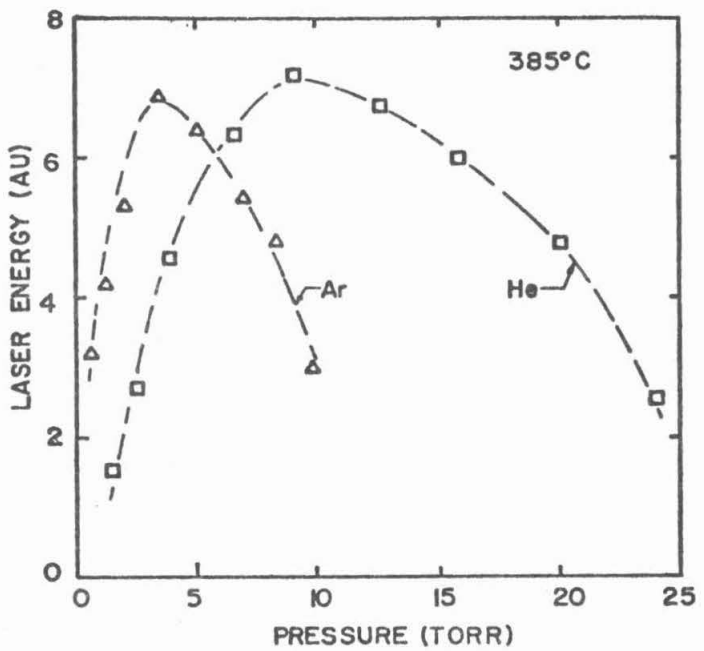

Figure I.4. Laser pulse energy optimized with respect to time delay as a function of buffer gas pressure for helium and argon.

I.C. Characterisitcs of the Copper/Copper Chloride Double Pulse Laser

Laser pulse energy in the Cu/CuCl double pulse laser is a sensitive function of discharge conditions, and tube geometry. As previously mentioned, there is an optimum time delay between discharge pulses. For otherwise fixed conditions there are also an optimum buffer gas pressure (e.g., He, Ne, Kr, Ar and N_2), tube diameter, dissociation pulse energy, pumping pulse energy, and tube temperature (i.e., copper chloride vapor pressure) [I-4]. See Figures I-2,3,4.

The fact that there is an optimum tube temperature at about 400^{o}C and hence an optimum copper chloride density has been one of the least understood aspects of the Cu/CuCl laser. The increase in laser pulse energy as the tube temperature is increased toward the optimum value is easily explained in terms of the increase in copper chloride vapor pressure. The decrease in laser pulse energy at temperatures greater than optimum has not been satisfactorily explained.

In one attempt to explain this temperature dependence, Sovero, et al [I-5] measured electron temperatures during the pumping pulse using a microwave radiometer. He found that as the tube temperature increased toward optimum, the electron temperature decreased. It reached a minimum value near 400^{o}C and then increased as the tube temperature increased away from optimum. When the buffer gas alone was placed in the tube, the electron temperature monotonically decreased with increasing tube temperature. Sovero suggested that increase in electron temperature in the presence of CuCl is due to

collisions with the buffer gas resulting in Penning ionizations, and that the decrease in laser energy is a result of these ionizations. This hypothesis will be investigated in a numerical solution of the Boltzmann equation (see Section IV.B).

I.D. A History of Copper Halide Lasers

Laser emission from copper vapor was first reported by Walter, et al [I-1] in 1966. By heating pure copper in an alumina tube with an oven to about 1500°C, peak powers of 1.2 kW on the green 5106Å and 0.4 kW on the yellow 5783Å transitions were obtained. The following year, Walter improved the laser's performance to 40 kW at a repetition rate of 1 kHz yielding an average power of .5W [I-6], and later to an average power of 11 watts [I-7]. A discharge efficiency (laser energy divided by discharge energy $\frac{1}{2} CV^2$) of 1.2% was reported.

With the exception of the work by Asmus and Moncur [I-8] who in 1968 achieved laser action in copper vapor using exploding wires as the source, little was reported concerning the copper laser until 1972. By this time, it had been realized that despite the encouraging discharge efficiency obtained by oven heated copper lasers the small wall plug efficiency would prevent their practical use. In addition, the elevated temperatures required (1500°C) proved to be an engineering problem for both electrical and structural components. In 1972, the first discharge heated pure copper laser was reported in Russia by Isaev, et al [I-9]. An average power of 15 W at a "practical" effi-

ciency of 1% was achieved at a repetition rate of 15kHz. No external means were used to heat the tube. Peak power obtained was 200 kW. Later work by Isaev and Lemmerman [I-10] in 1977 resulted in an average power of 43.5 W at 16.7 kHz with a practical efficiency of 1%. In that report, as well as an earlier work by Alaev, et al, [I-11] a decrease in laser power and efficiency was documented as the repetition rate exceeded 20 kHz. In this country, R. S. Anderson, et al [I-7,12] have been active with the discharge heated pure copper laser. Their work has concentrated on obtaining high energy pulses at low repetition rates (200 Hz to 2 kHz). As much as 12 mJ/pulse had been reported by 1977, compared to the 2.6 mJ/pulse achieved by Isaev and Lemmerman [I-10]. More recently considerable success in low repetition rate discharge heated pure copper lasers has been reported in Israel by Smilanski, et al [I-13]. In 1978, Smilanski, et al reported 9 mJ/pulse at 1 kHz, but, more important, demonstrated volumetric scalability with tube dimensions as large as 34 mmx640 mm.

A number of other schemes began appearing in 1972, all having the intent to circumvent the inefficiency and problems incurred with oven heated lasers. Russell, et al [I-14] at the Jet Propulsion Laboratory reported in 1972 a supersonic electric discharge laser. In that device powdered copper introduced to an arc heated argon-helium mixture, was vaporized and expanded through a supersonic nozzle. Excitation was by a multipin transverse discharge 11.5 cm downstream. Ferrar [I-15] reported in 1973 a closed cycle flowing system, where copper vapor from a boiler was allowed to diffuse ther-

mally across the optical axis, condense and return to the boiler. The idea of flowing systems is that laser pulses can be lengthened by sweeping metastables out of the optical path. Using a technique which later proved very successful for copper ion lasers [I-16,17] Fahlen in 1974 reported a hollow-cathode copper laser [I-18]. In that device, discharge heating and sputtering provided the copper atoms. Efficiency (0.025%) and peak power (270 mW) were low.

Copper halide lasers were first proposed in 1973 when Liu and his colleagues at Westinghouse [I-19,20] reported superradiant emission at 5106Å and 5782Å from a pulsed discharge in copper iodide vapor. This was the first demonstration of significant copper emission at low temperatures. Oven heated tubes at temperatures as low as 500°C yielded sufficient CuI vapor for superradiant emission to be observed. Actual laser action of copper from copper halide vapor was first reported by Chen, et al [I-21] at the Jet Propulsion Laboratory also in 1973. Using copper chloride as the source and a double pulse discharge, 1.25 mJ pulses (17μJ/cm^3) were obtained at 400°C. An optimum time delay between pulses, and an optimum tube temperature were also first reported by Chen, et al.

Since that first report, work in copper halide lasers has continued at JPL [I-4,22-27]. Progress has been made in scaling the double pulse CuCl laser to 10 mJ, and obtaining 19.5 W average power from a continuously pulsed (16.7 kHz) copper bromide laser. Copper halide research has also continued at Westinghouse [I-28,29-31]. Their diagnostic work has significantly added to the understanding of

continuously pulsed and burst mode (a packet of about 50 discharge pulses separated by approximately 100μs) lasers. The Russian effort in copper lasers continues to be with discharge heated pure copper systems. The only reported copper halide work has been a spectroscopic study of copper densities [I-32] and an investigation of excitation of copper from CuCl by pulse trains [I-33]. The Israeli reports of copper halide laser research have also been limited to spectroscopic studies [I-34,35].

There has been recent interest in transverse discharge copper halide lasers [I-36,37,38]. This work has shown potential to scale the active volume to large dimensions. The technological difficulties of constructing transverse devices for operation at high temperature has been overcome by Piper's segmented electrodes [I-38]. Piper has also been able to reduce greatly the pulse to pulse variation in laser energy which is often the result of inhomogeneity in the transverse discharge. By preconditioning the disassociation pulse with a separate short discharge pulse, Piper has obtained more uniform excitation [I-39]. Using the transverse discharge, Brandt and Piper [I-40] have been able to reduce the necessary dissociation energy by a factor of ten by using a low voltage, long duration dissociation pulse. This technique can significantly improve laser efficiency.

Although copper halides are to date the most promising low temperature source of copper atoms for lasers, copper complexes have yielded laser action at temperatures as low as 120°C. Chakrapani, et al [I-41] in 1977 reported laser emission from copper acetate ($Cu(CH_3COO)_2 \cdot H_2O$) using a double pulse excitation scheme. Threshold was achieved at

210°C, and was optimum at 230°C. Gokay, et al [I-42] followed in 1978 with a report of laser action in copper acetylacetonate at a minimum oven temperature of 120°C, and optimum temperature of 127°C.

I.E. Purpose and Scope of This Work

The purpose of this thesis is to use experimental diagnostics and computer modeling to identify the processes which dominate the Cu/CuCl laser and in turn use those processes to explain, predict and improve laser performance. The dissociation pulse, post-dissociation pulse afterglow, pumping pulse and laser pulse are treated simultaneously in an effort to provide a consistent analysis. As a result of this work, experimentally observed behavior such as the dependence of laser energy on buffer gas pressure has been explained. Recommendations are made concerning dissociation pulse efficiency and scaling the laser to larger dimensions.

The experimental work reported in this thesis includes measurements of electron densities in a pulsed Ne/CuCl discharge, measurements of temporal and spatial laser pulse properties, measurements of pumping rates and discharge properties, and the enhancement of laser energy by applying a continuous glow discharge. The numerical work provides a complete treatment of the Cu/CuCl double pulse laser. The dissociation pulse and afterglow are modeled by radially dependent rates equations. The pumping pulse and laser pulse are described by rate equations and the scalar wave equation which are integrated in a three dimensional resonator.

REFERENCES

1. W. T. Walter, N. Solimene, M. Piltch, G. Gould, "Efficient Pulsed Gas Discharge Lasers", IEEE J. Quant. Electronics QE-2, 474 (1966).
2. S. Trajmar, W. Williams, and S. K. Srivastava, "Electron-impact Cross Sections for Cu Atoms", J. Phys. B10, 3323 (1977).
3. G. G. Petrash, "Pulsed Gas-Discharge Lasers", Sov. Phys. Usp. 14, 747 (1972).
4. N. M. Nerheim, "A Parametric Study of the Copper Chloride Laser", J. of Appl. Phys. 48, 1186 (1977).
5. E. Sovero, C. J. Chen, and F. E. C. Culick, "Electron Temperature Measurements in a Copper Chloride Laser Utilizing a Microwave Radiometer", J. of Appl. Phys. 47, 4538 (1976).
6. W. T. Walter, "40 kW Pulsed Copper Laser", Bull. Am. Phys. Soc. 12, 90 (1967).
7. R. S. Anderson, R. J. Homsey, and T. W. Karras, "Low Repetition Rate Copper Vapor Laser", General Electric Company, #N00014-76-C-0975, 1977.
8. J. F. Asmus, and N. K. Moncur, "Pulse Broadening in a MHD Copper Vapor Laser", Appl. Phys. Letters 13, 384 (1968).
9. A. A. Isaev, M. A. Kazaryan, and G. G. Petrash, "Effective Pulsed Copper-Vapor Laser with High Average Generation Power", JETP Letters 16, 27 (1972).

10. A. A. Isaev and G. Yu Lemmerman, "Investigation of a Copper Vapor Pulsed Laser at Elevated Powers", Sov. J. Quant. Electronics 7, 799 (1977).

11. M. A. Alaev, A. I. Baranov, N. M. Vereshchagin, I. N. Gnedin, Yu. P. Zherebtsov, V. F. Moskalenko, and Yu. M. Tsukanov, "Copper Vapor Laser with a Pulse Repetition Frequency of 100 kHz", Sov. J. Quant. Electronics 6, 610 (1976).

12. R. S. Anderson, L. W. Springer, B. G. Bricks, and T. W. Karras "A Discharge Heated Copper Vapor Laser", IEEE J. Quant. Electronics QE-11, 173 (1975).

13. I. Smilanski, A. Kerman, L. A. Levin, G. Erez, "Scaling of the Discharge Heated Copper Vapor Laser", Opt. Commun. 25, 79 (1978).

14. G. R. Russell, N. M. Nerheim, and T. J. Pivirotto, "Supersonic Electrical-Discharge Copper Vapor Laser", Appl. Phys. Letters 21, 565 (1972).

15. C. M. Ferrar, "Copper-Vapor Laser with Closed-Cycle Transverse Vapor Flow", IEEE J. Quant. Electronics QE-9, 856 (1973).

16. J. R. McNeil, G. J. Collins, K. B. Persson, and D. L. Franzen, "Ultraviolet Laser Action from Cu II in the 2500 Å Region", Appl. Phys. Letters 28, 207 (1976).

17. F. J. de Hoog, J. R. McNeil, G. J. Collins, and K. B. Persson, "Discharge Studies of the Ne-Cu Laser", J. Appl. Phys. 48, 3701 (1977).

18. T. S. Fahlen, "Hollow-Cathode Copper-Vapor Laser", J. Appl. Phys. 45, 4132 (1974).

19. C. S. Liu, E. W. Sucov, L. A. Weaver, "Copper Superradiant Emission from Pulsed Discharges in Copper Iodide Vapor", Appl. Phys. Letters 23, 92 (1973).

20. L. A. Weaver, C. S. Liu, and E. W. Sucov, "Superradiant Emission at 5106, 5700, and 5782 Å in Pulsed Copper Iodide Discharges", IEEE, J. Quant. Electronics QE-10, 140 (1974).

21. C. J. Chen, N. M. Nerheim, and G. R. Russell, "Double-discharge Copper Vapor Laser with Copper Chloride as a Lasant", Appl. Phys. Letters 23, 514 (1973).

22. N. M. Nerheim, "Measurements of Copper Ground State and Metastable Level Populations in a Copper-chloride Laser", J. Appl. Phys. 48, 3244 (1977).

23. N. M. Nerheim, A. M. Bhanji, and G. R. Russell, "A Continuously Pulsed Copper Halide Laser with a Cable-Capacitor Blumhein Discharge Circuit", IEEE J. Quant. Electronics QE-14, 686 (1978).

24. N. M. Nerheim, A. A. Vetter, and G. R. Russell, "Scaling a Double-Pulsed Copper Chloride Laser to 10 mJ", J. Appl. Phys. 49, 12 (1978).

25. A. A. Vetter, "Quantitative Effect of Initial Current Rise on Pumping the Double-Pulsed Copper Chloride Laser", IEEE J. Quant. Electronics, QE-13, 889 (1973).

26. A. A. Vetter and N. M. Nerheim, "Addition of HCℓ to the Double-Pulse Copper Chloride Laser", Appl. Phys. Letters 30, 405 (1977).

27. C. J. Chen, A. M. Bhanji, and G. R. Russell, "Long Duration

High Efficiency Operation of a Continuously Pulsed Copper Laser Utilizing Copper Bromide as a Lasant", Appl. Phys. Letters 33, 146 (1978).

28. C. S. Liu, D. W. Feldman, J. L. Pack, and L. A. Weaver, "Axial Effects in Continuously Pulsed Copper Halide Lasers", J. Appl. Phys. 48, 194 (1977).

29. C. S. Liu, D. W. Feldman, J. L. Pack, and L. A. Weaver, "Kinetic Processes in Continuously Pulsed Copper Halide Lasers", IEEE J. Quant. Electronics, QE-13, 744 (1977).

30. C. S. Liu, D. W. Feldman, J. L. Pack, and L. A. Weaver, "Copper Halide Laser Research: Final Report", Westinghouse R & D Center, Pittsburgh, Pennsylvania, Dec. 1977.

31. J. L. Pack, C. S. Liu, D. W. Feldman, and L. A. Weaver, "High Average Power Pulser Design for Copper Halide Laser Systems", Rev. Sci. Instr. 48, 1047 (1977).

32. A. M. Shukhtin, V. G. Mishakov, G. A. Fedotov, and A. A. Ganeev, "Interference Methods for Observing the Dissociation of Copper Halide Molecules in a Pulsed Discharge", Opt. Spectrosc. 39, 444 (1976).

33. E. B. Gordon, V. G. Egorov, and V. S. Pavlenko, "Excitation of Metal Vapor Lasers by Pulse Trains", Sov. J. Quant. Electronics 8, 266 (1978).

34. J. Tenenbaum, I. Smilanski, S. Gabay, G. Erez, and L. A. Levin, "Time Dependence of Copper-atom Concentration in Ground State and Metastable States in a Pulsed CuCl Laser", J. Appl. Phys. 49, 2662 (1978).

35. J. Tenenbaum, I. Smilanski, S. Gabay, G. Erez, L. A. Levin, J. Katriel, and Shammai Speiser, "Buffer Gas Effect on Ground and Metastable Populations in a Pulsed CuBr Laser", IEEE J. Quant. Electronics, QE-14, 680 (1978).

36. J. A. Piper, "A Copper Iodide Laser Excited by Transverse Discharge", Opt. Commun. 14, 296 (1975).

37. J. A. Piper and C. E. Webb, "A TE Copper Iodide Laser", IEEE J. Quant. Electronics QE-11, 95D (1975).

38. J. A. Piper, "A Transversely Excited Copper Halide Laser with Large Active Colume", IEEE J. Quant. Electronics QE-14, 405 (1978).

39. James A. Piper, "Recent Advances in Metal Vapour Lasers", Proc. SPIE Lasers '78, Orlando, Florida 1978.

40. M. Brandt and J. A. Piper, "Improved Dissociation Efficiency in TE Pulsed Copper Halide Lasers", Proc. SPIE Lasers '78, Orlando, Florida 1978.

41. G. Chakrapani, T. A. Prasada Rao, A. A. N. Murty, and D. Ramachaudia Rao, "Laser Action in Copper with Copper Acetate as a Lasant", Appl. Phys. Letters 31, 832 (1977).

42. M. Cem Gokay, Mahmood Soltanoalkotabi, and Lee A. Cross, "Copper Acetylacetonate as a Source in the 5106 Å Neutral Copper Laser", J. Appl. Phys. 49, 4357 (1978).

II. MEASUREMENTS OF ELECTRON DENSITIES AND LASER ENERGY IN A Ne/CuCl DISCHARGE AND THE Cu/CuCl LASER

II.A. Introduction

Electron density measurements were made in a Ne/CuCl discharge and afterglow. Following those measurements, the same discharge tube was used as a laser. A correlation between extrema in electron densities and extrema in laser energy was made and is discussed in the following sections.

II.B. The Laser Interferometer for Measuring Electron Densities

The method chosen to measure the electron density in a pulsed CuCl discharge and afterglow uses a CO_2 continuous wave laser as the reference source for an infrared interferometer. The technique, first introduced by Ashby and Jephcott in 1963 [II-1] using a He-Ne laser at 3.39 μm, has been used successfully in a number of experiments [II-1-7].

The laser interferometer theory can be described by referring to Figure II-1. A CW laser operates in the interferometer reference leg of length d_ℓ, formed by the partially transmitting flat mirror M_2, and totally reflecting mirror M_1 of radius R_1. The pulsed discharge to be studied is placed in the adjoining interferometer leg of length d_p formed by the partially transmitting mirror M_3 of radius R_3, and mirror M_2. The resonant TEM_{mnq} modes of the laser cavity are [II-8]

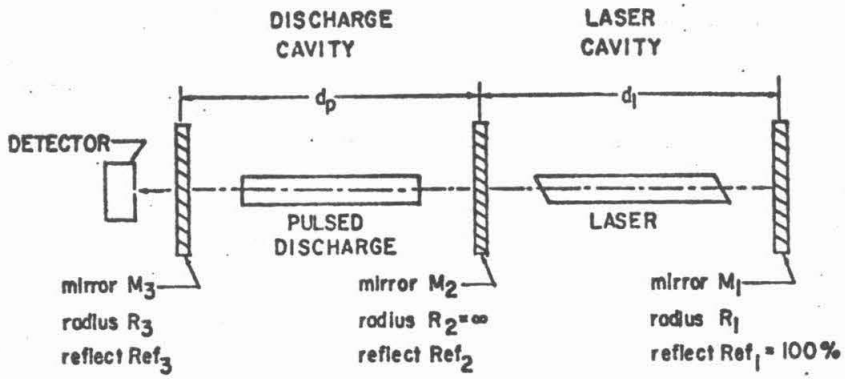

Figure II.1. Schematic of CO_2 laser interferometer used for measuring electron densities.

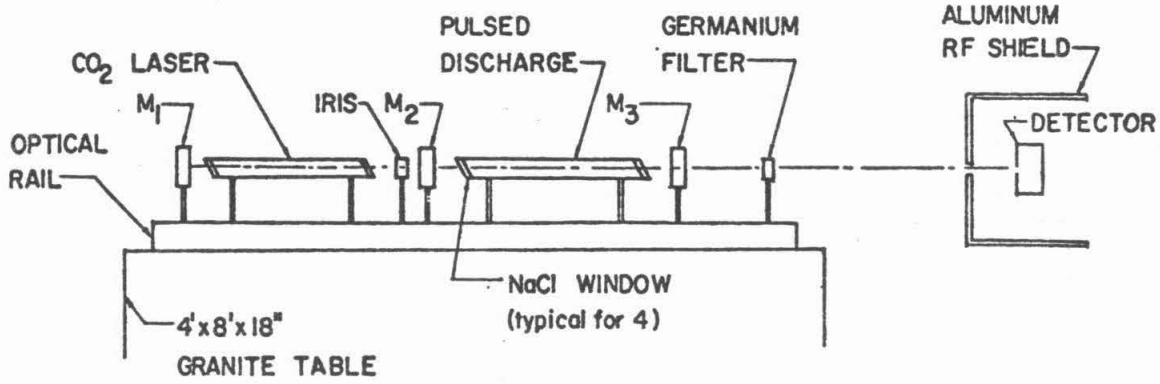

Figure II.2. Experimental arrangement used for measuring electron densities.

$$\frac{2d_\ell}{\lambda/n_\ell} = q + \frac{1}{\pi}(1 + m + n)\cos^{-1}\left(\left(1 - \frac{d_\ell}{R_1}\right)\left(1 - \frac{d_\ell}{R_2}\right)\right) \qquad \text{(II.B.1)}$$

where n_ℓ is the cavity index of refraction, λ is the resonant wavelength and m, n, and q are integers. Since M_2 is flat, $R_2 = \infty$, and (II.B.1) can be rewritten as

$$\frac{2d_\ell}{\lambda/n_\ell} = q + \frac{1}{2\pi}(1 + m + n)\cos^{-1}\left(1 - \frac{2d_\ell}{R_1}\right) \qquad \text{(II.B.2)}$$

An identical expression can be written for the discharge cavity where d_p, R_3, and n_p are substituted for d_ℓ, R_1, and n_ℓ; n_p being the discharge cavity index of refraction. If the cavity length d_ℓ and mirror radius of curvature R_1 are carefully chosen so that

$$\frac{1}{2\pi}\cos^{-1}\left(1 - \frac{2d_\ell}{R_1}\right) = \frac{r_\ell}{s_\ell} \qquad \text{(II.B.3)}$$

where r_ℓ and s_ℓ are relatively prime numbers, then (II.B.2) can be written as

$$n_\ell d_\ell = \frac{\lambda}{2}\left(q + \frac{r_\ell}{s_\ell}(1+m+n)\right) = \frac{\alpha_\ell \lambda}{2s_\ell} \qquad \text{(II.B.4)}$$

where $\alpha_\ell = qs_\ell + r_\ell(1+m+n)$ is an integer. Again an identical expression to (II.B.4) can be written for the discharge cavity by substituting d_p, α_p, n_p, and s_p for d_ℓ, α_ℓ, n_ℓ, and s_ℓ. If the wavelength λ is held constant, then from (II.B.4) cavity lengths resonant at λ are separated by a distance

$$\Delta(n_\ell d_\ell) = \frac{\lambda}{2s_\ell}$$

and (II.B.5)

$$\Delta(n_p d_p) = \frac{\lambda}{2s_p}$$

Returning to Figure II-1, the laser is operated at a wavelength λ, and d_p and R_3 are chosen so that (II.B.4) is satisfied. Because the wavelength of the CW laser signal entering the discharge cavity through M_2 is resonant in that cavity as well as the laser cavity, the laser signal passing through M_3 and monitored by the detector will be large. If $n_p d_p$ is changed monotonically by an amount $\lambda/2s_p$, the laser signal monitored by the detector will undergo one full cycle of modulation, as the discharge cavity passes from one resonant configuration to the next. For example, if λ = 10.6 μm, and s = 4 (R_3 = 2m, d_p = 1m), then $\Delta(n_p d_p)$ = 1.3 μm. Hence many cycles of modulation are obtained for macroscopic changes in $n_p d_p$.

Note that if d_p is held constant, then (II.B.5) can be written as

$$\Delta n_p = \lambda/2s_p d_p \qquad \text{(II.B.6)}$$

and

$$\chi = \Delta n / n_p = \frac{\Delta n 2 s_p}{\pi} d_p \qquad \text{(II.B.7)}$$

where χ is the number of cycles of modulation seen by the detector for a change in the discharge cavity index of refraction of Δn.

The time dependent index of refraction of a gas can be written as [II-7].

$$n(t) = (1 - \frac{\omega_p^2(t)}{\omega^2})^{\frac{1}{2}} + 2\pi\Sigma_j P_j N_j \qquad \text{(II.B.8)}$$

where

$\omega = 2\pi c/\lambda$ (/sec)

$\omega_p(t) = (\frac{4\pi N_e(t) e^2}{m_e})^{\frac{1}{2}}$

$N_e(t)$ = electron density (/cm^3)

m_e = electron mass (g)

e = electronic charge (esu)

P_j = polarizability of the j^{th} species

N_j = density of the j^{th} species (/cm^3)

Note that if λ = 10.6 μm, then $\omega_p^2/\omega^2 << 1$ for electron densities $N_e << 10^{19}$/cm^3. Because this is many orders of magnitude larger than the electron densities one would expect in a low pressure plasma (II.B.8) can be written

$$n(t) = 1 - \frac{\omega_p^2(t)}{2\omega^2} = 1 - \frac{\lambda^2 e^2 N_e(t)}{2\pi c^2 m_e} \qquad \text{(II.B.9)}$$

where the nonelectronic contributions to n(t) have been ignored. Hence, we see that if the discharge in the discharge cavity is pulsed, generating an absolute change in electron density of $\Delta N_e(t_o,t)$ during a time t_o to t, the number of cycles of modulation of the laser signal observed by the detector during the same period is

$$\chi = \frac{\Delta n(t_o,t)}{\Delta n_p} = \frac{\lambda e^2 s_p}{\pi c^2 m_e} d_p \, \Delta N_e(t_o,t) \, (\frac{L}{d_p})$$

$$= \frac{\lambda e^2 s_p L}{\pi c^2 m_e} \, \Delta N_e(t_o,t) \qquad \text{(II.B.10)}$$

where L/d_p is the ratio of discharge length to cavity length. Therefore, if the number of cycles of modulation of the laser signal as a result of pulsing the discharge is χ, then the absolute change in electron density in the discharge is

$$\Delta Ne(t_o,t) = \frac{\pi c^2 m_e \chi}{\lambda e^2 s_p L} \qquad \text{(II.B.11)}$$

The number of cycles of modulation are determined by counting the "fringes" in the output of the detector. This value $\Delta Ne(t_o,t)$ is the absolute change in electron density and therefore includes the buildup and decay of electrons in the discharge. These two regimes are easily separated by observing the temporal shape of the fringes (i.e., a wide fringe corresponding to maximum electron density) or by an apriori knowledge of the pulse timing. If the time response of the system (e.g., detector time response, scope rise time, and light transit time) is long compared to the discharge pulse length, then only the afterglow decay of electrons will be recorded.

The sensitivity of the system is limited not only by the time response of the electronics but by how well the fringes can be resolved.

In order to resolve one fringe, the half-width of that fringe must be less than or equal to separation between fringes. That is, [II-9]

$$\frac{f}{Q} \leq \Delta f = \frac{c}{2d_p s_p} \tag{II.B.12}$$

where f is the fringe frequency and Q is the discharge cavity quality factor

$$Q = 2\pi \frac{\text{Maximum energy stored}}{\text{energy dissipated per cycle}} .$$

If T_2 is the transmission factor of M_2, and T_3 is the transmission factor of M_3, then

$$Q = \frac{2\pi d_p}{\lambda(1 - T_2 - T_3)} \tag{II.B.13}$$

Placing (II.B.13) in (II.B.12) the maximum value of s_p for easily distinguishable resonances is seen to be

$$s_p \leq \frac{\pi}{(1 - T_2 - T_3)} \tag{II.B.14}$$

Note that in (II.B.13) and (II.B.14) we have ignored diffraction and scattering losses. Therefore, the maximum number of fringes one can expect to be able to distinguish for a change in electron density $N_e(t_o,t)$ is

$$\chi_{max} \approx \frac{e^2 \lambda L \, \Delta N_e(t_o,t)}{(1-T_2-T_3)c^2 m_e} \tag{II.B.15}$$

Conversely, the minimum change in electron density which can be confidently detected (i.e., produce 1 fringe) is

$$\Delta N_e(t_o,t)_{min} = \frac{(1-T_2-T_3)c^2 m_e}{e^2 \lambda L} \qquad \text{(II.B.16)}$$

For example if $T_2 = T_3 = .25$, $L = 100$ cm, $\lambda = 10.6$ μm, then $\Delta Ne(t_o,t)_{min} = 1.7 \times 10^{13}/cm^3$.

II.C. Experimental Setup for Measuring Electron Densities

The experimental arrangement used for measuring electron densities with a CO_2 laser interferometer is sketched in Figure II-2. (The labeling of the mirrors is the same as in Section II.B.). The interferometer was mounted on an optical rail which was secured to 4' x 8' x 18" granite table to reduce vibration.

II.C.1 Optics

Mirror M_2 was 1" in diameter and had a 2m radius of curvature. The mirror was coated with gold in an evaporation chamber. Mirrors M_2 and M_3 had 1" diameter, 3 mm thick ZnSe substrates. Their coatings provided 73% reflectivity at 10.6 μm with antireflection coatings on the second surface. Mirror M_2 was flat. Mirror M_3 had a 2 m radius of curvature. The windows on the CO_2 laser and discharge tube were 1/10 wave, 2" diameter, 1/4" thick NaCl. A 2" diameter, 1/4" thick germanium filter was mounted between the discharge and detector to reduce extraneous signal saturation of the detector.

II.C.2 The CO_2 Laser

The CO_2 laser used for the interferometer source was a conventional glow discharge (see Figure II-3). The flowing gas mixture was $CO_2/N_2/He$ at 1/3/16. The discharge tube was 12 mm I.D. with a water cooled jacket surrounding the discharge region. The electrodes were separated by 46 cm. Typical operating characteristics of the laser using mirrors M_1 and M_2 described above can be found in Figure II-4. During the experiment, normal operating conditions were a current of 10 ma at 4.8 kV, and a gas pressure of 13.5 Torr. The mode structure was controlled by using an adjustable iris in the laser cavity. The mode was determined by burning its pattern on a piece of thermally sensitive paper from an electronic thermal printing calculator, and was restricted to the TEM_{oo} mode during the experiment.

II.C.3 Ne/CuCl Discharge Tube and Gas Supply System

A schematic of the CuCl discharge tube and gas supply system is shown in Figure II-5. The discharge tube was made of 2.54 cm I.D. quartz. The electrode assemblies were separated by 35.5 cm and consisted of 4 equispaced tungsten post electrodes connected by a wire ring on the exterior of the tube. This electrode configuration was found to yield a uniform discharge throughout the discharge volume. The bottom of the tube contained a shallow trough which served as a reservoir for the copper chloride. For the interferometer measurements, the windows were 1/4" thick NaCl.

The window assemblies attached to the discharge tube by ground glass taper joints. This arrangement enabled windows and discharge

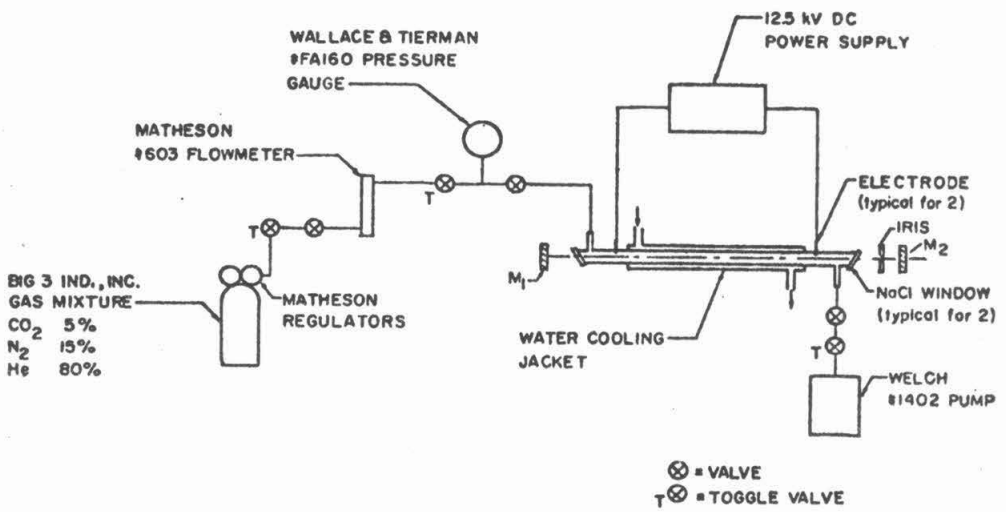

Figure II.3. Schematic of the CO_2 laser used in the electron density measurements.

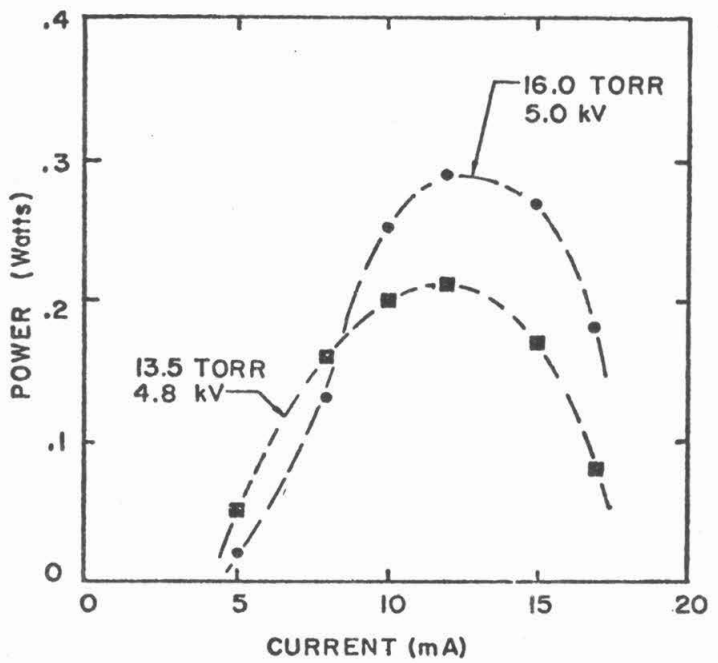

Figure II.4. Typical operating characteristics of the CO_2 laser used in the electron density measurements.

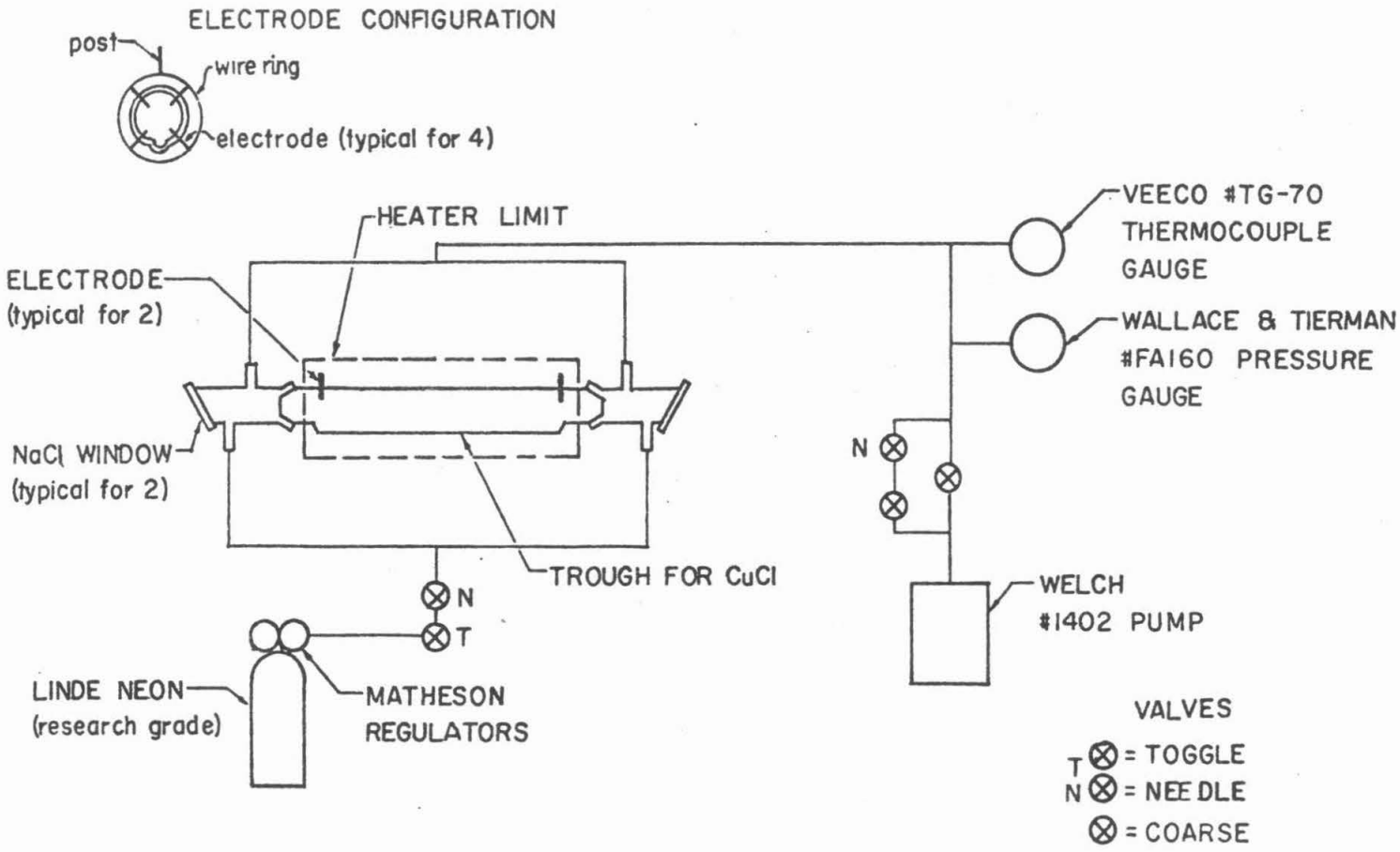

Figure II.5. CuCl discharge tube and gas system. Note the four pin electrode configuration.

tubes to be changed independently. Each window assembly had two gas ports. Buffer gas entered the tube by the port nearest the window, while vacuum was applied to the port nearest the taper joint. This arrangement prevented CuCl vapor from diffusing to the cooler window surfaces and condensing. With the same window assemblies on either side of the tube there is no net gas flow through the tube. This is verified by the symmetric deposition of CuCl on the discharge tube interior on either side of the heated region.

The discharge tube was placed in a cylindrical quartz liner, and the liner enclosed by an 18" long electrical resistance "clamshell" heater. The limits of the heater are shown in Figure II-5. A chromel-alumel thermocouple placed on the exterior of the discharge tube was used to measure the tube temperature. The tube temperature could be regulated to ±1°C. A typical axial temperature profile is shown in Figure II-6.

The neon buffer gas was 99.9% research grade. The CuCl was reagent grade which was distilled and kept under vacuum before being loaded into the discharge tube. The standard operating procedure was to load the CuCl powder into the tube, spreading it as evenly as possible along the trough. The system was then pumped down and heated to well above the CuCl melting point (≈450°C) to enable the CuCl to flow and fill the trough, thereby ensuring an even axial distribution of CuCl. At room temperature, the gas system was capable of sustaining pressures of a few microns.

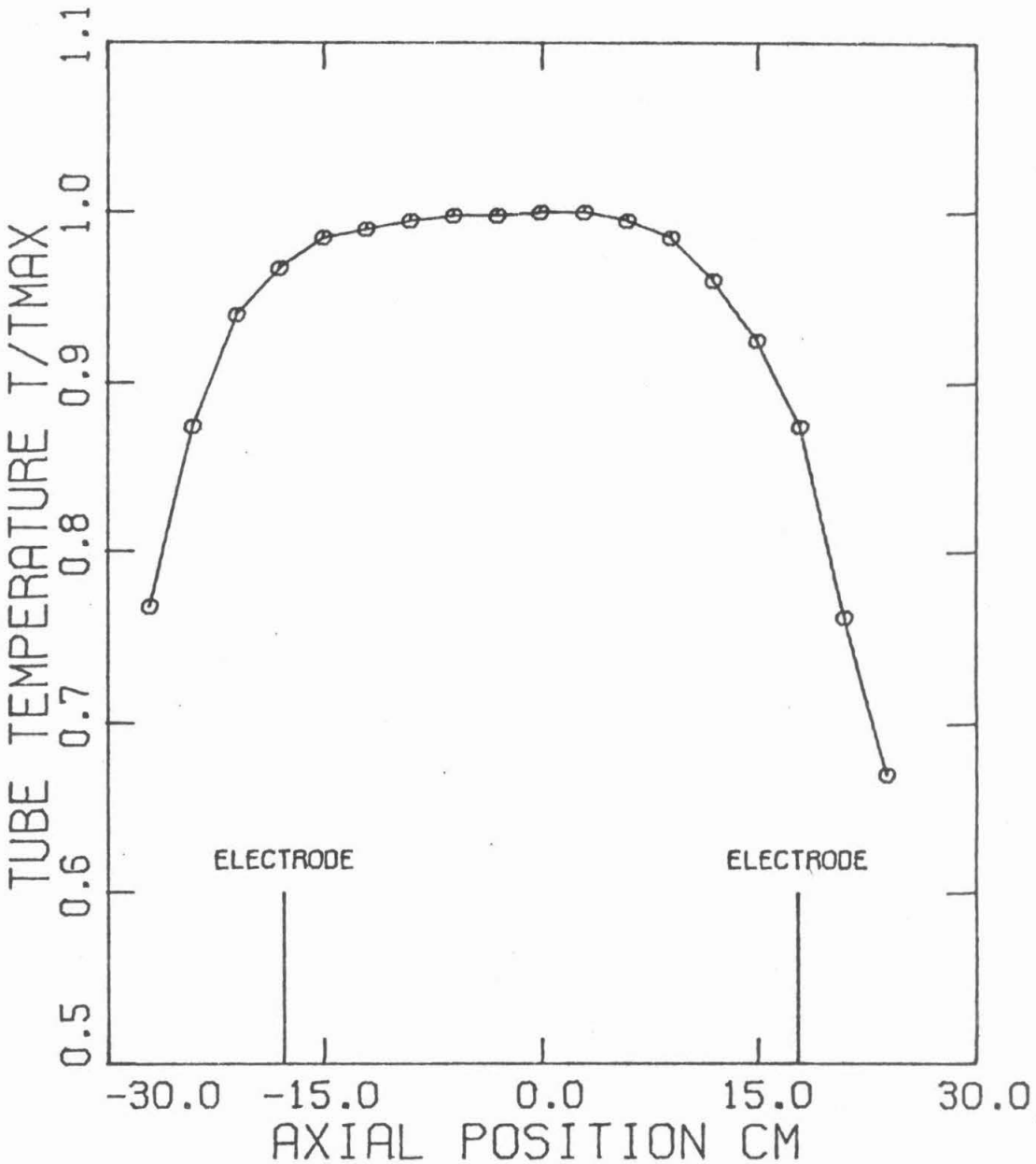

Figure II.6. Axial temperature profile for the CuCl discharge tube.

II.C.4 Electrical System

A schematic of the electrical system is shown in Figure II-7. The discharge was initiated by a single 5 kV breakdown pulse from the double-pulsed laser power supply (see Appendix A for a discussion of the power supply). After breakdown, a 60 μF capacitor charged to 1500 V was discharged through the tube. The same trigger signal (supplied by a pulse generator) that set off the breakdown pulse also triggered a storage oscilliscope, which recorded the modulated laser signal from a Au-Ge liquid nitrogen cooled detector.

RF noise proved to be a problem in taking data during and immediately following the discharge. This problem was in part alleviated by enclosing the detector in a large aluminum box with a small hole drilled in one face to allow the laser beam to enter. Coaxial cables were wrapped in aluminum foil for additional shielding.

II.C.5 Experimental Procedure

The interferometer was initially tested without the Ne/CuCl discharge in the discharge cavity. Instead, a rotatable NaCl flat was placed between mirrors M_2 and M_3. By rotating the NaCl flat, the effective length of the discharge cavity can be changed, as the distance which the CO_2 laser beam travels through the NaCl flat is effectively lengthened by the index of refraction of NaCl at 10.6 μm. The test satisfactorily demonstrated that the interferometer operated according to theory. (see Appendix B).

The wavelength of the CO_2 laser was assumed to be nominally 10.6

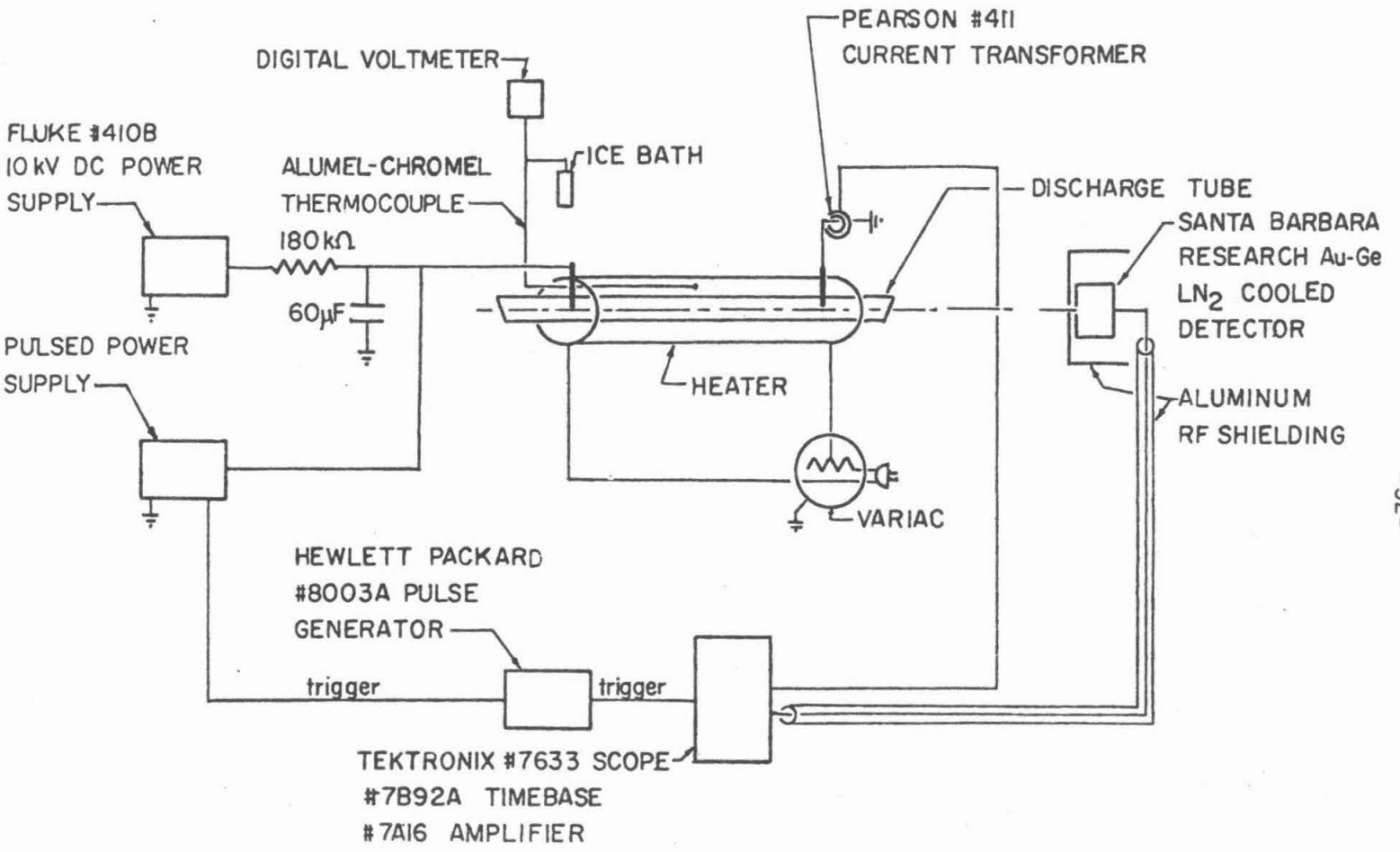

Figure II.7. Schematic of CuCl discharge electrical system.

μm. In reality, there are 11 P branch lines of the 001-100 transition spanning the range 10.51 μm to 10.71 μm which are commonly observed [II.11]. This range represents only a 2% uncertainty. The value is small compared to other experimental error so that the assumed nominal wavelength of 10.6 μm is justified. Vibrational rotational bands other than the 001-100 have been observed to lase, but these bands usually require wavelength selective devices (e.g., gratings) to be seen. This fact combined with mirrors coated for operation at 10.6 μm and the near threshold operating conditions would preclude oscillation on bands other than the 001-100.

The standard experimental procedure was to allow the tube to slowly heat up to a maximum temperature (≈475°C) over a period of 60 to 90 minutes. Periodically during the heating, the discharge would be pulsed, and fringes recorded. Once the maximum temperature was reached, the heater was turned off, and the tube allowed to cool. Again during the cooling off period, the discharge was pulsed. In this way, 35-50 data points were taken covering a range of 150°C to 200°C. (see Appendix C for a justification of this method).

II.D. Electron Densities in a Ne/CuCl Discharge: Results and Discussion

The maximum electron densities during a single pulse of a Ne/CuCl discharge and afterflow at constant buffer gas pressure as a function of tube temperature are displayed in Figure II-8. Note that there is

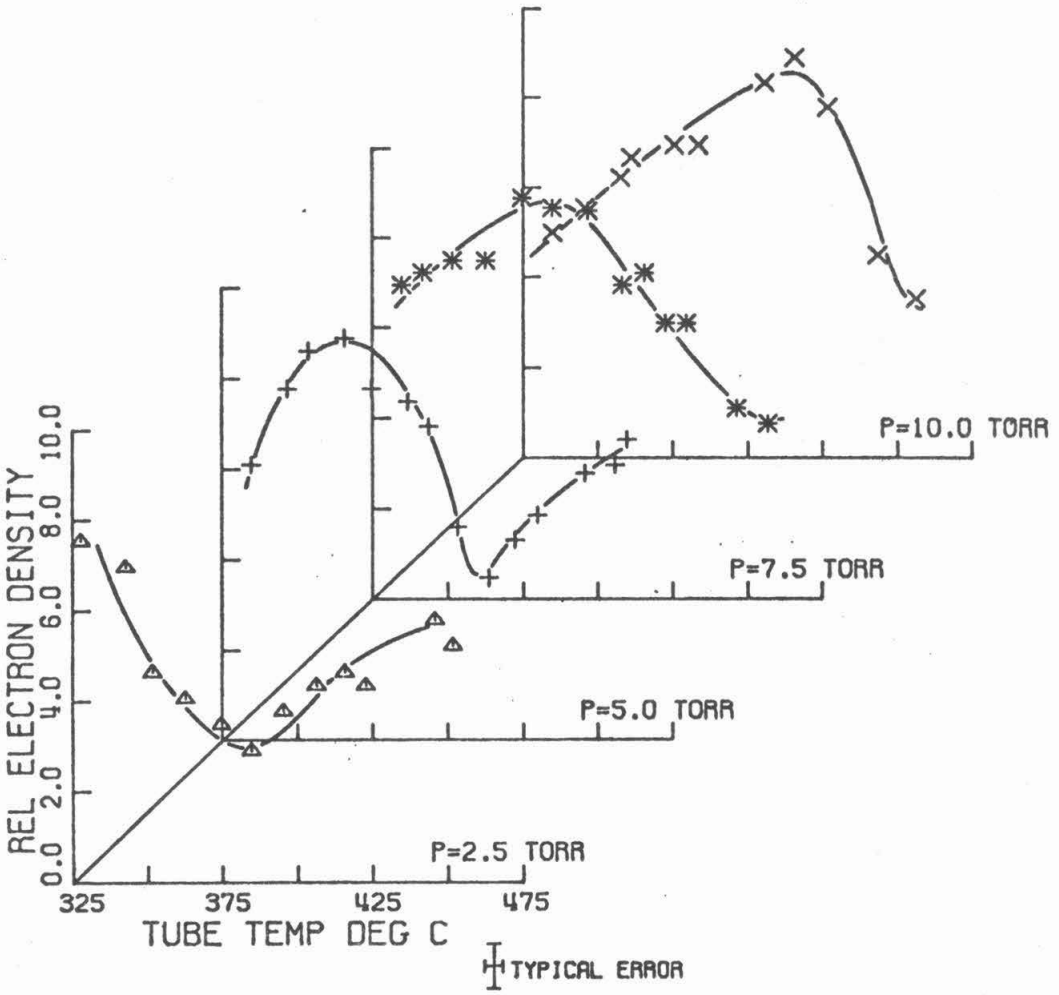

Figure II.8. Maximum electron densities measured in the afterglow of a Ne/CuCl discharge. The vertical scale is approximately in units of $10^{14} cm^{-3}$.

a maximum in electron density at low tube temperatures. This maximum in electron density is followed by a local minimum at a higher tube temperature. The tube temperatures at which these extrema appear shift to higher values at higher buffer gas pressures (see Figure II-16) The pattern shown in Figure II-9 is suggested. The same behavior was observed using the double pulse power supply for excitation (see Figure II-10). Due to extreme noise problems, few data were taken in this way.

The time dependent decay of electron density from its maximum values for the discharge in 2.5 Torr of Ne is shown in Figure II-11. The results are typical for a wide range of pressures. Electron densities for tube temperatures less than the value at which the minimum total density was found are on the left side of the figure. Electron densities for tube temperatures higher than the "minimum" value are on the right side of the figure. Note that electron density at higher CuCl densities decays with a rate constant larger than for low CuCl density. The times at which the electron densities fall below the detection limit ($5 \times 10^{13}/cm^3$) are also longer for low CuCl densities. Because a large density of highly electronegative chlorine is probably present, some electron attachment will occur. In the limit of diffusion dominated electron decay, electron attachment to an impurity manifests itself by increasing the effective ambipolar diffusion constant [II-11]. Hence for a given initial electron density, the decay will be more rapid. In the Ne/CuCl system the chemistry is far more complex. Reactions such as [II-12]

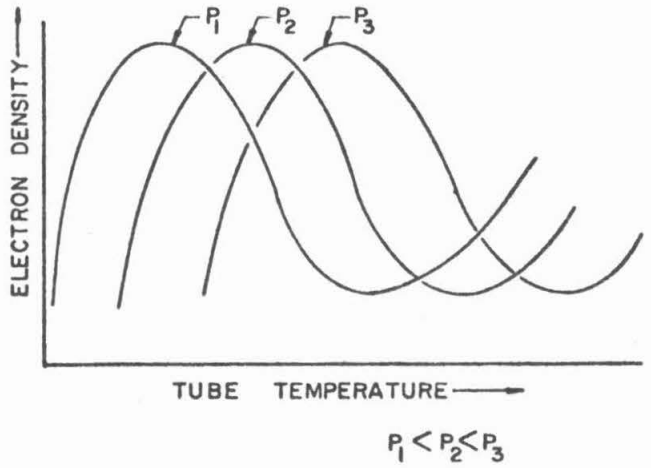

Figure II.9. The experimental results suggest the pattern illustrated here. As the buffer gas pressure is increased, the maximum and minimum in electron density shift to high tube temperatures (higher CuCl density).

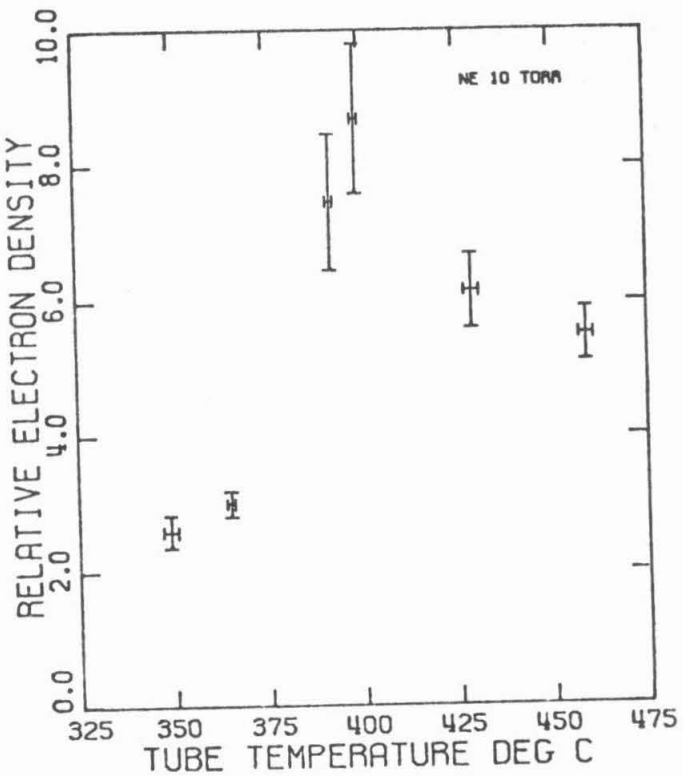

Figure II.10. Electron density measurements in a Ne/CuCl discharge using the double pulse power supply for excitation. For these data the tube temperature was held constant for each point.

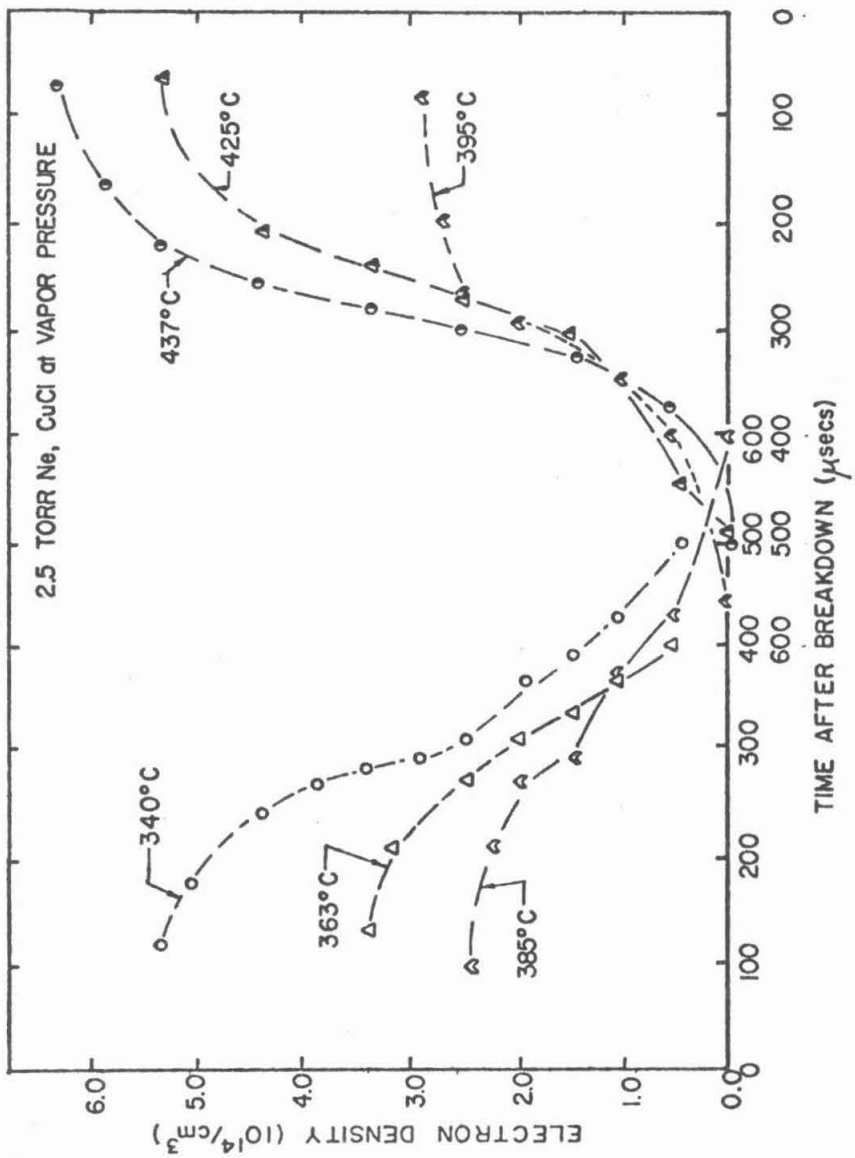

Figure II.11. The decay of electron density from its maximum value during the afterglow of a Ne/CuCl discharge.

$$Cl^- + Cu_mCl_n \rightarrow Cu_mCl_{n+1} + e$$

can be expected to occur with rate constants on the order of 10^{-9}-10^{-10}cm^3/sec which is comparable to expected electron attachment rates [II-11,13,14], and hence will tend to neutralize the effects of electron attachment.

A qualitative explanation of maxima in electron density as a function of buffer gas pressure and tube temperature follows. The charging voltages and tube geometry were not varied, so the maximum applied electric field can be considered a constant. The quantity E/N, the electric field divided by number density, is therefore a function of number density only; E/N ~ T/P where T is the gas temperature and P the gas pressure. At low values of E/N, the neon ionization coefficient and hence maximum electron density is a monotonically increasing function of E/N [II-11]. As E/N increases (i.e., temperature increases), the ionization coefficient reaches a maximum (at about E/N $\approx 1.4 \times 10^{-15}$Volt-cm^2) while simultaneously diffusion losses ($D \sim T^{\alpha}$, $1 < \alpha < 2$) begin to become important. The net result is a decrease in electron density. The sudden increase in electron density at higher temperatures reflects the exponential increase in the number density of CuCl ($N_{CuCl} \sim e^{.04T}$). The Cu and Cl have lower ionization potentials than neon (7.5 eV and 13 eV as compared to 21 eV for Ne), and can be ionized by a Penning reaction during a collision with a neon metastable. The effective ionization coefficient is larger, thereby increasing the maximum electron density. (Similar behavior

has been observed for argon as an impurity in neon [II-11].) This transition of the dominant ion from the noble gas to the impurity of lower ionization potential as the impurity level increases was reported by A. G. Gridnev, et al [II-15] for a discharge in neon and pure copper. Spontaneous emission from excited neutral and ionic neon was observed to decrease as the emission from neutral and ionic copper increased. Chen, et al [II-16] have also noted that spontaneous emission from excited helium decreases as the vapor pressure of CuCl and the spontaneous emission from copper increase.

The same experiment was performed for a discharge and afterglow in neon without CuCl. The maximum in electron density was again observed, but the increase in electron density at higher temperatures was absent.

Noble gas metastables may play a major role in explaining the results obtained above as they did in the discussion of electron temperatures in Section I.C. The influence of metastable Penning reactions on electron densities in the afterglow of discharges has been well documented (see for example [II-17]). Electron densities have been found to reach their highest values during the afterglow period [II-17]. The cause for the increase was attributed to electrons produced in Penning ionizations. The maximum in electron density was also found to occur in the afterglow during these measurements (see Figure II-11).

A correlation between the measured lifetime of neon metastables and the experimental results reported here has been made. It was

determined by Phelps and Molnar [II-18] that the lifetime of noble gas metastables in a microwave discharge afterglow is given by

$$\frac{1}{\tau} = \frac{D_o}{P\Lambda^2} + Ap + Bp^2 \qquad \text{(II.D.1)}$$

where

τ = metastable lifetime (sec)

D_o = Normalized diffusion constant (cm^2 - Torr/sec)

Λ = Diffusion length (cm)

P = Pressure (Torr)

A,B = constants

The terms on the RHS of (II.D.1) represent diffusion, two body reactions and three body reactions respectively. For neon at 300^oK, the values

D_o = 150 cm^2-Torr/sec, A = 50/sec-Torr, B = 0

were given. Using (II.D.1) and our experimental conditions the lifetimes of neon metastables are shown in Figure II-12. Also plotted in Figure II-12 is the relative number density of CuCl at a function of tube temperature. Note that over the wide range of temperatures plotted, the metastable lifetime at 2.5 Torr has no maximum. Metastable lifetimes at 5 Torr and 7.5 Torr show maxima, while that at 10 Torr has just reached its extreme value at the highest temperature shown. An exact correlation is not suggested here, as this experimental temperature range is much narrower than that shown in Figure II-12, and the characteristics of the microwave discharge and capacitor discharge used in the two studies are very different. However, the sequence of extrema in electron densities measured in the Ne/CuCl

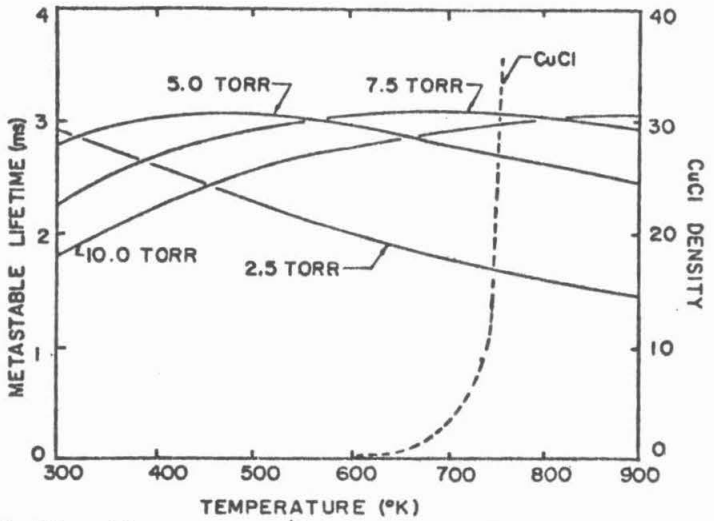

Figure II.12. The computed lifetime of neon metastable atoms in the absence of CuCl. The expression (II.D.1) and experimental parameters were used.

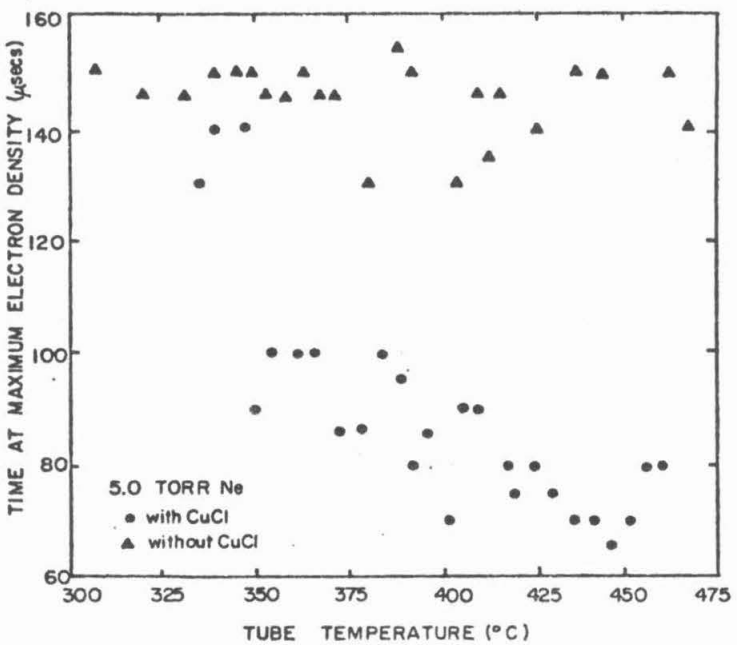

Figure II.13. The time after breakdown at which the electron density reaches its peak value in a Ne/CuCl discharge. As the CuCl vapor pressure increases, this value decreases.

discharge as a function of pressure and temperature follow exactly the sequence in extrema in metastable lifetimes shown in Figure II-12, provided the minima are associated with the intersection of the CuCl population curve and the metastable lifetime curves. One possible explanation for the experimental results suggested by this correlation is that a large fraction of the electron density measured is due to Penning reactions. The longer the lifetime of a metastable due to a non-Penning deactivation, the higher the probability of an electron being produced due to a Ne^*-Ne^* or Ne^*-CuCl reaction.

The production of a Penning electron requires the collision of two neon metastables (or excited neon atoms) or the collision of a single neon metastable with any other partner whose ionization potential is less than 16 eV. Hence if the Penning ionization cross sections for these possibilities are comparable (see Table IV.1), then as the CuCl "impurity" level exceeds the neon metastable density, the dominant Penning electron source will become due to Ne-Cu/Cl/CuCl collisions. Neon metastables are continually relaxing by non-Penning processes. Hence if the observed maximum in electron density is dominated by Penning reactions, the time at which the maximum occurs should decrease as the CuCl density increases. This is precisely the behavior that was observed. Figure II-13 shows the time at which the maximum electron density was observed for the discharge in 5.0 Torr of neon. The results are typical for all pressures. In the absence of CuCl, the time at which the maximum electron density occurs is constant. In the presence of increasing CuCl (i.e., tube temperature) the time

decreases.

II.E. Laser Pulse Energy: Experimental Arrangement

Following the electron density measurements, the same discharge tube was used as a copper laser, and laser energy measurements were made. To facilitate those measurements, the following changes were made to the setup. The NaCl windows were replaced by quartz windows. The excitation mechanism was replaced by a double-pulse power supply (see Appendix A). The discharge capacitor was 14.4 nF charged to 12.5 kV for both the dissociation and pumping pulses. The repetition rate was about 8 Hz. The mirrors were replaced by a 99% reflecting 4 m and a 20% reflecting 2 m mirror, dielectrically coated for 5106 $\mathring{A}$. The gas supply and heating systems remained the same.

Laser pulse energy is a sensitive function of the time delay between the dissociation and pumping discharge pulses. To display this dependence and determine the maximum laser energy as a function of delay (which are the values referred to here), the following scheme was employed. The first discharge pulse triggered the time base sweep of a storage oscilloscope whose intensity is controlled by the "z-axis" input. The second discharge pulse results in a laser pulse (a delta function for the time scales considered) which quickly charges a photodiode capacitor. Also with the second discharge pulse, a pulse generator is triggered. After a few microsecond delay (to avoid noise problems) the pulse generator sends a signal of a few microseconds

duration to the oscilloscope z-axis which records the photodiode capacitor discharge. By multiple exposure, a trace of laser energy as a function of time delay can be recorded (see Figure II-14).

II.F. Laser Pulse Energy Measurements and the Correlation with Electron Densities

For experimental convenience and reproducibility, the laser energy measurements were made while the tube temperature was held constant and the buffer gas pressure was varied. Optimum laser energy as a function of time delay and pressure are displayed in Figure II-15. Note that in each case the laser energy displays a maximum at low pressure, followed by a local minimum at higher pressure. The relative magnitude of the minimum increases as the tube temperature increases. If the local extrema in laser energy, and the local extrema in electron density are plotted on the gas pressure-tube temperature plane, the results found in Figure II-16 are obtained. One may correlate the maximum in laser energy with the local minimum in electron density, and the local minimum in laser energy with the local maximum in electron density. A similar correlation has been made in the positive column of the $He\text{-}Cd^+$ laser [II-19] where Penning ionization is believed to be a major pumping mechanism. (The correlation is much weaker in the $He\text{-}Se^+$ positive column laser where charge exchange is believed to be the pumping mechanism [II-20].) Again, the similarity between glow discharge characteristics and the results obtained here force one to consider the afterglow between discharge

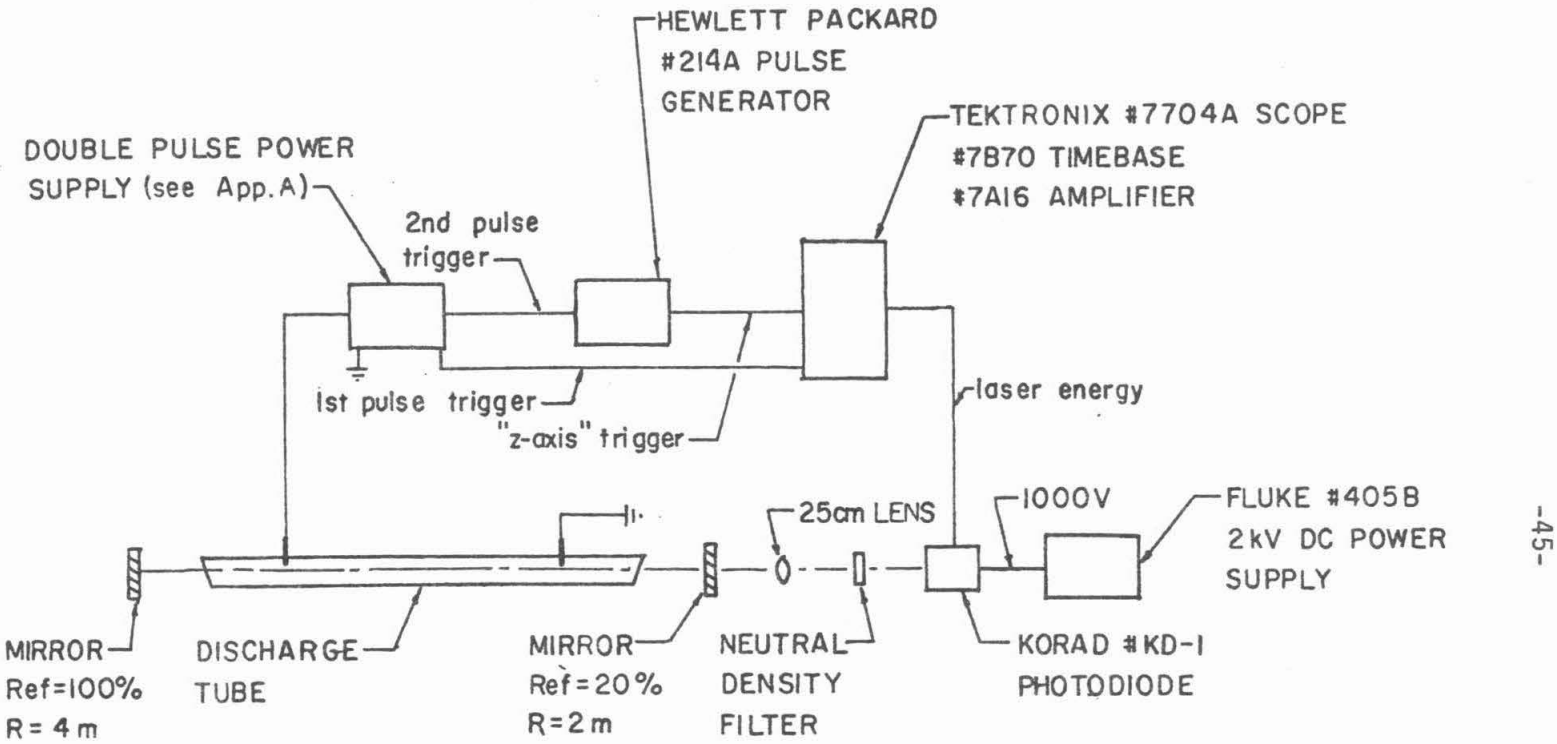

Figure II.14. Experimental setup for measuring laser energy as a function of time delay in a Cu/CuCl laser.

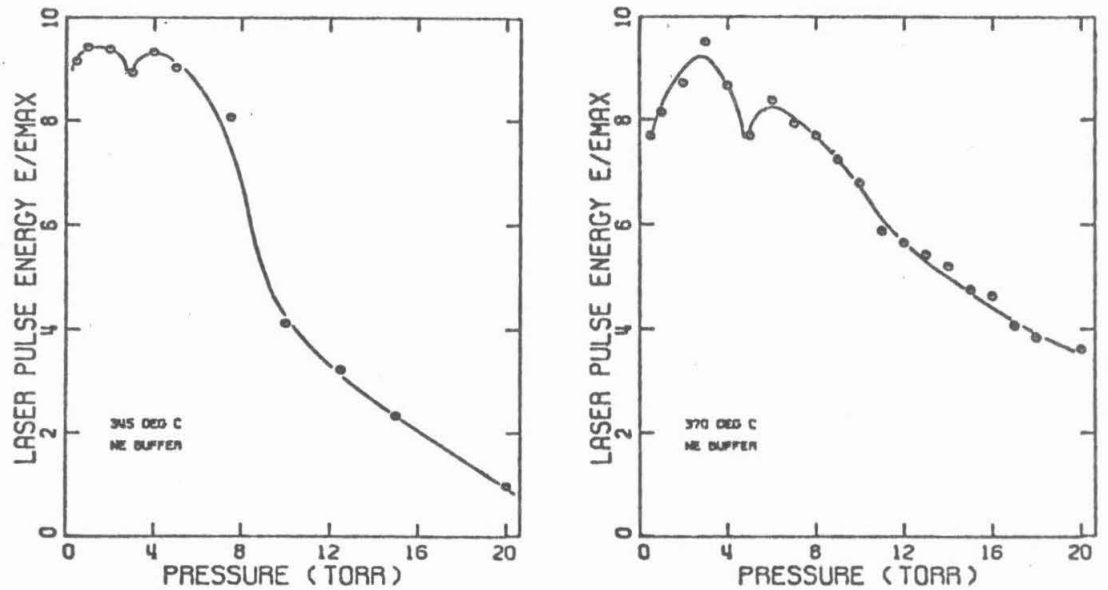

a) b)

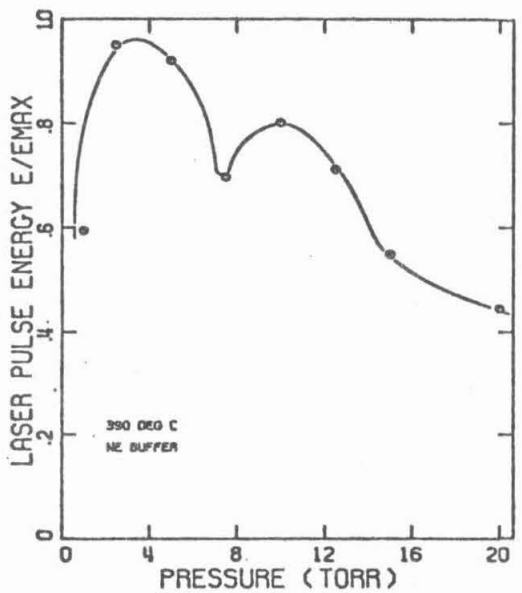

c)

Figure II.15. Optimum laser energy at constant tube temperature as a function of neon buffer gas pressure a) 345°C b) 370°C c) 390°C.

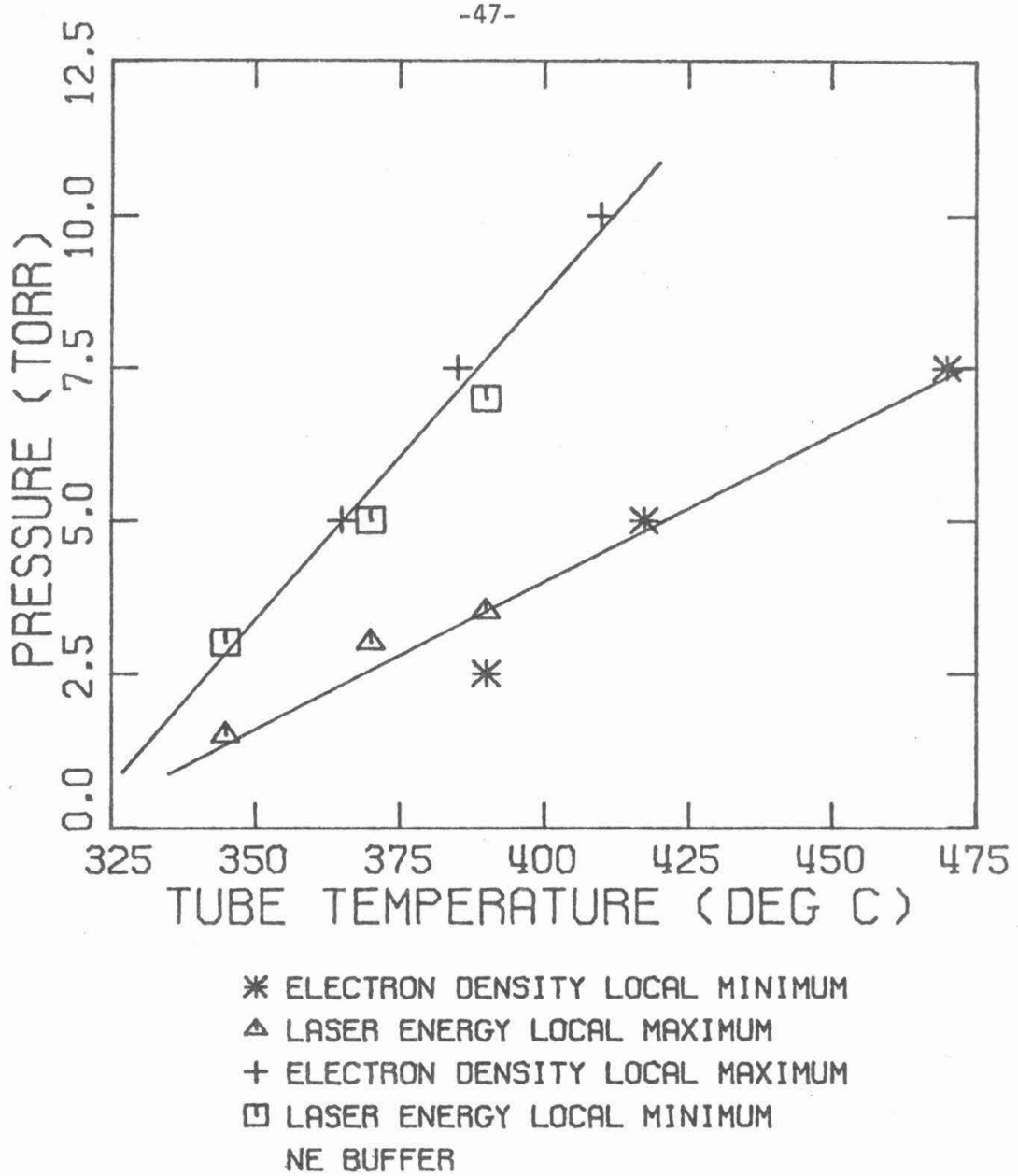

Figure II.16. When plotted as a function of tube temperature, pressures at which electron density is a minimum and laser energy is a maximum fall on a straight line. The same is true for electron density maximum and laser energy minimum.

pulses as a dominant factor in determining laser pulse energy.

If one were to assume a constant electron temperature independent of pressure, excitation rates would be directly proportional to the electron density. Hence the laser energy would be roughly proportional to the electron density. The opposite behavior has been observed here for all but the highest pressures and low electron densities. A monotonic decrease in electron temperature (at constant temperature and hence CuCl vapor pressure) with increasing buffer gas pressure is also unsatisfactory. For the range of electron temperatures measured experimentally (5-20 eV) [II-21] the total ionization rate for all species, as well as the Ne metastable excitation rate, is a monotonic increasing function of electron temperature [II-22,23]. Hence, the local minimum in laser energy would be difficult to explain. In the absence of a detailed accounting of the afterglow processes, one is led to assume that the electron temperature is proportional to the maximum electron density (at constant CuCl vapor pressure).

With the assumption made above, the behavior of laser energy as a function of gas pressure and tube temperature is explained as follows. The cross section for excitation to the upper laser level is known to be maximum near 18 eV [II-24]. The cross section for excitation to the lower level is maximum close to 10 eV. The ionization cross section from the ground state is maximum near 25 eV [II-25]. At low pressures (a few Torr), high electron density ($\sim 10^{15}/cm^3$) and high electron temperature ($\lesssim$20 eV), the ionization rate dominates. There are less copper ground state atoms available for excitation and laser

energy is low. As the electron temperature decreases to roughly 15 eV or less, the excitation rate to the upper laser level increases and the ionization rate decreases so that despite the lower electron density, the net excitation rate is higher and laser energy increases. At high pressure (~15 Torr), low electron density (~$10^{14}/cm^3$) and low electron temperature (~5 eV), the ionization rate is small as is the excitation rate to the upper level. Hence, despite the availability of ground state copper, the low electron density and excitation rate combine to keep laser energy small. The presence of extrema in laser energy is a consequence of a shift in electron temperature through the regions described above. A quantitative demonstration of the above will be found in the rate equation analysis, Section III.C.

The dependence of laser energy on buffer gas pressure is most complex for neon. The local minimum in laser energy has been previously observed in neon [II-26]. The dependence of laser energy on buffer gas pressure shown in Figure I-4 for helium is typical for tube temperatures less than optimum. When the temperature exceeds optimum, a local minimum in laser energy appears, and this minimum deepens as the temperature increases. This behavior is identical to that observed in neon at lower temperatures.

REFERENCES

1. D. E. T. F. Ashby and D. F. Jephcott, "Measurement of Plasma Density Using a Gas Laser as an Infrared Interferometer", Appl. Phys. Letters 3, 13 (1963).

2. J. B. Gerardo and J. T. Verdeyen, "Plasma Refractive Index by a Laser Phase Measurement", Appl. Phys. Letters 3, 121 (1963)

3. N. Konjevic and K. R. Hearne, "Measurement of Arc Electron Densities Using a CO_2 Laser", Phys. Letters 28A, 309 (1968).

4. J. B. Gerardo, J. T. Verdeyen and M. A. Gusinow, "High Frequency Laser Interferometry in Plasma Diagnostics", J. Appl. Phys. 36, 2146 (1965).

5. H. Herold and F. C. Jahoda, "CO_2 Laser Interferometer for the Measurement of Transient Low Density Plasmas", Rev. Sci. Instr. 40, 145 (1969).

6. K. S. Thomas, "Measurement of θ-Pinch End Loss Using a Gas Laser Interometer", Phys. Fluids 11, 1125 (1968).

7. R. A. Hill and J. B. Gerardo, "Stark Broadening of H_β, H_γ, and H_δ: An Experimental Study", Phys. Rev. 162, 45 (1967).

8. G. D. Boyd and H. Kogelnik, "Generalized Confocal Resonator Theory", Bell System Tech. J. 41, 1347 (1962).

9. J. B. Gerardo and J. T. Verdeyen, "The Laser Interferometer: Application to Plasma Diagnostics", Proc. IEEE 52, 690 (1964).

10. D. C. Tyte, "Carbon Dioxide Lasers", Advances in Quant. Electronics 1, 129 (1970).

11. S. C. Brown, Basic Data of Plasma Physics, MIT Press, Wiley, Massachusetts, 1959.

12. E. W. McDaniel, V. Cermak, A. Dalgarno, E. E. Ferguson, and L. Friedman, Ion Molecule Reactions, Wiley-Interscience, New York, 1970.

13. L. B. Loeb, Basic Properties of Gaseous Electronics, University of California Press, Berkeley, 1960.

14. E. W. McDaniel, Collision Phenomena in Ionized Gases, Wiley, New York, 1964.

15. A. G. Gridnev, T. M. Gorbunova, V. F. Elaev, G. S. Evtushenko, N. V. Osipova, and A. N. Soldatov, "Spectroscopic Investigation of a Gas Discharge Pulse Plasma of a Cu+Ne Laser", Sov. J. Quant. Electronics 8, 656 (1978).

16. C. J. Chen, N. M. Nerheim, and G. R. Russell, "Double-discharge Copper Vapor Laser with Copper Chloride as a Lasant", Appl. Phys. Letters 23, 514 (1973).

17. M. A. Biondi, "Diffusion, De-Excitation and Ionization Cross Sections for Metastable Atoms I", Phys. Rev. 88, 660 (1952).

18. A. V. Phelps and J. P. Molnar, "Lifetimes of Metastable States of Noble Gases", Phys. Rev. 89, 1202 (1953).

19. T. Goto, A. Kawahara, G. J. Collins and S. Hattori, "Electron Temperature and Density in Positive Column $HeCd^+$ Lasers", J. Appl. Phys. 42, 3816 (1971).

20. T. Goto, H. Hano, and S. Hattori, "Plasma Parameters in Gas Dis-

charges for Position-column He-Se^+ Lasers", J. Appl. Phys. 43, 5064 (1972).

21. E. Sovero, C. J. Chen, and F. E. C. Culick, "Electron Temperature Measurements in a Copper Chloride Laser Utilizing a Microwave Radiometer", J. Appl. Phys. 47, 4538 (1976).

22. C. Deutsch, "Excitation and Ionization of Neutral Atoms in a Dense Discharge", J. Appl. Phys. 44, 1142 (1973).

23. J. Delcroix, C. Ferreira, and A. Ricard, "Metastable Atoms and Molecules in Ionized Gases" in Principles of Laser Plasmas, ed. G. Bekifi, Wiley, New York, 1976.

24. S. Trajmar, W. Williams, and S. K. Srivastova, "Electron-impact Cross Sections for Cu Atoms", J. Phys. B10, 3323 (1977).

25. M. Gryzinski, "Classical Theory of Atomic Collisions.I. Theory of Inelastic Collisions", Phys. Rev. 138, A336 (1965).

26. T. Pivirotto, private conversation.

III. AN ANALYSIS OF THE Cu LASER BASED ON RATE EQUATIONS

III.A. Introduction

The copper laser, and cyclic metal vapor lasers in general, are ideal subjects for an analysis based on rate equations. The system is modeled nicely by three levels (ground, metastable and resonance states), and the length of the laser pulse is short enough (nanoseconds) so that most processes proceeding at thermal speeds can be ignored.

In the analysis that follows, we will first attempt to reproduce the experimentally measured laser energies discussed in Chapter II with rate equations using initial conditions based on the electron density measurements. With this preparation as a background, other experimentally observed behavior will be investigated.

This treatment was designed with computational speed and convenience in mind. Therefore all quantities are spatially averaged. For an exact treatment of the electric field in a pulsed copper laser, see Section VI. (The kinetic rates discussed here are also used in the exact treatment.)

III.B. The Rate Equation Model

For the purposes of this analysis, the following assumptions have been made:

a) The instantaneous electron density is proportional to the discharge current. The shape of the current pulse is taken to be parabolic which is a close fit to the experimentally observed shape.

The dependence of peak electron density on tube temperature and buffer gas pressure is given by the experimental results of Chapter II.

b) The electron temperature is constant for each current pulse and is proportional to the maximum electron density. This assumption is discussed in Section II.F.

c) Recombination processes are ignored.

d) CuCl is completely disassociated, and the chlorine is ignored.

e) Relaxation processes from the Cu metastable state are ignored.

f) Only the 5106$\mathring{A}$ $^2P_{\frac{3}{2}} \rightarrow {}^2D_{\frac{5}{2}}$ line is considered.

g) Stimulated emission is averaged over a Doppler lineshape for intensity and gain.

h) The optical cavity has a 100% reflection mirror and an output mirror of reflectivity R.

i) Direct coupling to the buffer gas is made by including a noble-gas-copper collision term.

The following species were included in the rate equations.

C_G Copper $^2S_{\frac{1}{2}}$ ground state

C_L Copper $^2D_{\frac{5}{2}}$ lower laser level

C_U Copper $^2P_{\frac{3}{2}}$ upper laser level

N_G Noble buffer gas ground state

N_m Noble buffer gas metastable state

I Cavity intensity (ergs/cm^2-sec)

The copper laser rate equations are:

$$\frac{d}{dt}C_U = n_e(t)\,(r_{G\to U}\,C_G - r_{U\to ION}C_U) - (A_1+A_2)C_U$$

$$- \sum_{\ell} r_{\ell} C_U N_{\ell} - \acute{B}I\left(C_U - \frac{g_U}{g_L}\,C_L\right) - \frac{D_1}{L_d^2} \qquad \text{(III.B.1)}$$

$$\frac{d}{dt}C_L = n_e(t)(r_{G\to L}C_G - r_{L\to ION}C_L) + A_1C_U - \sum_{\ell} r_{\ell} C_L N_{\ell}$$

$$+ \acute{B}I\left(C_U - \frac{g_U}{g_L}\,C_L\right) - \frac{D_1}{L_d^2}\,C_L \qquad \text{(III.B.2)}$$

$$\frac{d}{dt}C_G = -n_e(t)(r_{G\to U} + r_{G\to L} + r_{G\to ION})C_G + A_2C_U$$

$$- \sum_{\ell} r_{\ell} C_G N_{\ell} + \frac{D_1}{L_d^2}(C_L + C_U) \qquad \text{(III.B.3)}$$

$$\frac{d}{dt}N_m = n_e(t)(r_{G\to m}N_G - r_{m\to ION}N_m) - \frac{D_2}{L_d^2}\,N_m$$

$$-r_p N_m(C_G + C_L + C_U + 2N_m) \qquad \text{(III.B.4)}$$

$$\frac{d}{dt}N_G = n_e(t)N_G(r_{G\to ION} + r_{G\to m}) + \frac{D_2}{L_d^2} N_m + r_p N_m(C_G + C_L + C_U + 2N_m) \qquad \text{(III.B.5)}$$

$$\frac{d}{dt}I = IB(C_U - \frac{g_U}{g_L} C_L) + A_1\beta C_U - \frac{c}{L}(1-R)I \qquad \text{(III.B.6)}$$

where

C_K = density of copper level K(/cm^3)

N_K = density of noble gas level K(/cm^3)

$r_{J\to K}$ = rate constant for electron impact excitation from level J to K (where K may be the ionization continuum or other levels. See discussion below.) (cm^3/sec)

r_ℓ = rate constant for buffer gas collision process ℓ (cm^3/s)

$n_e(t)$ = electron density (/cm^3)

D_i = diffusion coefficient (cm^2/sec)

L_d = diffusion length (cm)

L = tube length (cm)

β = geometrical factor

A_1, A_2 = spontaneous emission coefficient $^2P_{\frac{3}{2}} \to {}^2D_{\frac{5}{2}}$, $^2P_{\frac{3}{2}} \to {}^2S_{\frac{1}{2}}$ (/sec)

B', B = stimulated emission coefficient (cm^2/erg, cm^3/sec)

R = output mirror reflectivity

g = level degeneracy

The model is illustrated in Figure III-1.

III.B.1 The Optical Model

We have assumed a uniform spatially averaged intensity I. The rate of loss of intensity from the cavity is given by $-I\frac{c}{L}(1-R)$. Parasitic losses can be included by the additional term $-IL\alpha$ where α is the fractional loss/cm, or by decreasing R. The laser output energy density averaged over the volume of the optical cavity is

$$E_L = \int_0^\infty I\frac{c}{L}(1-R)dt \text{ ergs/cm}^2 \qquad \text{(III.B.7)}$$

We have assumed a Doppler intensity profole

$$I_\nu d\nu = Ig(\nu)d\nu \qquad \text{(III.B.8)}$$

where I_ν is the monochromatic intensity per unit frequency and $g(\nu)$ is the Doppler lineshape. If we ignore for the moment spontaneous emission and assume the intensity to be directed along the z-axis, the power density per unit frequency is [III-1].

$$\frac{dI_\nu}{dz} = \frac{dI_\nu}{dt}\frac{1}{c} = \frac{c^2 A_1 I_\nu}{8\pi\nu^2}\left(C_U - \frac{g_U}{g_L}C_L\right)g'(\nu) \qquad \text{(III.B.9)}$$

where $g'(\nu)$ is the gain profile. The time rate of change of intensity

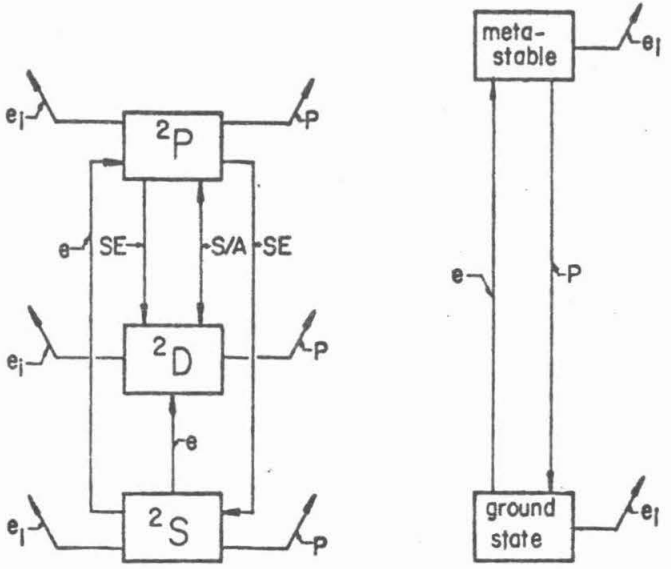

$$\frac{dI}{dt} = BI(^2P - \frac{g_u}{g_l}{}^2D) - I(a + \frac{c}{L}(1-R)) + Af^2P$$

LEGEND:

I	INTENSITY
g	LEVEL DEGENERACY
a	DISTRIBUTED LOSSES
L	CAVITY LENGTH
f	GEOMETRICAL FACTOR
A	SPONT. EMISSION COEF.
R	OUTPUT MIRROR REFLECTIVITY
SE	SPONTANEOUS EMISSION
S/A	STIMULATED EMISSION/ABSORPTION
B	STIMULATED EMISSION COEF.
P	PENNING IONIZATION
e	ELECTRON IMPACT EXCITATION
e_i	ELECTRON IMPACT IONIZATION/ LOSS

Figure III.1. Rate equation model of the copper laser.

is then

$$\frac{dI}{dt} = \int_0^\infty \frac{dI_\nu}{dt}\, d\nu = \frac{c^3 A_1 I_\nu}{8\pi\nu^2}\left(C_U - \frac{g_U}{g_L} C_L\right)\, g(\nu)d\nu$$
$$= I \int_0^\infty \frac{c^3 A_1}{8\pi\nu^2}\, g'(\nu)g(\nu)\left(C_U - \frac{g_U}{g_L} C_L\right)d\nu \qquad \text{(III.B.10)}$$

The Doppler lineshape and gain profile are given by [III-1]

$$g(\nu) = \frac{2(\ell n\ 2)^{1/2}}{\pi^{1/2}\Delta\nu_D} \exp(-4\ell n2(\nu-\nu_o)^2/\Delta\nu_D) \qquad \text{(III.B.11)}$$

where

$$\Delta\nu_D = 2\nu_o\left(\frac{2kT_g}{Mc^2}\ \ell n\ 2\right)^{1/2} \text{ (/sec)}$$

T_g = gas temperature (^oK)

M = atomic mass (g)

k = Boltzman's constant (ergs/^oK)

ν_o = center line frequency (/sec)

Let $\kappa = 2\frac{(\ell n2)^{1/2}}{\pi\Delta\nu_D}$, $\alpha = \frac{c^3}{8\pi} A_1\left(C_U - \frac{g_U}{g_L} C_L\right)$, $\delta = \frac{8\ell n2}{\Delta\nu_D{}^2}$

so that (III.B.10) becomes

$$\frac{dI}{dt} = I\kappa^2\alpha \int_0^\infty \frac{e^{-\delta(\nu-\nu_o)^2}}{\nu^2}\, d\nu \qquad \text{(III.B.12)}$$

The exponential is highly peaked about the centerline frequency ν_o, so that nonzero values can be expected only for $\nu \approx \nu_o$. Hence the ν^2 in

the denominator of (III.B.12) can be taken out of the integral and set equal to ν_o^2. The integral can now be done, and (III.B.12) becomes

$$\frac{dI}{dt} = \frac{I\kappa^2\alpha}{2\nu_o^2}\left(\frac{\pi}{\delta}\right)^{1/2} \tag{III.B.13}$$

The total time rate of change in cavity intensity is then

$$\begin{aligned}\frac{dI}{dt} &= I\left(\frac{c^4 A_1}{32\pi^{3/2}\nu_o^3}\left(\frac{kT_g}{M}\right)^{1/2}\right)\left(C_U - \frac{g_U}{g_L}C_L\right) - \frac{c}{L}(1-R)) \\ &= I(B(C_U - \frac{g_U}{g_L}C_L) - \frac{c}{L}(1-R))\end{aligned} \tag{III.B.14}$$

where

$$B = \frac{c^4 A_1}{32\pi^{5/2}\nu_o^3}\left(\frac{M}{kT_g}\right)^{1/2}$$

Initially I = 0, so to get the pulse started, the term $A_1\beta C_U$ is added to (III.B.14) where β is a geometrical correction factor, expressing the probability that spontaneous emission will remain within the cavity and form the basis for stimulated emission. The stimulated emission coefficient B' in terms of B is

$$B' = \frac{B}{2ch} \tag{III.B.15}$$

where h is Planck's constant.

III.B.2 Cross Sections and Excitation Rates

The excitation rate r is defined as

$$r = \int_0^\infty f(v) v \sigma(v)\, dv$$

where $f(v)$ is the electronic velocity distribution function and $\sigma(v)$ the cross section. The distribution function is in general non-Maxwellian (see Section IV.B). Instead, a semiempirical distribution function was used. Bond [III-2] found that in neon glow discharges a strong applied electric field actually shifts the distribution function in energy rather than merely imparting a drift velocity. Bond found that

$$f(v) = a\, v^2\, e^{-b^4 v^4} \qquad \text{(III.B.16)}$$

where a is a normalization constant and b is an experimental parameter. The normalization condition is

$$\int_0^\infty f(v) v^2 dv = 1 = a \int_0^\infty v^4 e^{-b^4 v^4}\, dv \qquad \text{(III.B.17)}$$

$$a = \frac{4b^5}{\Gamma(\frac{5}{4})}$$

To solve for b, define the electron temperature T_e and require that

$$\frac{3}{2} kT_e = \bar{\varepsilon} = \int^\infty \frac{1}{2} m v^2 f(v) v^2 dv = \frac{m}{2b^2} \frac{\Gamma(\frac{7}{4})}{\Gamma(\frac{5}{4})}$$

$$b = \left(\frac{m}{3kT_e} \frac{\Gamma(\frac{7}{4})}{\Gamma(\frac{5}{4})} \right)^{1/2} \sim \frac{1}{T_e^{1/2}} \qquad \text{(III.B.18)}$$

Therefore, by specifying an average electron energy, the distribution is determined.

The copper excitation cross sections were taken from the works of Trajmar, et al [III-3], Leonard [III-4] and Borozdin, et al [III-5]. Noble gas metastable excitation cross sections were taken from the work of Vriens [III-6]. Due to the high electron temperatures during the pumping pulse of the Cu/CuCl laser [III-7] ionization and other electron impact losses from all copper levels will be important. Ionization is included as a quenching mechanism. The ionization rate may be considered a generic electron impact loss term. Gryzinski cross sections were initially used for ionization. These were later revised (see discussion below).

III.B.3 Coupling of Copper to the Buffer Gas

Direct coupling of the buffer gas to the copper is obtained through the term $\sum_{\ell} r_{\ell} N_{\ell} Cu$ where r_{ℓ} is the rate constant for the ℓ^{th} process and N_{ℓ} is the density of the particular noble gas state. The only direct coupling considered here is Penning ionization, though the rate of quenching may be considered generic for all noble gas - Cu collision processes.

III.B.4 Diffusion

In general, the diffusion terms can be ignored. The self diffusion coefficient for Ne can be written as [III-8].

$$D \simeq 2.4 \times 10^{-5} \left(\frac{760}{P_{Torr}}\right) T_{^oK}^{1.8} \qquad \text{(III.B.19)}$$

For a cylindrical geometry, the typical diffusion time is [III-9]

$$\tau \approx \frac{a^2}{Dk_o^2} \qquad \text{(III.B.20)}$$

where a is the radius of the tube and k_o is the first zero of the first order Bessel function. For typical experimental values $\tau = 4 \times 10^{-4}$ sec which is long compared to the times of interest.

III.C. Computed Laser Pulse Energy as a Function of Buffer Gas Pressure

In Chapter II, a correlation was made between extrema in electron densities and extrema in laser energy for particular discharge conditions. A qualitative explanation given for the behavior stated that the electron density and electron temperature shifted as a function of tube temperature and buffer gas pressure in such a way that either the laser excitation rates or the ionization rates were dominant (see Section II.F). This hypothesis is put into more quantitative terms by attempting to simulate those results with the rate equations discussed above.

The rate equations were integrated over a parabolic current pulse having a full width of 100 ns. The maximum electron density for a given gas temperature and pressure was given by a fit to the experimental data taken in the neon discharge and afterglow. The electron temperature was assumed to scale linearly with the maximum electron density, and was kept constant throughout the current pulse. The gas temperature and pressure corresponding to the local minimum in

electron density as given by the discharge and afterglow measurements were assigned values of $n_{e_{max}} = 1.0 \times 10^{14}/cm^3$ and $T_e = 10.0$ eV.

The upper and lower laser levels were assumed to be empty at the start of the current pulse. This estimate is quite good for the upper level. The untrapped spontaneous emission lifetime of the upper level to the ground state is 10 ns, while typical optimum time delays are tens of microseconds. From the work of Nerheim [III-10] and Tenenbaum [III-11], the metastable state is virtually empty at the optimum delay.

Using the conditions discussed above, the results shown in Figure III-2 were obtained for neon at T = 370°C. Optimum laser pulse energy as a function of gas pressure closely resembles the experimental values. The dip at 2.5 Torr corresponds to the local minimum in excitation rate. By increasing the magnitude of the Gryzinski ionization cross section (while retaining its energy dependence) the fit to experimental results improved (see Figure III-3). The necessity to increase the Gryzinski cross sections may reflect the importance of other electron impact quenching reactions (such as excitation to other levels) or Gryzinski cross sections may be inappropriate for ionization out of excited states.

The case shown in Figure III-3 is typical for other temperatures. The laser energy maxima and local minimum are well reproduced but the second local maximum is too large and appears at a higher pressure than observed in the experiment. The decrease in laser energy at high pressure is also more prominant than that measured. This discrepancy

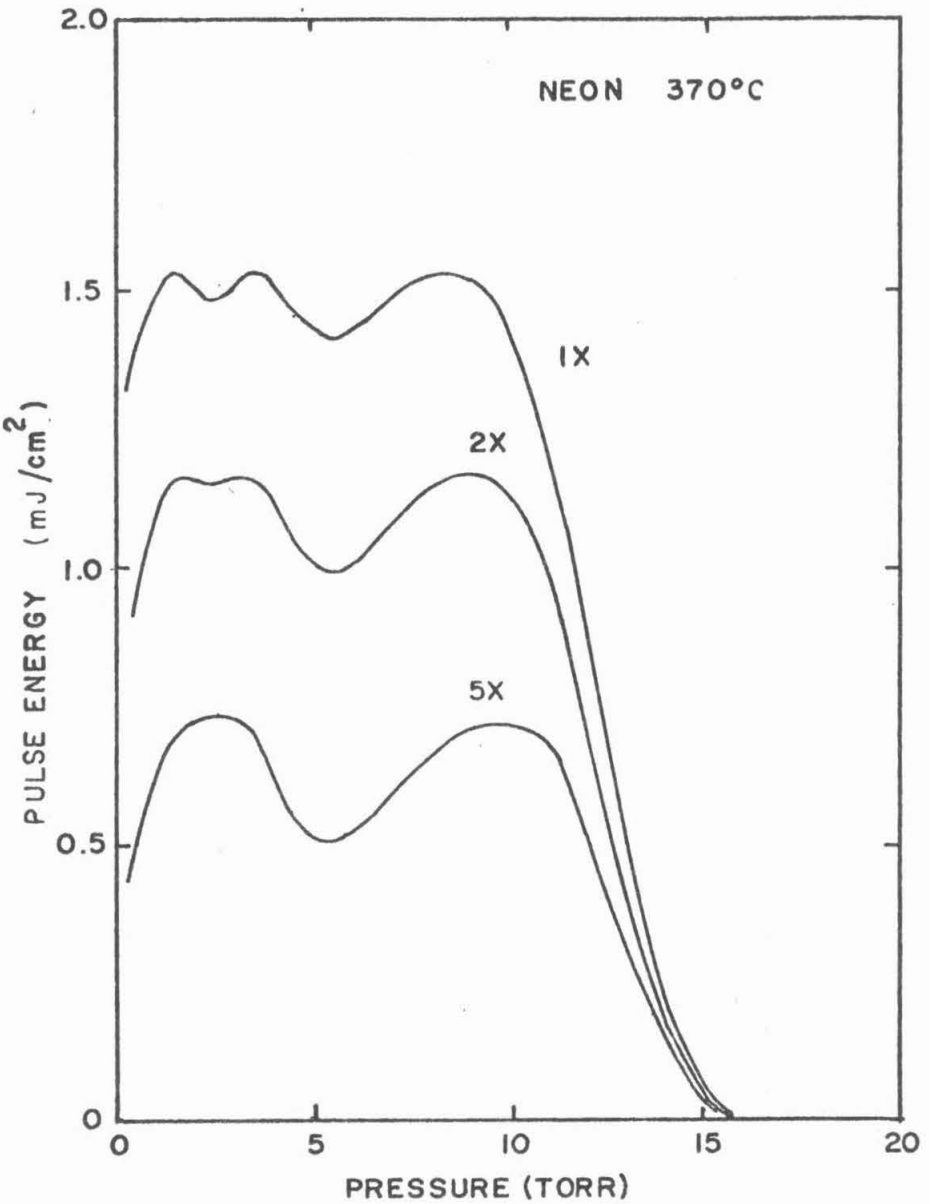

Figure III.2. Computed laser pulse energy as a function of neon buffer gas pressure. The powers indicate by what factor the Gryzinski cross section for electron impact losses was increased.

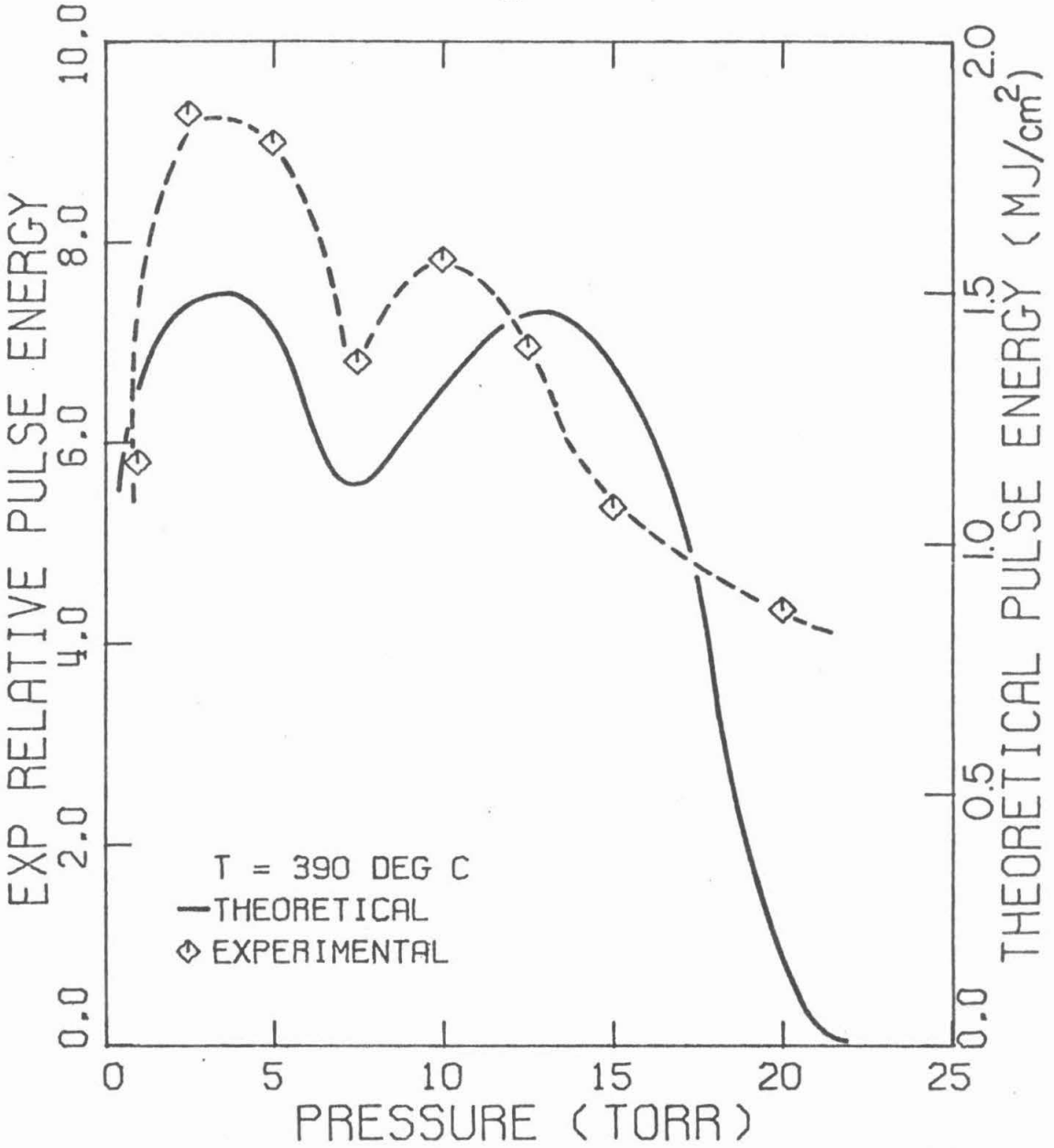

Figure III.3. Computed laser pulse energy as a function of neon buffer gas pressure compared with experimental data. The normalization of the experimental data is for ease of comparison.

can in part be attributed to the difference in characteristics between the double pulse laser discharge and interpulse afterglow, and the discharge which provided the basis for input data to the rate equations.

Since the discrepancy discussed above occurs at higher pressures, the magnitude of the coupling of the copper to the buffer gas was increased. With no neon metastables present at the beginning of the current pulse, the Penning ionization cross section was varied from $5x10^{-16}cm^2$ to $1.0x10^{-14}cm^2$. The change in laser energy at high pressure was at most a few percent. With a cross section of $5x10^{-15}cm^2$, the fraction of neon metastables present at the beginning of the pumping discharge pulse was varied from .001 to .1. The maximum at high pressure reduced only 5% with the largest fraction. The failure to match experimental results when the Penning ionization cross section was increased with no neon metastable initially present is a result of the rapid appearance of the laser pulse. The laser pulse appears in the first 20 ns of the current pulse, a time too short for the neon metastable population to build up. Increasing the initial fraction of neon metastables achieves some level of success in lowering the second extrema, however, the fractions required are unrealistically large (see Section VI).

Penning ionization, other quenching collisions (e.g., charge exchange), and diffusion proceed at thermal speeds. Hence their importance during the laser pulse (20-40 ns long) is minimized. During this short period, atomic processes are nearly frozen. If these

processes are to be important, their influence must come during the relatively long afterglow between discharge pulses. The qualitative agreement with experiment yielded by this analysis is further motivation to study the afterglow more carefully.

III.D. Laser Pulses

Despite the simplicity of the rate equation analysis, a great deal of insight into the CuCl double pulse laser operation can be obtained from its use. Many experimental results can now be explained.

Copper densities, output intensity and gain for a typical discharge pulse at 370°C are shown in Figures III-4 and 5 . The initial electron temperature was 10.0 eV and the maximum electron density was $1.0 \times 10^{14}/cm^3$. The current pulse was parabolic with a full width of 100 ns. The electron temperature was decreased as a function of time into the pulse; $T_e(t) = T_e(o)e^{-t/t_m}$ where t_m is the full width of the current pulse. (Because the laser pulse appears at the leading edge of the current pulse, decreasing the electron temperature instead of holding it constant has almost no effect on laser energy. It does affect the copper densities late into the pulse.) This time dependence closely fits experimental measurements of the electron temperature [III-7]. At the start of the pumping pulse, the excitation rate to the upper level is five times larger than the rate to the lower level. The gain reaches a maximum value of .11/cm at which time the cavity intensity obtains a critical value and the upper level rapidly dumps to the lower level. The number density of the upper level drops

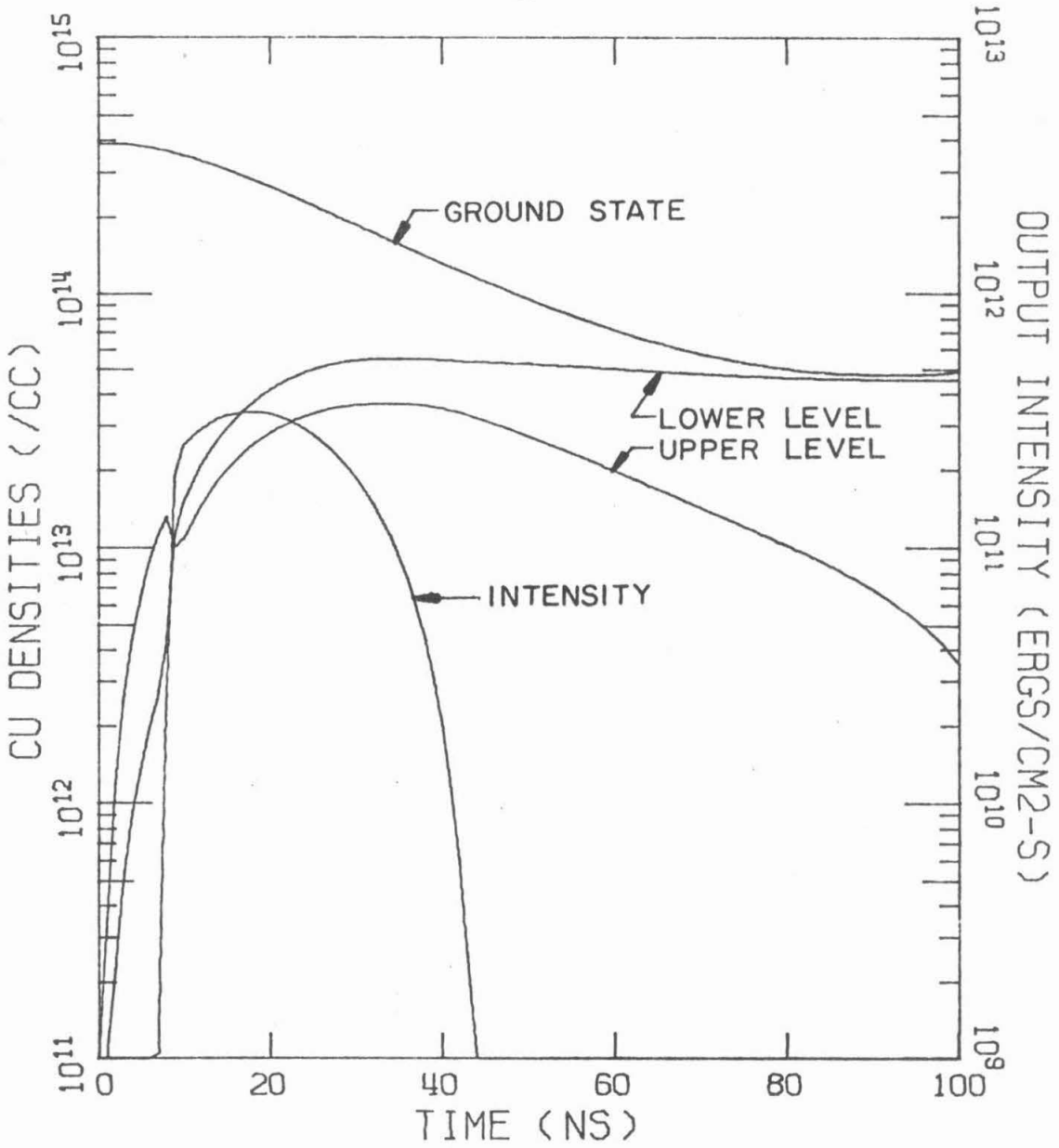

Figure III.4. Copper density and output laser intensity for a discharge in neon at 370°C. The initial electron temperature was 10.0 eV. Peak electron density was $1.0 \times 10^{14} cm^3$.

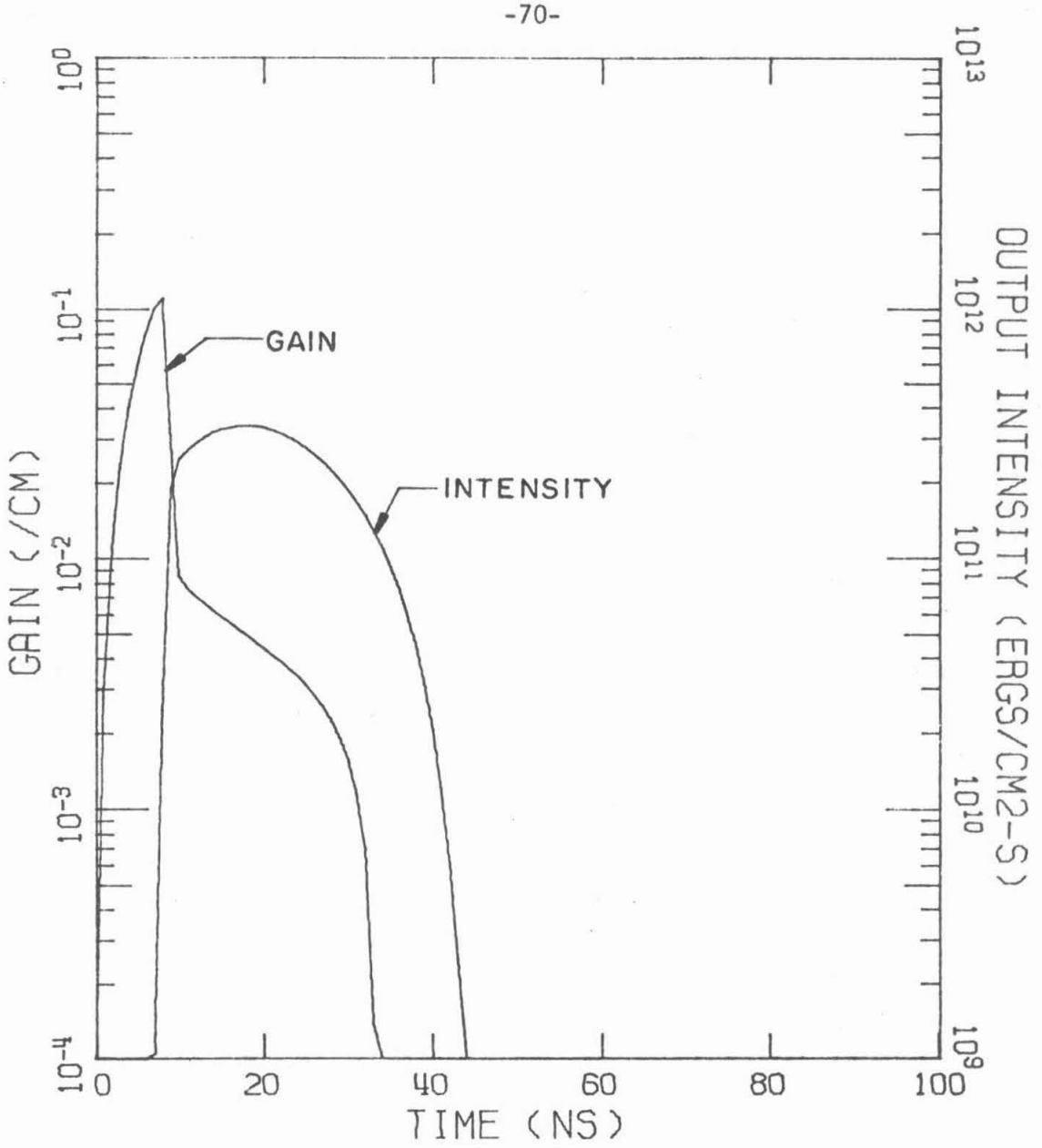

Figure III.5. Gain and output laser intensity for the conditions of Figure III.4.

below that of the lower level. The gain remains positive for a short time due to the favorable degeneracy ratio. Because of this gain switched behavior, laser energy will be determined largely by the magnitude of the gain at the time the upper level dumps to the lower level. A major quenching mechanism of the laser pulse is depletion of the ground state due to electron impact which reduces the rate of pumping to the upper level. The upper level is also quenched by electron impact.

Using the assumptions previously discussed for relating electron density and temperature to gas pressure and tube temperature, maximum gain, pulse width, laser energy, and peak gain are shown in Figure III-6.

III.E. The Dependence of Laser Energy on Output Mirror Reflectivity

The dumping of the upper laser level to the lower level at critical field and gain values helps to explain the relative independence of laser energy on mirror reflectivity. Experimentally, laser energy has been found to be nearly independent of mirror reflectivity for values from zero to 99% for the output mirror [III-12,13]. By varying the output mirror reflectivity in the rate equations, the results in Figure III-7 are obtained. Laser energy is found to be nearly constant at small reflectivity and diminish slightly high reflectivity. The maximum gain stays nearly constant, falling slightly at high reflectivity. The upper level dumps to the lower laser level at slightly earlier times at high reflectivity. The decrease

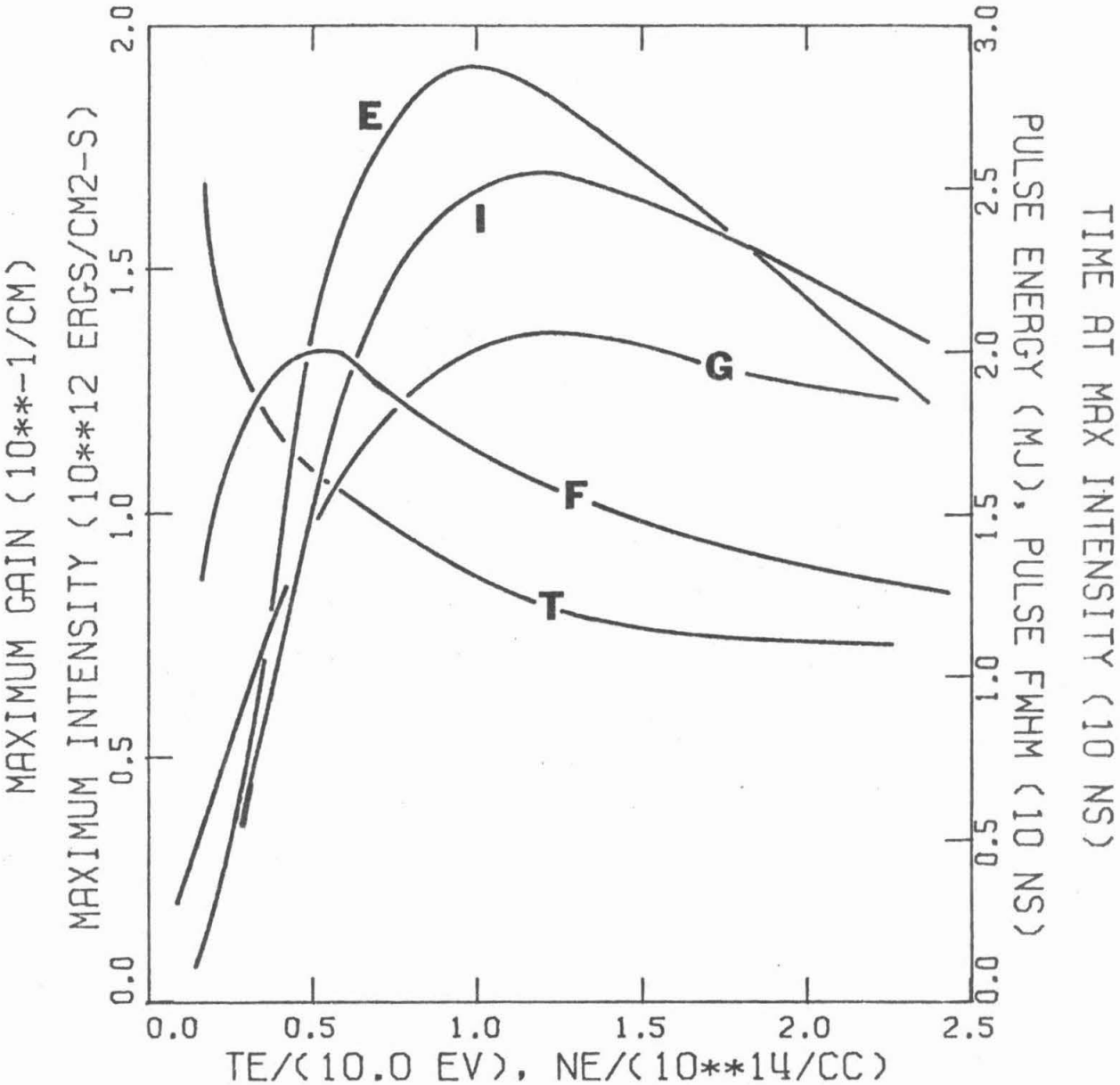

Figure III.6. Maximum gain (G), pulse width (F), laser energy (E), peak intensity (I), and the time (T) at which the peak intensity occurs as a function of electron temperature and density.

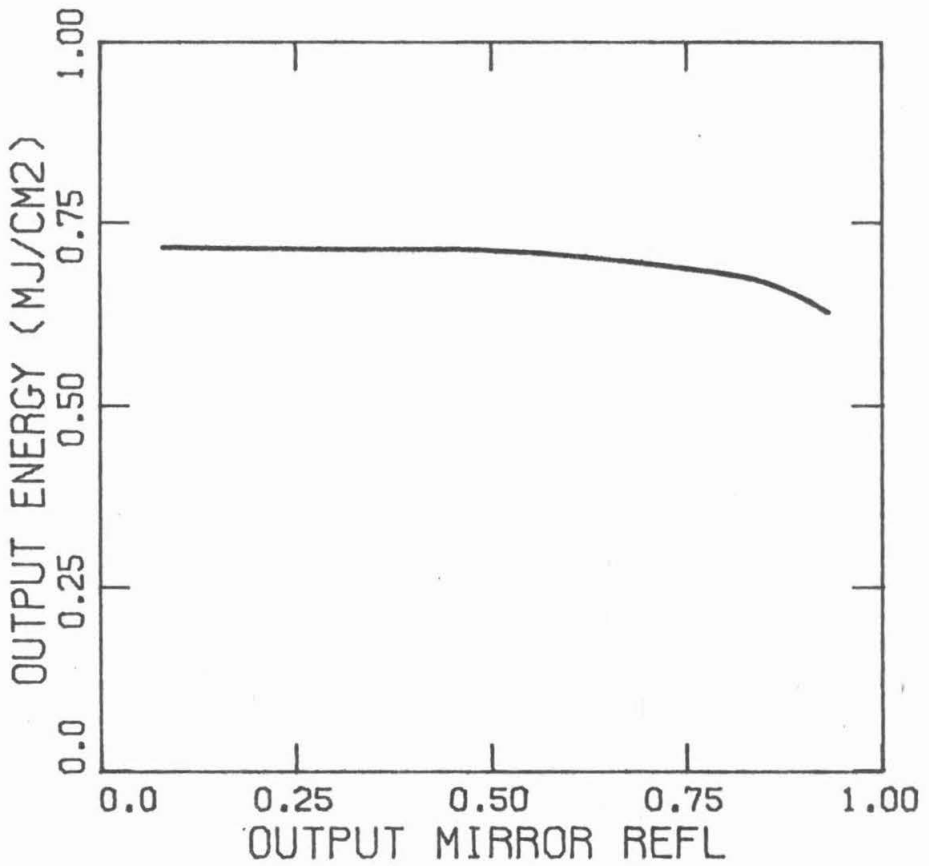

Figure III.7. Laser energy as a function of output mirror reflectivity.

in laser energy at high reflectivity is a result of the critical field being achieved before gain has been maximized. The relative independence of laser energy at low reflectivity indicates the rapidity with which the critical field is achieved.

In Figure III-8, the laser output intensity for various mirror reflectivities is shown. Remember that for each case, laser energy is nearly constant. In the absence of scattering and diffraction losses, the cavities with high Q values result in wider pulses. This increase in pulse width as the output mirror reflectivity is increased has been verified experimentally (see Figure III-9).

III.F. The Dependence of Laser Energy on the Rate of Current Rise of the Pumping Pulse

Another consequence of the gain switching discussed above can be found with experimental work by Vetter [III-14] and Bokhan, et al [III-15]. It was found that by lowering the circuit inductance and decreasing the current rise time, laser energy increased linearly with the log of the rate of current rise. To simulate the lowered inductance numerically, the slope of the current rise was increased while keeping the integrated electron density constant. The experimental results of Vetter [III-14] and calculated results are shown in Figure III-10. The rate equation analysis has reproduced the experimental dependence of laser energy on the rate of current rise. A similar dependence was computed for the maximum gain. The saturation of laser pulse energy at high current slopes seen numerically was also

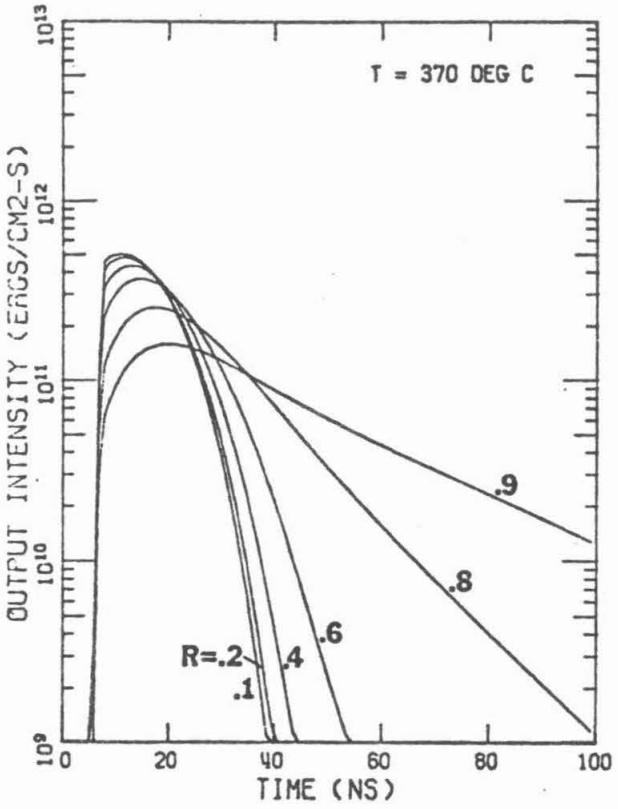

Figure III.8. Output intensity as a function of output mirror reflectivity.

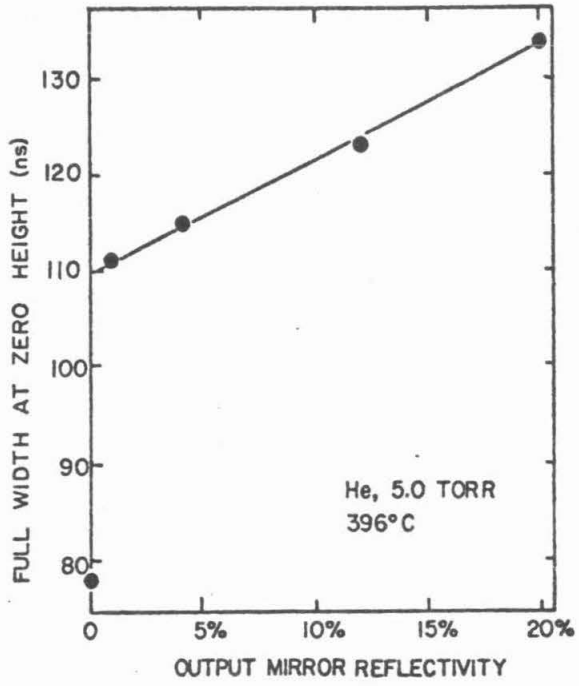

Figure III.9 Experimental laser pulse widths as a function of output mirror reflectivity.

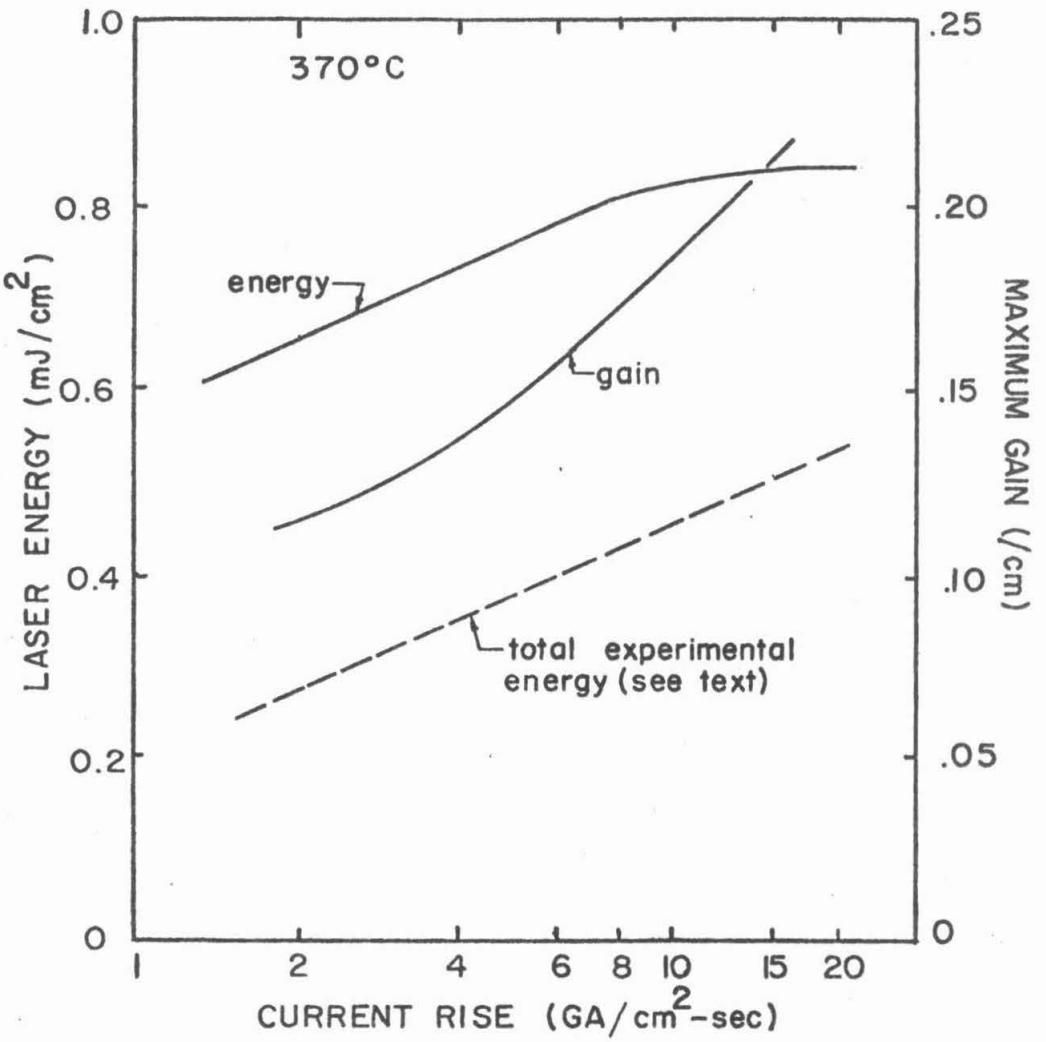

Figure III.10. Laser energy and gain as a function of the rate of current rise of the pumping pulse.

indicated experimentally [III-15,16]. Once the upper laser level is populated, a finite time is required (due to a finite spontaneous emission coefficient) for the cavity electric field to build up to its "critical value"; that value which will dump the upper level. A current which rises faster populates the upper level during this small but finite time more efficiently. The saturation seen for very short current rise times is due to there being a finite amount of copper to excite.

III.G. Optimum Gain and Scaling the Copper Laser

The implication of the previous discussion is that maximum gain in the copper laser is always small compared to its value in the absence of a radiation field. This in part explains the success of the oscillator-amplifier configuration [III-17] where by appropriate delay techniques, the laser pulse from the oscillator can be made to arrive at the peak gain of the amplifier.

The potential maximum gain of the copper laser may be estimated in the following manner. The gain is proportional to the inversion density.

$$\alpha = \zeta(C_U - \gamma C_L) \qquad \text{(III.G.1)}$$

where ζ is a function of gas temperature only and γ is the ratio of the level degeneracies. If spontaneous emission,cavity intensity and coupling to the buffer gas are ignored, then the rate equations simplify to

$$\frac{d}{dt}C_U = n_e(t)(r_{G\rightarrow U}C_G - r_{U\rightarrow ION}C_U) \qquad \text{(III.G.2)}$$

$$\frac{d}{dt}C_L = n_e(t)(r_{G\to L}C_G - r_{L\to ION}C_L) \qquad \text{(III.G.3)}$$

$$\frac{d}{dt}C_G = -n_e(t)(r_{G\to U} + r_{G\to L} + r_{G\to ION})C_G \qquad \text{(III.G.4)}$$

For early times in the current pulse, the electron density can be approximated by

$$n_e(t) = kt$$

where k is a constant. Integrating (III.G.4) from 0 to t

$$C_G = N_o e^{-r_T kt^2/2} \qquad \text{(III.G.5)}$$

where $r_T = r_{G\to U} + r_{G\to L} + r_{G\to ION}$, and N_o is the ground state population at t = 0. By substituting (III.G.5) into (III.G.2) and (III.G.3), we may integrate the equations to find

$$C_U = \frac{r_{G\to U}N_o}{(r_T - r_{IU})}\left(e^{-r_{IU}kt^2/2} - e^{-r_T kt^2/2}\right) \qquad \text{(III.G.6)}$$

$$C_L = \frac{r_{G\to L}N_o}{(r_T - r_{IU})}\left(e^{-r_{IL}kt^2/2} - e^{-r_T kt^2/2}\right) \qquad \text{(III.G.7)}$$

The first exponential in (III.G.6) and (III.G.7) represents the electron impact loss out of the level. The second exponential represents depletion of the ground state excitation source. The relative rates of pumping from the ground state are represented by the premultiplying factor. The gain is then

$$G = \zeta N_o \left(e^{-r_{IU}kt^2/2} \frac{r_{G\to U}}{(r_T - r_{IU})} - e^{-r_{IL}kt^2/2} \frac{\gamma r_{G\to L}}{(r_T - r_{IL})}\right.$$

$$\left. - e^{-r_T kt^2/2} \left(\frac{r_{G\to U}}{(r_T - r_{IU})} - \frac{\gamma r_{G\to L}}{(r_T - r_{IL})}\right)\right) \qquad \text{(III.G.8)}$$

The maximum gain is found by setting the time derivative of (III.G.8) equal to zero, and solving the resultant transcendental equation for t_{max}.

$$t_{max}^2 = -\frac{2}{kr_T} \ell n \left[\frac{1}{\left(\frac{r_{G\to U}}{r_T - r_{IU}} - \frac{\gamma r_{G\to L}}{r_T - r_{IL}}\right)} \left(e^{-r_{IU}kt^2/2} \frac{r_{G\to U} r_{IU}}{r_T(r_T - r_{IU})}\right.\right.$$

$$\left.\left. - e^{-r_{IL}kt^2/2} \frac{\gamma r_{G\to L} r_{IL}}{r_T(r_T - r_{IL})}\right)\right] \qquad \text{(III.G.9)}$$

As an example, three discharge conditions are considered from the discussion in Section III.C; optimum and one on either side of optimum in electron temperature. The results of (III.G.9) and the rate equation analysis are in Table III.1. These estimates are admittedly high, as the terms which were deleted from the rate equations in order to obtain analytic expressions (i.e., spontaneous emission and noble gas quenching) would tend to lower the maximum gain. Nevertheless, this does demonstrate that the maximum possible gain in the copper laser can be as much as five times that which is actually obtained. Note also that at the higher electron temperatures and densities,

TABLE III.1

Pressure (Torr)	Relative Laser Energy	T_e(eV)	Max Computed Gain with Field	Max Possible Gain without Field
12.6	0.62	4.6	.0904/cm @9 ns	.4738/cm @35.5 ns
2.5 (optimum)	1.00	10.0	.1317/cm @6 ns	.3839/cm @18.1 ns
3.9	0.89	15.3	.1337/cm @6 ns	.3537/cm @15.5 ns

$T=370^{o}C$

the maximum gain obtained is closer to its potential value. If the cavity field could be effectively damped until maximum gain is obtained, more moderate electron temperatures and densities would be optimum. The discharge energy could then be reduced and efficiency increased.

The implication of the preceding discussion is that large laser pulse energies cannot be obtained by volumetric scaling. As the optical depth increases in directions other than the optical axis, amplified spontaneous emission will become important isotropically. This, and the phenomenon of superadiant decay, may help to explain why the output energy of the laser decreases as the tube temperature and copper density increases. Hence true volumetric scaling may be limited to long discharges of narrow cross sectional area where the optical depth in directions other than the optical axis is minimized. To insure a uniform discharge under such conditions, transverse electrodes would be required [III-18,19,20]. Due to the short pulse duration, lengthening the discharge will result in large diffraction losses. Hence it will be difficult to increase the output energy of the laser beyond a few millijoules if a single discharge is used. Truly large pulse energies (tens of millijoules) may be possible only with an oscillator amplifier arrangement.

REFERENCES

1. A. Yariv, Quantum Electronics, John Wiley & Sons, New York, 1975.
2. R. H. Bond, "Directed Electron Velocity Distributions in Rare Gas Discharges Using Guard Ring Electrodes", Ph. D. Thesis, California Institute of Technology, 1965.
3. S. Trajmar, W. Williams, and S. K. Srivastava, "Electron-impact Cross Sections for Cu Atoms", J. Phys. B10, 3323 (1977).
4. D. A. Leonard, "A Theoretical Description of the 5106Å Pulsed Copper Vapor Laser", IEEE J. Quant. Electronics QE-3, 380 (1967).
5. V. S. Borozdin, Yu. M. Smirnov, and Yu. D. Sharnov, "Measurement of the Cross Sections of Copper Atoms for Excitation by Electron Impact", Opt. Spectrosc. 43, 227 (1977).
6. L. Vriens, "Binary-Encounter Electron-Atom Collision Theory" Phys. Rev. 141, 88 (1966).
7. E. Sovero, C. J. Chen, and F. E. C. Culick, "Electron Temperature Measurements in a Copper Chloride Laser Utilizing a Microwave Radiometer", J. of Appl. Phys. 47, 4538 (1976).
8. A. C. Jenkins, and G. A. Cook, "Gas Phase Properties" in Argon, Helium, and the Rare Gases, G. A. Cook, ed. Interscience Publishers, New York, 1961.
9. F. F. Chen, Introduction to Plasma Physics, Plenum, New York, 1974.
10. N. M. Nerheim, "A Parametric Study of the Copper Chloride Laser", J. Appl. Phys. 48, 1186 (1977).
11. J. Tenenbaum, I. Smilanski, S. Gabay, G. Erez, and L. A. Levin,

"Time Dependence of Copper-Atom Concentration in Ground State and Metastable States in a Pulsed CuCl Laser", J. Appl. Phys. 49, 2662 (1978).

12. N. M. Nerheim and C. J. Chen, "Final Report - Phase I Follow-On: Visible Wavelength Laser Development", Jet Propulsion Laboratory, 1976.
13. R. S. Anderson, L. W. Springer, B. G. Bricks, and T. W. Karras, "A Discharge Heated Copper Vapor Laser", IEEE J. Quant. Electronics QE-11, 173 (1975).
14. A. A. Vetter, "Quantitative Effect of Initial Current Rise on Pumping the Double-pulsed Copper Chloride Laser", IEEE J. Quant. Electronics QE-13, 889 (1973).
15. P. A. Bokhan, V. I. Solomonov, V. B. Schcheglov, "Investigation of the Energy Characteristics of a Copper Vapor Laser with a Longitudinal Discharge", Sov. J. Quant. Electronics 7, 1032 (1977).
16. A. A. Vetter, private communication, 1978.
17. N. M. Nerheim, A. A. Vetter, and G. R. Russell, "Scaling a Double-Pulsed Copper Chloride Laser to 10 mJ", J. Appl. Phys. 49, 12 (1978).
18. J. A. Piper, "A Copper Iodide Laser Excited by Transverse Discharge", Opt. Commun. 14, 296 (1975).
19. J. A. Piper and C. E. Webb, "A TE Copper Iodide Laser", IEEE J. Quant. Electronics QE-11, 95D (1975).
20. J. A. Piper, "A Transversely Excited Copper Halide Laser with Large Active Volume", IEEE J. Quant. Electronics QE-14, 405 (1978).

IV. THE INFLUENCE OF PENNING REACTIONS ON AVERAGE ELECTRON ENERGY: A NUMERICAL SOLUTION FOR THE BOLTZMANN EQUATION

IV.A. Introduction

In the discussion of the electron temperatures measured in a CuCl discharge [IV.1], it was suggested that Penning ionizations might be partly responsible for the observed behavior (see Figure IV-1). Penning ionizations represent a source of relatively high energy electrons independent of the electron flux. A Penning ionization of a Cu^2P atom by a 21 eV He metastable atom results in an electron having energy as high as 17 eV. In the noble gas-CuCl system, there are two sources of these Penning electrons. One is a result of noble gas-noble gas reactions. The second is a result of noble gas - Cu,Cl or CuCl reactions. The first source depends on gas temperature and pressure as $(\frac{P}{T})^2$, whereas the second source varies as $(\frac{P}{T})e^{\gamma T}$. The ratio $\frac{P}{T}$ arises from the noble gas density; the CuCl vapor pressure and hence density, varies as $e^{\gamma T}$.

Let the average energy of a Penning ionization (PI) electron from a noble gas-noble gas collision be ε_1. Let that from a noble gas-CuCl collision be ε_2. The average PI electron should then have an average energy which depends on the gas temperature and pressure according to

$$\bar{\varepsilon} \sim T^{1/2}\sigma_1\varepsilon_1(\frac{\alpha P}{T})^2 + \sigma_2 T^{1/2}\varepsilon_2\beta\alpha\frac{P}{T}e^{\gamma T} \qquad \text{(IV.A.1)}$$

where

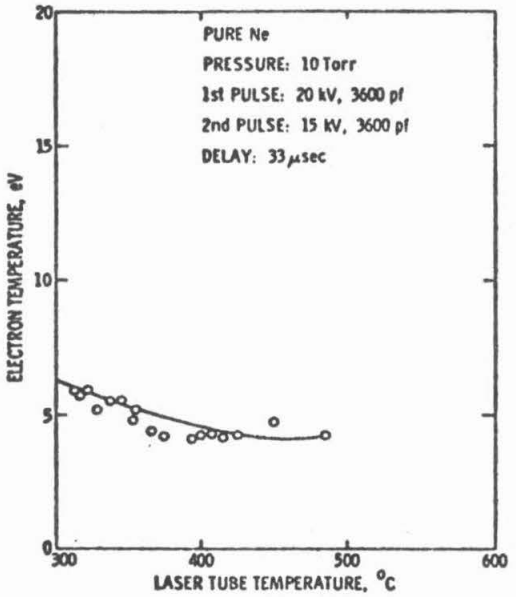

Figure IV.1. Experimental measurements of electron temperature during the pumping pulse of a Ne/CuCl discharge.
a) Pure neon

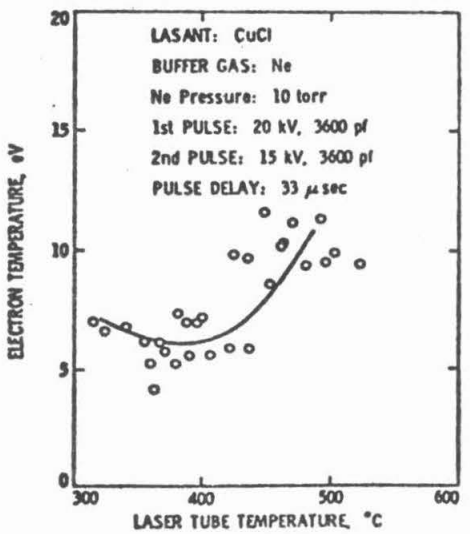

b) Neon with CuCl at its vapor pressure

σ_i = relative cross section for the particular PI reaction (cm^2)

$\frac{\alpha P}{T}$ = number density of noble gas ($/cm^3$)

$\beta e^{\gamma T}$ = number density of Cu/Cl ($/cm^3$)

The factor of $T^{1/2}$ represents the temperature dependence of the collision rate. For example, assume that the CuCl is completely dissociated in neon as the buffer gas, and that all species are in equilibrium with a Maxwellian electron distribution having a temperature of 5 eV. Then ε_1 = 2.2 eV and ε_2 = 9.2 eV. If it is also assumed that the cross sections are equal, PI electrons will be produced with the average energy shown in Figure IV-2. Note the similarity to Figure IV-1.b. If the average energy of PI electrons is greater than the average electron energy in their absence, then they could be partly responsible for the observed electron temperatures.

To examine quantitatively the effect of a flux free source such as Penning ionizations on an electron distribution function, a numerical solution to the Boltzmann equation has been obtained. The calculation is based on similar studies by Judd [IV-2], Schlie [IV-3], Rockwood [IV-4] and Elliot and Green [IV-5], but the procedure followed here is a variation on the group theory method used in neutron diffusion calculations [IV-6].

IV.B. Theory and Numerical Method

The range of electron energies is divided into k discrete groups.

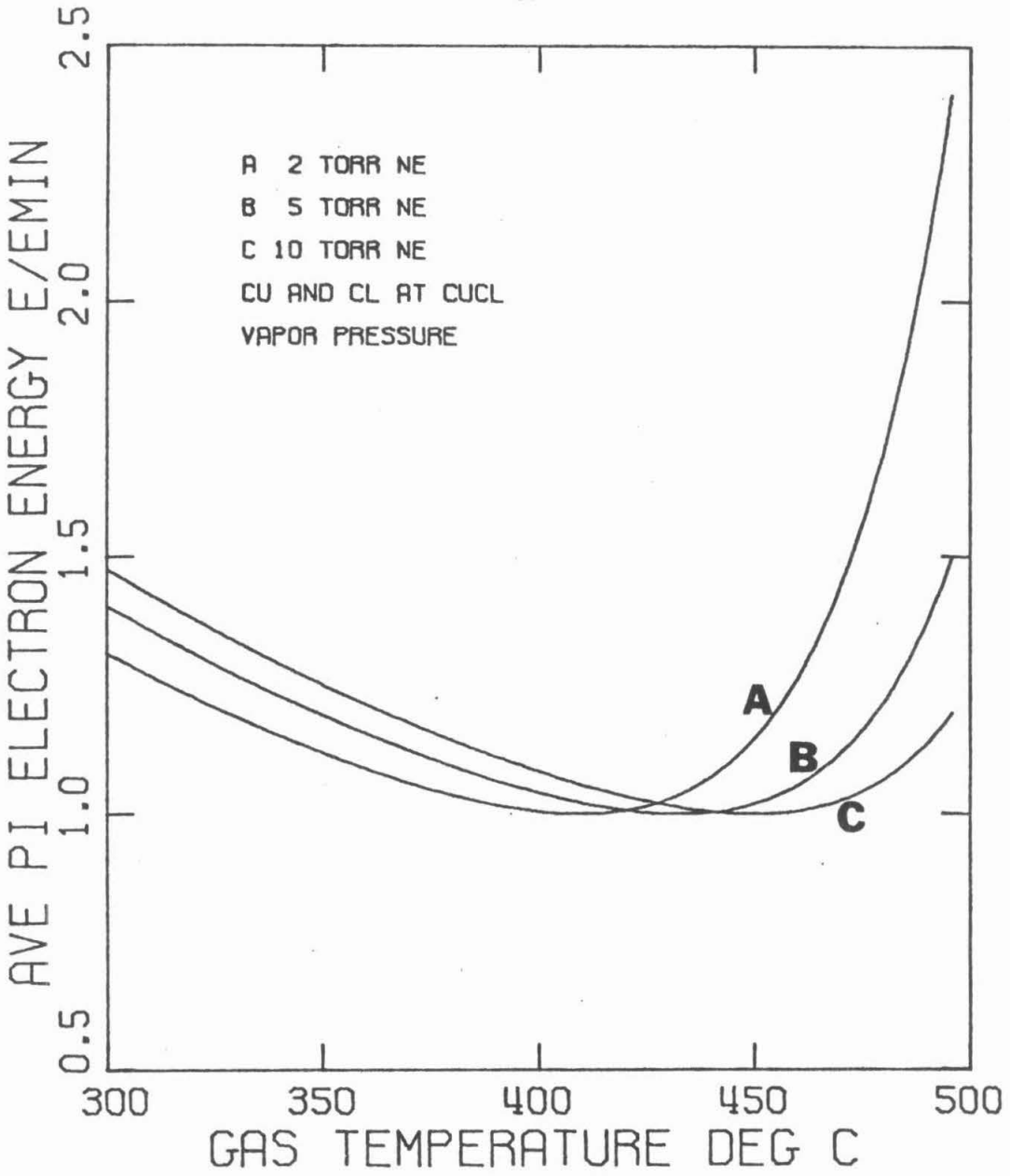

Figure IV.2. Average energy of electrons produced by Penning ionizations between neon metastables, and neon, copper and chlorine. All collisions cross sections are equal.

The electrons in a particular group are assigned the midpoint energy of the range covered by that group. Each group is assigned an electron density n_j which represents the integrated energy dependent electron density over the group's energy range. If each group has width $\Delta\varepsilon$ then

$$n_j = \int_{(j-1)\Delta\varepsilon}^{j\Delta\varepsilon} n(\varepsilon')d\varepsilon' \qquad \text{(IV.B.1)}$$

Cross sections and transport coefficients are formulated for each group, their energy dependence based on the midpoint energy of that group.

The volume averaged Boltzmann equation can be written as

$$\frac{dn_j}{dt} = \frac{-D_j n_j}{\Lambda_j^2} - n_j\Big(\underbrace{\sum_{\ell,m} N_{\ell m} v_j \sigma^i_{\ell m}(j)}_{(a)\qquad (b)} + \underbrace{\sum_{\ell,m<n} N_{\ell m} v_j \sigma^e_{\ell m\to n}(j)}_{(c)}$$

$$+ \underbrace{\sum_{\ell,m>n} N_{\ell m} v_j \sigma^s_{\ell m\to n}(j)}_{(d)}\Big) + \sum_k n_k \Big(\underbrace{\sum_{\ell,m,p} N_{\ell m} v_k \sigma^i_{\ell mp}(k)}_{(e)}$$

$$+ \underbrace{\sum_{\ell,m<n} N_{\ell m} v_k \sigma^e_{\ell m\to n}(k)}_{(f)} + \underbrace{\sum_{\ell,m>n} N_{\ell m} v_k \sigma^s_{\ell m}(k)}_{(g)}\Big)$$

$$+ \underbrace{F^j_{ee}(\underline{n})}_{(h)} + \underbrace{F^j_{e\ell}(\underline{n})}_{(i)} + \underbrace{F^j_E(\underline{n})}_{(j)} - \underbrace{R_j n_j}_{(k)} + \underbrace{S_j}_{(l)} \qquad \text{(IV.B.2)}$$

where

$\underline{n}$ = electron density vector $(n_1, n_2, \ldots n_k)(/cm^3)$

$N_{\ell m}$ = density of ℓ^{th} atomic species excited to its m^{th} state $(/cm^3)$

v_j = velocity of electron in j^{th} group (cm/s)

$\sigma^a_{\ell m}(j)$ = cross section for a^{th} process involving atom (ℓm) for j^{th} group

Λ_j = diffusion length for j^{th} group (cm)

D_j = diffusion coefficient for the j^{th} group (cm^2/s)

The various terms in (IV.B.2) are identified as follows: Losses from group j occur due to

a) diffusion

b) ionization of $N_{\ell m}$

c) excitation of N_ℓ from $m \rightarrow n$

d) super elastic de-excitation of N_ℓ from $m \rightarrow n$

Contributions from group k to group j occur due to

e) ionization of $N_{\ell m}$

f) excitation of N_ℓ from $m \rightarrow n$

g) superelastic de-excitation of N_ℓ from $m \rightarrow n$

Other changes in the population of group j occur due to

h) electron-electron collisions

i) elastic collisions with $N_{\ell m}$

j) electric field E

k) recombination

1) sources independent of $\underline{n}$

The superelastic cross section $\sigma^{s}_{\ell m \to n}$ is expressed in terms of the excitation cross section $\sigma^{e}_{\ell n \to m}$ through the Klein-Rosseland Formula [IV-7]

$$\sigma^{s}_{m\to n}(j) = \frac{(\varepsilon_j + E_m - E_n)}{\varepsilon_j} \frac{g_{\ell n}}{g_{\ell m}} \sigma^{e}_{\ell n \to m}(k) \qquad \text{(IV.B.3)}$$

where

E_m = energy of m^{th} atomic level

ε_j = midpoint energy of j^{th} group

$g_{\ell m}$ = statistical weight of atom level (ℓ,m)

k = group corresponding to the energy

$$\varepsilon_j + E_m - E_n$$

In any ionization when the incident electron has energy above threshold, there is a probability that some of the "excess" energy will be imparted to the secondary electron. Term e) above therefore has the possibility of two contributions: one from the slowed primary electron and one from the secondary electron. Many attempts have been made to obtain an expression for the spectrum for the secondary electron energy given the incident energy and ionization potential. Unfortunately these studies have been carried out for primary energies far in excess of those of interest here, or for heavy particle primaries [IV-8,9]. Opal, et al [IV-10] made measurements of differential secondary electron distributions for a variety of gases, helium being the only one of interest here. The lowest primary energy was 50 eV.

In order that the ionization cross section implicitly included the secondary electron spectrum, the theoretical form due to Vriens [IV-11] was chosen. The cross section for ionization of a neutral atom with ionization potential $E^i_{\ell m}$ by primary electron of energy ε_j with loss of energy $\delta\varepsilon$ is given by

$$\sigma^i_{\ell m}(\varepsilon_j \rightarrow \varepsilon_j - \delta\varepsilon) = \frac{\pi e^4}{(\varepsilon_j + E^i_{\ell m} + E^A_{\ell m})} \left(\frac{1}{(\delta\varepsilon)^2} + \frac{4E^A_{\ell m}}{3(\delta\varepsilon)^3}\right) \qquad \text{(IV.B.4)}$$

where $E^A_{\ell m}$ is the electronic orbital energy given by the Slater's Formula [IV-12]. By setting $\delta\varepsilon = E^i_{\ell m} + \varepsilon_s$ where ε_s is the secondary electron energy, one can synthesize a secondary electron spectrum. After normalizing the calculated peak cross section to Opal's data for 50 eV primaries, the calculated cross section for secondary electron production agrees to within about 7% with his data.

Due to the absence from the literature of cross sections for excitations between excited states for Cu and Cl, a Vriens cross section was used for this purpose also [IV-11]. The necessity for having heavily populated excited states and hence the cross sections above is evident when one examines the experimental electron temperature data. Electron temperatures measured in excess of 10 eV suggest not only excited neutrals but a heavily ionized plasma as well.

In the pressure of an external DC electric field E_{DC}, the diffusion length Λ_j is given by [IV-13]

$$\frac{1}{\Lambda_j^2} = \left(\frac{\pi}{\ell}\right)^2 + \left(\frac{2.405}{R}\right)^2 + \left(\frac{\mu_j}{D_j}\frac{E_{DC}}{2}\right)^2 \qquad \text{(IV.B.5)}$$

where the discharge tube has length ℓ, radius R, and group j has mobility μ_j.

The electron-electron collision term (IV.B.2.h) is due to an analysis of the Fokker-Plank equation by Rosenbluth, et al [IV-14]. For free electrons with an isotropic velocity distribution [IV-5].

$$F^j_{ee}(\underline{n}) = - \frac{A^{j+1} - A^{j-1}}{2\Delta\varepsilon} \qquad \text{(IV.B.6)}$$

where

$$A^j = \frac{2}{3}\pi e^4 \left(\frac{2}{m_e}\right)^{1/2} \ell n\gamma \left(L\left(\frac{n_j}{2\varepsilon_j} - \frac{n_{j+1} - n_{j-1}}{2\Delta\varepsilon}\right) - Pn_j\right)$$

$$\gamma = \left(\frac{kT_e}{4\pi n_T e^2}\right)^{1/2} \frac{\varepsilon_j}{2e^2}$$

$$L = \frac{2}{\varepsilon_j^{1/2}} \sum_{\ell=1}^{j-1} \varepsilon_\ell n_\ell + 2\varepsilon_j \sum_{\ell=j}^{k} \frac{1}{\varepsilon_\ell^{1/2}} n_\ell$$

$$P = \frac{3}{\varepsilon_j^{1/2}} \sum_{\ell=1}^{j-1} n_\ell$$

$$n_T = \sum_{\ell=1}^{k} n_\ell$$

The elastic collision term (IV.B.2.i) is given by [IV-4]

$$F^j_{e\ell}(\underline{n}) = - \frac{B^{j+1} - B^{j-1}}{2\Delta\varepsilon} \qquad \text{(IV.B.7)}$$

where

$$B^j = \bar{\nu}\left(n_j\left(\frac{kT_g}{2} - \varepsilon_j\right) - kT_g\varepsilon_j\left(\frac{n_{j+1}-n_{j-1}}{2\Delta\varepsilon}\right)\right.$$

T_g = gas temperature (^oK)

$$\bar{\nu} = 2m_e\left(\frac{2\varepsilon_j}{m_e}\right)^{1/2} \sum_{\ell} N_\ell \frac{\sigma_\ell^{e\ell}(j)}{M_\ell}$$

M_ℓ = mass of atom ℓ

The electric field term (IV.B.2.j) is given by [IV-4]

$$F_E^j(\underline{n}) = -\frac{C^{j+1}-C^{j-1}}{2\Delta\varepsilon} \qquad \text{(IV.B.8)}$$

where

$$C^j = \frac{2e^2E\varepsilon_j}{2n\nu_c}\left(\frac{n_j}{2\varepsilon_j} - \frac{n_{j+1} - n_{j-1}}{2\Delta\varepsilon}\right)$$

$$\nu_c = \left(\frac{2\varepsilon_j}{m_e}\right)^{1/2} \sum_{\ell} N_\ell\sigma^{e\ell}(j)$$

The volumetric recombination term (IV.B.2.k) can be ignored in this study. The dominant recombination mechanism in dense plasmas is collisional-radiative recombination which has an electron temperature dependence of $T_e^{-\frac{9}{2}}$ [IV-15]. At the elevated temperatures expected here, volumetric recombination is negligible.

High energy electrons resulting from Penning ionizations were included as the flux free source term (IV.B.2.l). The source electron

was assumed to have energy $E_m - E^i_{\ell m}$ where E_m is the metastable energy, and $E^i_{\ell m}$ is the ionization potential of atomic species $N_{\ell m}$.

When the contributions to each energy group are summed, one can write

$$\frac{\partial \underline{n}}{\partial t} = (\underline{\underline{M}}_1 + \underline{\underline{M}}_2 (\underline{n})) \cdot \underline{n} + \underline{S} \qquad \text{(IV.B.9)}$$

where $\underline{\underline{M}}_1$ is a square matrix independent of $\underline{n}$ and $\underline{\underline{M}}_2$ is a square matrix which is a function of $\underline{n}$. Letting $\underline{n}^j$ be the value of $\underline{n}$ at the j^{th} time a step, (IV.B.9) can be written as

$$\underline{n}^{j+1} = (\underline{\underline{I}} - \underline{\underline{M}}_1 \Delta t)^{-1}((\underline{\underline{I}} + \underline{\underline{M}}_2(\underline{n}^j)\Delta t)\underline{n}^j + \underline{S}\Delta t) \qquad \text{(IV.B.10)}$$

where Δt is the time step and $\underline{\underline{I}}$ is the identity matrix. The inverted matrix is calculated only once for a given atomic state distribution. To obtain the steady state distribution $\underline{n}$, equation (IV.B.10) is solved by iteration until a given order of convergence is reached. The matrices $\underline{\underline{M}}_1$ and $\underline{\underline{M}}_2$ may be revised at intervals greater than the basic time step for iteration.

IV.C. Calculated Electron Spectra, Average Electron Energies, and Excitation Rates

For the examples which follow, the discharge conditions are

Tube radius	1.0 cm
Discharge length	50.0 cm
Electric field	200 Volts/cm
Convergence criteria	.01 - .001

None of the required Penning ionization cross sections have been reported in the literature. Based on the values of typical Penning ionization cross sections which have been reported and are listed in Table IV.1, the metastable-metastable cross section was fixed at $1.0 \times 10^{-15} cm^2$. The value of metastable-nonmetastable Penning ionization cross sections was parameterized.

As a calibration or "control" for each case, the average electron energy was computed with Penning ionization ignored. For the examples which follow, an atomic state distribution in equilibrium with a Maxwellian plasma with a temperature of 5 eV was chosen. In each case, the calculated source free average electron energy was nearly 6.0 eV. The slope of population vs energy at high electron energies indicates a Maxwellian temperature of 4.2 eV ($\partial n/\partial T_e \sim 1/T_e$) requiring an averaging energy of 6.3 eV to be actually Maxwellian.

IV.C.1 Average Electron Energies

Average electron energies for a Ne (5.0 Torr) discharge are shown in Figure IV-3. The metastable-nonmetastable cross section for Penning ionization was taken to be $1.0 \times 10^{-15} cm^2$. The average electron energies for a Ne/CuCl discharge are shown in Figure IV-4. Compare Figures IV-3 and IV-4 with the experimental data of Figure IV-1. The decrease in electron energy measured experimentally for the pure neon discharge as the gas temperature is increased is larger than that calculated here, but the decreasing trend is reproduced. The top curve of Figure IV-4 closely resembles the experimental measurements, suggesting

TABLE IV.1

Penning Ionization Cross Sections

Metastable Atom	Collision Partner	Cross Section 10^{-16} cm^2	Reference (Chapter IV)
Ne	Ar	4	21
		50	22
		14.5*	23
		2.6	24
	Zn	41.8	25
	Cd	46.1	25
	$O_2 \rightarrow O+O$	28	26
He (2^3S)	He 2^3S	140±20	27
(2^3S)	He 2^1S	340±40	27
	Ar	11.7 *	23
		0.97	24
(2^3S)		7.6	36
(2^3S,2^1S)		9.0	28
		6.6	29
(2^1S)		4.0	29
(2^3S)	(Theoretical)	8.0	30
	Hg	140	24
(2^3S)		90	31
		0.8	32
(2^1S)	O	124	33
(2^3S)		44	33
	N_2	20*	23
	Zr	29	25
(2^3S)		≈10	18
	Cd	45	25
		≈10	18
(2^3S)	Pb	14.8	34
(2^3S,2^1S)	H	≈100	35
Ar	Zn	52.8	25
	Cd	65.4	25
Kr	Zn	92.8	25
	Cd	108	25

* Extrapolated to thermal energy.

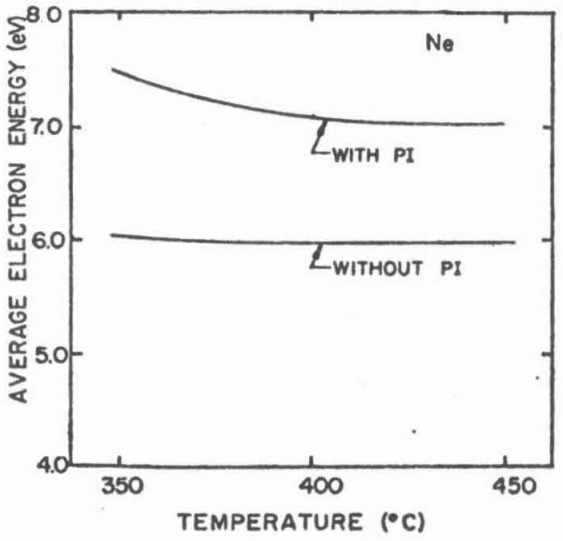

Figure IV.3. Average electron energy for a continuous discharge in pure neon (5 Torr) with and without Penning ionizations.

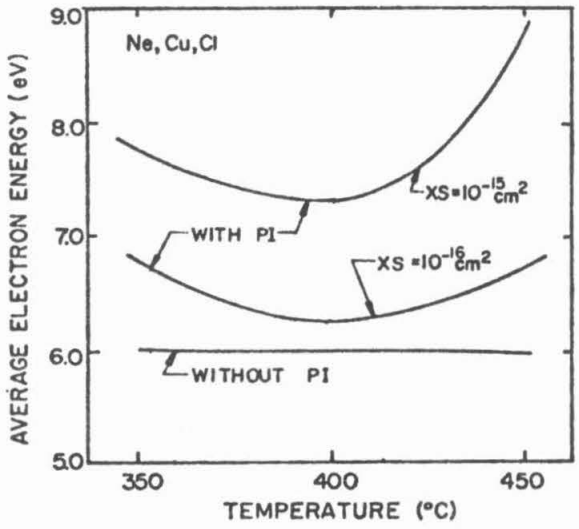

Figure IV.4. Average electron energy for a continuous discharge in neon (5 Torr) and Cu and Cl at the CuCl vapor pressure.

that the metastable-nonmetastable cross sections are at least equal to that for metastable-metastable reactions.

IV.C.2 Electron Energy Spectra

The electron energy spectra for the cases discussed above are found in Figures IV-5 and IV-6. The increasing contribution of Penning ionization electrons from Ne^*-Cu/Cl collisions as the tube temperature is raised emphasizes electrons with energies near 10 eV, thereby depressing the normalized distribution at the lower electron energies. The largest energy a source electron may have is 16 eV (equal to the neon metastable energy). The enhanced distribution at energies greater than 16 eV as the tube temperature increases is in part due to electrons being accelerated by the electric field.

IV.C.3 Excitation Rates

Using experimental cross sections for excitation of the copper ^2D and ^2P states [IV-16], and a Vriens cross section [IV-11] for ionization, the excitation and ionization rates for the electron distributions corresponding to $1.0 \times 10^{-15} cm^2$ Penning ionization cross sections were calculated (see Figure IV-7). Note that the greatest relative change occurs in the ionization rates. The threshold energy for ionization occurs at higher values than for excitation, and hence ionization rates will be more sensitive to excursions of the average electron energy to higher values.

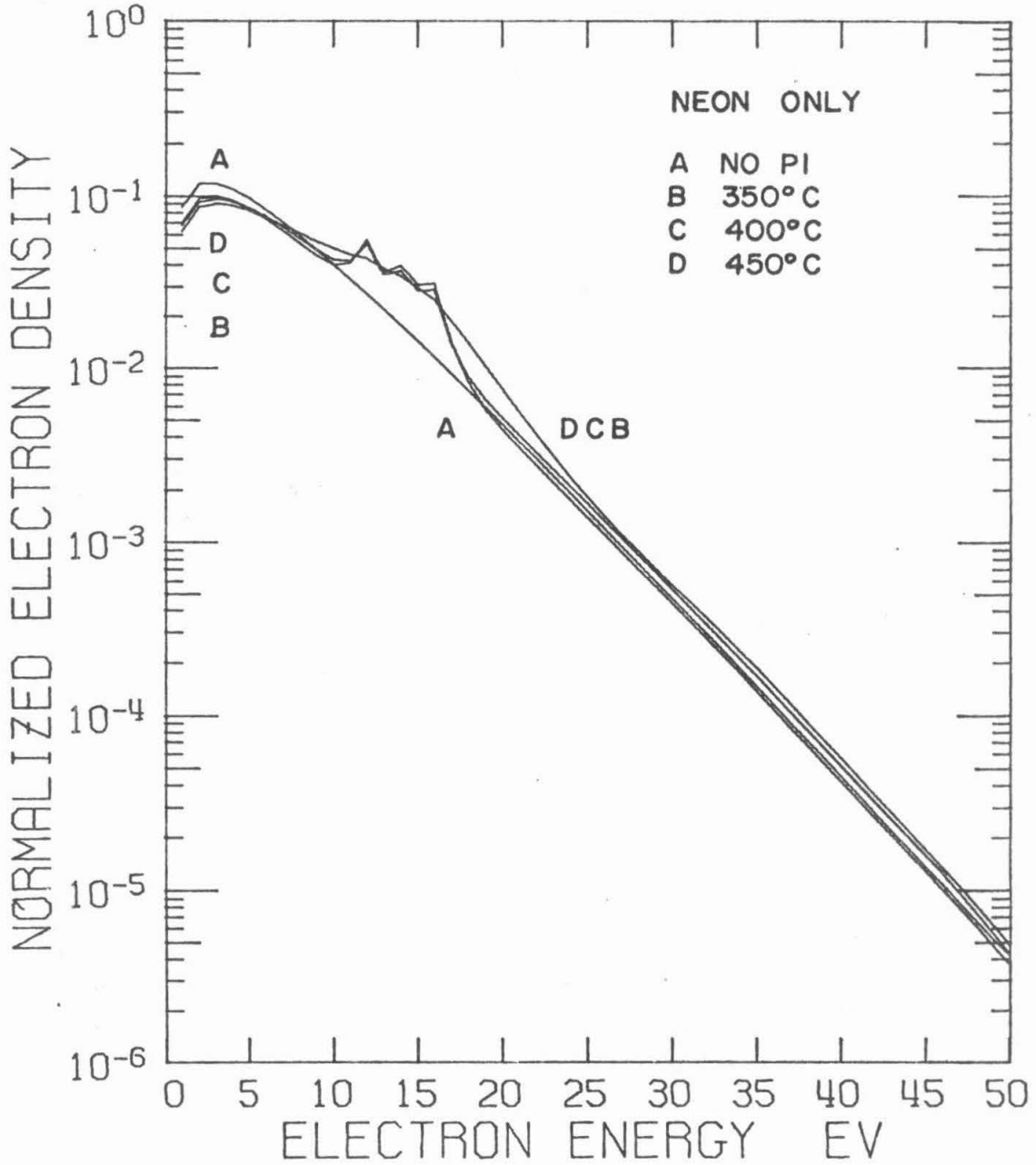

Figure IV.5. Electron energy spectrum for a discharge in neon (5 Torr).

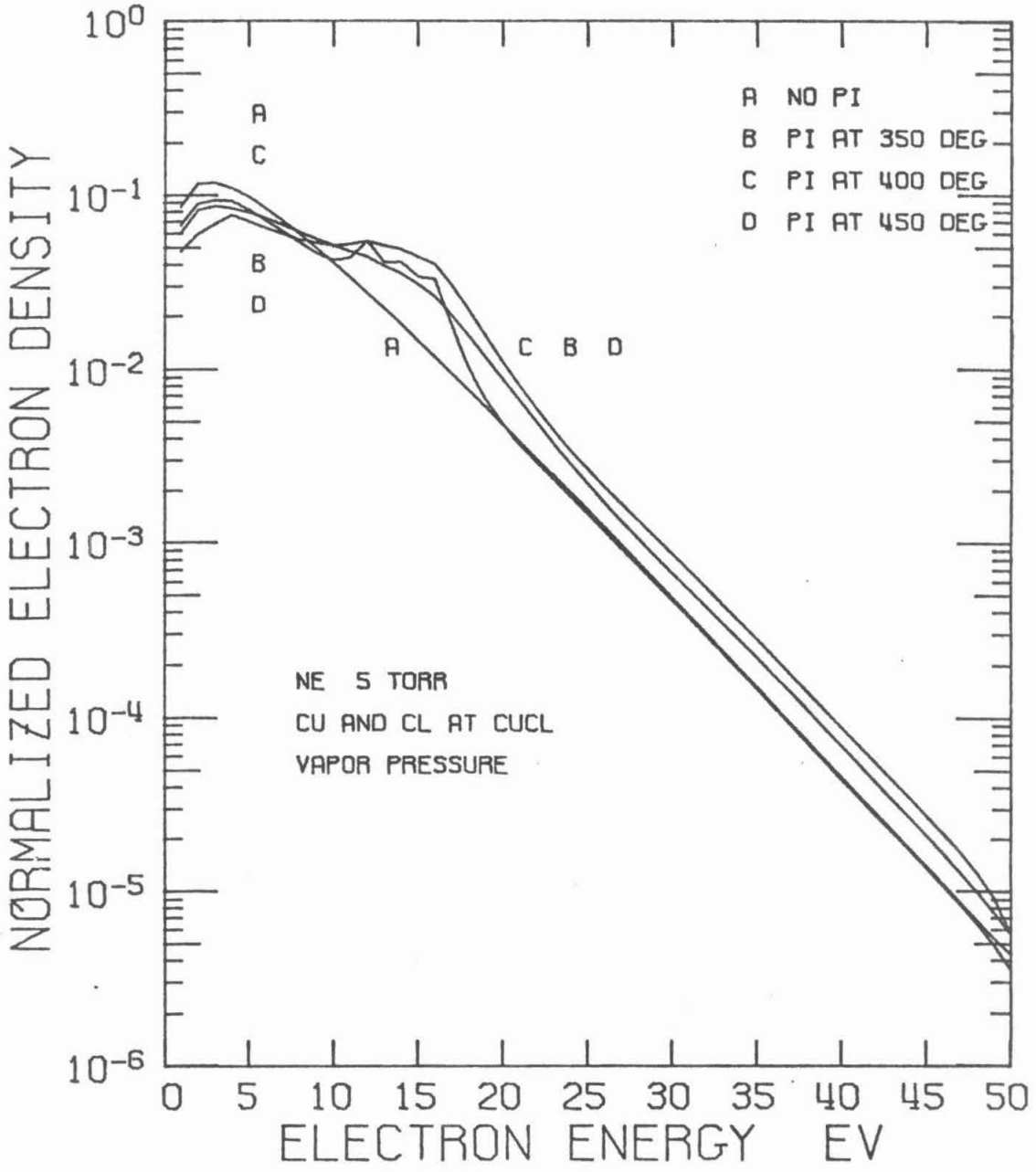

Figure IV.6. Electron energy spectrum for a discharge in neon, and Cu and Cl at the CuCl vapor pressure.

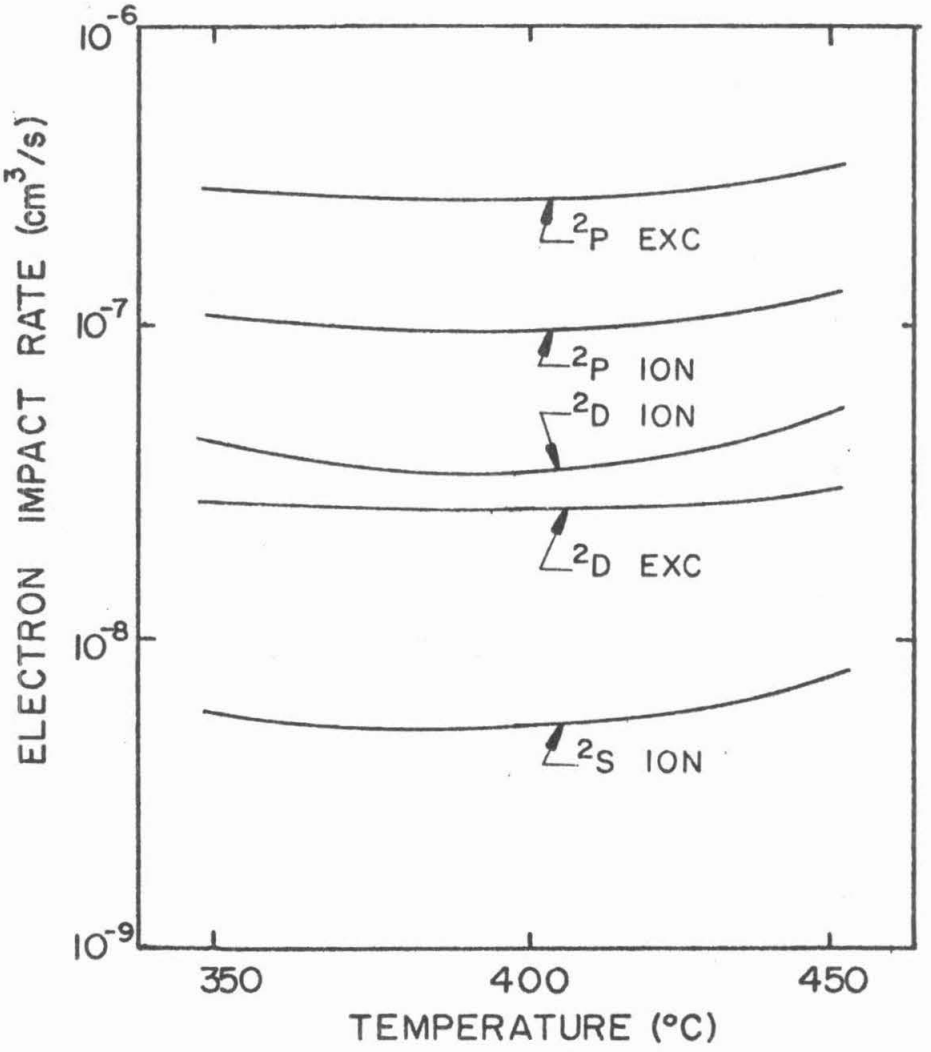

Figure IV.7. Electron impact rates for the excitation (EXC) and ionization (ION) of the ^2S, ^2D and ^2P states of copper.

IV.D. Summary

The analysis discussed above has demonstrated that Penning ionization may in part be responsible for the electron temperature behavior measured experimentally. The analysis is at best an approximation to the actual conditions, but nevertheless emphasizes the importance of considering noble gas-CuCl/Cu/Cl reactions when discussing the Cu/CuCl laser. This concern is far from unreasonable, as an entire class of metal ion lasers rely on Penning ionization and charge exchange pumping mechanisms [IV-17,18,19,20]. Although the metal ion lasers operate continuously, the afterglow period between the dissociation pulse and pumping pulse in the Cu/CuCl double pulse laser is similar to a low energy glow discharge plasma. Because the pumping discharge pulse (for which the electron temperature data was taken) is a sensitive function of its initial conditions, the conditions provided by the interpulse afterglow, processes normally associated with CW or quasi-CW discharges, will greatly influence the pulsed laser characteristics. The possible importance of Penning ionization demonstrated here, and the inherent coupling of the pumping pulse to the interpulse afterglow, emphasize the importance of examining all three discharge domains (dissociation pulse, afterglow, and pumping pulse) in the Cu/CuCl double pulse laser.

REFERENCES

1. E. Sovero, C. J. Chen, and F. E. C. Culick, "Electron Temperature Measurements in a Copper Chloride Laser Utilizing a Microwave Radiometer", J. Appl. Phys. 47, 4538 (1976).

2. O. Judd, "Electron-Collisional Excited-State Kinetics in Argon and Mercury Electrical Discharges", J. Appl. Phys. 47, 5297 (1976).

3. L. A. Schlie, "Electron Velocity Distributions, Fractional Energy Transfer, and Collision Rates for Potential Na, NaHe, and NaXe Electrically Excited Laser Discharges", J. Appl. Phys. 47,1397(1976).

4. S. D. Rockwood, "Elastic and Inelastic Cross Sections for Electron-Hg Scattering from Hg Transport Data", Phys. Rev. A8, 2348 (1973).

5. C. J. Elliot and A. E. Greene, "Electron Energy Distributions in e-Beam Generated Xe and Ar Plasmas", J. Appl. Phys. 47, 2946 (1976).

6. J. R. Lamarsh, Introduction to Nuclear Reactor Theory, Addison-Wesley, Massachusetts, 1966.

7. A. C. G. Mitchell, M. W. Zemansky, Resonance Radiation and Excited Atoms, Cambridge University Press, New York, 1971.

8. R. H. Lo and G. H. Miley,"Electron Energy Distribution in a Helium Plasma Created by Nuclear Radiations", IEEE Trans. on Plasma Sci. PS-2, 198 (1974).

9. H. A. Hassan and J. E. Deese, "Electron Distribution Function in a Plasma Generated by Fission Fragments", Phys. Fluids 19, 2005 (1976).

10. C. B. Opal, E. C. Beaty, and W. K. Peterson, "Tables of Secondary-Electron-Production Cross Sections", Atomic Data 4, 209 (1972).

11. L. Vriens, "Binary-Encounter Electron-Atom Collision Theory", Phys. Rev. 141, 88 (1966).

12. D. N. Tripath and D. K. Rai, "Importance of the Kinetic-energy Expression for a Bound Electron in Classical Theory", J. Quant. Spectrosc. Radiaion Transfer 10, 1329 (1970).

13. S. C. Brown, Basic Data of Plasma Physics, MIT Press/Wiley, Massachusetts, 1959.

14. M. N. Rosenbluth, W. M. MacDonald, and D. L. Judd, "Fokker-Planck Equation for an Inverse-square Force", Phys. Rev. 107, 1 (1957).

15. M. A. Biondi, "Recombination" in Principles of Laser Plasmas, ed. George Bekefi, Wiley Interscience, New York, 1976.

16. S. Trajmar, W. Williams, and S. K. Srivastava, "Electron-impact Cross Sections for Cu Atoms", J. Phys. B10, 3323 (1977).

17. F. J. de Hoog, J. R. McNeil, G. J. Collins, and K. B. Persson, "Discharge Studies of the Ne-Cu Laser", J. Appl. Phys. 48, 3701 (1977).

18. G. J. Collins, "Excitation Mechanisms in He-Cd and He-Zn Ion Lasers", J. Appl. Phys. 44, 4633 (1973).

19. J. R. McNeil, G. J. Collins, K. B. Persson, and D. L. Franzen, "Ultraviolet Laser Action from CuII in the 2500 Å Region", Appl. Phys. Letters 28, 207 (1976).

20. J. A. Piper, and D. F. Neely, "CW Laser Oscillation on Transitions of Cu^+ in He-Cu Halide Gas Discharges", Appl. Phys. Letters 33, 621 (1978).

21. S. Y. Tang, A. B. Marcus, and E. E. Muschlitz, Jr., "Velocity Dependence of the Ionization of Ar, Kr, and Xe on Impact of Metastable Neon Atoms", J. Chem. Phys. 56, 566 (1972).

22. R. H. Neynaber and G. D. Magnuson, "Chem-ionization of Metastable Neon with Argon", Phys. Rev. A11, 865 (1975).

23. J. T. Mosely, J. R. Peterson, D. C. Lorents, and M. Hollstein, "De-excitation of Fast He, Ne, and Ar Metastable Atoms in Various Gases", Phys. Rev. A6, 1025 (1972).

24. M. A. Biondi, "Diffusion, De-Excitation and Ionization Cross Sections for Metastable Atoms I", Phys. Rev. 88, 660 (1952).

25. L. A. Riseberg, W. F. Parks, and L. D. Schearer, "Penning Ionization of Zn and Cd by Noble Gas Metastable Ions", Phys. Rev. A8, 1962 (1973).

26. E. W. McDaniel, Collision Phenomena in Ionized Gases, Wiley, New York, 1964.

27. N. B. Kolokolov and P. M. Pramatarov, "Interaction Between Metastable Helium Atoms in a Helium Afterglow", Sov. Phys.-Tech. Phys. 23, 176 (1978).

28. D. A. Machenvar, "Electron Ejection from an Atomically Clean Tungsten Surface by Helium and Neon Metastable Atoms", Phys. Rev. 148, 218 (1966).

29. A. L. Schmeltekopf and F. C. Fehsenfeld, "De-excitation Rate Constants for Helium Metastable Atoms with Several Atoms and Molecules", J. Chem. Phys. 53, 3173 (1970).

30. R. E. Olson, "Semiempirical Calculations of the He^+ (2^3S and 2^1S) + Ar Ionization Total Cross Sections", Phys. Rev. A6, 1031 (1972).

31. H. Kano, T. Shay, and G. J. Collins, "A Second Look at the Excitation Mechanism of the He-Hg^+ Laser", Appl. Phys. Letters 27, 610 (1975).

32. M. A. Biondi, "Processes Involving Ions and Metastable Atoms in Mercury Afterglows", Phys. Rev. 90, 730 (1953).

33. T. B. Cook, W. P. West, F. B. Dunning, R. D. Rundel, and R. F. Stebbings, "Absolute Penning Cross Section by He Metastables", J Geophys. Res. 79, 678 (1974).

34. L. A. Cross, M. Cem Gokay, "Excitation Processes in a Pb-He Discharge", J. Appl. Phys. 49, 2639 (1978).

35. W. H. Miller, H. F. Schaefer III, "Theoretical Treatment of Penning Ionization - He (1s2s's, 3s) + H($1s^2s$) ", J. Chem. Phys. 53, 1421 (1970).

36. W. P. Sholette and E. E. Muscheitz, Jr., "Ionizing Collisions of Metastable Helium Atoms", J. Chem. Phys. 36, 3368 (1962).

V. PUMPING PULSES AND LASER PULSES AS A FUNCTION OF TIME DELAY: THE INFLUENCE OF THE INTERPULSE AFTERGLOW

V.A. Introduction

It is clear from the experimental results discussed in Chapter II, from the analysis by rate equations given in Chapter III, and numerical solution to the Boltzmann equation given in Chapter IV that the complex dependence of laser energy on discharge conditions, time delay, and buffer gas pressure cannot be explained on the basis of the pumping discharge pulse alone. Because the laser pulse is tens of nanoseconds wide, and it appears at the leading edge of the pumping pulse, processes which occur at thermal speeds cannot influence significantly laser energy during that discharge pulse (see Figure V-1). In order to explain the observed laser characteristics, an understanding of the processes occurring in the afterglow between the two discharge pulses is required. These processes provide initial conditions for the pumping pulse and hence limit (or enhance) laser energy.

The interpulse afterglow has been the subject of several spectroscopic studies[IV.1-5]. The general consensus of these studies is that the density of ground state copper is maximum at times tens to hundreds of microseconds into the afterglow. In contrast, the densities of the metastable states are usually many times smaller,and are maximum at up to tens of microseconds into the afterglow. An explanation offered for this behavior is that the increase in copper ground state density is due to ion recombination while the long delay decrease in copper density

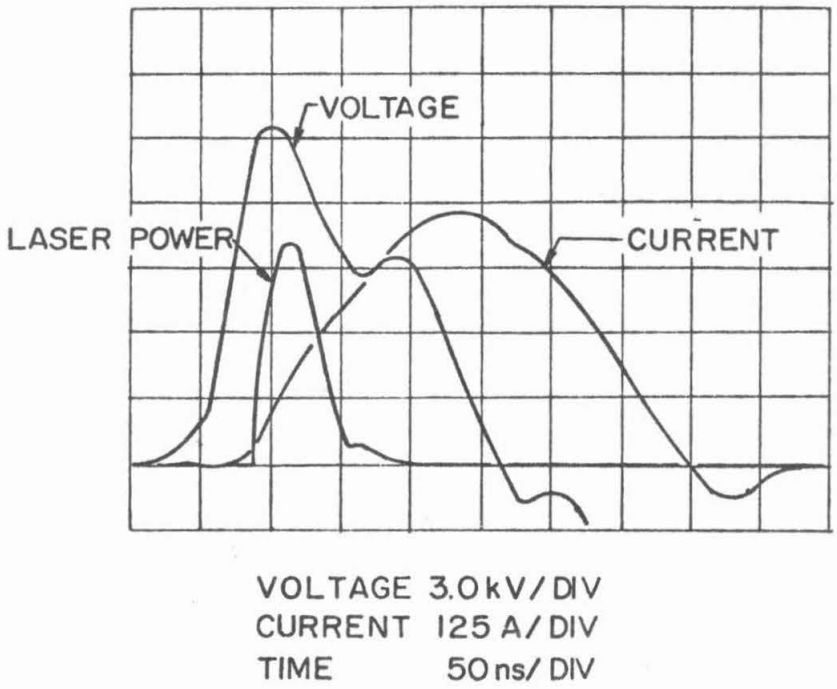

Figure V.1. Typical pumping pulse current and voltage, and laser power. Note that the laser pulse starts as soon as the current begins to flow. Processes which proceed at thermal speeds cannot significantly affect the laser pulse during the pumping pulse.

is due to reassociation to form the parent molecule [IV-2]. The complicated time dependence of the density of ground state copper during the afterglow [IV-3,5], and the complicated dependence of laser energy on time delay require that more processes than these be present. Figure V-2 is an example of the complicated dependence that laser energy can have on time delay. Laser energy as a function of time delay and helium buffer gas pressure are plotted for constant tube temperature (385^{o}C). It appears that there are three separate regimes to this behavior. The first process has a time scale of about 20 μs and dominates the laser pulse at early delays. Beginning at 4.0 Torr, and about 70 μs into the afterglow, a second process dominates, raising the laser energy to a maximum value at 9.0 Torr. This second process has a time scale of about 50 μs. The third process can be seen from 2.5 to 24.0 Torr as a slight increase in laser energy past the maximum value. It has been suggested that the wavy appearance of the laser energy at high pressure is due to acoustic oscillations.

V.B. The Pumping Pulse and Laser Pulse as a Function of Time Delay

V.B.1 Introduction

In Section III.F, the sensitivity of laser pulse energy to the current rise time for the pumping pulse was discussed. For otherwise constant discharge conditions, by increasing the rate of current rise, laser pulse energy can be increased. The dependence is quite strong, and for one set of discharge conditions was found to be [V-6]

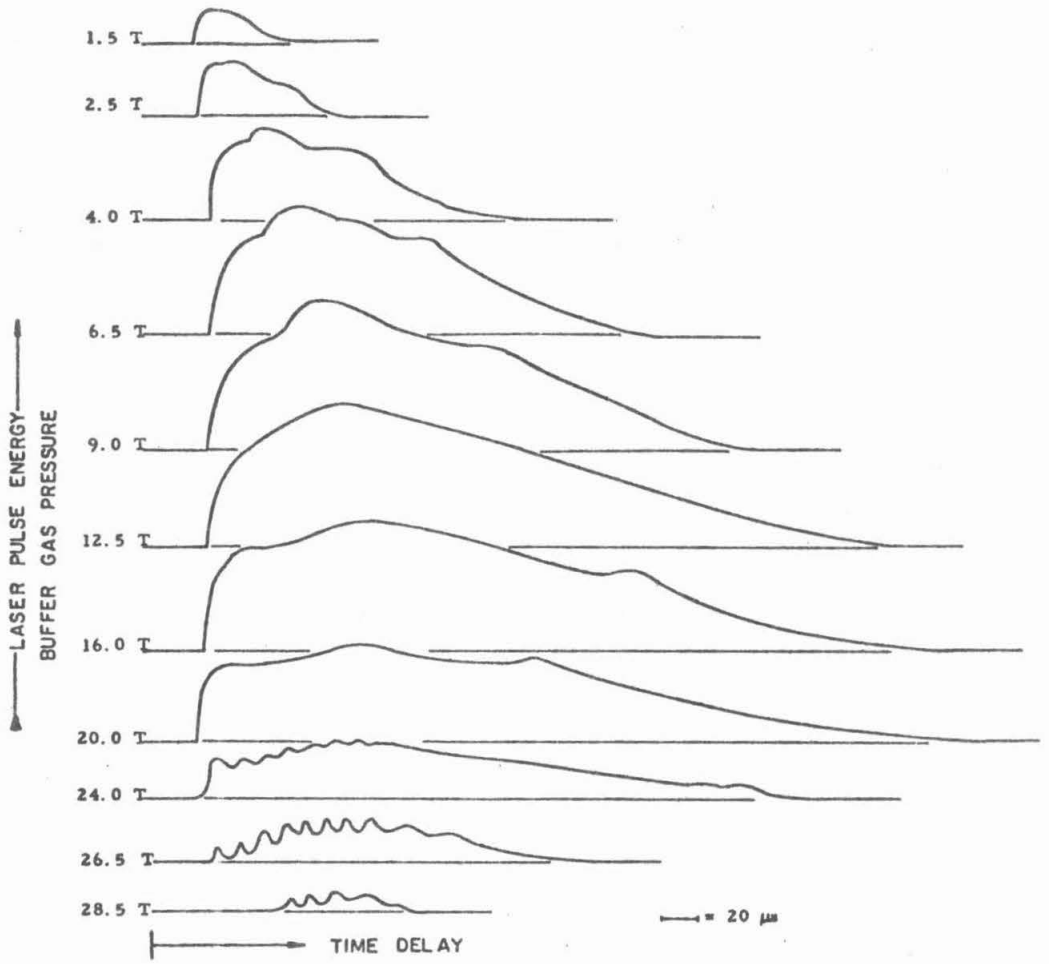

Figure V.2. Laser energy as a function of time delay and helium buffer gas pressure at 385°C.

$$\frac{dE}{dI} = .126 \frac{mJ}{I} \quad .$$

Even though charging voltage and capacitance for the pumping pulse, tube temperature, and gas pressure are all constant as a function of time delay, the pumping pulse itself cannot be expected to remain unchanged as the time delay is varied. At short delays, the electron density is high during the early part of the afterglow so that the pumping pulse need not break down the gas. At long delays, the afterglow electron density is low and the density of molecular CuCl is large compared to shorter delays so that average electron energy will be smaller.

With the above motivation, the characteristics of the pumping discharge pulse and laser pulse were measured as a function of time delay.

V.B.2 Experimental Results and Discussion

The experimental arrangement for these measurements was essentially the same as that shown in Figure II-14. The venue of the experiment was changed from the Jet Propulsion Laboratory to Caltech, with the following equipment changes.

Pulse Generators:	Data Pulse #101, Hewlett Packard #8012A
Vacuum Pump:	Welch #1400
Oscilloscopes:	Hewlett Packard #181/AR with
	#1801A Dual Channel Amp and
	#1821 Time Base

	Hewlett Packard #1722B
Voltage Divider:	T & M Research 1005:1
Gases:	Helium; Gardner Cryogenics Research Grade
	Argon; Big 3 Industries Research Grade

In order to measure the current and laser pulse on nanosecond time scales, the oscilloscope was isolated in a screen room. The discharge tube used for this and the remainder of the experimental work presented in this thesis is shown in Figure V-3.

V.B.2.a The Pumping Discharge Pulse

The rate of current rise for the pumping pulse and peak current as a function of time delay and buffer gas pressure is shown in Figure V-4. (The dissociation and pumping pulse capacitors were .005 μF charged to 15 kV.) Note that as the time delay increases, both the rate of current rise and the peak current decrease. For constant time delay, increasing the pressure decreases the rate of current rise and peak current. The decrease in these quantities with increasing time delay must in part be due to the decrease in afterglow electron density and increase in plasma impedance. The decrease with increasing pressure is in part due to dependence on E/P, and in part to the more rapid rate of electron cooling (and hence recombination) experienced at higher pressures. Note that at very short delays, the rate of cur-

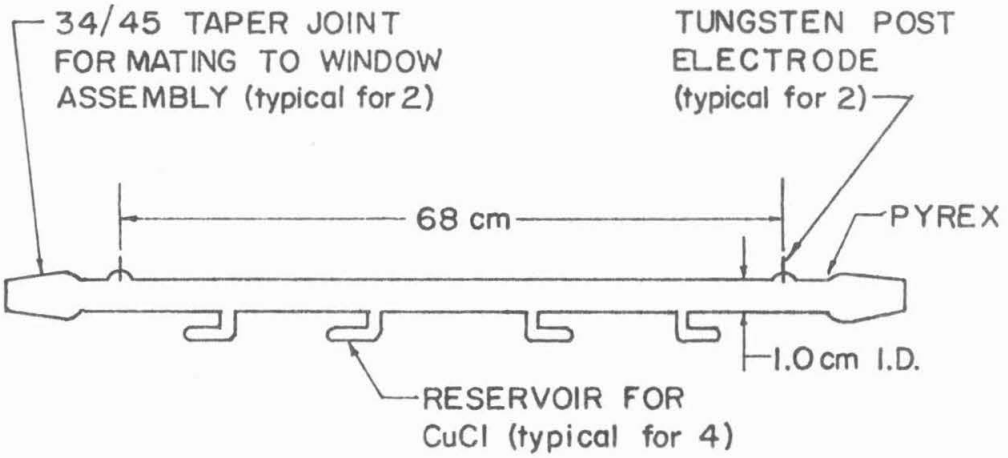

Figure V.3. Laser discharge tube used for the remaining work in this thesis.

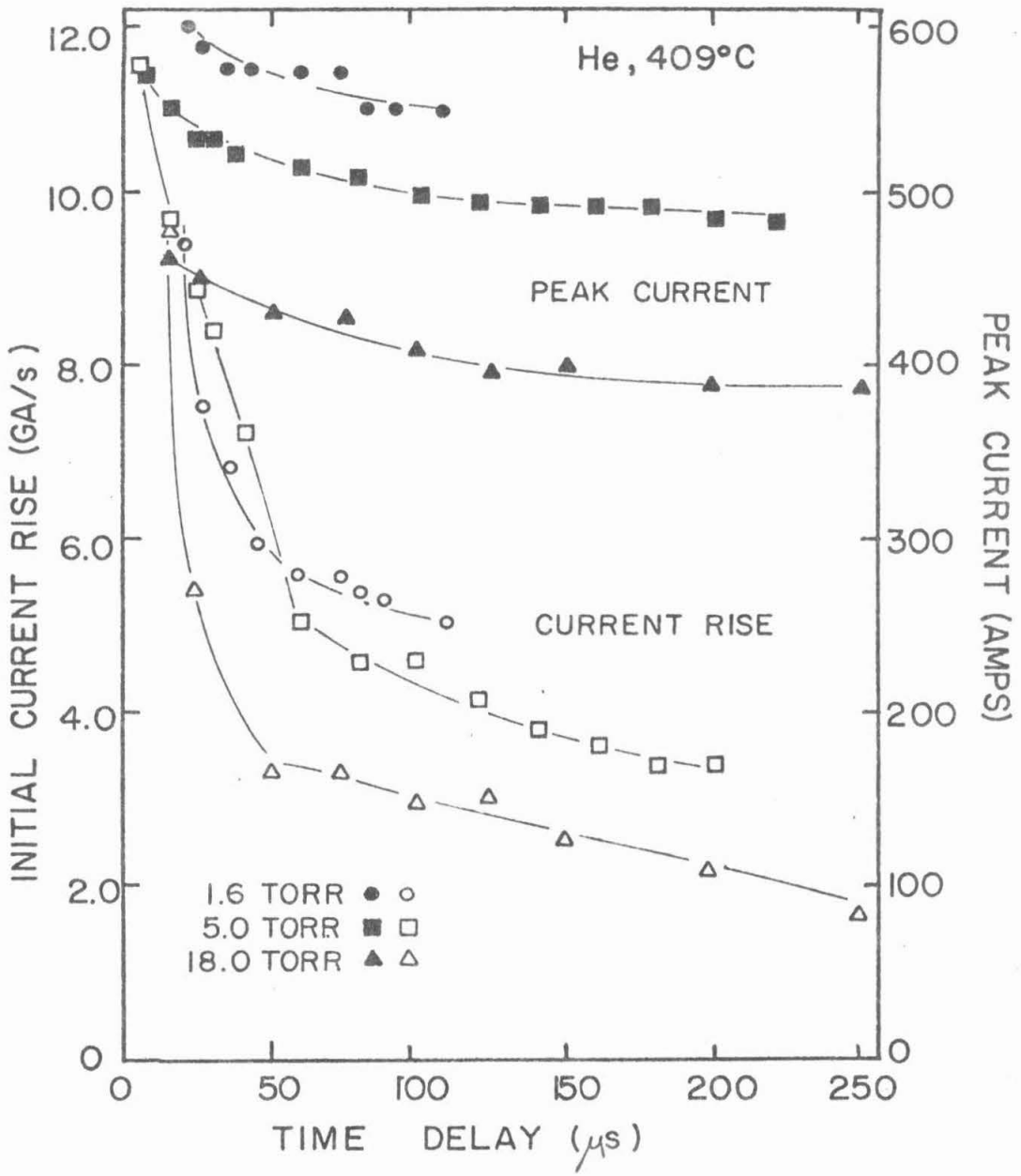

Figure V.4. The rate of current rise and peak current of the pumping pulse as a function of time delay and buffer gas pressure in helium at 409°C. Full width at zero height of the current pulse was typically 275-350 ns.

rent rise is nearly the same for all pressures.

The peak voltage across the discharge tube during the pumping pulse as a function of time delay is shown in Figure V-5. Also shown is the pre-peak voltage at which the current begins to rise. At short time delays, the ambient electron density is high so that breakdown need not be initiated. Hence the current flows with the onset of the voltage pulse. As the time delay increases, the ambient electron density decreases, impedance increases, and the voltage required to initiate the current increases. At the maximum delay shown, the peak voltage coincides with the onset of the current pulse, characteristic of breakdown. Therefore at short delays, more of the discharge energy is channeled into the electron gas, and hence the electron temperature will be higher. Because the pumping rates are proportional to the current, rate of current rise, and electron temperature, these rates decrease with increasing time delay and pressure.

V.B.2.b The Laser Pulse

The dependence of laser pulse energy on time delay has already been discussed; it can be rather complicated. The shape of the laser pulse, and its relation to the current pulse is also a function of time delay. Figure V-6 shows laser pulse energy, peak power and full width at zero height (FWZH) as a function of time delay. The behavior is typical for a wide range of pressures. Note that peak power occurs at an earlier time delay than does optimum energy. Optimum energy is a result of a longer pulse of less than optimum peak power.

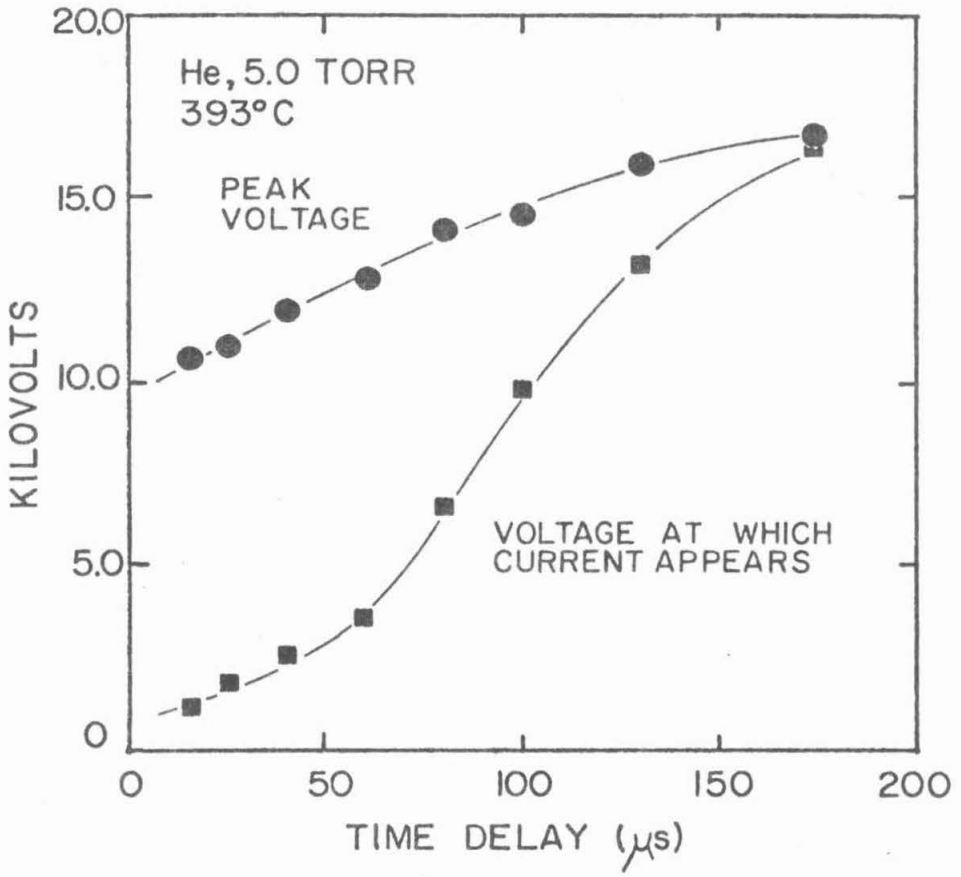

Figure V.5. Peak voltage and the voltage at which the current begins to rise during the pumping pulse. Charging voltage was 16.0 kV.

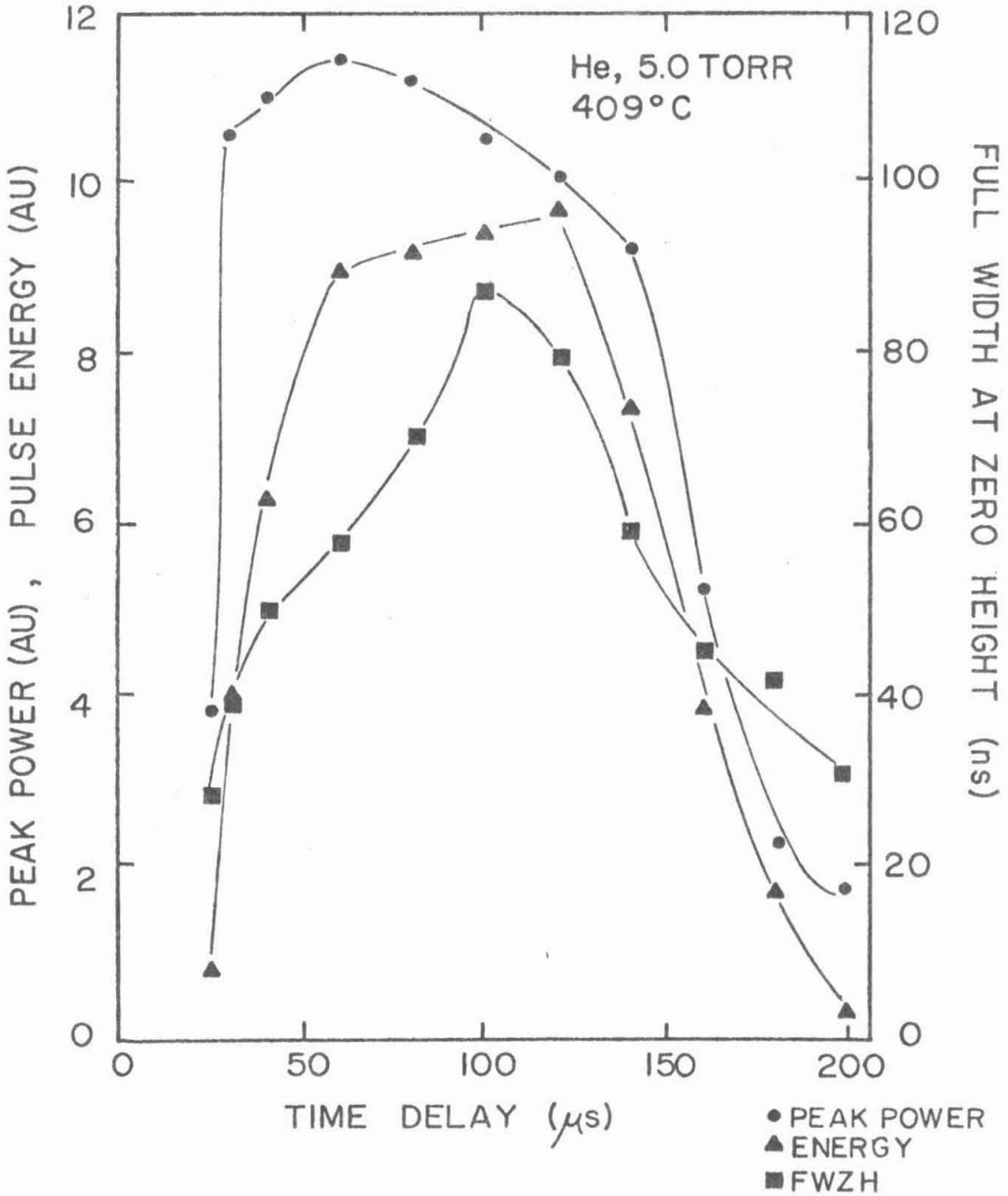

Figure V.6. Laser pulse energy, peak power during the pulse, and full width at zero height as a function of time delay. Note that optimum power is obtained at a shorter time delay than optimum energy.

We have already seen that the rate at which the pumping pulse current rises decreases as the time delay increases. Figure V-7 shows typical laser pulses computed with rate equations as a function of the rate at which the pumping pulse current rises (see Section III.F). Note that as this rate decreases, the peak power decreases and the pulse width increases. This is precisely the behavior seen experimentally. If the rapid rise in current seen at short delays could be maintained in order to coincide with the optimum densities of ground state and metastable copper, then peak power and laser energy would be improved. This is discussed further in Section V.C.

The time at which the laser pulse appears during the pumping current pulse is a function of time delay and pressure. Figure V-8 shows the time after the initial current rise that the laser pulse appears. At short delays, the laser pulse does not appear until late into the current pulse. As the time delay increases, the laser pulse moves towards the start of the current pulse, reaches some minimum value, then moves back into the current pulse. The delay at which the pulse appears the earliest increases with increasing buffer gas pressure, and the time of this earliest appearance decreases as the buffer gas pressure is increased. At short time delays, there is still a significant population of metastable copper which must be overcome, so that a long pumping period is required to reach threshold. As the time delay increases, the metastable population decreases, requiring less pumping to reach threshold, so the laser pulse moves

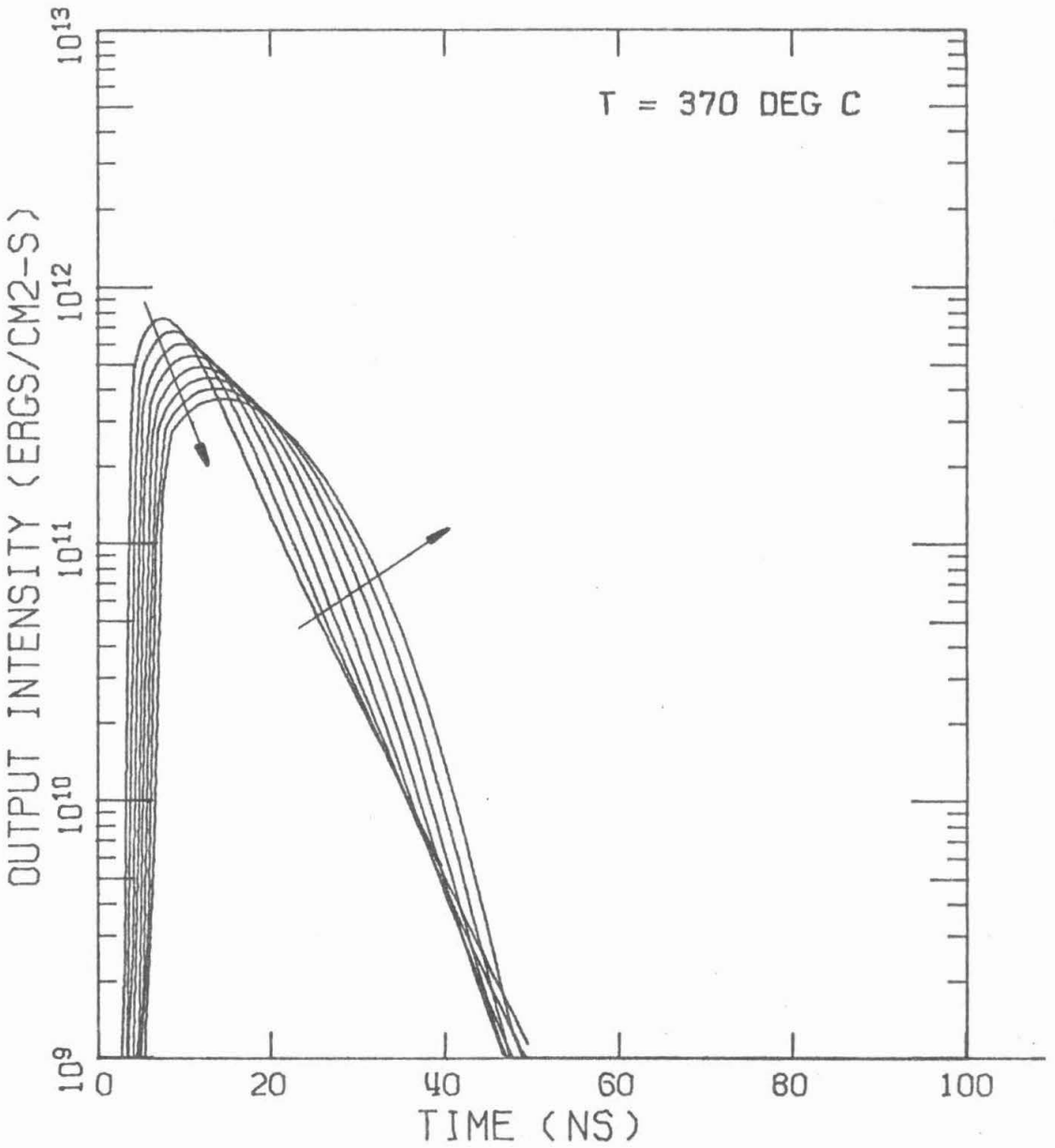

Figure V.7. Typical laser pulses computed using rate equations as a function of the rate of current rise in the pumping pulse. The arrows point in the direction of decreasing rate of current rise (16 GA/s - 2 GA/s). Note that as the peak power decreases, the pulse width increases.

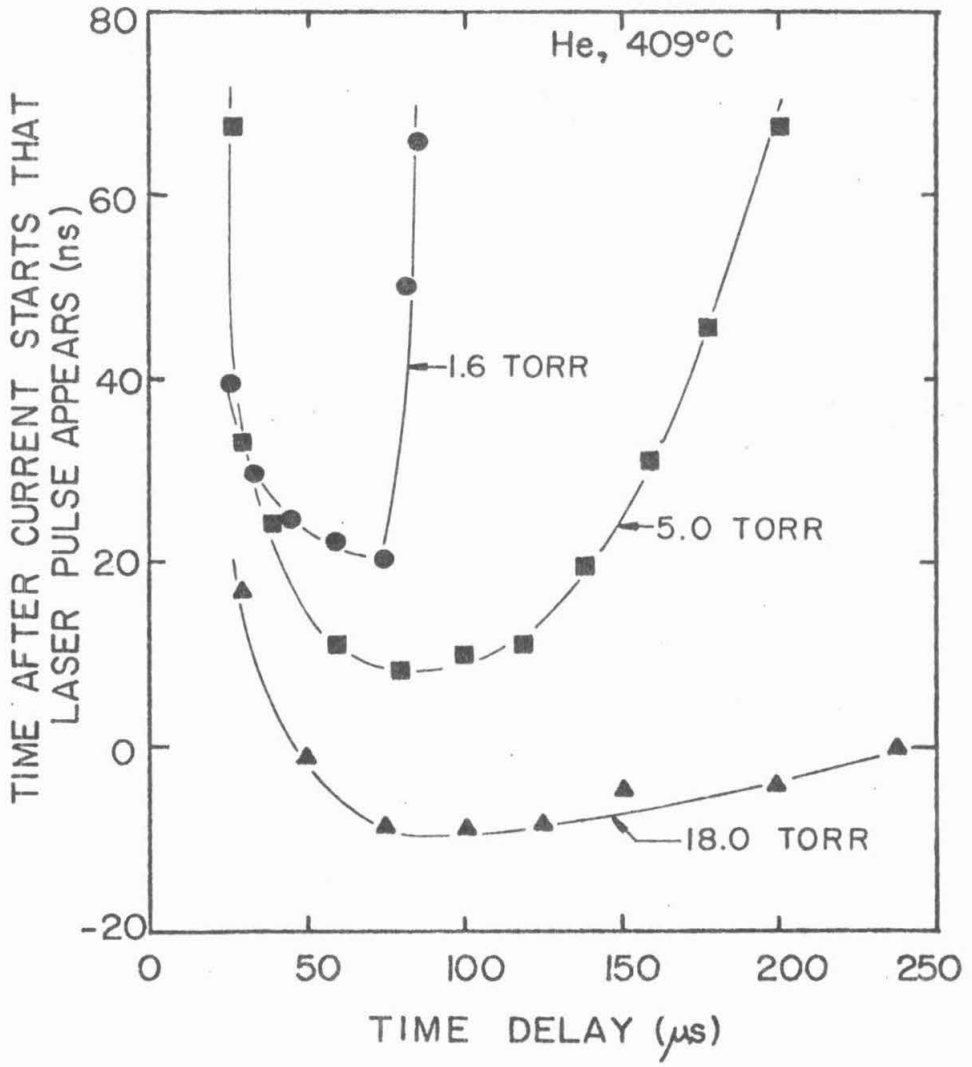

Figure V.8. The time after the pumping pulse current begins to rise, that the laser pulse appears as a function of time delay and helium buffer gas pressure at 409°C. The optimum time delays for the cases shown are 40 μs (1.6 Torr), 120 μs (5.0 Torr) and 80 μs (18 Torr). The optimum delays occur near the minimum times shown above.

forward in time. At long time delays, despite the lack of metastables, the pumping rates and copper densities are sufficiently small that a long pumping period is again required to reach threshold. The decrease in time of appearance as the pressure is increased may be due to more rapid collisional deactivation of the metastable level.

Note that the minimum time required before the laser pulse appears is actually negative for given discharge conditions. On a coarse oscilloscope scale, the laser pulse appears to arise before the current pulse. If the vertical scale is expanded, one finds a small leading edge to the current pulse of about 15 amps for about 20 ns duration. This is very small compared to the hundreds of amps in the actual pumping pulse. Despite their few numbers, these "prepulse" electrons will be relatively hot compared to the primary pulse electrons as the voltage is at or near its peak value at this early time. The fact that the laser pulse can be produced before the primary current pulse emphasizes the necessity to shorten the pumping pulse for maximum efficiency. The 80-90% of the pumping pulse subsequent to the laser pulse constitutes wasted energy.

V.C. Continuous Discharge Enhancement of Laser Energy

V.C.1 Introduction

The afterglow period between discharge pulses is of interest primarily for two reasons. The first is that during this period thermal collisional processes occur (e.g., reassociation, charge exchange, collisional deactivation) which determine the availability

of ground state copper. The second is that initial conditions are provided for the pumping discharge pulse. It has been shown that for otherwise fixed discharge conditions, the optimum laser pulse energy is proportional to the rate of current rise of the pumping pulse [V-6], and that the rate of current rise is a function of time delay (see Section V.B.2.a).

A continuous discharge should maintain the interpulse afterglow,and eliminate the necessity for the second pulse to break down the gas. Consequently, the rate of current rise in the pumping pulse should be increased. We have studied the influence of a continuous glow discharge sustained in the laser tube simultaneously with the double discharge pulse excitation. The results of that procedure are reported here.

V.C.2 Experimental Results and Discussion

The change in optimum laser pulse energy as a function of glow discharge current in 4.0 Torr of helium and CuCl at its vapor pressure at 385^{o}C ($\approx$ .04 Torr) is shown in Figure V-9. The power supply used to sustain the glow discharge was connected between the high voltage electrode and ground. It was homemade using a Hippotronics #25C transformer. Note that the optimum laser energy is increased by as much as 6%, and that the glow dischage current at which this enhancement occurs is less than 1 mA. The glow discharge current is that value going to ground through the anode. The current delivered by the power supply was approximately twice as much. The

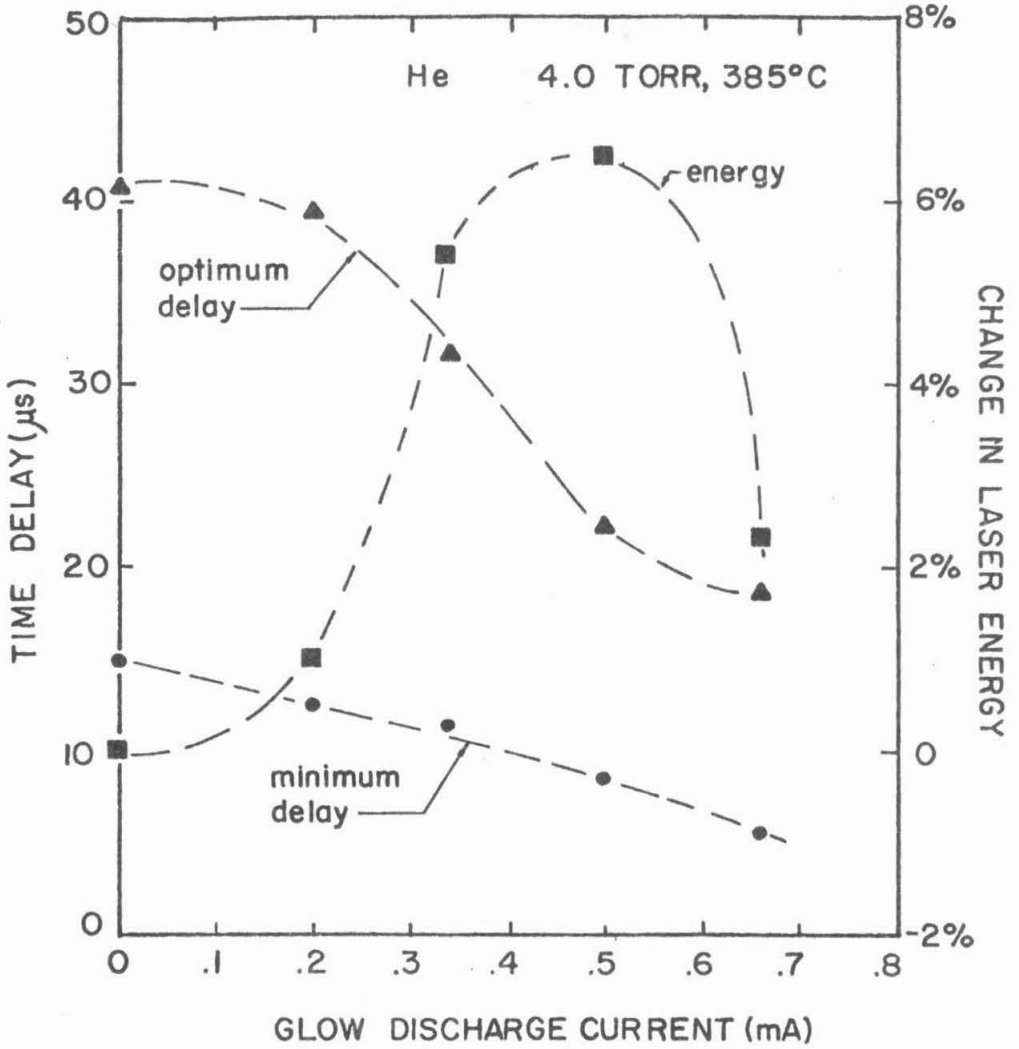

Figure V.9. The change in optimum laser energy, the minimum delay, and the optimum delay as a function of glow discharge current. There is an optimum glow discharge current for the increase in laser energy while the minimum and optimum delays decrease monotonically with increasing glow discharge current. The results are typical for a large range of buffer gas pressures and tube temperatures.

remainder went to ground through the gas system. Note also that the minimum and optimum time delays monotonically decrease as the glow discharge current is increased. The results shown in Figure V-9 are typical for a large range of buffer gas pressures and tube temperatures. Figure V-10 shows the laser output pulse energy, optimized with respect to time delay and glow discharge current, as a function of helium buffer gas pressure. Note that at low pressures the enhancement in laser energy is as much as 35%, but this decreases as the optimum buffer gas pressure is approached ($\approx$ 8 Torr). The glow discharge became unstable as the optimum pressure was approached with helium so that the enhancement could not be confirmed at pressures greater than optimum. For the tube geometry and discharge conditions described above, the optimum buffer gas pressure for argon was low enough so that the glow discharge remained stable above the optimum pressure. Enhancement in output pulse energy was observed at and above the optimum argon pressure. The increase in laser energy was about 3.5% at the optimum pressure (see Figure V-11). This enhancement is not due to discharge heating. The optimum output energy is increased in the presence of the glow discharge at temperatures both less than and greater than the optimum temperature ($\approx 400^{o}C$).

The decrease in optimum and minimum delays, and the increase in optimum laser energy observed with increasing glow discharge current is consistent with the results obtained by increasing the rate of the rise in pumping pulse current [V-6]. But the rate of rise increased only a few percent for the experiments reported here, much less

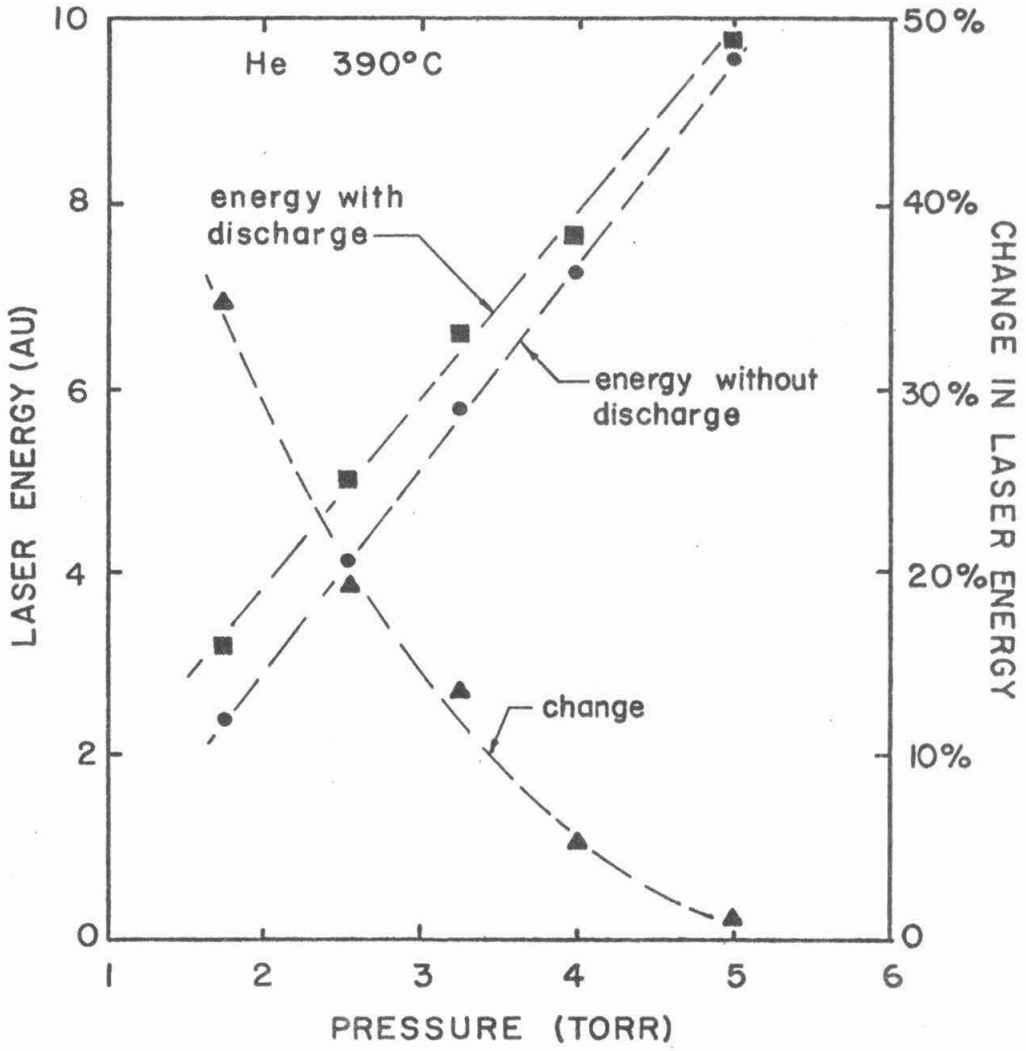

Figure V.10. Laser energy and the change in laser energy optimized with respect to time delay and glow discharge current as a function of buffer gas pressure in helium. Note that as the optimum pressure is approached (≈8 Torr) the change in laser energy decreases.

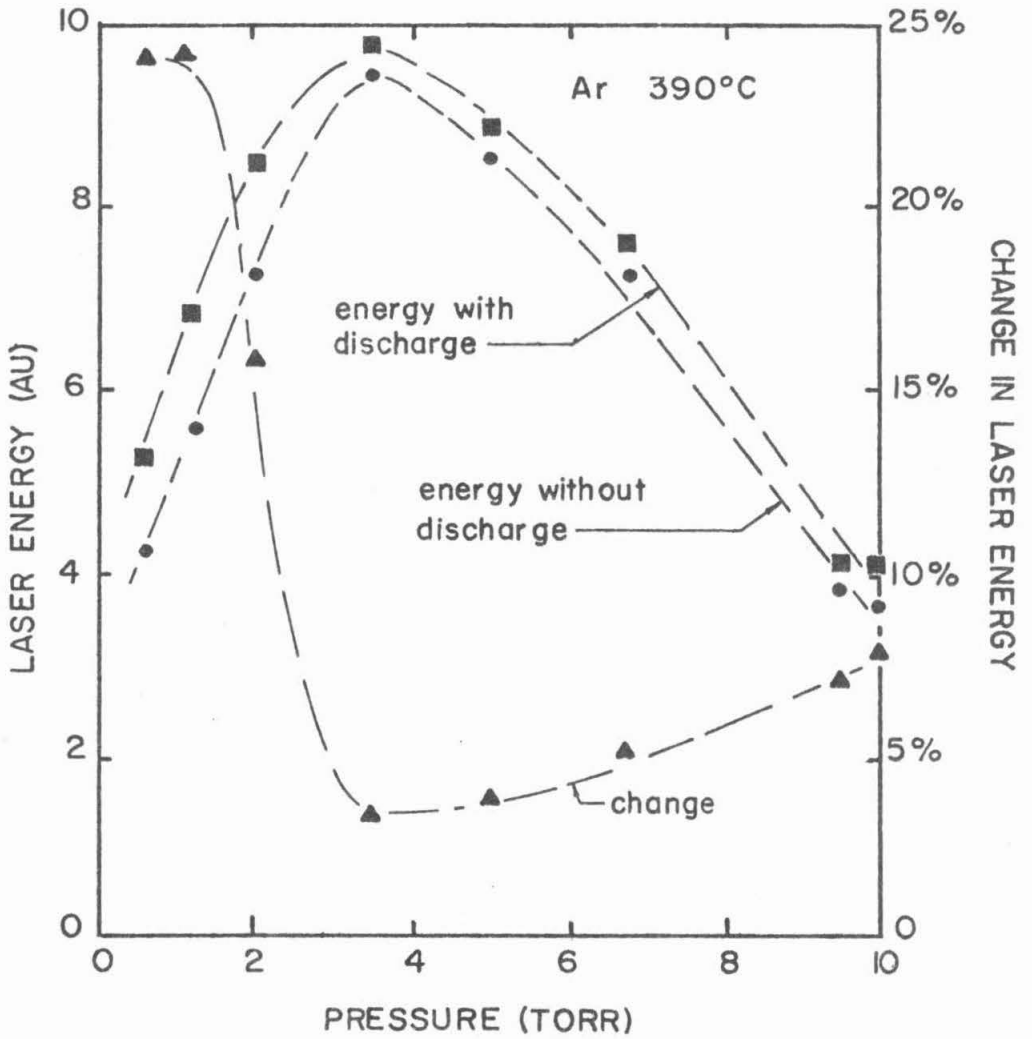

Figure V.11. Laser energy and the change in laser energy optimized with respect to time delay and glow discharge current as a function of buffer gas pressure in argon. Laser energy is enhanced by 3.5% at the optimum buffer gas pressure.

than the value required to cause the observed change in output energy according to earlier work [V-6,8]. The decrease in minimum and optimum delays are also large for the observed change in the rate of rise of pumping pulse current. The rate of current rise and peak current of the dissociation pulse were essentially unchanged by the glow discharge.

During "double pulsing" in the presence of a glow discharge, the electron temperature during the interpulse afterglow will tend to a value determined by the glow discharge and not by the gas temperature. Without the DC discharge, collisional radiative recombination is dominant, varying with the electron temperature as $T_e^{-9/2}$ [V-7]. With the glow discharge, this channel of ion recombination is effectively eliminated and is replaced by ambipolar diffusion. The time delays of interest here are short compared to the diffusion time required for neutral copper to return to the center of the tube after recombination at the walls. Hence in the presence of a glow discharge, contributions to the neutral copper population by ion recombination are eliminated. The fractional ionization caused by the dissociation pulse is large compared to that caused by the glow discharge (see Section II.D). Despite this loss of neutral copper, the optimum laser energy increases. This can only occur if the population of metastable copper is reduced by an even larger fraction. After the electron temperature falls from its peak value, and the dissociation rate of CuCl becomes small, the only sources of metastable copper are cascading from higher lying levels and ion recombination. By eliminating

this second source of metastable copper, the ratio of ground state copper to metastable copper is increased. The optimum laser energy is therefore also increased. In order for this explanation to be valid, ion recombination without the glow discharge, which populates the lower laser level, must be significant. The work of Gridnev, et al [V-18] indicates that this may indeed be the case.

To determine how the laser energy depends on the ratio of metastable (^2D) to ground state (^2S) copper present at the time of the pumping pulse, the rate equation analysis discussed in Chapter III was used. For otherwise fixed discharge conditions, the ratio of metastable and ground state copper densities was varied. The results are shown in Figure V-12. Note that a change of only a few percent in the ratio of densities can produce a large enhancement of laser energy.

A second effect which may be important in explaining why the output pulse energy is enhanced by a glow discharge is dissociation of copper chloride at relatively low electron energies. From the theory of Dorgelo, Alting and Boers [V-9,10], the electron temperature in the glow discharge is of the order of an electron volt (see Figure V-13). Hence some dissociation of copper chloride will still occur late in the afterglow. But unlike dissociation at high electron energies which occurs during the dissociation pulse, the energy excess will be small. Therefore the fractional yield of metastable copper from the dissociation will be smaller. The rate of dissociation due to the glow discharge will be small compared to that during the

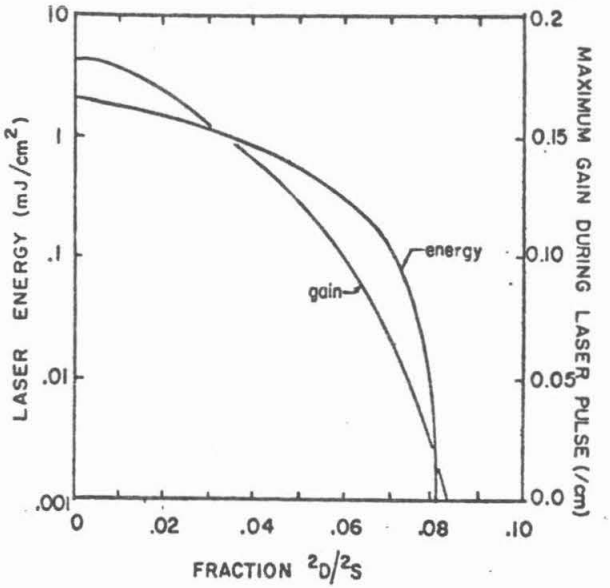

Figure V.12. Results of a rate equation analysis in which the ratio of metastable (^2D) to ground state (^2S) copper densities at the beginning of the pumping discharge pulse is varied. Discharge conditions are otherwise fixed.

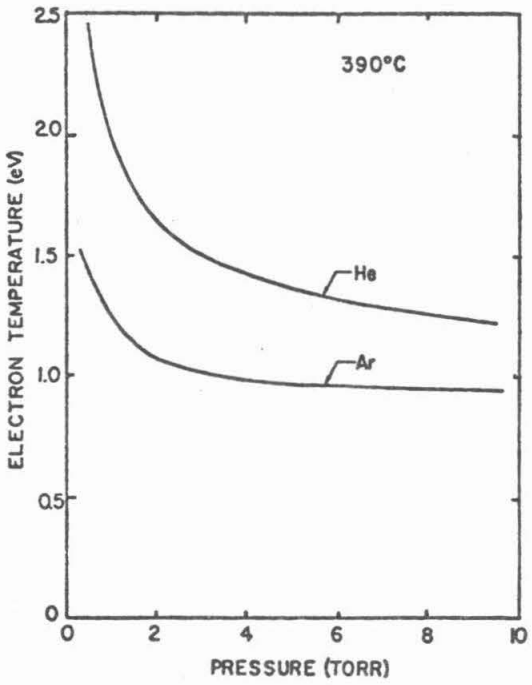

Figure V.13. Using the theory of Doregla, Alting and Boers [V-9,10] the electron temperature in the positive column of a glow discharge in helium and argon 390°C is shown above as a function of buffer gas pressure. CuCl was assumed to be completely dissociated. These temperatures are an indication of the value to which the afterglow electron temperatures will approach at long time delays.

dissociation pulse but the rate may be large enough to compensate temporarily for the loss of copper due to reassociation. Figure V-14 shows laser pulse energy as a function of time delay and glow discharge current. Note that as the glow discharge current increases, the pulse energy at long delays increases relative to the optimum value, creating a plateau appearance. This suggests that a quasisteady condition has been produced between reassociation and dissociation of CuCl at low electron energies.

The results and discussion above are consistent with the results of Brandt and Piper [V-11] who investigated the effect of dissociation pulse shape and energy on laser energy. They used a low voltage (500V) quasi-CW ($\approx$ 10 μs duration) dissociation pulse and contrasted it with the standard high voltage (18 kV) dissociation pulse in a transverse discharge. They found that comparable laser power was obtained with the low voltage dissociation pulse for only a tenth of the energy input (1 mJ/cm^3 of active volume) of the high voltage pulse. Of equal interest is that they observed that the minimum and optimum delays shifted to smaller values in the low voltage mode. The cause was attributed to a smaller fraction of copper metastables obtained in the low voltage discharge as compared to the high voltage discharge.

In summary, the laser pulse energy from a Cu/CuCl double pulse laser has been enhanced by as much as 35% at low buffer gas pressure and 3.5% at optimum conditions by the application of a continuous glow discharge. This increase may be due to three causes: 1) increasing

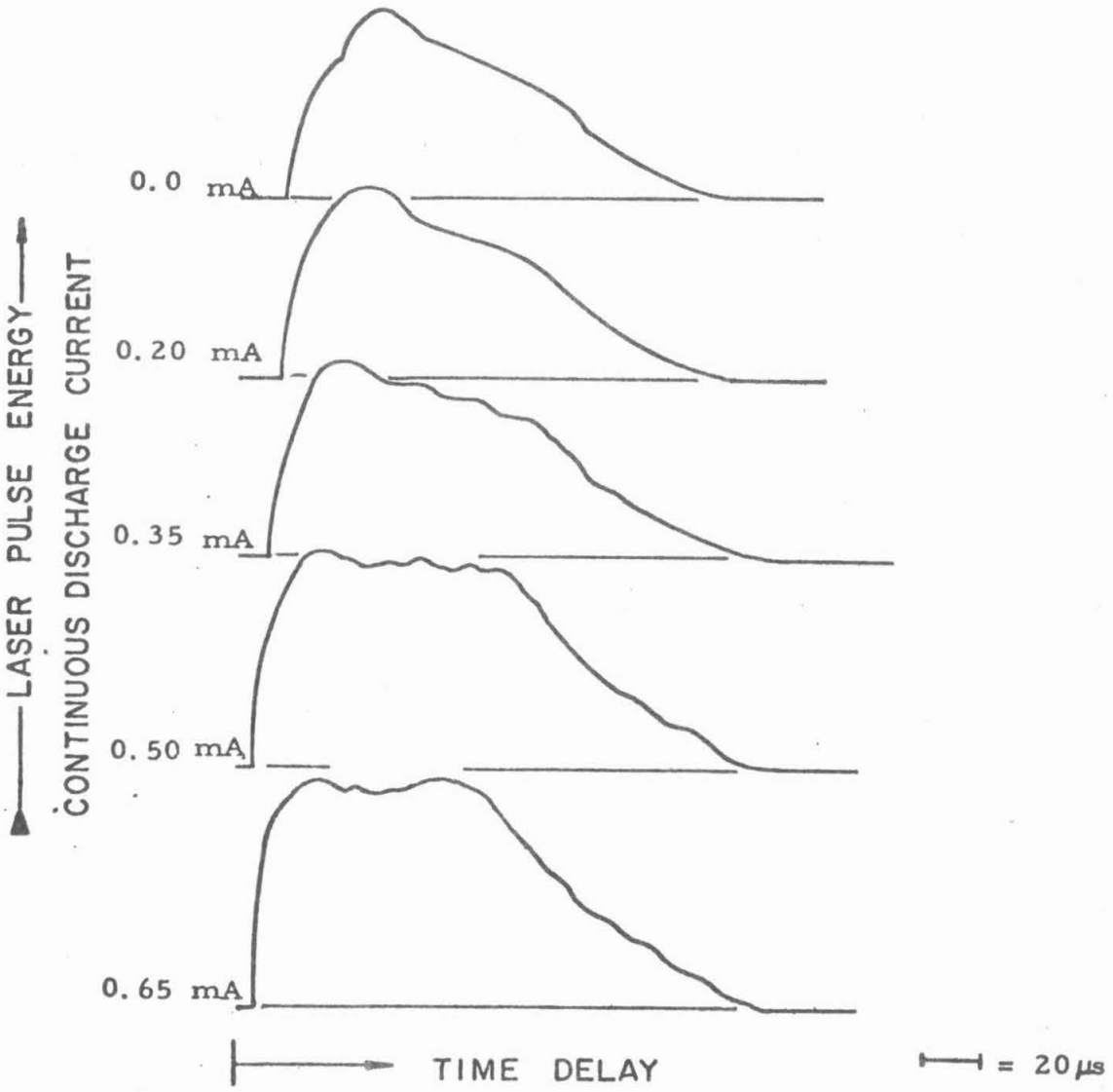

Figure V.14. Laser energy as a function of time delay and glow discharge current. Note that laser energy at long delays increase relative to the optimum delay as the glow discharge current increases. The plateau appearance suggests a quasisteady condition between reassociation and dissociation of CuCl.

the rate of current rise of the pumping pulse; 2) eliminating contributions to the metastable lower laser level due to ion recombination; and 3) dissociation of CuCl at low electron energies, yielding a smaller fraction of metastable copper. The energy input of the glow discharge is negligible compared to the energy input of the high voltage discharge pulses so that the increase in laser energy is nearly free of charge. The results discussed above, along with those of Vetter [V-6], and Brandt and Piper [V-11] indicate that ideal discharge conditions for the Cu/CuCl double pulse laser comprise dissociation of CuCl by low energy electrons; small rates of collisional radiative recombination of ionic copper; and sustained afterglow electron densities during the afterglow to reduce the impedance of the discharge and to increase the rate of rise of current during the pumping pulse.

V.D. Spatial and Temporal Dependence of Laser Energy Density during the Afterglow: Laser Spots

V.D.1 Introduction

Just as the total laser energy is a function of time delay, the shape of the laser spot (the laser energy density as a function of radial position) is also a function of time delay. Curious behavior has been reported for laser spot shapes in continuously pulsed (15-30 kHz) and in the "burst" mode (10 kHz in packets of tens of pulses having an average pulse rate of .7 kHz) copper lasers. Using the continuously pulsed mode, Nerheim, et al [V-12] reported that annular laser spots were observed at low laser power in neon buffer gas.

As the power was increased (CuCl density raised), the ring filled in. In helium, the annular appearance was barely detectable. Liu, et al [V-4], using the "burst" mode, made radial measurements of copper ground state and metastable densities (CuBr in neon). They obtained high resolution using dye laser absorption spectroscopy. Ground state densities were found to be depleted by as much as a factor of two at the center of the tube relative to an annular region halfway to the tube wall. Again the effect was most severe at low CuBr density, where an annular laser spot could be observed. They suggested that the axial depletion is due to thermal diffusion driven by a temperature gradient established by discharge heating and charged particle diffusion out of the region of maximum current. Liu, et al [V-13] have calculated that for their tube geometry with an average power loading of 78 W/cm, a temperature rise of 1300^{o}C is possible at the center of the tube relative to the wall, resulting in gas density being reduced by a factor of 3.5 at the center of the tube.

For the laser pulse durations considered here (tens of nanoseconds) resonator optics should play a secondary role in determining the spot shape. From the work of Fox and Li [V-14] it is known that hundreds of resonator passes requiring nearly a microsecond are required to establish a single TEM mode. Double pulsed copper lasers will usually lase over the entire tube or mirror area whichever is smaller. Hence spot shapes should first be explained kinetically (see Section VI.D).

V.D.2 Experimental Results and Discussion

To measure laser spot shapes, the experimental setup was the same as discussed in Section II.E. The neutral density filter and focusing lens were removed, and the photodiode mounted on a micrometer controlled translator with motion perpendicular to the optical axis. A flat black shield with a 1 mm hole was placed over the photodiode entrance lens. The photodiode entrance hole was placed as close as possible to the output mirror (≈8 cm). The spot center was assumed to be the very small spot observed at maximum time delay.

Laser spot profiles for various helium buffer pressures are found in Figure V-15. The "rear" mirror had a 2m radius of curvature dielectrically coated for 99% reflection at 5106Å. The output coupler was a quartz flat (≈4% reflectivity). The spot size (radial dimension at which laser energy falls to 1/e of maximum) decreases near and past the optimum time delay and increases with buffer gas pressure. The maximum 1/e spot size occurs 10-30 μs before the optimum delay. The absolute spot size (the radial distance at which laser energy can no longer be detected) behaves differently. Except for delays very near the minimum delay, the absolute spot size remains constant at the tube radius until the optimum time delay is reached. For time delays greater than optimum, the absolute spot size recedes with speeds of a few times 10^4 cm/sec. This speed increases as the time delay increases. The speed of recession decreases with increasing pressure.

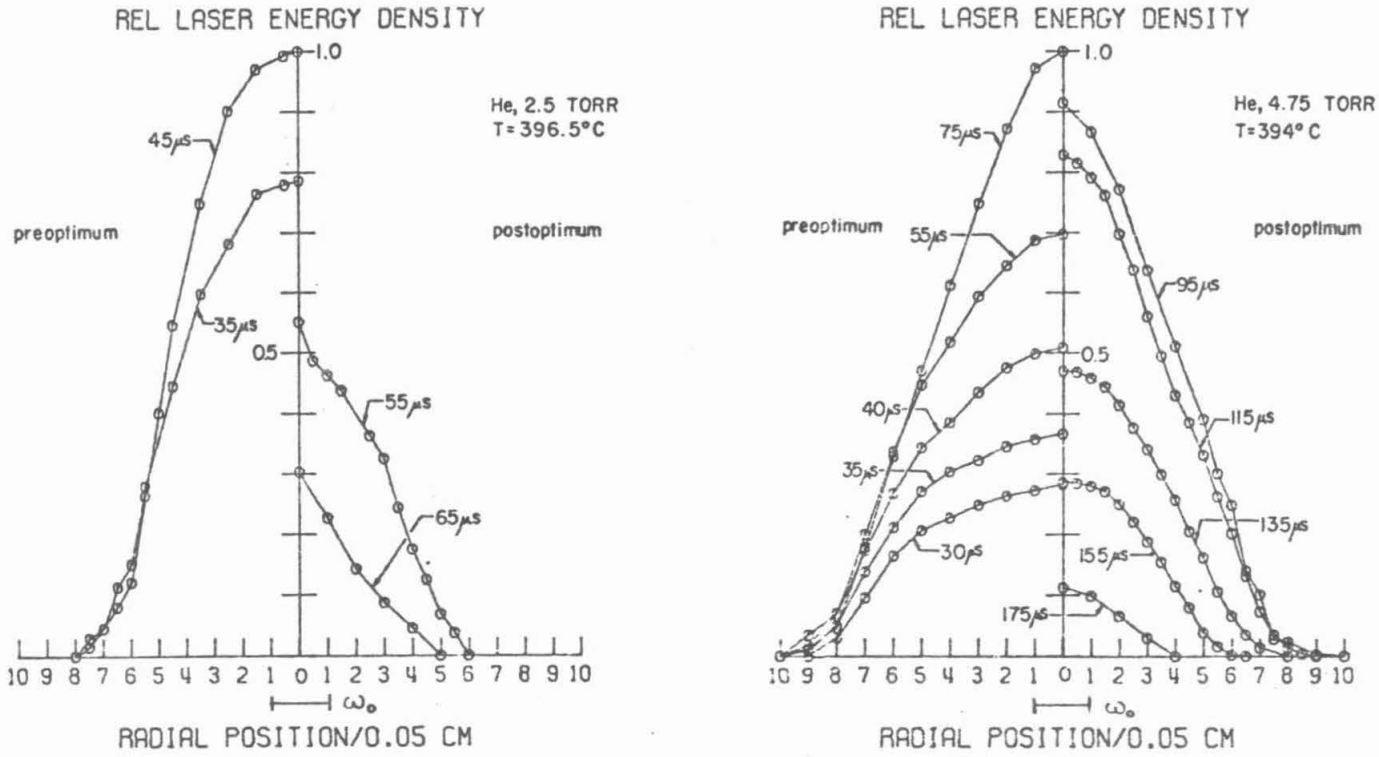

Figure V.15. Laser energy density as a function of time delay, radius and helium buffer gas pressure. The optical cavity was a 2m, 99% mirror and a quartz flat output coupler. The TEM_{00} Gaussian beam spot size (ω_0) is indicated by the bars.
a) 2.5 Torr
b) 4.75 Torr

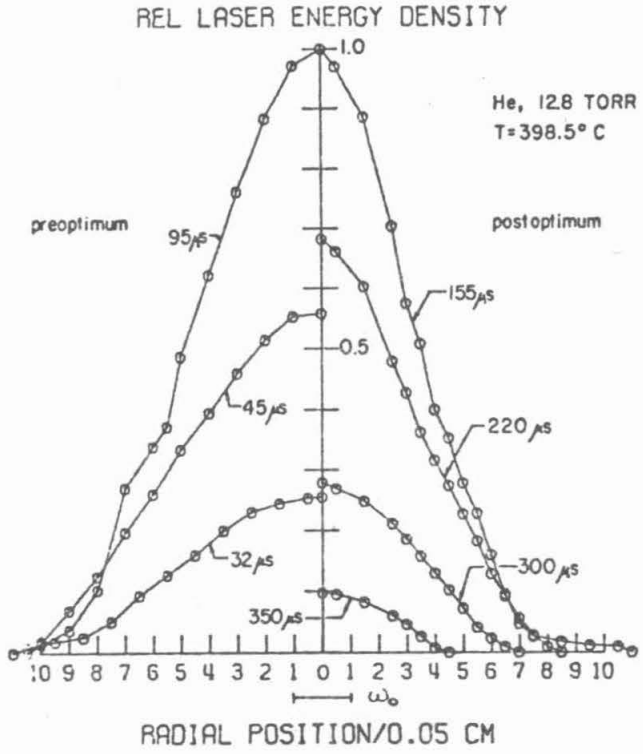

c) 12.8 Torr

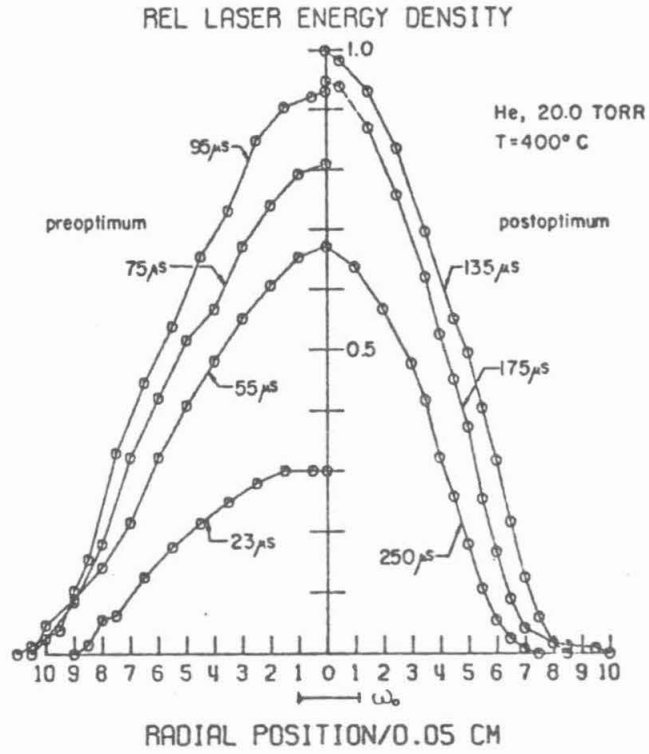

d) 20.0 Torr

Based on the description above, one might conclude that the dependence on pressure of the speed of spot recession is dominated by diffusion. The average diffusion speed is $V_{dif} \approx D\alpha_o^2/a$ [V-15], where α_o is the first zero of the zeroeth order Bessel function and a is the tube radius. For copper in helium, the diffusion constant D can be estimated by $12.86\ T^{1/2}/P_{Torr}\ cm^2/sec$ [V-16]. For the conditions of Figure V-15, $V_{dif} \approx 3900/P$ cm/sec. Hence neutral species diffusion is too slow to account for the spot recession. A volumetric process must dominate. The constant absolute spot size before optimum delay would tend to support volumetric deactivation of copper metastables as being the dominant relaxation mechanism. With similar reasoning, one can argue that volumetric reassociation of copper should dominate over wall reassociation.

Due to the larger ambipolar diffusion constant, diffusion will dominate the radial discharge pulse electron distribution, yielding a profile which resembles a first order Bessel function. Hence the distribution of copper from dissociated CuCl initially has this profile, as does the distribution of excited Cu. Hence despite the apparent dominance of volumetric atomic and molecular processes, the laser spot shapes will appear to be diffusion limited.

With higher resolution, Figure V-16 shows the laser spot as a function of radius and time delay with helium at 4.75 Torr. Note that laser energy appears at the walls of the tube at the minimum delay. Note also the shallow dip in laser energy at the center of the spot. As the time delay increases, this dip decreases from a maximum

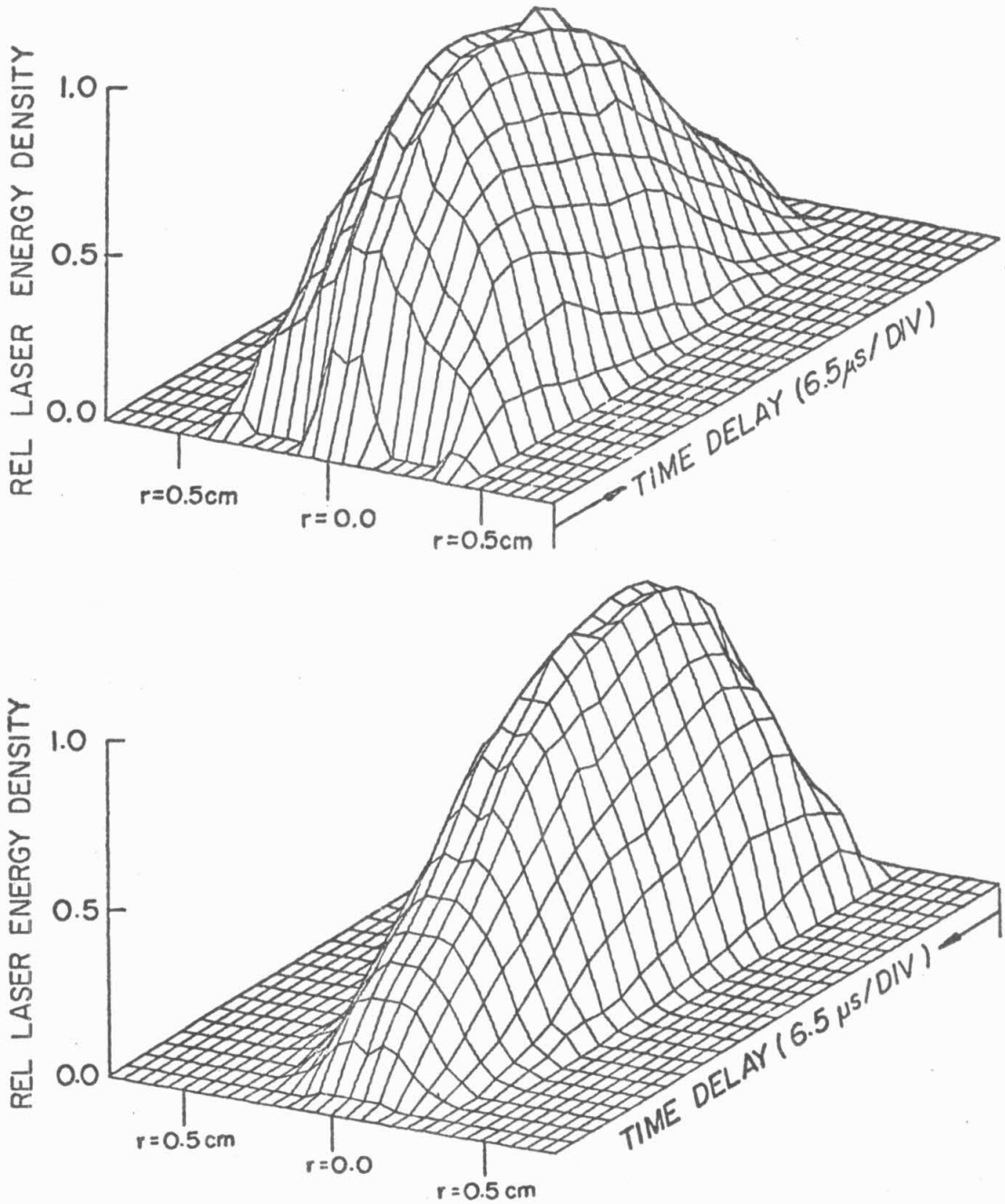

Figure V.16. Laser energy density as a function of radius and time delay in 4.75 Torr of helium.

of about 12% until it finally disappears after the maximum time delay. Figure V-17 is a laser spot with argon at 4.75 Torr. The dip is more severe. The behavior of this defect is consistent with the hypothesis that the gas is heated very rapidly on the axis by the dissociation pulse, cooling and equilibrating as the time delay increases. For constant energy deposition, the increase in the axial gas temperature relative to the wall temperature is inversely proportional to the thermal conductivity. Hence gas with the smaller thermal conductivity should have the larger laser defect if the defect is due to thermal depletion. The thermal conductivity of argon is about 1/8 that of helium [V-17]. The defect in argon is as much as 29% compared to the 12% maximum in helium. This is consistent with the previous discussion.

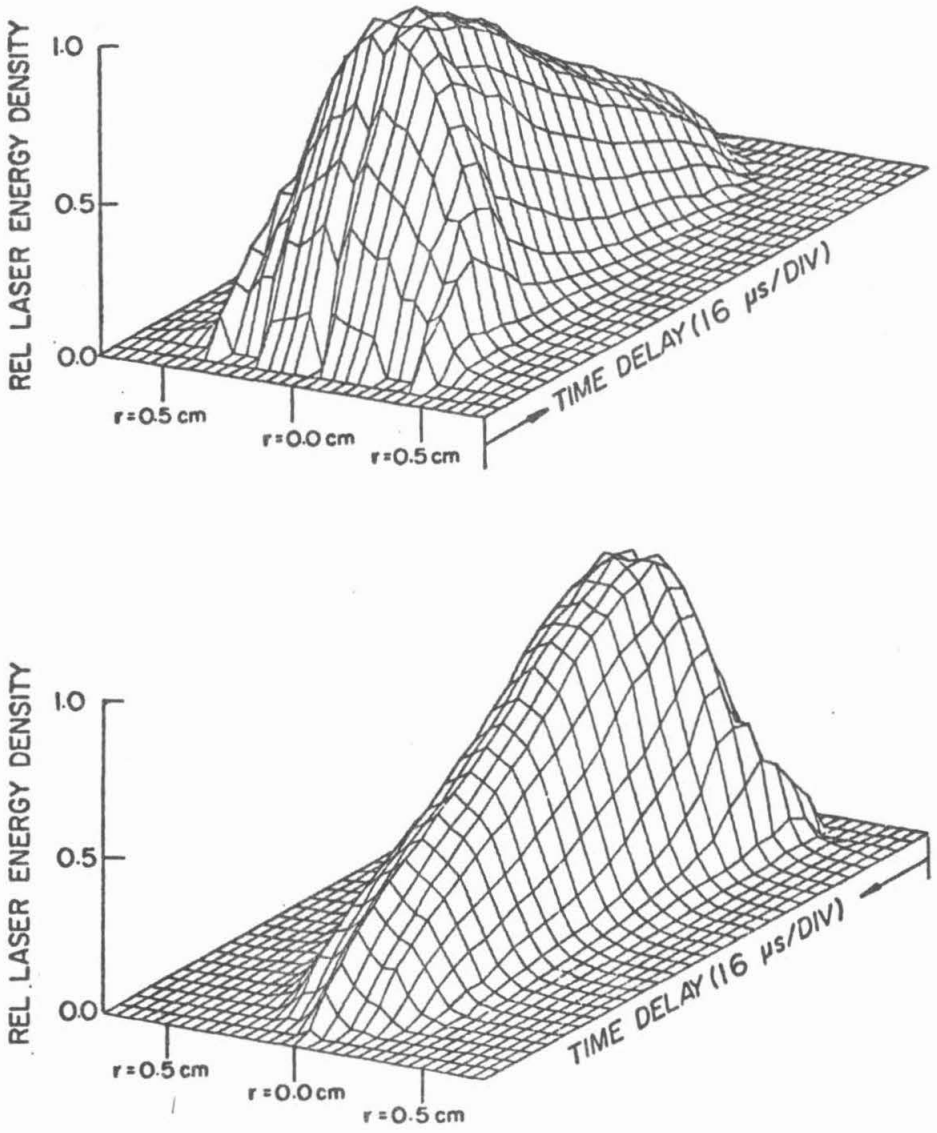

Figure V.17. Laser energy density as a function of radius and time delay in 4.75 Torr of argon.

REFERENCES

1. A.M. Shukhtin, V. G. Mishakov, G. A. Fedotov, and A. A. Ganeev, "Interference Methods for Observing the Dissociation of Copper Halide Molecules in a Pulsed Discharge", Opt. Spectrosc. 39, 444 (1976).

2. N. M. Nerheim, "Measurements of Copper Ground State and Metastable Level Populations in a Copper-Chloride Laser", J. Appl. Phys. 48, 3244 (1977).

3. J.Tenenbaum, I. Smilanski, S. Gabay, G. Erez, and L. A. Levin, "Time Dependence of Copper-atom Concentration in Ground State and Metastable States in a Pulsed CuCl Laser", J. Appl. Phys. 49, 2662 (1978).

4. C. S. Liu, D. W. Feldman, J. L. Pack, and L. A. Weaver, "Copper Halide Laser Research: Final Report", Westinghouse R & D Center, Pittsburgh, Pennsylvania, December, 1977.

5. J. Tenenbaum, I. Smilanski, S. Gabay, G. Erez, L. A. Levin, J. Katriel, and Shammai Speiser, "Buffer Gas Effect on Ground and Metastable Populations in a Pulsed CuBr Laser", IEEE J. Quant. Electronics QE-14, 680 (1978).

6. A. A. Vetter, "Quantitative Effect of Initial Current Rise on Pumping the Double-pulsed Copper Chloride Laser", IEEE J. Quant. Electronics, QE-13, 889 (1973).

7. M. A. Biondi, "Recombination" in Principles of Laser Plasmas, ed. George Bekefi, Wiley Interscience, New York, 1976.

8. A. A. Vetter, Private Communication, 1978.

9. H. B. von Dorgelo, H. Alting, and C. J. Boers, "Elektronentemperaturen in der Positiven Säule in Gemischen von Neon and Argon oder Quecksilber", Phys. Haag 2, 959 (1935).

10. R. T. Young, "Calculations of Electron Energies in He-Ne Discharges", J. Appl. Phys. 36, 2324 (1965).

11. M. Brandt and J. A. Piper, "Improved Dissociation Efficiency in TE Pulsed Copper Halide Lasers", Proc. SPIE Lasers 1978, Orlando, Florida, 1978.

12. N. M. Nerheim, A. M. Bhanji, and G. R. Russel, "A Continuously Pulsed Copper Halide Laser with a Cable-Capacitor Blumlein Discharge Circuit", IEEE J. Quant. Electronics QE-14, 686 (1978).

13. C. S. Liu, D. W. Feldman, J. L. Pack, and L. A. Weaver, "Kinetic Processes in Continuously Pulsed Copper Halide Lasers", IEEE J. Quant. Electronics, QE-13, 744 (1977).

14. A. G. Fox and T. Li, "Resonant Modes in a Maser Interferometer", BSTJ 40, 453 (1961).

15. F. F. Chen, Introduction to Plasma Physics, Plenum, New York, 1974.

16. J. O. Hirschfelder, C. F. Curtiss, and R. B. Bird, Molecular Theory of Gases and Liquids, Wiley, New York, 1954.

17. A. C. Jenkins and G. A. Cook, "Gas Phase Properties" in Argon, Helium, and the Rare Gases, G. A. Cook, ed. Interscience Publishers, New York, 1961.

18. A. G. Gridnev, T. M. Gorbunova, V. F. Elaev, G. S. Evtushenko, N. V. Osipova, and A. N. Soldatov, "Spectroscopic Investigation of a Gas Discharge Pulse Plasma of a Cu+Ne Laser", Sov. J. Quant. Electronics 8, 656 (1978).

VI. COMPUTER MODELS FOR THE DISSOCIATION PULSE, AFTERGLOW, AND LASER PULSE IN A Cu/CuCl LASER

VI.A. Introduction

A computer model of the dissociation pulse and afterglow in a Cu/CuCl laser has been written. Together with the rate equations discussed in Chapter III or the laser pulse model presented in Section VI.D, a complete numerical description of the Cu/CuCl double pulse laser is possible.

The afterglow model was written to have spatially averaged quantities, or to have a radial dependence. Rate equations were used for the laser pulse for spatially averaged results. The laser pulse model was used for the radially dependent results. Due to the computational expense of the radial codes, the majority of the results which follow are spatially averaged.

VI.B. Description of the Dissociation Pulse and Afterglow Model

The dissociation pulse and afterglow model begins at t = 0 with CuCl present at its vapor pressure for the specified tube temperature, and the buffer gas at a selected pressure. Breakdown is assumed to have occurred, so that a small electron density and ion population are also present. The dissociation discharge pulse is simulated by specifying that the electron temperature is constant for a given length of time, after which it is allowed to decay as described below. The electron distribution at all times is assumed to be given by a Maxwellian at temperature T_e.

The following species are considered:

N	Noble gas (buffer ground state)
N_m	Noble gas metastable state
N^+	Noble gas ion
Cu	Copper ground state
Cu_m	Copper metastable state
Cu^+	Copper ion
CuCl	Copper chloride diatomic molecule
n_e	Electrons

Since the afterglow time scale is tens to hundreds of microseconds, N and Cu excited states, except for the metastable states, are assumed to rapidly relax to the ground state, so only the metastable and ground states are considered. Although CuCl can be present as the dimer and trimer, only the monomer is considered. Although chlorine is explicitly ignored, it is assumed at all times that the number densities of Cu and Cl are equal. The effect of including chlorine is examined in Section VI.C.2. In Section V.D. it was shown that discharge heating is detectable in laser spot shapes. The effect, though, is on the average small and is therefore ignored.

The molecular noble gas ion, N_2^+ was initially included in the model, but was later deleted. Although the majority of noble ions exist as molecular ions under some conditions, at the pressure and time scales considered here, they turn out to be unimportant. Molecular noble gas ions are formed by the process

$$N^+ + 2N \rightarrow N_2^+ + N$$

with a rate constant of 4.4×10^{-32}cm^6/sec for neon [VI-1] and 1.0×10^{-31}cm^6/sec for helium [VI-2]. They recombine very rapidly by dissociative recombination, and neutral assisted dissociative recombination

$$N_2^+ + e \rightarrow 2N$$

$$N_2^+ + e + M \rightarrow 2N + M$$

with rate constants for the first process of $1.8\times10^{-7}(\frac{Te}{300})^{-.43}$cm^3/sec [VI-3] for neon and $6\times10^{-9}(\frac{Te}{300})^{-\frac{1}{2}}$ cm^3/sec [VI-3] for helium, and for the second process $2.0\times10^{-27}(\frac{Te}{300})^{-\frac{5}{2}}$ cm^6/sec [VI-2,4] for helium. Hence ignoring recombination, the time scale for helium molecular ions to be as abundant as single ions at room temperature is $\frac{1}{1.0\times10^{-31}N^2} \approx \frac{2.2\times10^4 \text{ sec}}{P^2_{\text{Torr}}} \approx 900$ μs at 5 Torr. This is long compared to times of interest.

VI.B.1 Processes and Reaction Rates

The major processes included in the dissociation pulse and afterglow model are shown in schematic form in Figure VI-1, and listed below. (Diffusion terms are discussed separately.)

Electron Impact:

a) Ionization

$$e + \binom{N}{N_m} \rightarrow N^+ + e + e - \Delta\varepsilon_1 \qquad \text{(VI.B.1a)}$$

$$e + \binom{Cu}{Cu_m} \rightarrow Cu^+ + e + e - \Delta\varepsilon_2$$

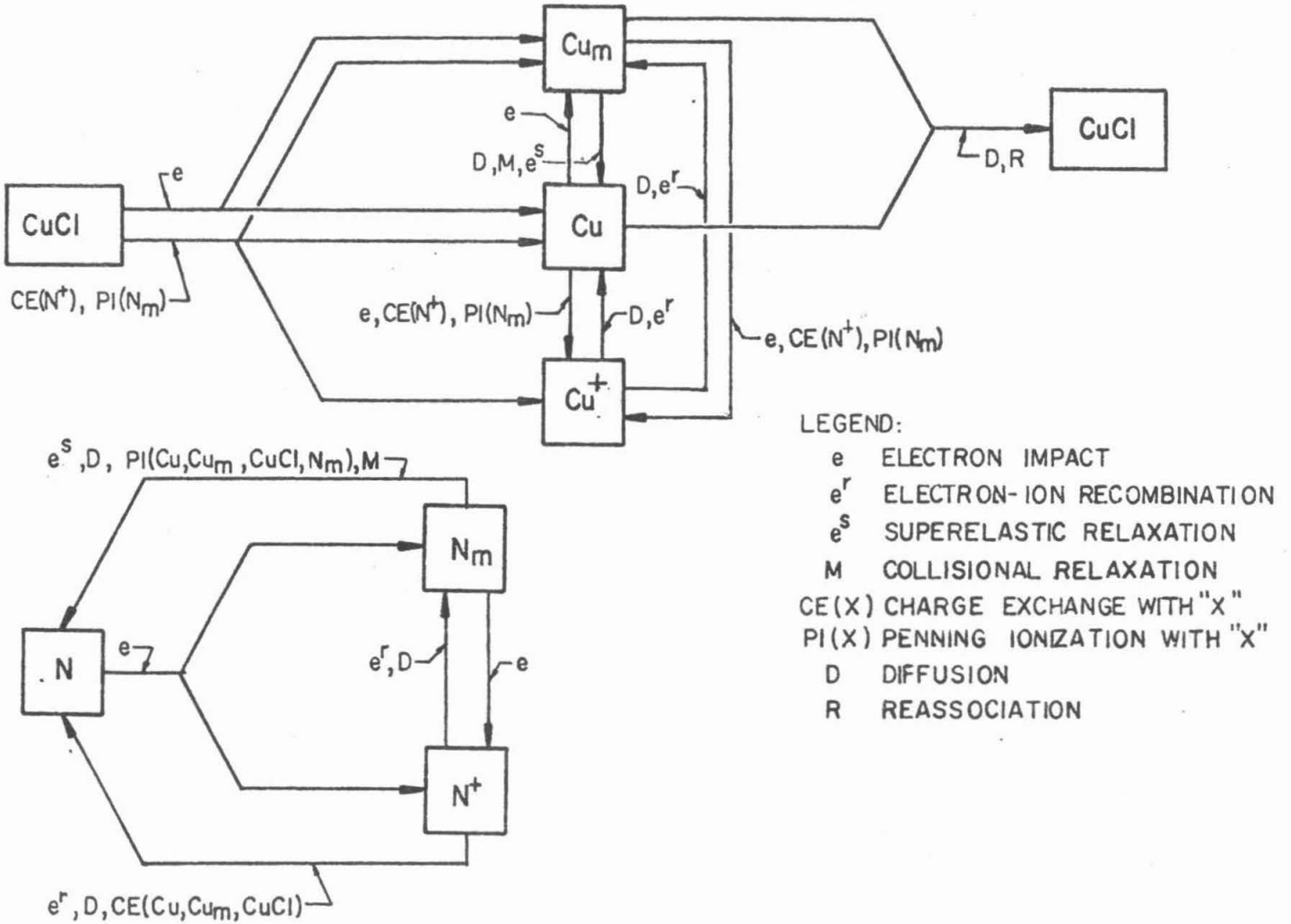

Figure VI.1. The dissociation pulse and afterglow model.

b) Metastable excitation

$$e + \binom{N}{Cu} \rightarrow \binom{N_m}{Cu_m} + e - \Delta\varepsilon_3 \qquad \text{(VI.B.1b)}$$

c) Molecular dissociation

$$e + CuCl \rightarrow \alpha Cu_m + (1-\alpha)Cu + [+C\ell] + e - \Delta\varepsilon_4 \qquad \text{(VI.B.1c)}$$

d) Superelastic deactivation

$$e + \binom{N_m}{Cu_m} \rightarrow e + \binom{N}{Cu} + \Delta\varepsilon_5 \qquad \text{(VI.B.1d)}$$

e) Elastic

$$e + M \rightarrow e + M - \Delta\varepsilon_6 \qquad \text{(VI.B.1e)}$$

Electron recombination:

a) Collisional radiative

$$\begin{aligned} &e + e + N^+ \rightarrow e + \delta N_m + (1-\delta)N + \Delta\varepsilon_7 + h\nu \\ &e + e + Cu^+ \rightarrow e + \alpha Cu_m + (1-\alpha)Cu + \Delta\varepsilon_8 + h\nu \end{aligned} \qquad \text{(VI.B.2a)}$$

b) Radiative recombination

$$\begin{aligned} &e + N^+ \rightarrow \delta N_m + (1-\delta)N + h\nu \\ &e + Cu^+ \rightarrow \alpha Cu_m + (1-\alpha)Cu + h\nu \end{aligned} \qquad \text{(VI.B.2b)}$$

Penning ionization (PI):

$$N_m + \binom{Cu}{Cu_m} \rightarrow N + Cu^+ + e + \Delta\varepsilon_9 \qquad \text{(VI.B.3)}$$

Dissociative Penning ionization:

$$N_m + CuCl \rightarrow \zeta Cu^+ + (1-\zeta)(\alpha Cu_m + (1-\alpha)Cu) + [C\ell] + \zeta e + \Delta\varepsilon_{10} \qquad \text{(VI.B.4)}$$

Charge exchange (CE):

$$N^+ + \binom{Cu}{Cu_m} \rightarrow N + Cu^+ \qquad \text{(VI.B.5)}$$

Dissociative Charge exchange:

$$N^+ + CuCl \rightarrow Cu^+ + [Cl] + N \qquad \text{(VI.B.6)}$$

CuCl reassociation:

$$\binom{Cu}{Cu_m} + [Cl] + M \rightarrow CuCl + M \qquad \text{(VI.B.7)}$$

Collisional deactivation:

$$\binom{N_m}{Cu_m} + M \rightarrow \binom{N}{Cu} + M \qquad \text{(VI.B.8)}$$

where

α = fraction of metastable Cu resulting from a CuCl dissociation or Cu^+ recombination (see discussion in Section VI.C.2.e)

$\Delta\varepsilon_i$ = energy contribution to electron temperature for the i^{th} process

δ = fraction of N_m resulting from N^+ recombination

ζ = fractional ionization in a dissocative Penning collision

M = neutral atom density

The rate equations for the above reactions and species follow. Diffusion terms and the equation governing electron temperature will be discussed separately.

$$\frac{dN}{dt} = -n_e(r_{NI} + r_{Nm})N + N^+[(1-\delta)n_e\,(r_r + n_e r_{cr}) \\ (r_{CE}(Cu + Cu_m) + r'_{CE}(CuCl)] \\ + N_m[(r_{PI}(Cu + Cu_m) + r'_{PI}\,CuCl + r''_{PI}Nm) \\ + M(r_{CD2} + r_{CD3}M) + n_e r^s_{Nm}] \qquad \text{(VI.B.9a)}$$

$$\frac{dN_m}{dt} = n_e\, r_{Nm}N + \delta n_e N^+(r_r + n_e r_{cr}) - N_m[(r_{PI}(Cu + Cu_m) \\ + r'_{PI}CuCl + 2r''_{PI}N_m) + M(r_{CD2} + r_{CD3}M) + n_e(r^s_{N_m} + r_{Nm}I)] \qquad \text{(VI.B.9b)}$$

$$\frac{dN^+}{dt} = n_e(r_{NI}N + r_{NmI}N_m) - N^+[n_e(r_r + n_e r_{cr}) + (r_{CE}(Cu+Cu_m) \\ + r'_{CE}CuCl)] + N_m N_m r''_{PI} \qquad \text{(VI.B.9c)}$$

$$\frac{dCu}{dt} = n_e[-(r_{CuI} + r_{Cum})Cu + (1-\alpha)(r_D CuCl + Cu^+(r'_r + n_e r'_{cr}) + r^s_{Cu_m} Cu_m] + N_m[(1-\zeta)(1-\alpha)r'_{PI} CuCl - r_{PI} Cu] - N^+ Cur_{CE} - r_{CA} Cu(Cu + Cum)M + r'_{CD2} Cu_m M \quad \text{(VI.B.9d)}$$

$$\frac{dCu_m}{dt} = n_e[r_{Cu_m} Cu - (r_{Cu_m I} + r^s_{Cu_m})Cu_m + \alpha r_D CuCl + \alpha Cu^+(r'_r + n_e r'_{cr})] + N_m[(1-\zeta)\alpha r'_{PI} CuCl - r_{PI} Cu_m - N^+ Cu_m r_{CE} - r_{CA} Cu_m(Cu \quad Cu_m)M - r'_{CD2} Cu_m M \quad \text{(VI.B.9e)}$$

$$\frac{dCu^+}{dt} = n_e[r_{Cu_m I} Cu_m + r_{CuI} Cu - Cu^+(r'_r + n_e r'_{cr})] + N^+[r_{CE}(Cu + Cu_m) + r'_{CE} CuCl] + N_m[r'_{PI}\ \zeta CuCl + r_{PI}(Cu + Cu_m)] \quad \text{(VI.B.9f)}$$

$$\frac{dCuCl}{dt} = r_{CA}(Cu + Cu_m)(Cu + Cu_m)M - (N^+ r'_{CE} + N_m r'_{PI} + n_e r_D)CuCl \quad \text{(VI.B.9g)}$$

$$\frac{dn_e}{dt} = \frac{dN^+}{dt} + \frac{dCu^+}{dt} \quad \text{(VI.B.9h)}$$

where r denotes the rate constant. The superscript s denotes the inverse superelastic rate calculated using the Klein-Rosseland Formula [VI-5]. The subscripts are as follows:

XI = electron impact ionization of X(cm^3/sec)

X = electron impact excitation of X from the ground state (cm^3/sec)

D = electron impact dissociation (cm^3/sec)

r = electron-ion radiative recombination (cm^3/sec)

Cr = electron-ion collisional radiative recombination (cm^6/sec)

PI = Penning ionization (cm^3/sec)

CE = charge exchange (cm^3/sec)

CD2 = two body collisional deactivation (cm^3/sec)

CD3 = three body collisional deactivation (cm^6/sec)

CA = CuCl reassociation (cm^6/sec)

VI.B.2 The Electron Temperature

The rate equation for the electron temperature, exclusive of diffusion effects, can be written as

$$\frac{d}{dt}\left(\frac{3}{2}kT_e\right) = -\sum_i \nu_{e_i}\left(\frac{2m_e}{M_i}\right)\frac{3}{2}k(T_e-T_g) - \sum_i E_i r_{I_i} N_i$$

$$+ \sum_i (E_{m_i} - \frac{3}{2}kT_e)\, r_{PI_i} N_i N_m/n_e + \sum_i r_{r_i} n_e N_i^+ \Delta\varepsilon_{r_i} + \sum_i r_i^s E_i N_{m_i}$$

where

ν_e = elastic collision frequency (/sec)

m_e = electronic mass (g)

M = atomic/ionic mass (g)

r_r = collisional radiative recombination rate (cm^3/sec)

r^s = super elastic relaxation rate (cm^3/sec)

r_I = excitation/ionization rate (cm^3/sec)

r_{PI} = Penning ionization rate (cm^3/sec)

E = excitation/ionization energy (ergs)

E_{m_i} = energy released to electron in PI (ergs)

$\Delta\varepsilon_{r_i}$ = energy liberated in electronic recombination (ergs)

The first term on the RHS of (VI.B.10) describes the fractional loss of energy ($\frac{2m_e}{M}$) incurred by an electron during an elastic collision with an atom or ion. This is the major contributing term of (VI.B.10) at high electron temperatures. The second term describes the loss in energy due to inelastic collisions (excitations and ionizations). The third term represents the source of energetic electrons due to Penning ionizations. The fourth term denotes "recombination heating". The last term of (VI.B.10) represents electron heating due to superelastic collisions. The terms are discussed individually below.

Despite the small fractional energy loss experienced in an elastic electron-atom/ion collision, the large collision frequency makes elastic collisions the major sink of electron energy. At low electron energy (<1eV) the collision frequency in helium is a function of gas pressure only (due to the large threshold for excitation) and can be written as [VI-6]

$$\nu_e \approx 6.9\times10^{11} \frac{P_{Torr}}{T_{gas}} /\text{sec} \qquad \text{(VI.B.11)}$$

For a wider range of energy, one must return to the definition of collision frequency.

$$\nu_e = \left(\frac{8kT_e}{\pi m_e}\right)^{1/2} \sigma_{e\ell} N \qquad \text{(VI.B.12)}$$

For helium, and T_e in eV, (VI.B.12) can be written as [VI-7] $\nu_e = 3.4\times10^{11}\left(\frac{P_{Torr}}{T_{gas}}\right)T_e^{1/2}$/sec. For elastic collisions with ions, the Landau formula can be used [VI-7]

$$\nu_{e\ell} = \frac{4e^4 n_e N_I}{3(kT_e)^{\frac{3}{2}}} \left(\frac{\pi}{2m}\right)^{1/2} L \qquad \text{(VI.B.13)}$$

where L = 5.7 is the Coulomb logarithm. For helium (VI.B.13) is $\nu_{e\ell} = 8.28\times10^{-6}[He^+]/T_e^{3/2}$. It was assumed that (VI.B.13) is applicable to all ions. For elastic collisions in neon, Sol, et al report a collision frequency of [VI-8]

$$\frac{\nu_{e\ell}}{10^8} = 0.99\ T_e^{1/2} + 13.2\ T_e + 0.78\ T_e^{3/2}(\ell n T_e - 0.95)\ P_{Torr}\left(\frac{273}{T_{gas}}\right)/\text{sec} \qquad \text{(VI.B.14)}$$

The rate of loss of electron energy due to inelastic collisions is a threshold event, and hence is a sensitive function of the electron distribution function. For this study, the electron distribution was assumed at all times to be Maxwellian so that with the cross section $\sigma_i(\varepsilon)$ for process i, the rate constant is given by

$$r_i = \langle\sigma v\rangle = \frac{2\pi}{(\pi kT_e)^{3/2}} \int_{E_i}^{\infty} \sigma_i(\varepsilon)\left(\frac{2\varepsilon}{m_e}\right)^{1/2} \varepsilon^{1/2} e^{-\varepsilon/kT_e}\, d\varepsilon$$

$$= 6.69\times10^9\ T_e^{1/2} \int_{E_i/T_e}^{\infty} \sigma(x) x e^{-x} dx \quad \text{cm}^3/\text{sec} \qquad \text{(VI.B.15)}$$

where $x = \varepsilon/T_e$, and the electron temperature T_e and threshold energy E_i are expressed in eV. When estimating a rate one must determine the fraction of electrons with energy greater than the threshold value which is able to participate. This fraction is given by

$$f_i(T_e,E_i) = 1.0 - \frac{2\pi}{(\pi kT_e)^{3/2}} \int_0^{\varepsilon_i} \varepsilon^{1/2}\, e^{-\varepsilon/kT_e} d\varepsilon$$

$$= 1.0 - P(\tfrac{3}{2},E_i/kT_e) \approx 1.0 - \tanh(\tfrac{3}{7}\frac{E_i}{kT_e})$$

where $P(a,x) = \frac{1}{\Gamma(a)} \int_0^x e^{-t} t^{a-1} dt$ is the incomplete gamma function.

In a Penning ionization (the third term of (VI.B.13)) a "new" electron is injected into the distribution, so the contribution to the average electron energy is proportional to the difference in energy given to the Penning electron and the average electron energy. The Penning electron energy is not simply the energy excess $E_m - E_i$, as the final state involves three bodies, and the electron energy can range from zero to the total energy excess. Ingraham and Brown [VI-6] have considered the joint probability of producing each of the particles with momentum vectors terminating in prescribed volume elements in momentum space. They found that the average Penning electron has an energy of 5/8 E_{excess}. This value was used in (V.B.10)*

* The factor 5/8, was not included in the earlier numerical treatment of the Boltzmann equation in Chapter IV. It is within the uncertainty of the estimated Penning cross sections, and is included here for completeness only.

Electron heating due to collisional radiative recombination (the fourth term of (VI.B.10)) is a consequence of the "third body" electron carrying off collisional energy which enables the recombining electron to "fall into" an atomic orbital. This energy can be written as

$$\Delta\varepsilon_r = T_e - (T_e - E_I - E_{exc}) = E_I - E_{exc} \qquad \text{(VI.B.17)}$$

where E_I is the ionization potential and E_{exc} is the excitation energy of the atomic orbital into which the electron falls prior to radiative relaxation. For lack of a measured value for $\Delta\varepsilon_r$, it was assumed that those electrons not recombining into the metastable state, end up in a state halfway between the metastable state and the ionization level. Hence if a fraction δ recombine into the metastable state,

$$\begin{aligned}\Delta\varepsilon_r &= \tfrac{1}{2}(1-\delta)(E_I - E_m) + \delta(E_I - E_m) \\ &= \tfrac{1}{2}(1+\delta)(E_I - E_m)\end{aligned} \qquad \text{(VI.B.18)}$$

The electron heating due to recombination is then

$$\sum_i r_{r_i} \tfrac{1}{2}(1-\delta_i)(E_{I_i} - E_{m_i}) n_e N_i^+ \qquad \text{(VI.B.19)}$$

The electron heating due to superelastic heating (the fifth term of (VI.B.10)) is simply the rate at which the event occurs times the energy carried off by the electron. The superelastic rate was calculated using the Klein-Rosseland formula and the metastable excitation

cross section. The energy dependent cross sections calculated in this manner were found to be somewhat larger than the average rates cited in the literature (see for example [VI-9]). Hence, the cross section was reduced while retaining its relative energy dependence.

VI.B.3 Diffusion

The discussion up to this point applies either to the spatially averaged or to the radial dependent treatments. The differentiation is now made in the diffusion terms. Binary diffusion through the buffer gas is assumed. Charged particle diffusion is ambipolar.

The ion ambipolar diffusion constant D_a can be approximated by [VI-10]

$$D_a \approx \frac{V^2}{3\nu_c} = \frac{V^2 \mu M}{3e} = \frac{kT_g}{e}\mu \text{ cm}^2/\text{sec} \qquad \text{(VI.B.20)}$$

where the momentum transfer collision frequency ν_c is defined in terms of the mobility μ by

$$\nu_c = \frac{e}{\mu M}/\text{sec} \qquad \text{(VI.B.21)}$$

and

$$\mu = \mu_o\left(\frac{T}{273}\right)\left(\frac{760}{P}\right) \frac{\text{cm}^2}{\text{V-sec}} \qquad \text{(VI.B.22)}$$

where μ_o is the STP mobility. Hence $D_a = 2.4\text{x}10^{-4}\frac{T^2{}^{o}_{K}}{P_{Torr}}\mu_o \text{ cm}^2/\text{sec}$. This expression is valid when ions and electrons are in thermal

equilibrium. For $T_e \neq T_{gas}$, D_a can be approximated by $\frac{D_a}{2}(1+\frac{T_e}{T_{gas}})$ [VI-11]. Values of ionic mobility are listed in Table VI.1. Since during an afterglow, there is no applied electric field, the mobilities in Table VI.1 were found by extrapolating to zero field.

When a published value for the neutral binary diffusion constant could not be found, it was approximated by expressions given by Hirschfelder, Curtis and Bird [VI-12]. The binary diffusion constant is given by

$$D = 1.4\frac{T_g^{\frac{1}{2}}}{P_{Torr}}\left(\frac{M_1+M_2}{M_1 M_2}\right)^{\frac{1}{2}}\frac{\varepsilon_{LJ}}{\sigma^2_{LJ}\Omega} \qquad \text{(VI.B.23)}$$

where

M_i = mass of atom/molecule i

Ω = hard sphere correction factor

ε_{LJ} = Leonard Jones well depth (^oK)

σ_{LJ} = Leonard Jones well width ($\overset{o}{A}$)

Binary diffusion coefficients are listed in Table VI.2.

VI.B.3.a Spatially Averaged

For the spatially averaged treatment the rate of diffusion losses to the walls are given by D/Λ^2 where Λ is the container diffusion length. For tube length L, and radius R,

$$\frac{1}{\Lambda^2} = \left(\frac{\pi}{L}\right)^2 + \left(\frac{2.405}{R}\right)^2 \qquad \text{(VI.B.24)}$$

TABLE VI.1

Ionic Mobilities with no Electric Field

Ion	Mobility μ_o $\frac{cm^2}{V\text{-}sec}$ in Ne	Mobility μ_o $\frac{cm^2}{V\text{-}sec}$ in He	Reference (Chapter VI)
He^+	---	10.7	10
Ne^+	4.0	---	54
Cu^+	7.0	21.0	10

TABLE VI.2

Binary Neutral Diffusion Coefficients

Species	D $\frac{cm^2}{sec}$ in Ne	D $\frac{cm^2}{sec}$ in He	Reference
He_m (2^3S)	-----	1.19 T/P	4
He_m (2^1S)	-----	1.45 T/P	4
Ne_m	.205 $\frac{T^{3/2}}{P}$	-----	5
Cu, Cu_m	24.6 $\frac{T^{1/2}}{P}$	58.7 $\frac{T^{1/2}}{P}$	12
CuCl	5.4 $\frac{T^{1/2}}{P}$	12.9 $\frac{T^{1/2}}{P}$	12

At the wall, all ions are assumed to recombine. A specified fraction of the metastables deactivate, and a specified fraction of neutral copper reassociates to form CuCl. The "products" return to the plasma (see Figure VI-2).

VI.B.3.b Radially Dependent Diffusion

The diffusion equation for species with number density n is

$$\frac{\partial n}{\partial t} = \vec{\nabla} \cdot (D\vec{\nabla} n) \qquad \text{(VI.B.25)}$$

For a radially independent diffusion constant, and azimuthally symmetric circular geometry

$$\frac{\partial n}{\partial t} = D\frac{1}{r}\frac{\partial}{\partial r}(r\frac{\partial n}{\partial r}) \qquad \text{(VI.B.26)}$$

Radial dependent diffusion is added to the rate equations by simultaneously integrating each rate equation with respect to time at selected radial points, and handling the spatial diffusion derivatives with a finite difference technique. Referring to Figure VI-3, the discharge tube is divided into I_{RAD}-1 annular regions, and one circular region at the center. Each region has width Δr and midpoint at $r_i = (i-1)\Delta r$. The finite difference representation for (VI.B.26) at the radial point i is [VI-13]

$$(\frac{\partial n}{\partial t})_i = \frac{D}{2(i-1)\Delta r^2}((2(i-1)+1)n_{i+1} - 4n_i + (2(i-1)-1)n_{i-1}) \qquad \text{(VI.B.27)}$$

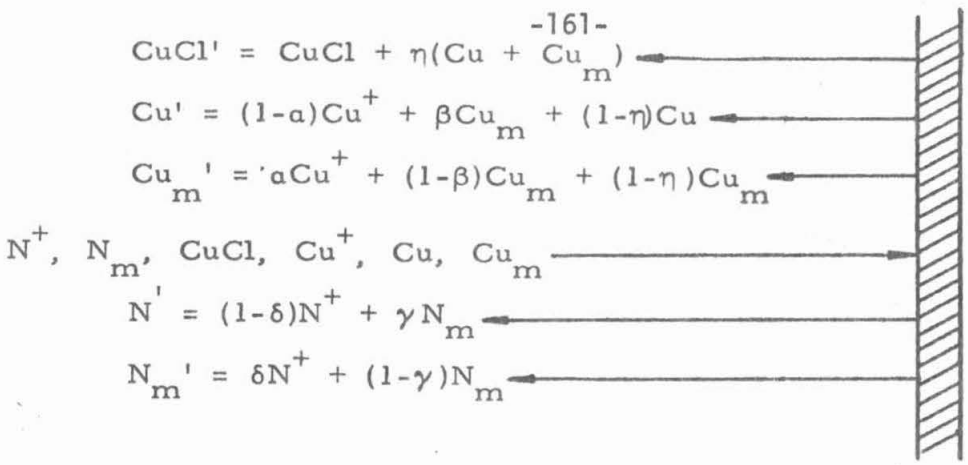

α = Fraction of Cu^+ recombining to form Cu_m

β = Fraction of Cu_m deactivating to form Cu

γ = Fraction of N_m deactivating to form N

δ = Fraction of N^+ recombining to form N_m

η = Fraction of Cu and Cu_m which reassociate to form CuCl

Figure VI.2. Reactions for species diffusing to the wall. The primes indicate species returning to the volume from the wall.

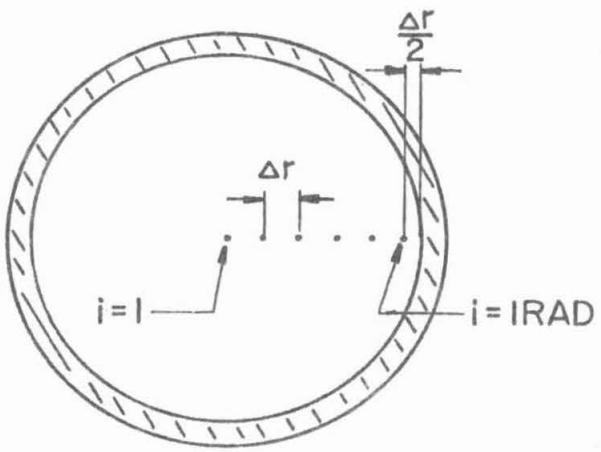

Figure VI.3. Geometry for calculation of radially dependent diffusion.

At $i = 1$ $(r=0)$, $\frac{\partial n}{\partial r} = 0$, and $n_{i+1} = n_{i-1}$ so that

$$(\frac{\partial n}{\partial t})_1 = \frac{4}{(\Delta r)^2} (n_2 - n_1) \qquad \text{(VI.B.28)}$$

For the radial position $i = I_{RAD}$ adjacent to the wall, the density at n_{i+1} is set equal to zero, so that the diffusion loss to the wall can be written as

$$(\frac{\partial r}{\partial t})_{\text{IRAD to wall}} = \frac{-D(2(IRAD-1)+1)}{2(IRAD-1)\Delta r^2} n_{IRAD} \qquad \text{(VI.B.29)}$$

The same boundary conditions for diffusion loss to the wall as discussed for volume averaged diffusion hold for the radial region adjacent to the wall.

An electron distribution whose average energy has been lowered because fast electrons are lost by diffusion to the walls at a greater rate than slow electrons is said to have been "diffusion cooled". The phenomenon has been observed experimentally by a reduction in the ambipolar diffusion constant $D_a \sim (1 + \frac{T_e}{T_{gas}})$ [VI-55]. By starting with the diffusion equation VI.B.25, the change in electron temperature as a result of diffusion can be written as

$$\frac{\partial T_e}{\partial t} = \frac{D_a}{2}[(1+\frac{T_e}{T_g})(\frac{\partial T_e}{\partial r}(\frac{2}{n_e}\frac{\partial n_e}{\partial r} + \frac{1}{r}) + \frac{T_e}{n_e}\frac{\partial^2 n_e}{\partial r^2} + \frac{\partial^2 T_e}{\partial r^2}$$

$$+ \frac{T_e}{n_e r}\frac{\partial n_e}{\partial r}) + \frac{1}{T_g}\frac{\partial T_e}{\partial r}(\frac{\partial T_e}{\partial r} + \frac{T_e}{n_e}\frac{\partial n_e}{\partial r})] - \frac{T_e}{n_e}\frac{\partial n_e}{\partial t} \qquad \text{(VI.B.30)}$$

The derivation of Equation (VI.B.30) can be found in Appendix D. The

diffusion cooling term (VI.B.30) is included in the expression for $\frac{\partial T_e}{\partial t}$ at each grid point by formulating the spatial derivates with finite differences.

VI.C. Dissociation Pulse and Afterglow Model: Results and Discussion

The rate equations discussed in the previous section were integrated using a Runge-Kutta-Gill scheme with Adams-Moulten corrections. The integration routine is a modified version of MODDEQ, a Caltech Computer Library subroutine [VI-14].

The numerical results which follow are exclusively for a discharge in helium. Rate constants for most of the atomic collisional processes had to be estimated. Rate constants for similar processes in helium are fairly well established for a variety of metallic vapors and diatomic molecules. Therefore more accurate approximations could be made for He-Cu and He-CuCl collision rates. Reaction rates and cross sections are listed in Table VI.3. The results which follow should be considered typical for a discharge in a noble gas and a metallic halide. The major difference between an afterglow in helium and a heavier noble gas will be the rate of elastic-collision cooling. Since the rate of cooling is inversely proportional to the atomic mass, a helium discharge afterglow will cool more quickly than one in neon. Standard initial conditions and parameters are listed in Table VI.5.

TABLE VI.3

REACTION RATES AND CROSS SECTIONS FOR THE AFTERGLOW MODEL

PROCESS	RATE/CROSS SECTION		REFERENCE
$e+x \rightarrow x^+ + e + e$	$2.186\times10^{-10} T_e {}^oK u\ \psi(u)\ cm^3/sec$ u = E ionization/kT_e $\psi(u) = \frac{e^{-u}}{1+u}\left(\frac{1}{20+u} + \ell n(1.25(1+\frac{1}{u}))\right)$		39
$e+Cu \rightarrow Cu_m + e$	$\langle\sigma V\rangle^a\ cm^3/sec$		40
$e+He \rightarrow He_m + e$	$\langle\sigma V\rangle^a\ cm^3/sec$		41
$e+CuCl \rightarrow \alpha Cu_m + (1-\alpha)Cu$	-------		b
$e+e+He^+ \rightarrow He+e+h\nu$	$7.1\times10^{-20}(\frac{300}{T_e})^{-4.3} cm^6/sec$		4
$e+e+Cu^+ \rightarrow Cu^+ + e + h\nu$	$7.1\times10^{-20}(\frac{300}{T_e})^{-4.5} cm^6/sec$	(estimate)	4
$e+He^+ \rightarrow He+h\nu$	$4.2\times10^{-12}(\frac{300}{T_e})^{-.7} cm^3/sec$		4,42
$e+Cu^+ \rightarrow Cu+h\nu$	$8.05\times10^{-13}(\frac{300}{T_e})^{-1.05} cm^3/sec$		43
$He_m + Cu_{(m)} \rightarrow Cu^+ + He + e$	$4.2\times10^{-15} cm^2$		d
$He_m + He_m \rightarrow He^+ + He + e$	$0.71\times10^{-9} T_{gas}^{1/6}\ cm^3/sec$		7
$He^+ + Cu_{(m)} \rightarrow He + Cu^+$	$3.2\times10^{-10}(\frac{T_g}{300})^{1/2} cm^3/sec$		c
$He_m + CuCl \rightarrow \zeta Cu^+ + (1-\zeta)$ $(\alpha Cu_m + 1-\alpha)(Cu)$	$10^{-16} cm^2$		d

$He^+ + CuCl \rightarrow Cu^+ + He$	$8\times10^{-10}(\frac{T_g}{300})^{1/2}$ cm^3/sec		34,c
$Cu_{(m)} + Cu_{(m)} + M \rightarrow CuCl + M$	1.0×10^{-27} cm^6/sec	(estimate)	18,19
$He_m + M \rightarrow He + M$	$6\times10^{-15}(\frac{T_{gas}}{300})^{1/2}$ cm^3/sec		4
$He_m + M + M \rightarrow He + M + M$	$2.5\times10^{-34}(\frac{T_{gas}}{300})^{1/2}$ cm^6/sec		4
$Cu_m + M \rightarrow Cu + M$	2.0×10^{-12} cm^3/sec	(estimate)	21,44

a) Cross section for the process given in the reference is averaged over a Maxwellian with electron temperature T_e.

b) The CuCl dissociation was estimated to be twice the ionization rate of $e + x \rightarrow x^+ + e + e$ if the dissociation energy is substituted for the ionization potential.

c) Estimate. For typical charge exchange cross sections, see Table VI.4.

d) Estimate. For typical Penning ionization cross sections, see Table IV.1.

e) Cross section taken to be the same as for zinc.

TABLE VI.4

Typical Charge Exchange Cross Sections

Ion	Target	Cross Section ($10^{-16}cm^2$)	Reference (Chapter VI)
He^+	Cd	37	45
	I	3	46
	Hg	130	47,48
	He	35	49
	Pb	4.0	50
	Xe	10	51
	$N_2 \rightarrow N^+ + N$	53	52
	$CO \rightarrow C^+ + O$	36	52
	$NO \rightarrow N^+ + O$	32	52
	$O_2 \rightarrow O^+ + O$	32	52
Ne^+	Ne	32	49
	$H_2 \rightarrow H^+ + H$	2.3	53
Cu^+	Cu	190	49

TABLE VI.5

STANDARD INITIAL CONDITIONS AND PARAMETERS FOR THE DISSOCIATION PULSE AND AFTERGLOW MODEL

Buffer Gas: He

Buffer Gas Pressure: 5.0 Torr

Tube Temperature: 400^{o}C

Tube Radius: 0.5 cm

Tube Length: 50.0 cm

Dissociation Pulse Electron Temperature: 5.0 eV

Dissociation Pulse Length: 250 ns

Fraction of He Metastables from Recombination: 0.2

Fraction of Cu Metastables from Recombination: 0.2

Fractional He Metastable Deactivation at Walls: 1.0

Fractional Cu Metastable Deactivation at Walls: 0.5

Fractional Cu Metastable Reassociation at Walls: 0.5

Fraction Cu Ground State Reassociation at Walls: 0.5

Component	Density (/cm^3)
Ne	1.0×10^{12}
He_m	0.0
He	7.17×10^{16}
He^+	1.0×10^{12}
Cu_m	0.0
Cu	0.0
Cu^+	0.0
CuCl	1.21×10^{15}

VI.C.1 Spatially Averaged Results

VI.C.1.a A Helium Afterglow

The calculated afterglow for a discharge in 5.0 Torr of pure helium at 400°C is shown in Figure VI-4. Note that the electron temperature falls rapidly after the dissociation pulse is over, and that the electron density is maximum well after the pulse is turned off. The slowing of electron cooling at t ≈ 2 μs is due primarily to superelastic relaxation of metastable helium and secondarily due to Penning ionization heating*. The heating is temporary as the metastable helium is soon depleted. Note that the ion density does not fall appreciably until the electron temperature becomes asymptotic to the gas temperature, indicative of the $T_e^{-\frac{9}{2}}$ temperature dependence of collisional radiative recombination. The ion decay after ≈ 80 μs is exponential with an 1/e decay time of ≈ 95 μs.

VI.C.1.b A Helium/CuCl Afterglow and Laser Pulses as a Function of Time Delay

Using the same conditions as above but including CuCl at its vapor pressure at 400°C (≈.08 Torr) the results in Figure VI-5 are obtained. Note the difference in the populations of He^+ and He_m as compared to the afterglow in pure helium. Charge exchange and Penning ionization quickly deplete these populations. Ion and electron den-

* Superelastic and Penning ionization heating in helium afterglows have been observed experimentally by Ingraham and Brown [VI-6].

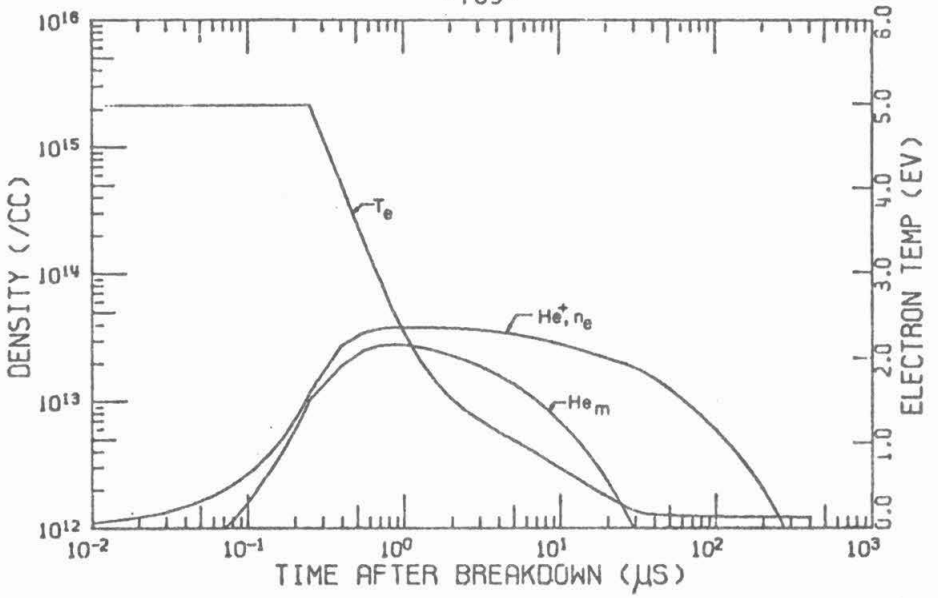

Figure VI.4. A discharge and afterglow in 5.0 Torr of pure helium at 400°C.

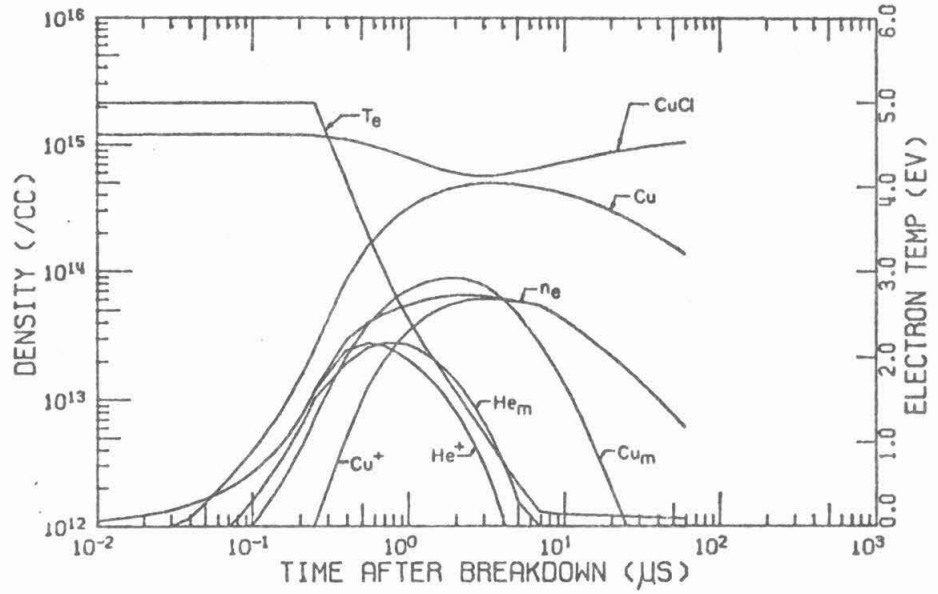

Figure VI.5. A discharge and afterglow in 5.0 Torr of helium and CuCl at its vapor pressure for 400°C (≈.08 Torr).

sities rise faster and peak at higher values than in the pure helium example. The ion population is virtually all copper by 5 μs *. Note that in the absence of He_m superelastic heating, the electron temperature becomes asymptotic to the gas temperature at ≈ 8 μs (compared to ≈ 35 μs in pure helium) thereby allowing ion recombination to become important much earlier. The increase in atomic copper after the dissociation pulse is due primarily to continued CuCl dissociation by electron impact. Maximum CuCl dissociation is 47%. This value is comparable to the 44% reported by Tenenbaum, et al [VI-15].

In order to obtain laser energy as a function of time delay, the copper and helium densities from the results above were placed in the laser rate equations (see Section III.B). Recall from the discussion in Section V.B.2.a that pumping rates during the pumping discharge pulse are a function of time delay and are for the most part determined by the density of afterglow electrons remaining when the discharge is triggered. To simulate this behavior, the following scheme was used to obtain discharge conditions for the rate equations. If n_a is the density of afterglow electrons, then the peak pumping pulse electron density was simply

$$n_p = n_a + n_o$$

where n_o is the long delay value. The electron temperature was chosen to be

* This transition of the dominant ion from the noble gas to the metal has been seen experimentally. See the discussion in Section II,D.

$$T_e = \begin{cases} \alpha T_{e,min}, & \alpha < \dfrac{T_{e,max}}{T_{e,min}} \\ T_{e,max}, & \alpha > \dfrac{T_{e,max}}{T_{e,min}} \end{cases}$$

where $\alpha = n_p/n_o$. For the examples which follow, $n_o = 7.0 \times 10^{13}/cm^3$, $T_{e,min} = 5.0$ eV, and $T_{e,max} = 15.0$ eV.

When the densities from the "standard case" (Figure VI-5) are placed in the laser rate equations, the results of Figure VI-6 are obtained. Note that the optimum time delay is ≈10 μs while the copper ground state population is maximum at ≈ 3.5 μs. At the time of maximum copper ground state density, laser energy is only 28% of optimum, while at the optimum time delay, ground state copper is only 79% of its maximum value. The factor responsible for this behavior is the fraction of metastable copper still present.

In Section V.B.2.b, the laser pulse characteristics as a function of time delay were discussed. The same characteristics computed from the afterglow calculation and rate equations are plotted in Figure VI-7 (compare with Figures V-6 and V-8). Note that the calculated time after the start of the current pulse that the laser pulse appears reproduces the experimentally observed behavior. The same is true with the peak power occurring at a shorter time delay than the optimum energy. The FWZH which falls to small values at long delays experimentally, does so only fractionally in the calculation. The explanation for the behavior of Figures V-6,7 and 8 found in Section V.B.2.b

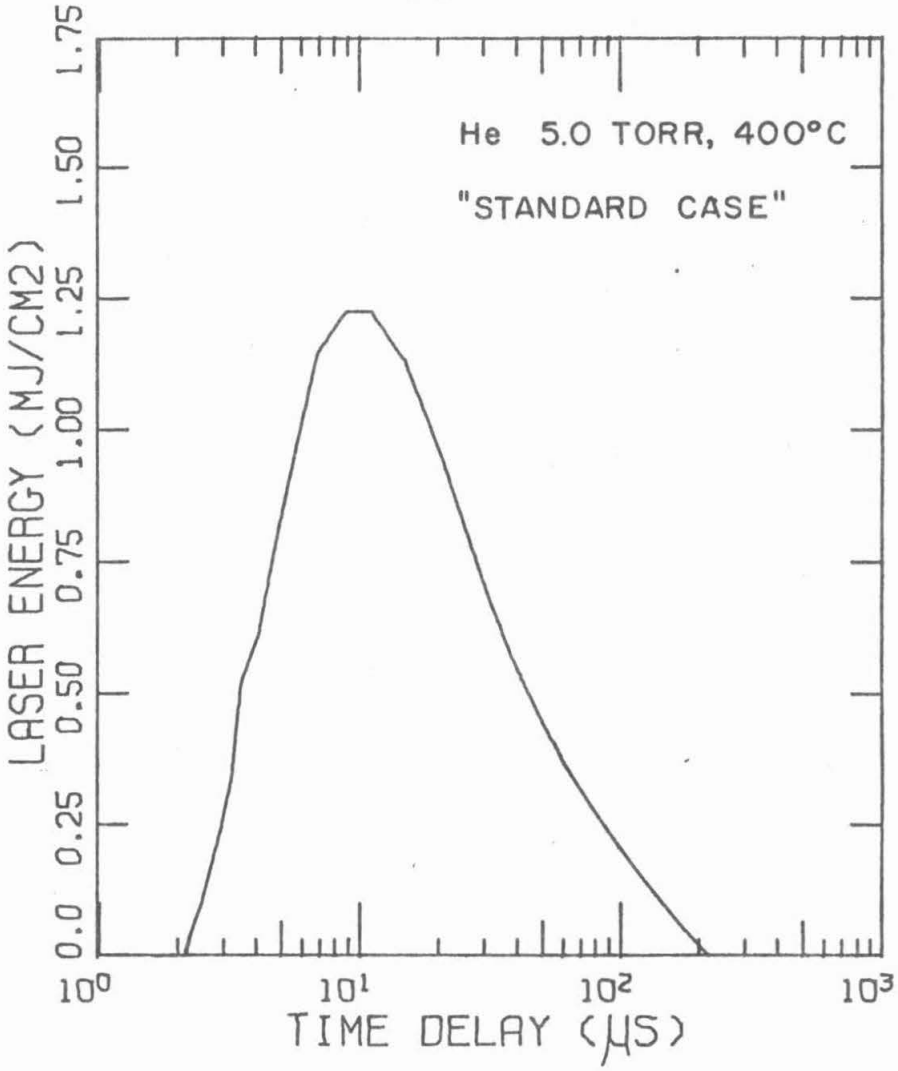

Figure VI.6. Laser pulse energy as a function of time delay for the conditions of Figure VI.5.

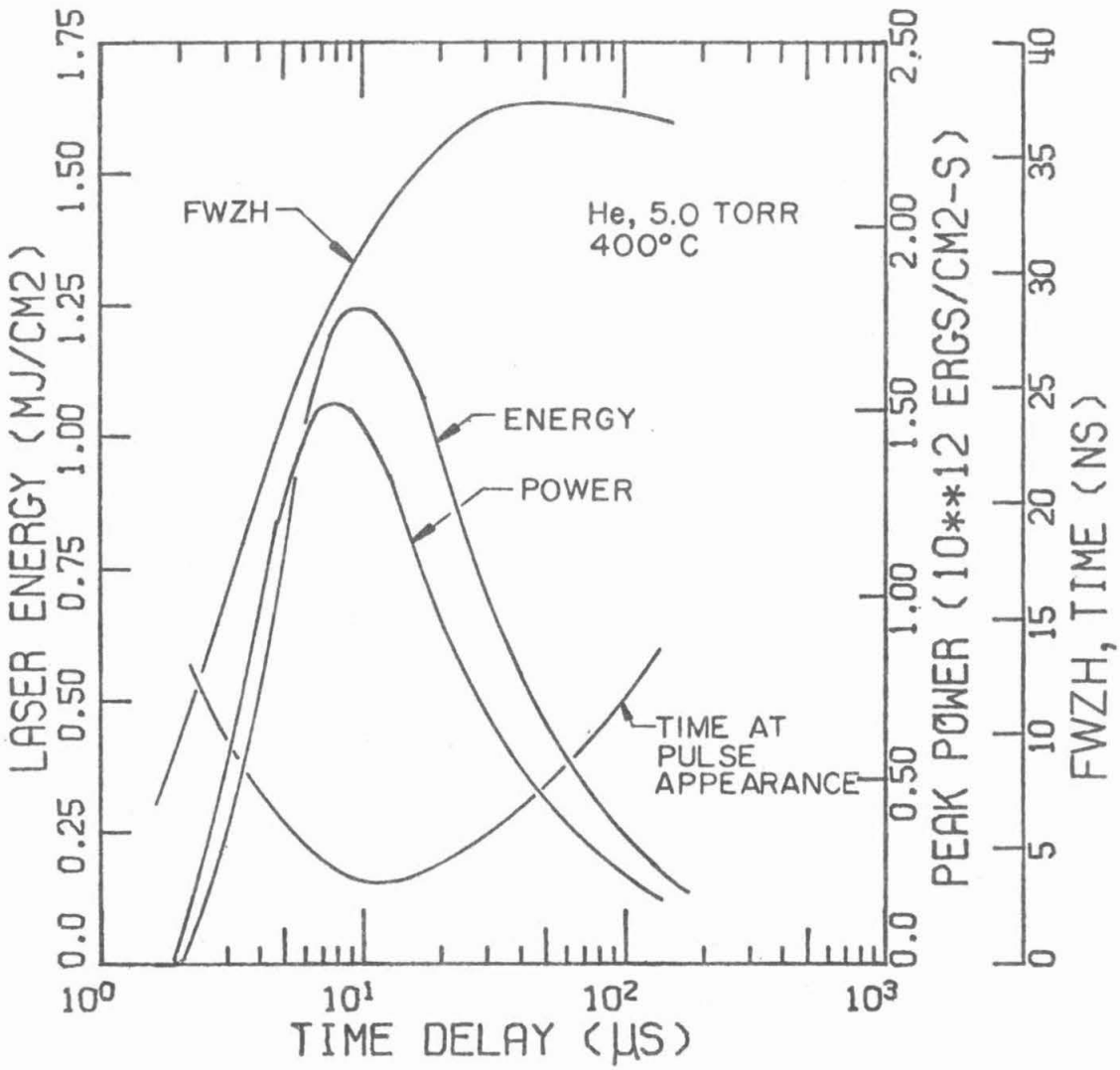

Figure VI.7. Laser pulse energy, peak power, full width at zero height, and the time after the start of pumping that the laser pulse appears as a function time delay for the conditions of Figure VI.5.

is consistent with the calculated results presented here.

VI.C.1.c. Dissociation Yield of Metastable Copper and Laser Pulse Energy

The majority of metastable copper comes from dissociation of CuCl rather than electron impact excitation of copper ground state. Hence the fraction of metastable copper obtained from a CuCl dissociation is a sensitive parameter effecting optimum laser energy. This fraction, α, was varied with the results shown in Figures VI-8, 9 and 10. The optimum and minimum time delays decrease and optimum laser energy increases with decreasing α.

The electron temperature and density during the afterglow are virtually unchanged by the change in α so the amount of CuCl dissociated is independent of α. Since the metastable copper relaxes to densities below $10^{12}/cm^3$ by 35 μs in each case, the long delay laser energy and the maximum time delay are independent of α. Although the maximum density of metastable copper scales nearly linearly with α, the time at which that density is maximum, (about 1.9 μs) is nearly constant. The decrease in minimum and optimum delay with decreasing α is a consequence of the critical fraction of metastable copper to ground state copper, above which oscillation cannot occur, being breached at earlier times. The increase in optimum laser energy with decreasing α is seen to be a result of the optimum time delay moving closer to the time at which ground state copper is maximum rather than the small

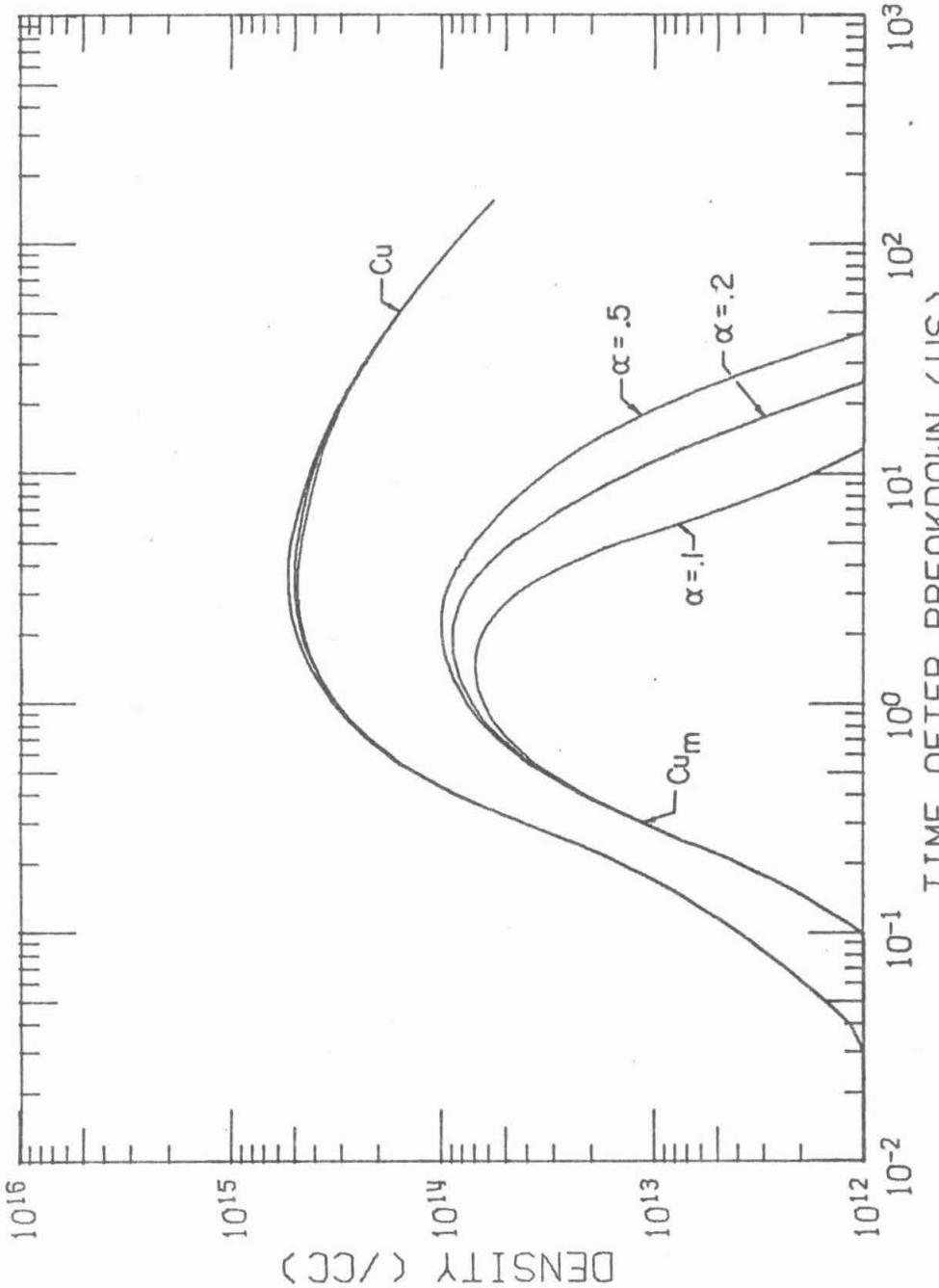

Figure VI,8. Copper ground state and metastable densities as a function of α, the fraction of metastable copper atoms obtained in the dissociation of CuCl.

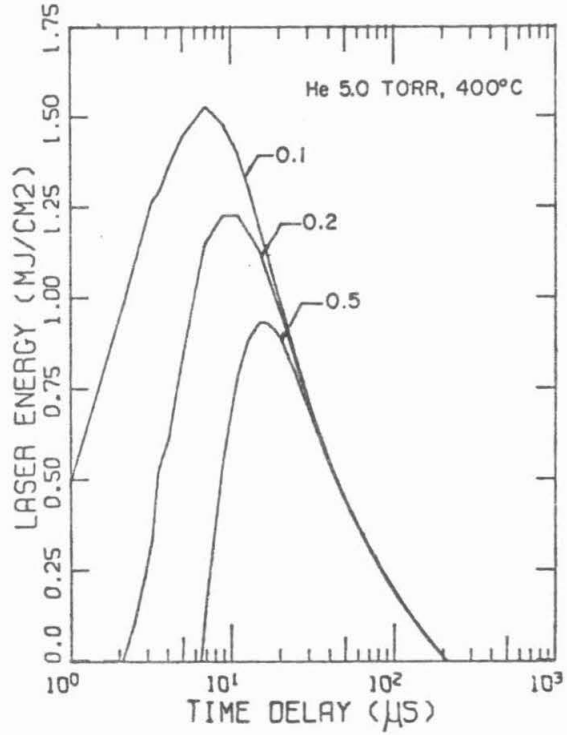

Figure VI.9. Laser pulse energy as a function of time delay and the fraction of metastable copper atoms obtained in the dissociation of CuCl.

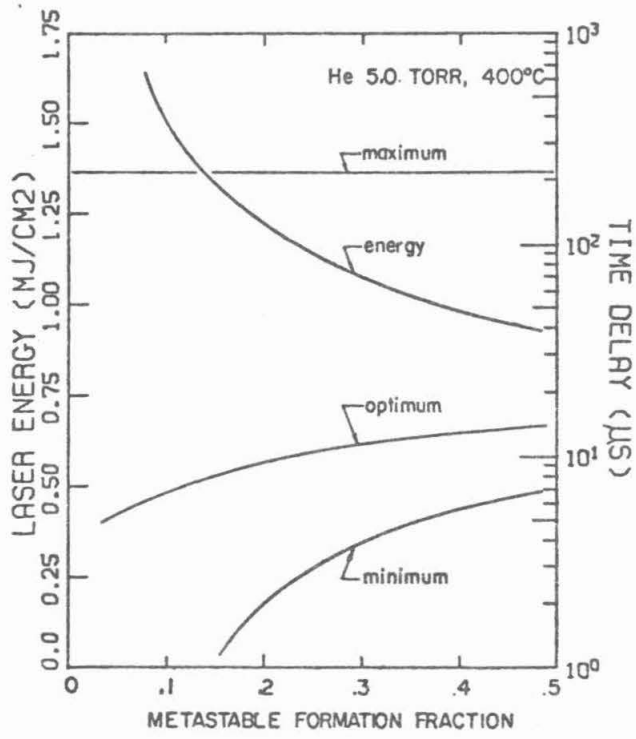

Figure VI.10. Minimum, optimum, and maximum delays, and optimum laser pulse energy as a function of the fraction of metastable copper atoms obtained in the dissociation of CuCl.

absolute change in that maximum value. The available ground state copper is used more efficiently.

VI.C.1.d Collisional Relaxation of Metastable Copper and Laser Pulse Energy

The rate of collisional relaxation of metastable copper, β, was varied with the results shown in Figures VI-11, 12 and 13. Again the effect on discharge characteristics is nominal so that the same amount of CuCl is dissociated in each case. The long delay laser energy is therefore independent of β. With decreasing β, the minimum and optimum delays decrease and optimum laser energy increases. Over the range of β, the density of ground state copper increases by only 11% while optimum laser energy increases by 144%. Again one sees that the increase in maximum ground state copper density alone cannot account for the increase in laser energy. Rather it is the shift in optimum time delay toward the time of maximum ground state copper density, which allows a more efficient use of dissociated copper, that accounts for the increase in optimum laser energy.

It is clear that the "worth" of a copper metastable at the time of the pumping pulse is greater than that of a copper groundstate. Since gain is proportional to $C_U - \frac{2}{3}Cu_L$, gain at the start of the pumping pulse is in general negative, and for given discharge conditions, there is a specified fraction of Cu_m/Cu_{gs} above which positive gain cannot be achieved. This value was found to range from

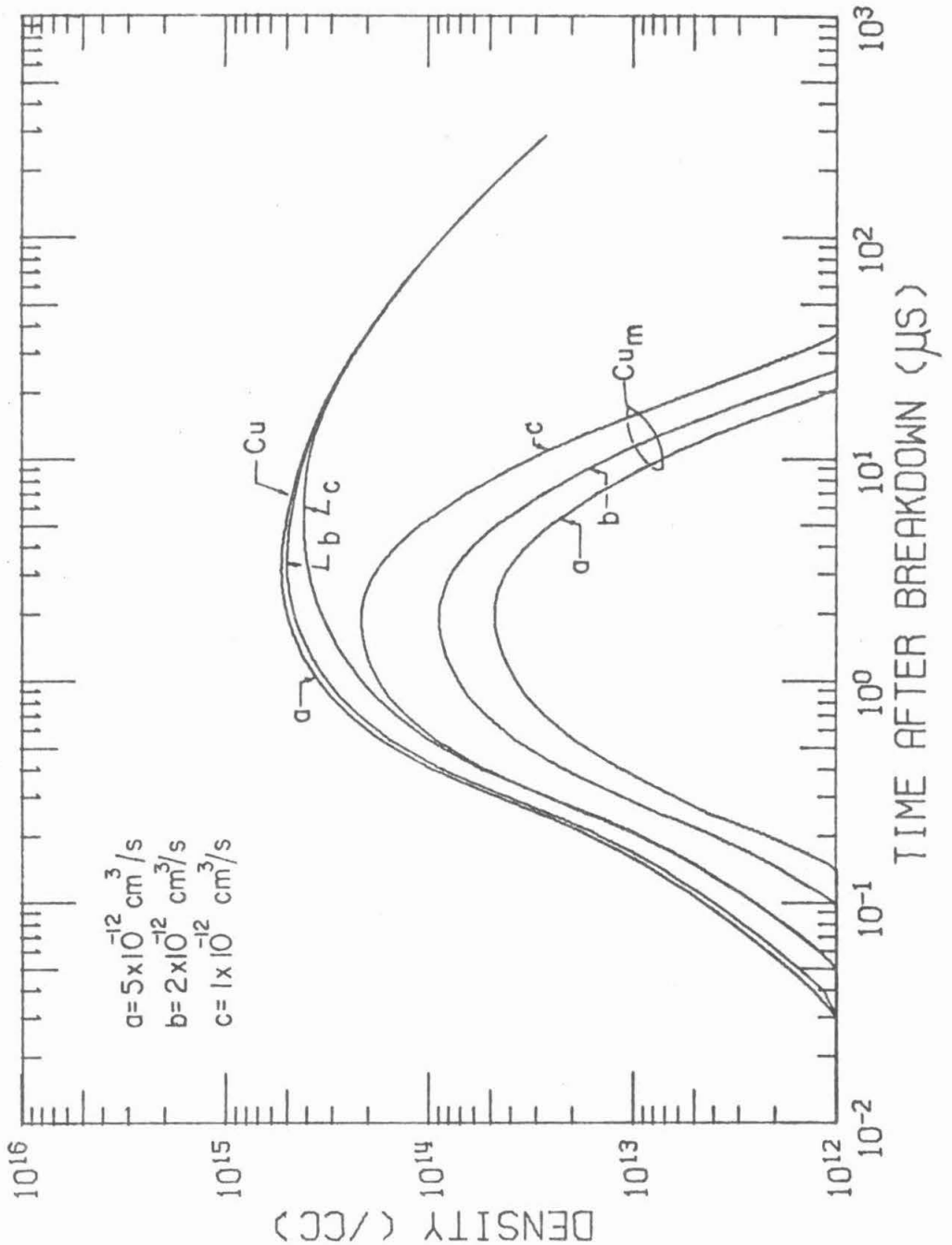

Figure VI.11. Copper ground state and metastable densities as a function of the rate of collision relaxation of metastable copper.

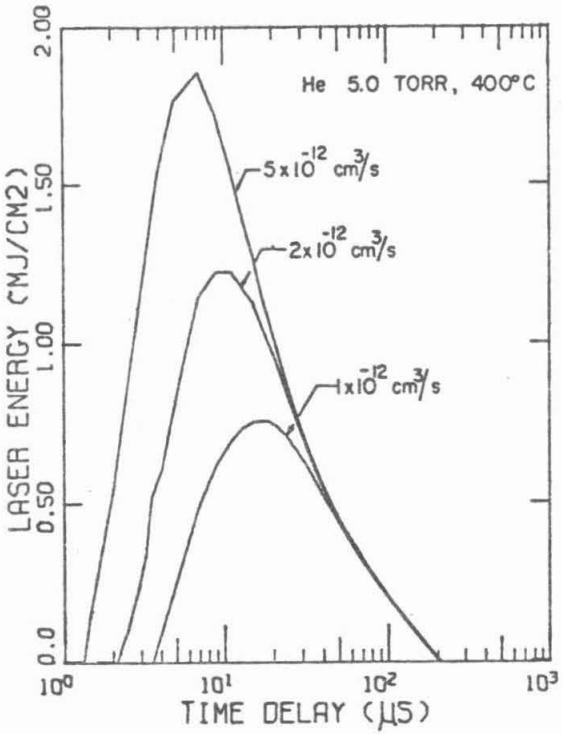

Figure VI.12. Laser pulse energy as a function of time delay and the rate of collisional relaxation of metastable copper.

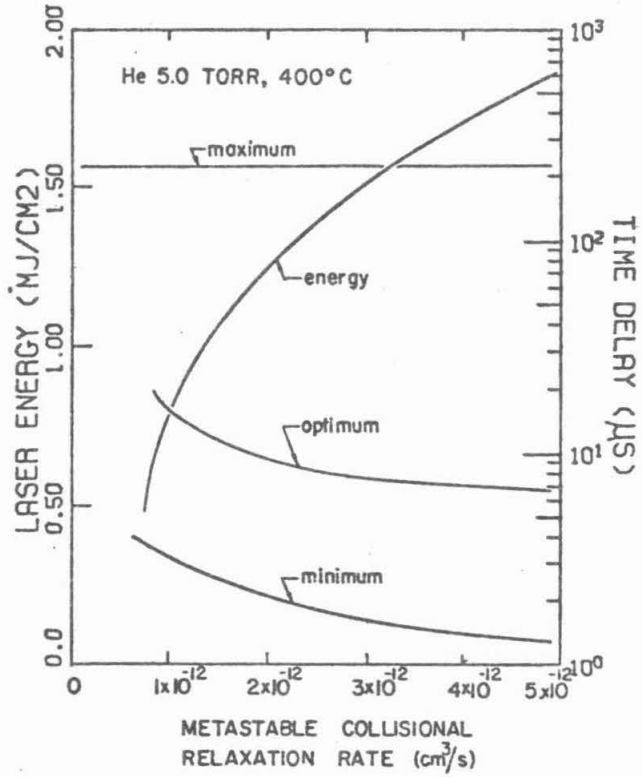

Figure VI.13. Minimum, optimum and maximum delays, and optimum laser pulse energy as a function of the rate of collisional relaxation of metastable copper.

5% to about 20%.

VI.C.1.e CuCl Reassociation and Laser Pulse Energy

Since copper chloride vapor exists primarily as the trimer at the temperatures and pressures of interest [VI-16], the approximation that copper chloride is present only as the monomer is weakest when one considers reassociation. By allowing copper chloride to exist as Cu_nCl_m, where n and m can take the values 1, 2 or 3, a large number of reassociation channels open up, and a variety of parameters are introduced which have been used to great advantage in fitting experimental data [VI-17]. For simplicity, and to avoid the arbitrary selection of reassociation channels one would have to make with Cu_nCl_m, only the monomer was considered. The standard reassociation rate was estimated by examining the reassociation rates of similar molecules [VI-18,19] and comparing those values to experimental rates of copper halide reassociation [VI-20,21]*. The monomer reassociation rate, α_2, was varied with the results shown in Figures VI-14,15 and 16.

As expected laser energy and copper densities are inversely proportional to α_2. For the case of $\alpha_2 = 5\times10^{-26} cm^6/sec$ (see Figure VI-17), the reassociation rate is sufficiently fast so that copper ground state density falls below the ion density. The change in slope of Cu ground state at about 15 μs is due to the rapid increase in Cu^+ recombination as the electron temperature becomes asymptotic to the gas temperature. Compare Figure VI-5 to VI-17 and note that the electron temperature for the larger reassociation rate becomes

* The experiments measured the rate at which ground state copper is removed due to all processes.

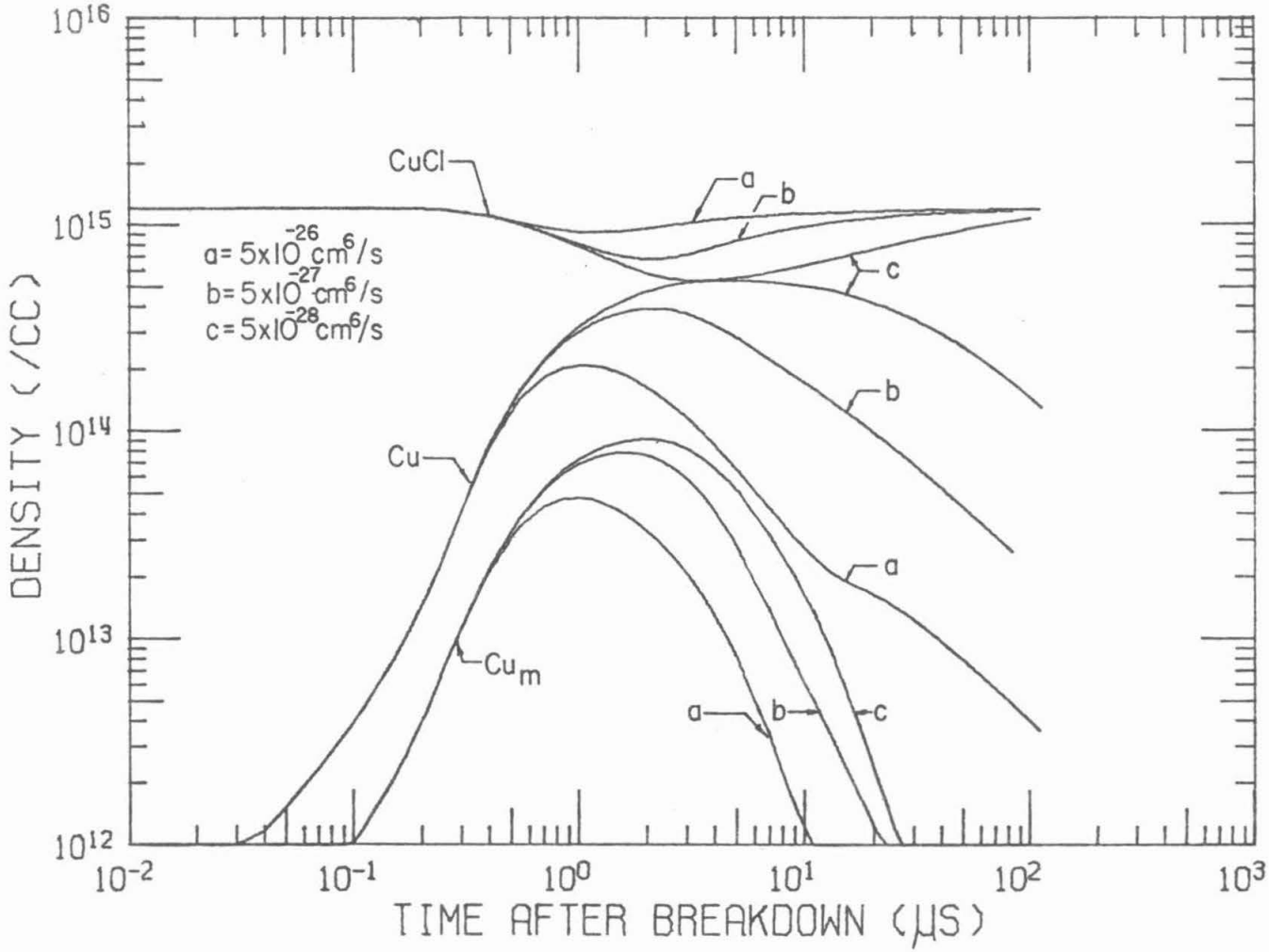

Figure VI.14. CuCl, ground state copper and metastable copper densities as a function of the rate of CuCl reassociation.

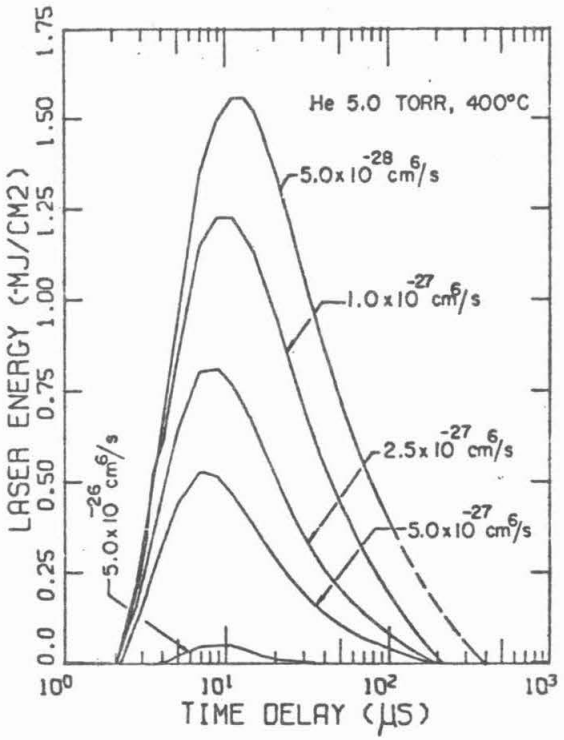

Figure VI.15. Laser pulse energy as a function of time delay and the rate of CuCl reassociation.

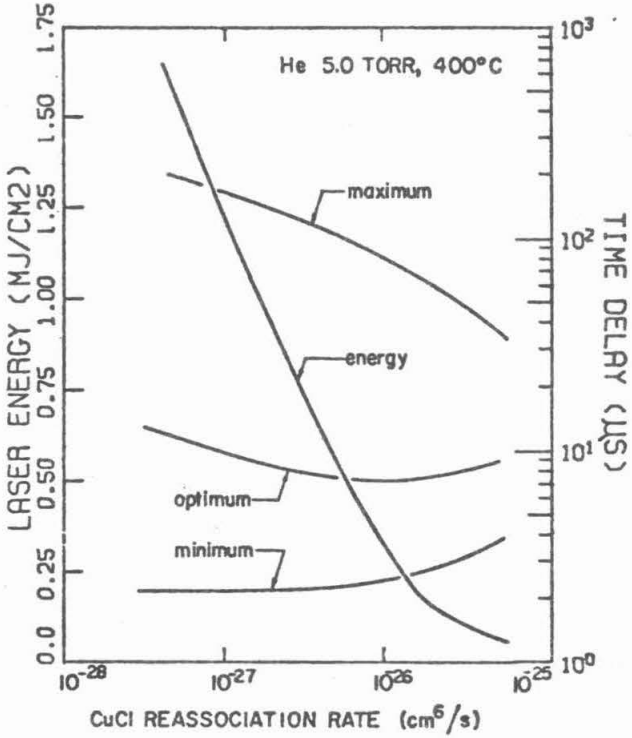

Figure VI.16. Minimum, optimum, and maximum delays, and optimum laser pulse energy as a function of the rate of CuCl reassociation.

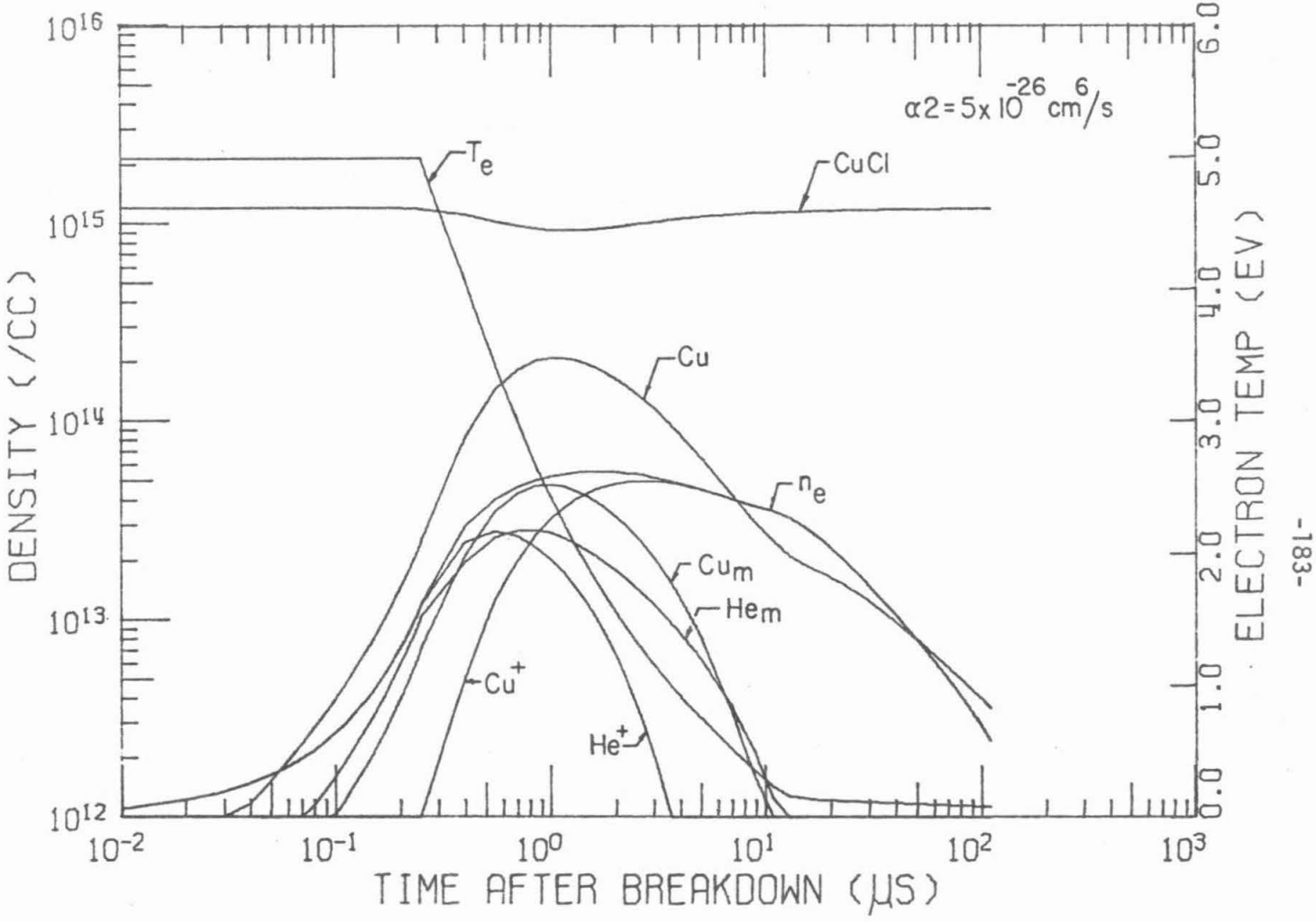

Figure VI.17. Densities during the dissociation pulse and afterglow when the rate of CuCl reassociation is 5×10^{-26} cm^6/sec.

asymptotic to the gas temperature at a later time than for the "standard case" and that metastable helium persists longer for the larger reassociation rate. Because the Penning ionization rate for copper was estimated to be larger than the dissociative Penning collision rate for CuCl, if less Cu is present due to a large reassociation rate, then more metastable helium is available to relax in some other fashion. The electron heating seen for large α_2 is due to superelastic relaxation of this surplus metastable helium. Once the helium metastables and ions have relaxed to the ground state, the only loss mechanism for ground state copper is reassociation. Metastable copper, though, is always collisionally relaxing. Hence for large α_2, the time at which the metastable and ground state copper densities are maximum nearly coincide, while for small α_2, the time at which ground state copper density is maximum occurs at times longer than those for metastable copper. This trend tends to move the optimum time delay to larger values. For very large values of α_2, reassociation dominates all other processes, and the trend in optimum time delay reverses.

VI.C.1.f Buffer Gas Pressure and Optimum Laser Energy

It has already been discussed that for constant tube temperature and discharge conditions, there is an optimum buffer gas pressure. The dependence of laser energy on time delay is also a function of buffer gas pressure (see Figure V-2). Before buffer gas pressure could be varied in the afterglow model in order to illuminate some of

the processes responsible for this behavior, a consistent representation of the electron temperatures during the dissociation pulse had to be chosen. Appendix E summarizes the procedure which one may use to obtain consistent electron temperatures for the dissociation pulse.

Electron temperatures for the dissociation pulse calculated in the manner described in Appendix E were used to obtain optimum laser pulse energy as a function of buffer gas pressure and time delay as shown in Figure VI-18. Examples of laser pulse energy as a function of time delay are found in Figure VI-19. Note that at low pressure, laser pulse energy as a function of time delay displays structure similar to that found in the experimental examples of Figure V-2.

The behavior of copper and copper chloride densities illustrated in Figure VI-20a for a discharge and afterglow in 1.0 Torr of helium can be explained as follows. The electron temperature is initially high (about 6.3 eV) so that during its relaxation from its dissociation pulse value, the CuCl dissociation rate and copper ionization rates remain large. The CuCl dissociation rate dominates, resulting in a net increase of copper. The CuCl is soon depleted, removing the source term for the copper metastable and ground states. This produces the decline in copper density at about 2 μs, as the copper ionization rate remains high. Large densities of metastable and ionic helium also contribute to this decline through charge exchange and Penning ionization. About this time the electron temperature falls to a sufficiently small value so that volumetric ion recombination becomes important. But of even more importance is ion recombination at the

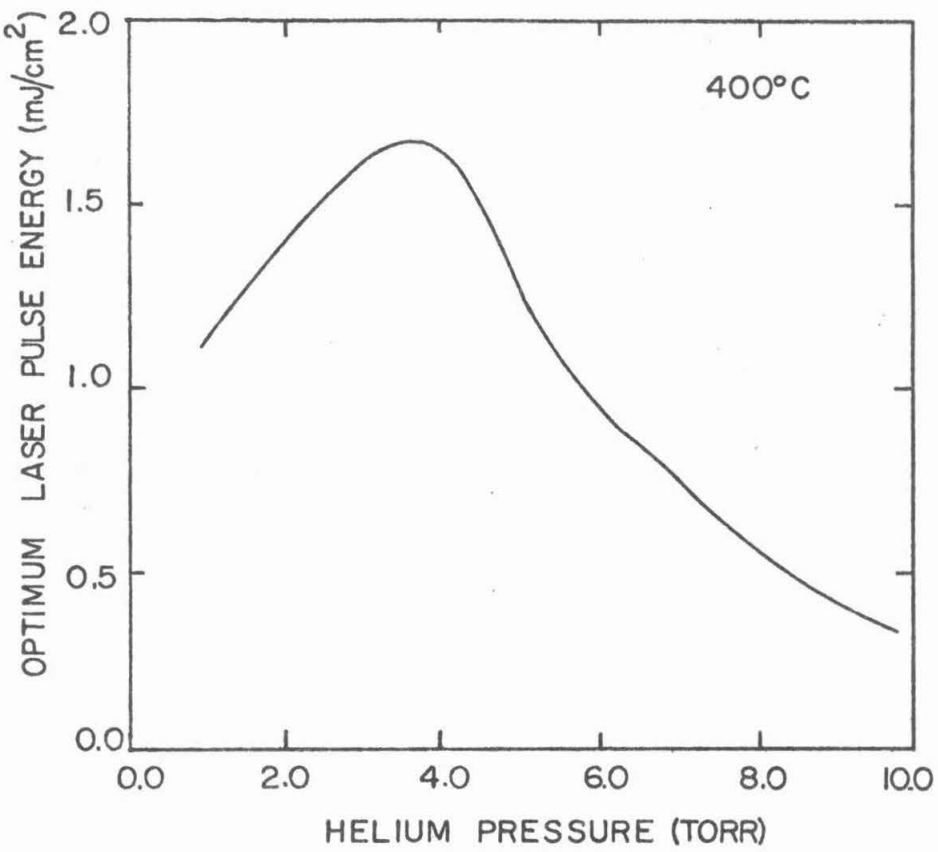

Figure VI.18. Calculated optimum laser pulse energy as a function of buffer gas pressure.

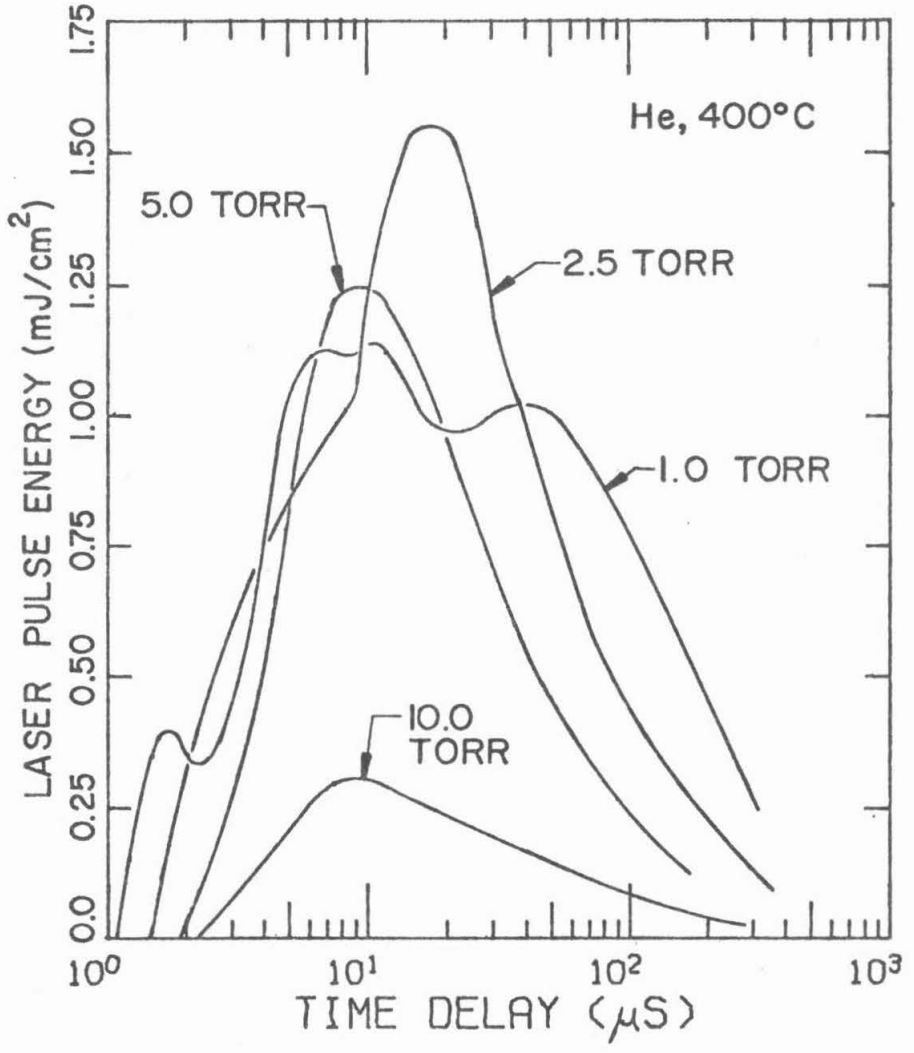

Figure VI.19. Laser pulse energy as a function of time delay and buffer gas pressure.

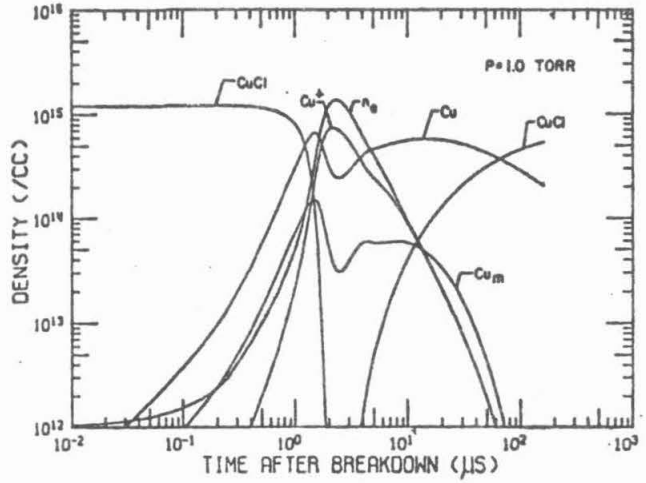

a) 1.0 Torr

b) 10.0 Torr

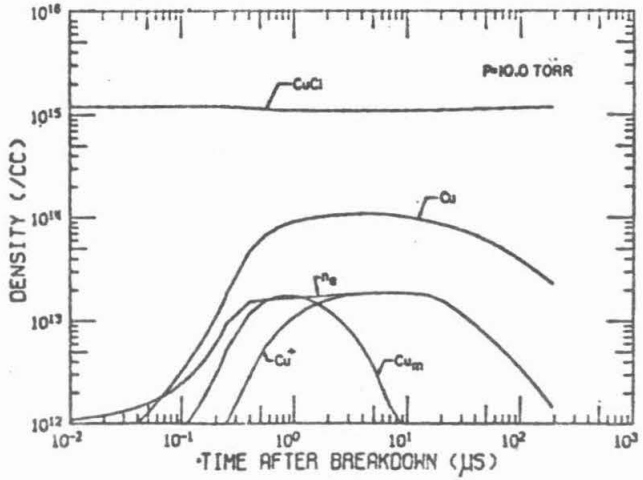

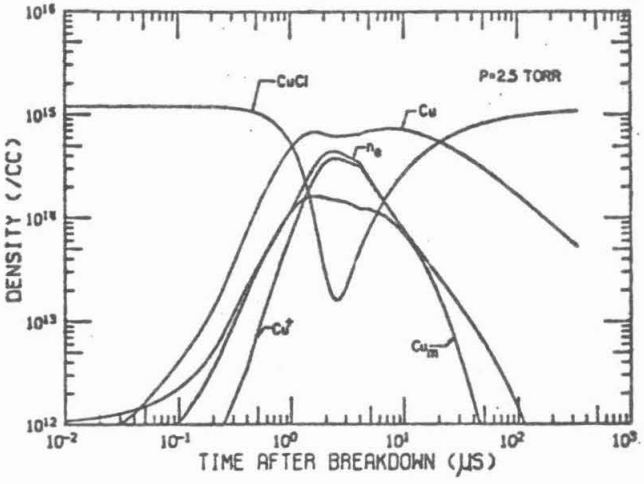

c) 2.5 Torr

Figure VI.20. A discharge and afterglow at 400°C for various buffer gas pressures (see Figure VI-5 for 5.0 Torr).

walls, enhanced by the low pressure. The increase seen in copper densities after 4 μs is due primarily to the diffusion of ions to the walls and their subsequent recombination. The flattened appearance of metastable copper at about 8 μs is something of a balance between collisional relaxation and contributions from ionic recombination. As the ionic copper is exhausted, the source of metastable copper disappears, and the remaining metastable copper is lost to collisional relaxation and reassociation. Similarly, ground state copper is lost to reassociation.

The processes at 2.5 Torr (Figure VI-20b) are essentially the same as at 1.0 Torr, but are somewhat subdued, as the dissociation pulse electron temperature (5.5 eV) is smaller, and diffusion rates are held back by the higher pressure.

The maximum value of copper ground state density at 1.0 Torr was computed to be $6.6 \times 10^{14}/cm^3$ which is 92% of the value computed at 3.75 Torr, the pressure at which laser energy is maximum. The optimum laser energy at 1.0 Torr is 1.16 mJ/cm^2, only 70% of the optimum value at 3.75 Torr. Despite a large copper ground state density, laser pulse energy at low pressure remains small. Contributions to the metastable copper density from diffusion-recombination prevents the laser pulse energy from becoming large. The Beutler states of ionized copper (excitation energy ≈ 7.74-10 eV) are coupled more strongly to the ^2D lower laser levels than the higher excited states. Hence a large fraction of recombinations can be expected to reach the metastable level [VI-22].

At 10.0 Torr (Figure VI-20c),excitation and dissociation rates are relatively small due to a low dissociation pulse electron temperature (4.3 eV), while collisional relaxation rates are large due to the high pressure. The high pressure inhibits diffusion so recombination at the walls is negligible. The electron density changes little until the electron temperature becomes asymptotic to the gas temperature at about 15 μs. The main reasons for low pulse energy at higher pressures are the low CuCl dissociation rate, and the low pumping rate resulting from small electron densities during the afterglow.

In view of the previous discussion, the ideal dissociation pulse is one which maximizes the amount of CuCl dissociated but minimizes the ionization of neutral copper, as the metastable copper formed during their recombination is detrimental to laser energy. This would correspond to a long, low energy dissociation pulse where the average electron temperature is well below the copper ionization potential but comparable to the CuCl dissociation limit. This is consistent with the dissociation pulse studies conducted by Brandt and Piper [VI-23] and the discussion in Section V.C of continuous discharge enhancement of laser pulse energy.

The mechanism responsible for the local minimum in optimum laser energy as a function of buffer gas pressure seen experimentally and discussed in Section II.D has not been found in this analysis. Such behavior, most dramatic in neon, has been observed to occur in

helium for tube temperatures in excess of 400°C. The calculated optimum energies of Figure VI-18 resemble the experimental results of Figure I-4, which are typical over a wider range of conditions. A more accurate description of the electron temperature during the dissociation pulse is necessary to reproduce the behavior.

VI.C.2 Chlorine and the Negative Chlorine Ion

In the previous analysis, chlorine was explicitly ignored. For purposes of computing the CuCl reassociation rate, its density was assumed to be the same as for copper. The weak point of this argument is the exclusion of the chlorine negative ion. The decision to exclude chlorine was based on two premises. The first was the belief that chlorine (halogen) does not significantly perturb laser performance since comparable laser energy and power can be obtained with a copper halide laser as with a pure copper laser. The second was the lack of any measured rate constants for electron attachment and detachment processes in a metallic halide system. The degree of guesswork required discouraged extending the model to include chlorine.

Despite the difficulties cited, an attempt was made to include chlorine in the model. The formulation, and results which are discussed below, must be considered typical for a metallic-halide system, and not necessarily particular to chlorine.

In addition to the species and reactions discussed in Section VI.B, three chlorine species were included in the extended model

Cl Neutral chlorine

Cl^- Chlorine negative ion

Cl^+ Chlorine positive ion.

With the exception of reactions (VI.B.1.b), (VI.B.1.c) and (VI.B.8) which are particular to the metastable level of copper, all of the electron impact, recombination, diffusion, reassociation and noble gas impact processes included for neutral and ionic copper were also used for neutral chlorine and its positive ion. The following processes involving the negative ion were included.

Electron Attachment:

$$e + Cl \rightarrow Cl^- \qquad \text{(VI.C.1)}$$

$$e + CuCl \rightarrow Cu + Cl^- \qquad \text{(VI.C.2)}$$

$$e + CuCl \rightarrow Cu^+ + Cl^- + e - \Delta\varepsilon_{11} \qquad \text{(VI.C.3)}$$

Electron Detachment and Neutralizing Collisions:

$$e + Cl^- \rightarrow Cl + e + e - \Delta\varepsilon_{12} \qquad \text{(VI.C.4)}$$

$$Cl^- + \begin{pmatrix} Cl^+ \\ Cu^+ \\ N^+ \end{pmatrix} \rightarrow Cl + \begin{pmatrix} Cl \\ Cu \\ N \end{pmatrix} \qquad \text{(VI.C.5)}$$

$$Cl^- + Cu \rightarrow CuCl + e \qquad \text{(VI.1.6)}$$

$$Cl^- + Cu^+ \rightarrow CuCl \qquad \text{(VI.C.7)}$$

Appropriate revisions to the rate equations (VI.B.9) to include the processes above were made. Each process, as well as necessary revisions to diffusion and wall reactions, will be discussed below.

The attachment process (VI.C.1) has the rate $h\nu_c$ where ν_c is the electron collision frequency, and h is the probability for attachment per collision. Typical values for h range from 10^{-3} to 10^{-4} [VI-10,24]. The electron collision frequency was computed from the electron-chlorine total elastic cross section measured by Cooper and Martin [VI-25]. The attachment probability was estimated to be $5x10^{-4}$.

The attachment collision (VI.C.2) is a resonant process. Typical peak cross sections for the resonance collision to produce O^- from O_2, NO, CO_2 and CO are $10^{-18}cm^2$ with a full width at zero height of about 4 eV [VI.26-30]. The threshold energy for the reaction is $E_{DISS}-E_{EA}$ where E_{DISS} is the molecular dissociation energy, and E_{EA} is the chlorine electron affinity. For CuCl and Cl, E_{DISS}=3.8 eV[VI-16] and E_{EA}=3.6 eV[VI-37]. The resonance cross section was estimated to have a peak value of $1.0x10^{-18}cm^2$, a base of 4 eV, and threshold of .2 eV.

The third attachment process (VI.C.3) has a cross section typical of threshold excitation. The threshold energy is $E_{DISS}+E_{ION}-E_{EA}$ where E_{ION} is the copper ionization potential. Typical values for the peak cross section to produce O^- are a few times $10^{-19}cm^2$ [VI.26-30]. The energy dependence of this cross section was chosen to be the same as that for an ionization with threshold $E_{DISS}+E_{ION}-E_{EA}$=7.95 eV (see Table VI.3). The peak cross section was chosen to be $3.0x10^{-19}cm^2$.

The cross section for electron detachment by electron impact (VI.C.4) was assumed to be the same as measured by Tiscone and

Branscomb for detachment in O^- [VI-32]. Neutralizing collisions (VI.C.5) are exothermic if the ionization potential of Cl^- is less than the electron affinity of the positive ion, a condition which holds for all species here. The thermal reaction rates for neutralization of H^-, O^-, O_2^-, NO_2^- and NO_3^- with a variety of collision partners all have values between 1.0×10^{-7} and $8.1 \times 10^{-7} cm^3/sec$ [VI-32]. The neutralization of O^- with N^+, O^+, Na^+, H_2^+, NO^+, and O_2^+ has an average thermal rate constant of $3.0 \pm 1.5 \times 10^{-7} cm^3/sec$ [VI-32]. This value was used for all neutralizing collisions (VI.C.5).

The detaching reassociation reaction (VI.C.6) is exothermic by .2 eV. It was estimated to have a thermal rate constant of $4.0 \times 10^{-10} cm^3/sec$ based on similar reactions of O^- with O, N, H_2, NO, CO, and N_2; H^- with H; and Cl^- with H [VI-33,34]. The neutralizing reassociation reaction (VI.C.7) was assigned the same rate constant.

In the absence of the negative chlorine ion, the ambipolar diffusion coefficient has a temperature dependence of $\frac{1}{2}(1+T_e/T_{gas})$. In the presence of the negative chlorine atom, the diffusion coefficient can be written as

$$D_a \sim \frac{1}{2}\left(1 + \frac{1}{T_{gas}(n_e+Cl^-)} \cdot (T_e n_e + T_{gas} Cl^-)\right) \qquad \text{(VI.C.8)}$$

In the limit of a negligible electron density, the ambipolar diffusion rate is thermal. In the limit of a negligible negative ion density, the temperature dependence is given by the previous expression.

All negative ions diffusing to the wall were assumed to react with a positive ion. The negative ion wall reactions are

$$\begin{aligned} \delta_{Cl+} Cl^- + Cl^+ &\rightarrow Cl+Cl \\ \delta_{Cu+} Cl^- + Cu^+ &\rightarrow CuCl \\ \delta_{N+} Cl^- + N^+ &\rightarrow N + Cl \end{aligned} \qquad \text{(VI.C.9)}$$

where

$$\delta_{x^+} = \frac{D_{a_{x^+}} x^+}{(Da_{Cl^+} Cl^+) + (Da_{Cu^+} Cu^+) + (Da_{N^+} N^+)}$$

The calculated densities for a discharge and afterglow in 5.0 Torr of He with Cl and Cl^+, but excluding Cl^- is shown in Figure VI-21. Comparing this result with Figure VI-5, the calculated afterglow for the same discharge conditions but without Cl, the copper ground state, metastable state, and CuCl densities are nearly identical for the two cases. The helium ion and metastable state densities having the additional chlorine collision partners, peak at smaller values. The chlorine positive ion density remains small, never exceeding $9 \times 10^{13}/cm^3$. The electron temperature approaches the gas temperature more gradually so that the electron density is higher for times longer than 7.5 μs. This increase in electron density for the case with Cl relative to the case without Cl results in larger pumping rates. The final result is that by explicitly including Cl and Cl^+, the minimum delay decreases fractionally, the optimum laser energy increases by 5.5%, and the maximum time delay

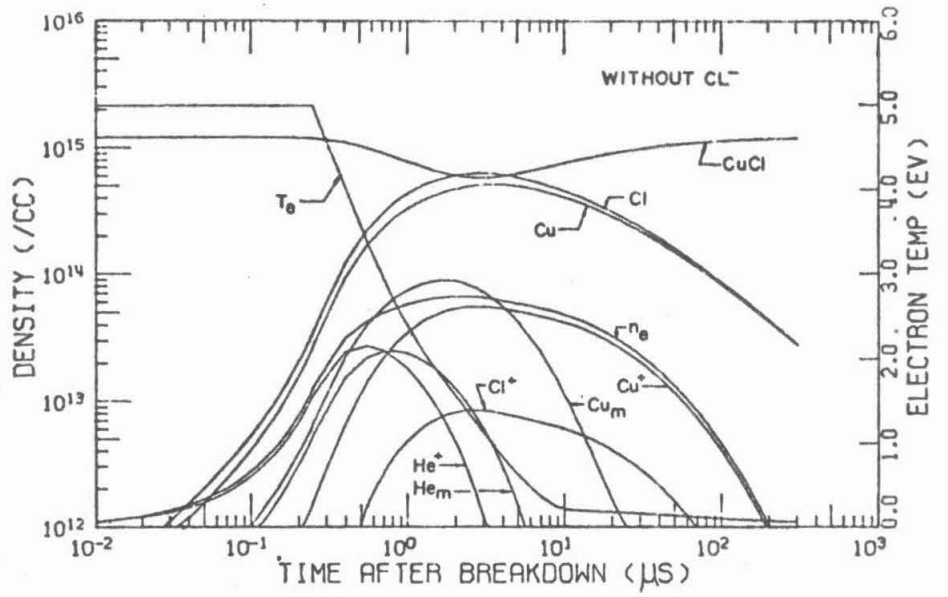

Figure VI.21. A discharge and afterglow including chlorine but excluding the negative ion.

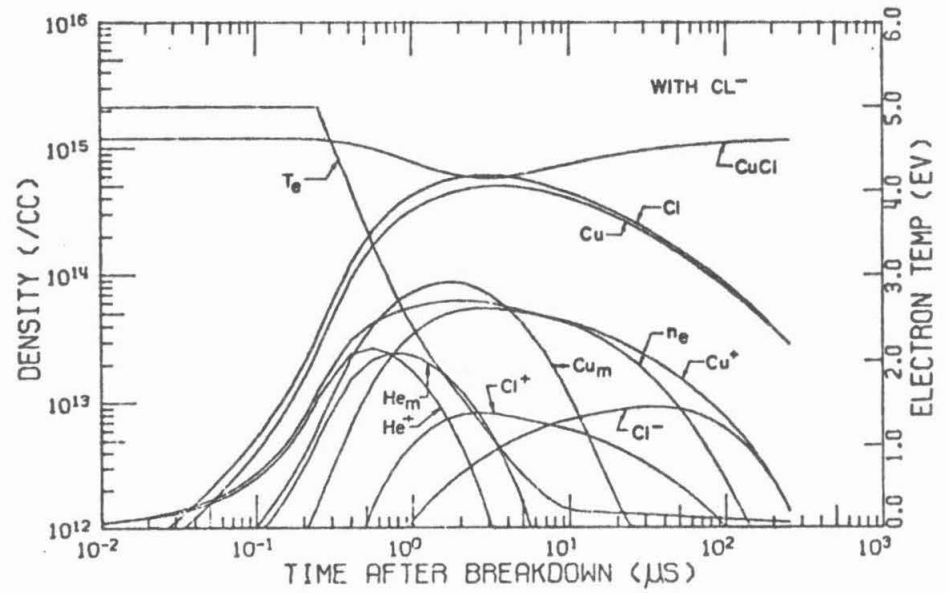

Figure VI.22. A discharge and afterglow including chlorine and the negative ion.

increases fractionally.

By including the negative chlorine ion, the results of Figure VI-22 are obtained. Neutral copper densities are nearly identical to the previous case, as are the helium densities, CuCl densities and the electron temperature. The chlorine negative ion begins to significantly reduce the electron density as early as 5 μs, becoming the dominant negative charge carrier 50 μs later. This charge transfer slows down the loss of ions due to diffusion, thereby extending their lifetime. The reduction in electron density results in lower pumping rates. The net effect is that the characteristic time delays remain virtually the same, but laser pulse energy is reduced fractionally (see Figure VI-23). In the presence of the negative chlorine ion, optimum laser energy decreases by 4.7%.

The change in calculated laser energy by including Cl^- resulted from its effect on electron density and subsequent pumping rates, and not from a change in copper density. Gabay, et al [VI-35] found that for optimum conditions, laser energy with CuBr was larger than for CuCl, and CuCl yielded larger laser energy than CuI. These results may in part be explained by different rates of electron attachment providing different initial conditions to the pumping pulse and hence different pumping rates.

VI.C.3 Radially Dependent Afterglow

For the conditions listed in Table VI.5, the results for the radial-

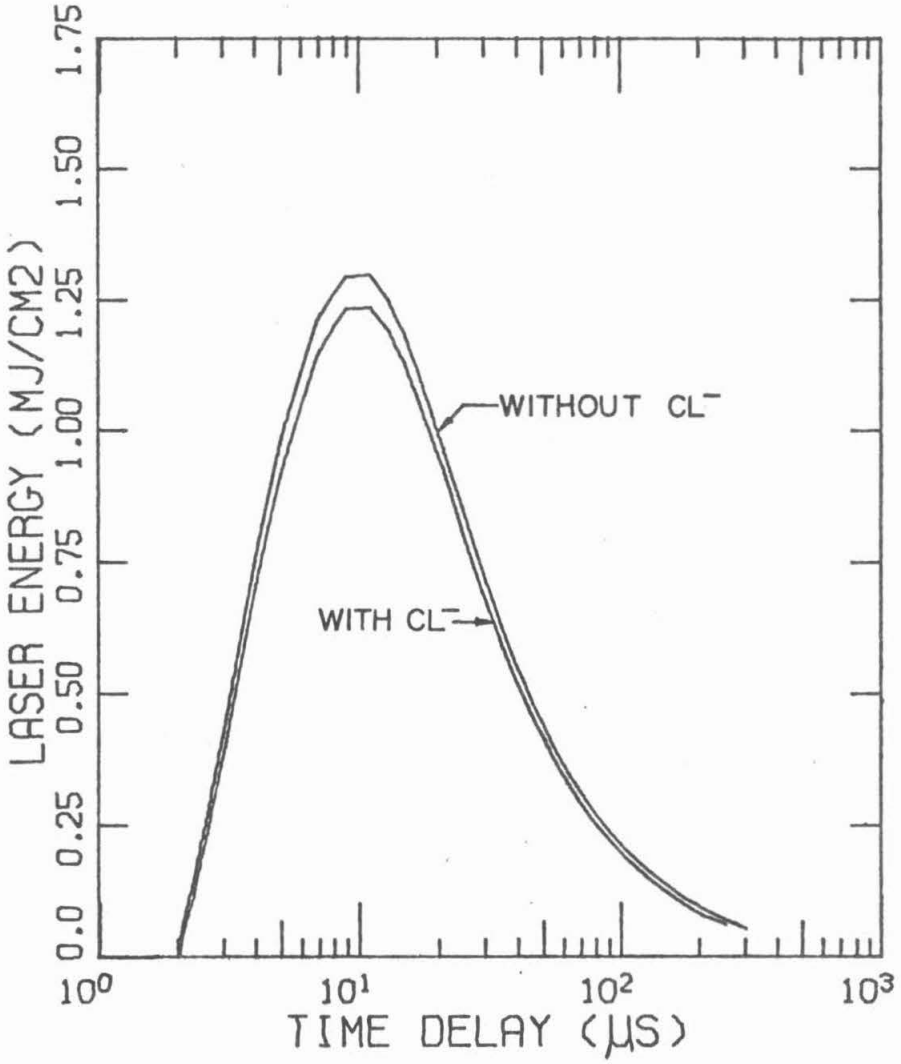

Figure VI.23. Laser pulse energy as a function of time delay, with and without the negative Cl ion.

ly dependent afterflow, can be found in Figure VI-24.* Examine first the electron temperature (Figure VI-24a). During the dissociation pulse, the electron temperature is held radially constant. After the dissociation pulse, cooling is mainly due to neutral atom elastic collisions and is therefore radially uniform. Near 1 μs, the electrons at the center of the tube heat relative to those near the wall. This is due almost entirely to the larger number of helium metastables superelastically relaxing at the center of the tube (see Figure VI-24c). The electron temperature profile reverses itself at about 3 μs and becomes hotter near the wall than at the center of the tube. The temperature at this time has fallen sufficiently low so that the rate of formation of helium metastables by electron impact is small. The only source for helium metastables is as a result of ion recombination. Since the electron temperature is still too high for collisional-radiative recombination to be important, diffusion to the walls is the dominant recombination process. Hence the relative population of metastables near the walls increases , and superelastic relaxation and heating become important near the wall. This in part accounts for the heating seen at about 10 μs in Figure VI-24a. Another equally important factor is the rate of electron-ion elastic collision cooling. This rate is proportional to $n_e/T_e^{\frac{3}{2}}$. Hence in regions of high electron density and low electron temperature, the

* Note that this case is without the diffusion cooling terms,

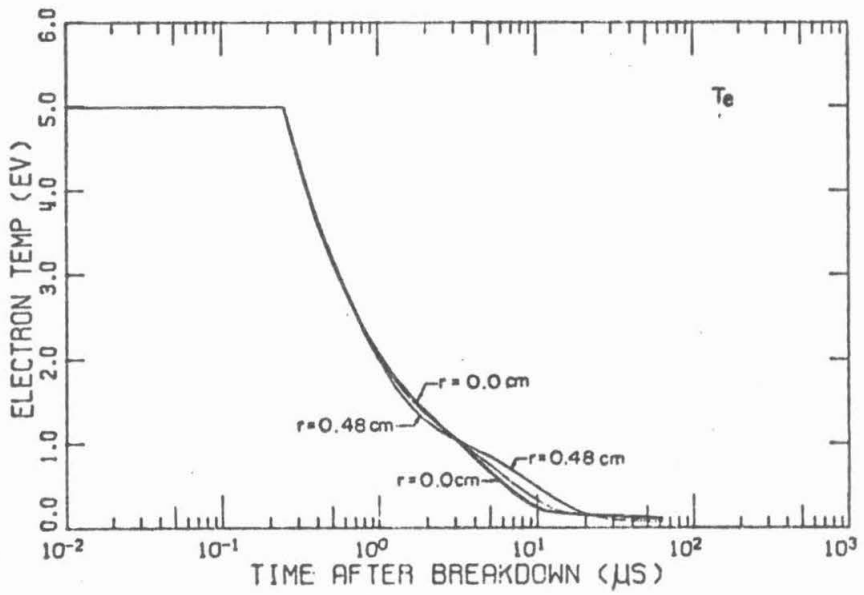

a) Te

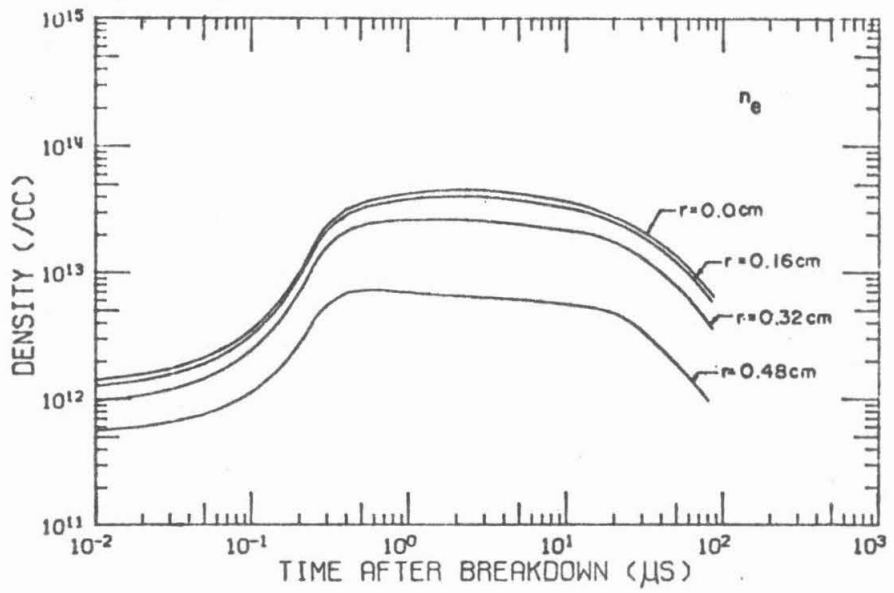

b) Ne

Figure VI.24. A discharge and afterglow at 400^{0}and 5.0 Torr helium as a function of radius.

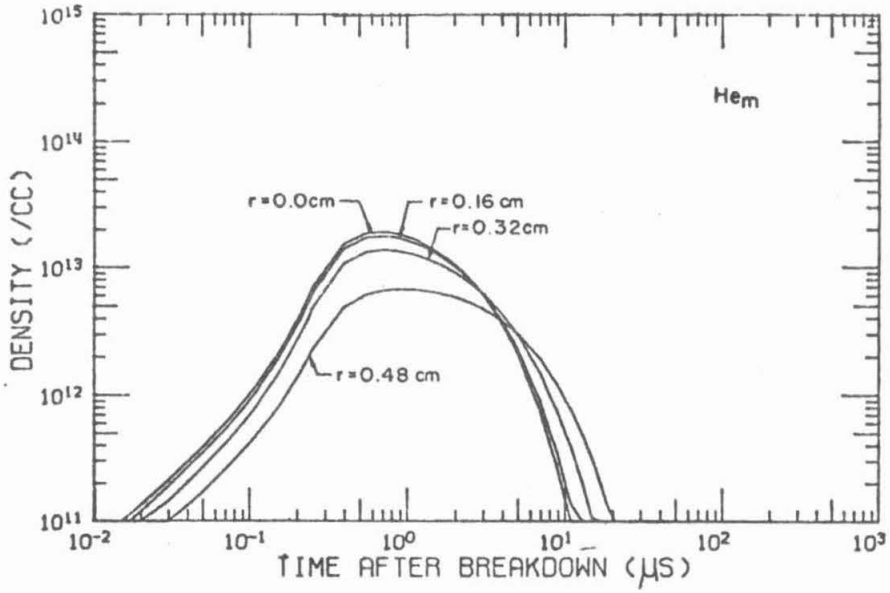
Hem
r=0.0cm
r=0.16 cm
r=0.32cm
r=0.48 cm
DENSITY (/CC)
TIME AFTER BREAKDOWN (μS)

c) He_m

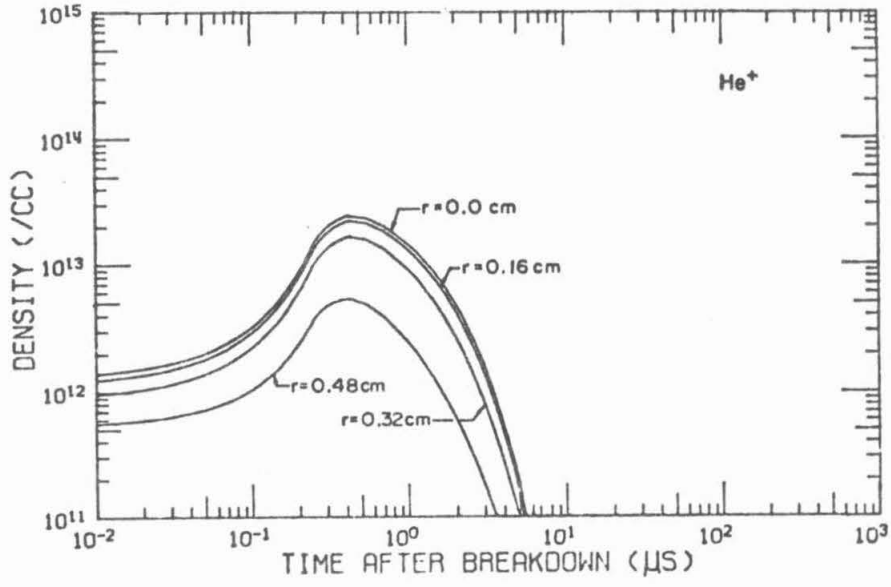
He+
r=0.0 cm
r=0.16 cm
r=0.48cm
r=0.32cm
DENSITY (/CC)
TIME AFTER BREAKDOWN (μS)

d) He^+

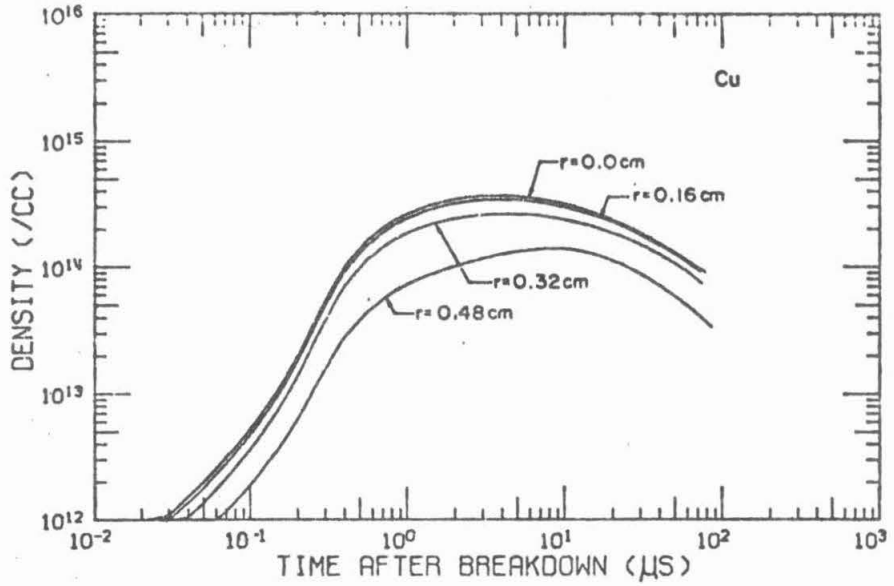
Cu
r=0.0cm
r=0.16cm
r=0.32cm
r=0.48cm
DENSITY (/CC)
TIME AFTER BREAKDOWN (μS)

e) Cu

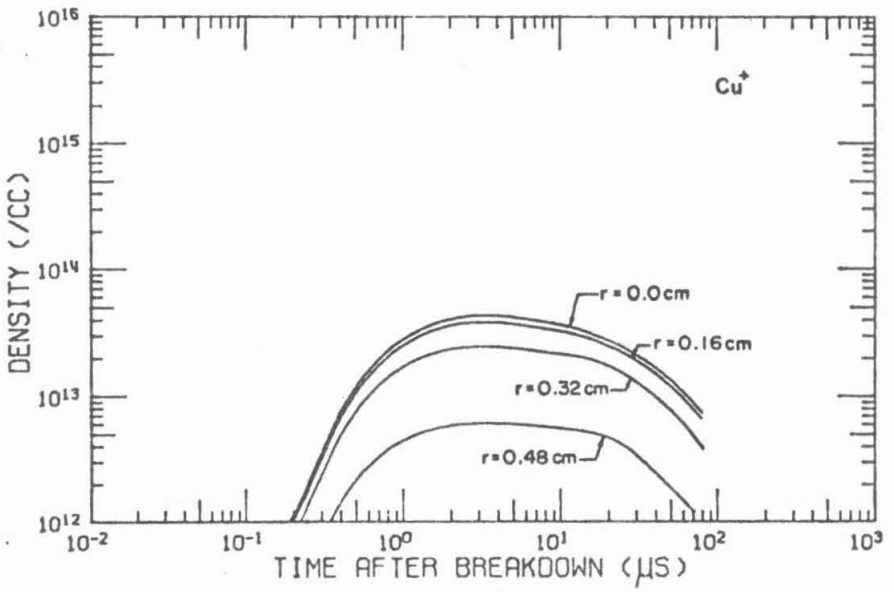
Cu+
r=0.0cm
r=0.16cm
r=0.32cm
r=0.48cm
DENSITY (/CC)
TIME AFTER BREAKDOWN (μS)

f) Cu^+

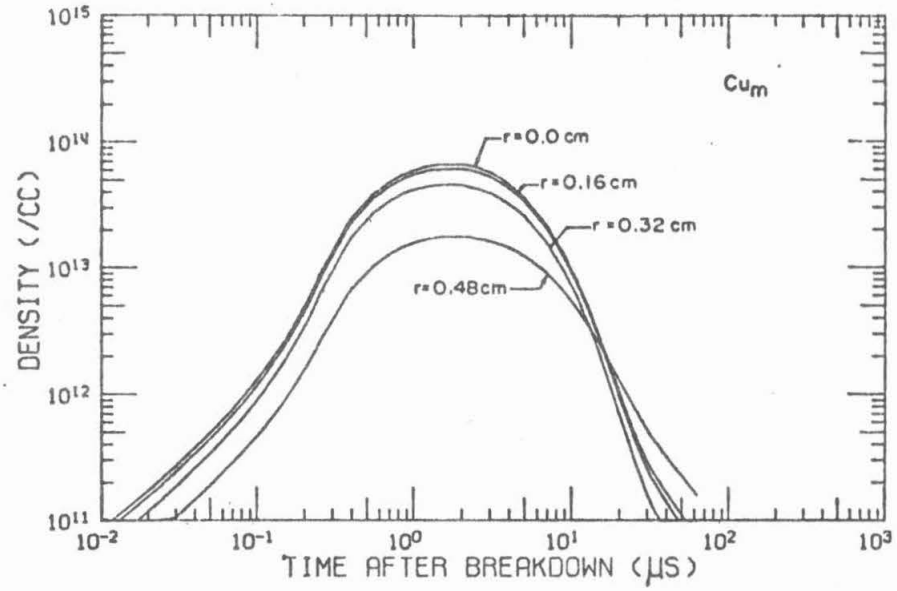
Cu$_m$
r=0.0 cm
r=0.16 cm
r=0.32 cm
r=0.48cm
DENSITY (/CC)
TIME AFTER BREAKDOWN (μS)

g) Cu_m

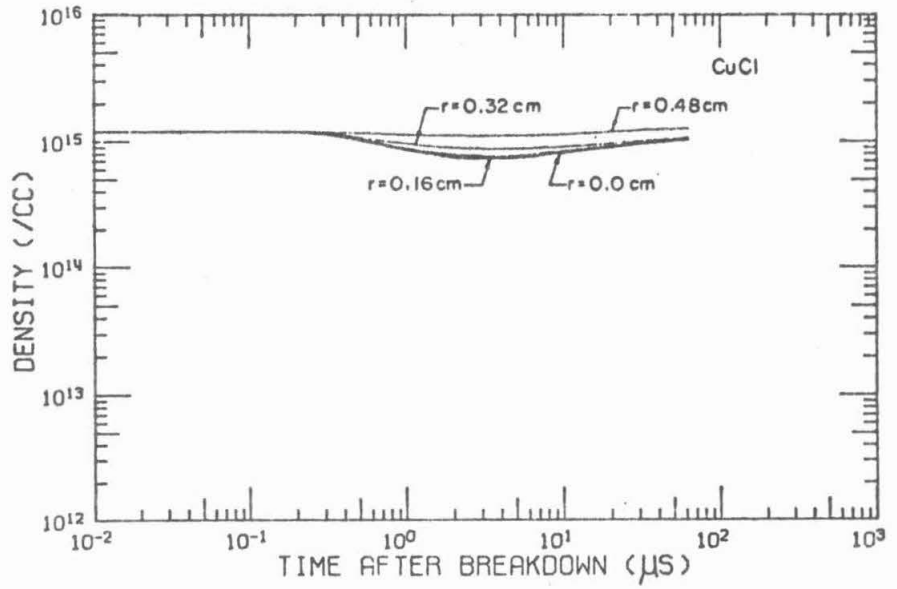
CuCl
r=0.32 cm
r=0.48cm
r=0.16cm
r=0.0 cm
DENSITY (/CC)
TIME AFTER BREAKDOWN (μS)

h) CuCl

process is more important. Near the walls, (3 μs < t < 20 μs) the electron density is low and the electron temperature is high relative to the center of the tube. Hence cooling by electron-ion elastic collisions near the walls is small compared to the center of the tube.

There are few deviations from the expected behavior of the remaining species. Densities are in general a monotonically decreasing function of radius. Note in Figure VI-24b for the electron density that collisional radiative recombination sets in at a slightly later time near the wall due to the higher electron temperature found there. The centerline electron density appears little affected by diffusion and heating effects near the wall. Note that the copper ground state density (see Figure VI-24e) peaks at a later time near the tube wall, a result of ion recombination contributions at the wall. The behavior of copper metastable densities is similar to that of the helium metastable densities (see Figure VI-24g). Densities near the wall become higher late in the afterglow due to diffusion recombination at the wall.

With the same initial conditions as used above, terms to describe diffusion cooling were included with the results shown in Figure VI-25. At times immediately following the discharge, cooling, as much as .5 eV is observed relative to the "uncooled" case. The same phenomena described above for the electron temperature occur, but radial gradients are less severe. The reversal in the gradient of the electron temperature occurs at later times as does the time at which the electron temperature becomes asymptotic to the gas

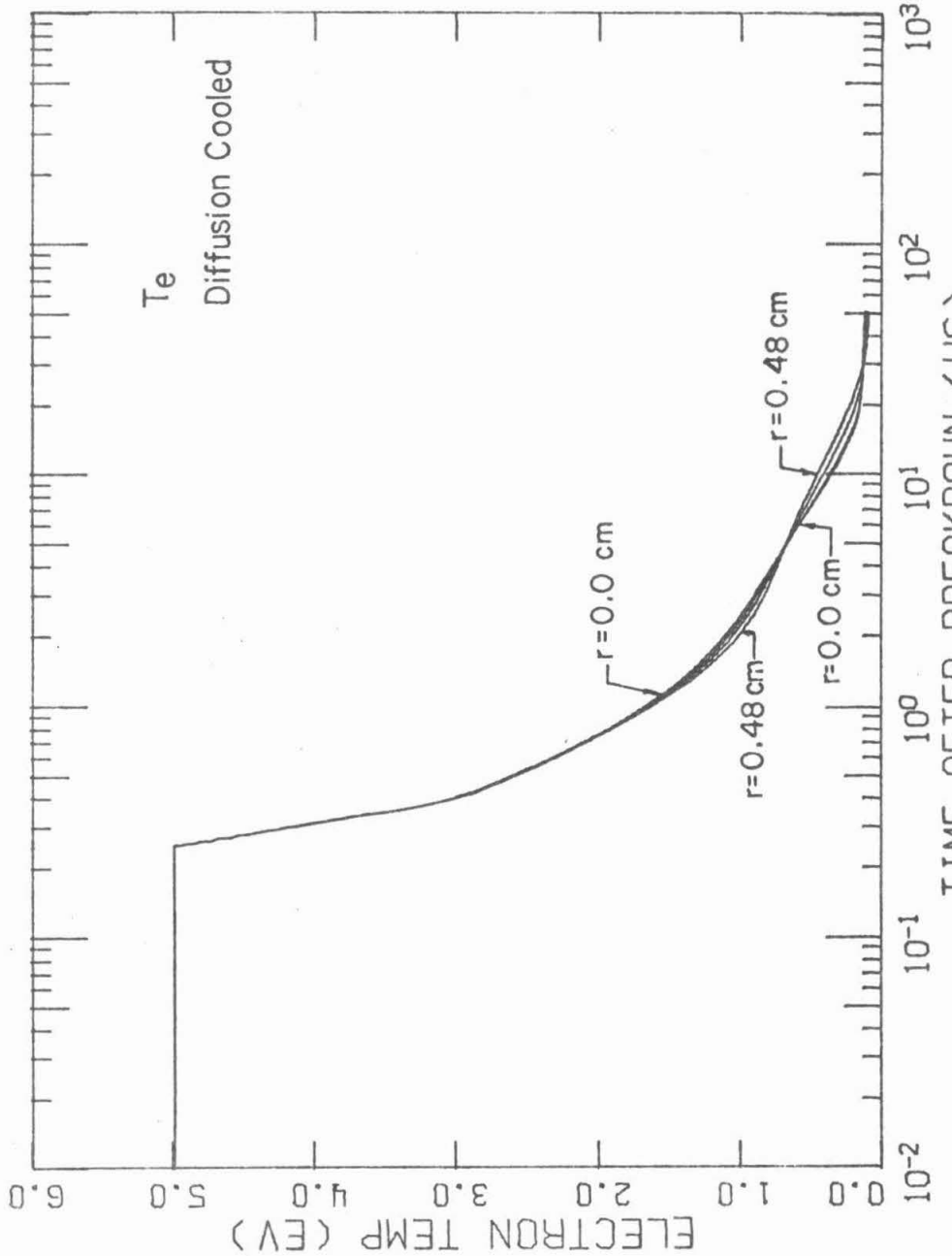

Figure VI.25. The diffusion cooled electron temperature as a function of radius.

temperature. Note that after the time at which the electron temperature gradient reverses, the electron temperature is higher at a given radial position than in the "uncooled" case. This is due to the change in the sign of $\frac{\partial T_e}{\partial r}$ which was previously negative. Since at this time in the afterglow $\frac{\partial n_e}{\partial r}$ and $\frac{\partial T_e}{\partial r}$ have opposite signs, previously positive terms in $\frac{\partial T_e}{\partial t}(r)$ (see equation D.2 of Appendix D) are now negative. The contributions of those terms denote a diffusion of energy in a direction opposite to that of the electron flux.

The remaining species behave essentially the same as they did without diffusion cooling. Their maximum values are in general lower due to the reduced reaction rates resulting from the "cooled" electrons. These extreme values also occur a few microseconds earlier than in the "uncooled" example.

VI.D. A Model for the Laser Pulse

VI.D.1 Introduction

A numerical model was developed to describe the three dimensional time dependent electric field in an optical resonator with coupling to the laser medium and discharge. The laser cavity is divided into a three dimensional grid. The scaler wave equation is integrated at each grid point within the laser cavity. The spatial derivatives are handled by a finite difference technique. The time derivatives are integrated using a Runge-Kutta-Gill scheme with Adams-Moulton corrections.*

* The integration routine is a modified version of MODDEQ, a Caltech Computer Library subroutine [VI-14].

VI.D.2 Description of the Laser Pulse Model

Start by considering the scaler wave equation

$$\nabla^2\mathcal{E} - \frac{1}{c^2}\frac{\partial^2\mathcal{E}}{\partial t^2} = \frac{4\pi}{c^2}\frac{\partial^2 P}{\partial t^2} \qquad \text{(VI.D.1)}$$

Assume cylindrical geometry and azimuthal symmetry. Write the polarization as

$$P(r,z,t) = \chi(r,z,t)\mathcal{E}(r,z,t) \qquad \text{(VI.D.2)}$$

where χ is the complex susceptibility. Let the electric field be written as

$$\mathcal{E}(r,z,t) = E(r,z,t)e^{i(\omega t-kz)} \qquad \text{(VI.D.3)}$$

where $\omega = ck$ is the angular frequency and $k = 2\pi/\lambda$ is the wavenumber (real and constant). The susceptibility χ and E are assumed to be slowly varying functions of time compared to ω. Place (VI.D.2) and (VI.D.3) in (VI.D.1) and obtain

$$\nabla^2(Ee^{-ikz}) + [(1+4\pi\chi)(k^2E-\frac{2ik}{c}\frac{\partial E}{\partial t}) \qquad \text{(VI.D.4)}$$

$$- i\frac{8\pi k}{c}E\frac{\partial\chi}{\partial t}]e^{-ikz} = 0$$

with $\nabla^2 = \frac{1}{r}\frac{\partial}{\partial r} + \frac{\partial^2}{\partial r^2} + \frac{\partial^2}{\partial z^2}$, (VI.D.4) becomes

$$\frac{\partial^2 E}{\partial z^2} - 2ik\frac{\partial E}{\partial z} + \frac{\partial^2 E}{\partial r^2} + \frac{1}{r}\frac{\partial E}{\partial r} + 4\pi\chi k^2 E - 2ik(1+4\pi\chi)\frac{\partial E}{\partial t} \qquad \text{(VI.D.5)}$$

$$- i\frac{8\pi k}{e}\frac{\partial \chi}{\partial t} = 0$$

The envelope function is in general complex. Hence let

$$E(r,z,t) = B(r,z,t)e^{iA(r,z,t)} \qquad \text{(VI.D.6)}$$

where B and A are real. Place (VI.D.6) in (VI.D.7) and obtain

$$\frac{\partial^2 B}{\partial z^2} - 2i\frac{\partial A}{\partial z}\frac{\partial B}{\partial z} - \left(\frac{\partial A}{\partial z}\right)^2 B - i\frac{\partial^2 A}{\partial z^2}B - 2ik\left(\frac{\partial B}{\partial z} - i\frac{\partial A}{\partial z}B\right)$$

$$+ \frac{\partial^2 B}{\partial r^2} - 2i\frac{\partial A}{\partial r}\frac{\partial B}{\partial r} - \left(\frac{\partial A}{\partial r}\right)^2 B - i\frac{\partial^2 A}{\partial r^2}B + \frac{1}{r}\left(\frac{\partial B}{\partial r} - i\frac{\partial A}{\partial r}B\right) \qquad \text{(VI.D.7)}$$

$$+ 4\pi k^2\chi B - \frac{2ki}{c}(1+4\pi\chi)\left(\frac{\partial B}{\partial t} - i\frac{\partial A}{\partial t}B\right) - i\frac{8\pi k}{c}B\frac{\partial \chi}{\partial t} = 0$$

The real and imaginary parts of χ can be written as

$$\mathrm{Re}(\chi) = 2n^2\left(\frac{\Delta k}{k}\right), \quad \mathrm{Im}(\chi) = \frac{\gamma n^2}{k} \qquad \text{(VI.D.8)}$$

where Δk is the delay in phase shift per unit length, which is the source of "mode pulling", γ is the gain "constant" and n is the real index of refraction. Because this treatment is monochromatic and taken at line center, $\Delta k=0$. For the expected electron densities, $n \approx 1$. The gain is a function of the population inversion density ΔN (see Section III.B.1).

$$\gamma = \beta\Delta N, \qquad \beta = \frac{c^4 A_1}{32\pi^{5/2}\nu_o^3}\left(\frac{M}{kT_g}\right)^{1/2} \tag{VI.D.9}$$

Place (VI.D.8) in (VI.D.9), set the real and imaginary parts separately equal to zero and obtain

$$\frac{\partial A}{\partial t} = \frac{4\pi}{k}\left(\frac{\partial \gamma}{\partial t} + \frac{\gamma}{B}\frac{\partial B}{\partial t}\right) - \frac{c}{2kB}\left(\left(\frac{\partial A}{\partial z}\right)^2 B - \frac{\partial^2 B}{\partial z^2}\right.$$
$$\left. + 2k\frac{\partial A}{\partial z}B - \frac{\partial^2 B}{\partial r^2} + \left(\frac{\partial A}{\partial r}\right)^2 B - \frac{1}{r}\frac{\partial B}{\partial r}\right) \tag{VI.D.10}$$

$$\frac{\partial B}{\partial t} = \frac{4\pi c B\gamma}{k}\left(\frac{k}{2} - \frac{1}{c}\frac{\partial A}{\partial t}\right) - \frac{c}{k}\left(\frac{2\partial A}{\partial z}\frac{\partial B}{\partial z}\right.$$
$$\left. + \frac{\partial^2 A}{\partial z^2}B + 2k\frac{\partial B}{\partial z} + \frac{2\partial A}{\partial r}\frac{\partial B}{\partial r} + \frac{\partial^2 A}{\partial r^2}B + \frac{1}{r}\frac{\partial A}{\partial r}B\right) \tag{VI.D.11}$$

Finally solving the simultaneous Equations (VI.D.10) and (VI.D.11) for the envelope amplitude time derivative,

$$\frac{\partial B}{\partial t} = \frac{c}{2k\left(1+\frac{16\pi}{k^2}\gamma^2\right)}\left[8\pi B\gamma\left(\frac{k}{2} - \frac{4\pi}{c}\frac{\partial \gamma}{\partial t}\right) + \frac{4\pi\gamma}{k}\left(\left(\frac{\partial A}{\partial z}\right)^2 - \frac{\partial^2 B}{\partial z^2}\right.\right.$$
$$+ 2k\frac{\partial A}{\partial z}B - \frac{\partial^2 B}{\partial r^2} + \left(\frac{\partial A}{\partial r}\right)^2 B - \frac{1}{r}\frac{\partial B}{\partial r} - \frac{2\partial A}{\partial z}\frac{\partial B}{\partial z}$$
$$\left.\left. - \frac{\partial^2 A}{\partial z^2}B - 2k\frac{\partial B}{\partial z} - \frac{2\partial A}{\partial r}\frac{\partial B}{\partial r} - \frac{\partial^2 A}{\partial r^2}B - \frac{1}{r}\frac{\partial A}{\partial r}B\right]\right.$$

The envelope phase time derivative is obtained by placing (VI.D.12) in (VI.D.10). The derivatives for the envelope function amplitude and phase are separately integrated at each cavity point for a right traveling and left traveling wave. Coupling to the laser medium is obtained through the gain constant γ. The rate equations, discussed in Section III.B, are simultaneously integrated at each cavity point. (Only the three rate equations for the ground state, lower level and upper laser level are used.) The inversion density calculated from the rate equations is placed in (VI.D.9) to obtain the gain. The intensity required for the rate equations is obtained from the field amplitude by

$$I = \frac{c}{4\pi} B^2 \qquad \text{(VI.D.13)}$$

The laser cavity (see Figure VI.26a) is formed by two circular mirrors of radius R_m and separated by a distance L. One mirror is totally reflecting, while the other has field reflectance R_f. They may have arbitrary radii of curvature (handled by introducing radially dependent phase delays at each mirror) but are assumed to be flat here. The cavity is composed of a set of grid points identified by (i,j), denoting axial position $z_i = (i-\frac{1}{2})\Delta z$ and radial position $r_j=(j-1)\Delta r$.

Numerically, having a right and a left moving field is clumsy. Consider alternately the geometry of Figure VI-26b. Here only a right-hand field is necessary. For $1 \leq i \leq IZ$, the field corresponds to the RH field of Figure VI-26a, for $IZ < i \leq 2*IZ$, the fields correspond to the LH field of Figure VI-26a. Consider a field packet starting

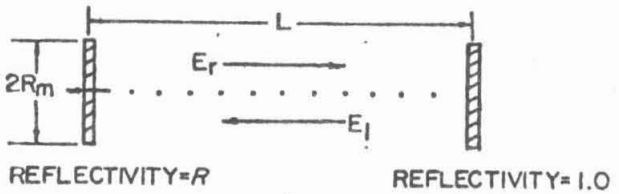

a)

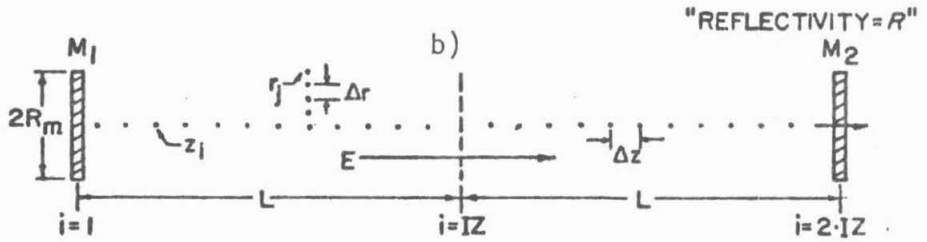

Figure VI.26. Geometry for the laser pulse model
a) conventional cavity b) expanded cavity

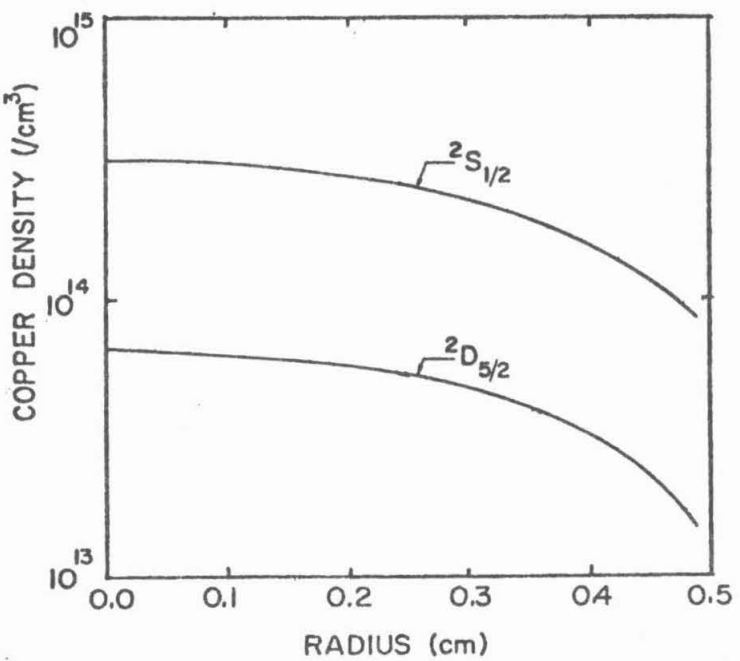

Figure VI.27. Initial ground state copper ($^2S_{1/2}$) and metastable copper ($^2D_{5/2}$) densities for the laser pulse model.

at the "output" mirror M_1 at i=1. It propagates to the right until it reaches i=IZ. This is the virtual location of the 100% mirror. Instead of being reflected and propagating to the left, it proceeds to the right, but the amplitude of the field at any point $r_j > R_m$ is set equal to zero. (That portion of the field at a radius greater than the "mirror" is not "reflected".) Appropriate phase delays due to reflection are introduced at i=IZ+1. The "reflected" field continues to propagate until it reaches M_2 at i=2*IZ, a distance 2L from M_1. But the field, having propagated a distance 2L should be back at M_1, the"output" mirror. Hence $(1-R_f)$ of the field arriving at M_2 is taken as output. The field at points $r_j > R_m$ is set equal to zero. The field amplitude at points $r_j \leq R_m$ is reduced by the factor $(1-R_f)$, appropriate phase delays are added for reflection, and the field is translated to i=1, thereby completing one round trip of the cavity.

Given the conditions above, the spatial derivatives of $(\frac{dB}{dt})_{ij}$ and $(\frac{dA}{dt})_{ij}$ take on the finite difference form

$$(\frac{\partial x}{\partial z})_{ij} = \frac{x_{i+1,j} - x_{i-1,j}}{2(\Delta z)} \qquad \text{(VI.D.14a)}$$

$$(\frac{\partial^2 x}{\partial z^2})_{ij} = \frac{x_{i+,j} - 2x_{ij} + x_{i-1,j}}{(\Delta z)^2} \qquad \text{(VI.D.14b)}$$

$$\left(\frac{\partial x}{\partial r}\right)_{ij} = \frac{x_{i,j+1} - x_{i,j-1}}{2(\Delta r)} \qquad \text{(VI.D.14c)}$$

$$\left(\frac{\partial^2 x}{\partial r^2}\right)_{ij} = \frac{x_{i,j+1} - 2x_{ij} + x_{i,j-1}}{(\Delta r)^2} \qquad \text{(VI.D.14d)}$$

At t=0, the field is initialized as having zero amplitude and random phase. (Spontaneous emission, which starts the laser pulse, occurs with random phase). The phase of the incident field is retained during stimulated emission. The initial values for the copper and electron densities are obtained from the radial afterglow model. Since the model gives only a radial distribution, the initial values are assumed to be distributed uniformly along the axis. A Lorentz approximation is used for the gas.

VI.D.3 Results and Discussion

Pulse propagation codes of the type described above are costly to run because the characteristic time step must be shorter than the light travel time between grid points, and the grid points must be close enough together so that spatial derivatives remain small. When optimum initial conditions were chosen, the laser pulse was long and the intensity high. As a result, unphysically large spatial derivatives developed. The solution, decreasing the grid size, proved to be too costly. In order to reduce the length of the pulse, non-optimum initial condi-

tions were chosen (a near minimum time delay). These conditions are characterized by a large fraction of metastable copper.

VI.D.3a A Typical Laser Pulse

The calculated laser output pulse for the conditions of Table VI.6 and Figure VI-27 is shown in Figure VI-28. Figure VI-29 shows the cavity intensity along the axis of the tube. The integrated laser pulse energy density is shown in Figure VI-30 (R_f= 0.5). The laser pulse totaled 1.00 mJ (1.27 mJ/cm^2) for an average energy density of 50 μJ/cm^2 of active medium. The initial fraction of metastable copper decreased from a maximum of 21% at the center of the tube to 19% near the wall. Despite the gain initially being most negative at the center of the tube, the laser pulse is initially highly peaked at the center of the spot. After only 2ns, the laser pulse has a nearly flat profile with the intensity falling off by only a factor of two at the edge. This profile remains fairly intact until late into the pulse (about 7ns) when the intensity at the center of the spot falls sharply while the intensity at the edge of the spot remains relatively large.

The relative complexity of the laser pulse can be understood by inspecting Figure VI-31. This figure displays radial gain at the middle of the cavity. Plotted above the midplane is log (positive gain). Below the midplane is log (- negative gain). Note that the gain is initially negative and most negative at the center of the tube. As the discharge pulse progresses the profile reverses, and at 3ns reaches a maximum of .03/cm at the center of the tube. At this

TABLE VI.6

STANDARD INITIAL CONDITIONS AND PARAMETERS

FOR THE LASER PULSE MODEL

Tube Radius = 0.50 cm (6 radial grid points)

Mirror Radius = 0.50 cm (16 field axial grid points)

Field Radius = 0.60 cm

Resonator Length = 25.0 cm

Output Mirror Field Reflectance (R_f) = 0.50 (Reflectivity=0.25)

Initial Electron Density at Tube Center = $2.5 \times 10^{14}/cm^3$

Maximum Electron Density at Tube Center = $5.0 \times 10^{14}/cm^3$

Pumping Pulse Rise Time = 40 ns

Electron Temperature = 15.0 eV

Electron Distribution = Maxwellian

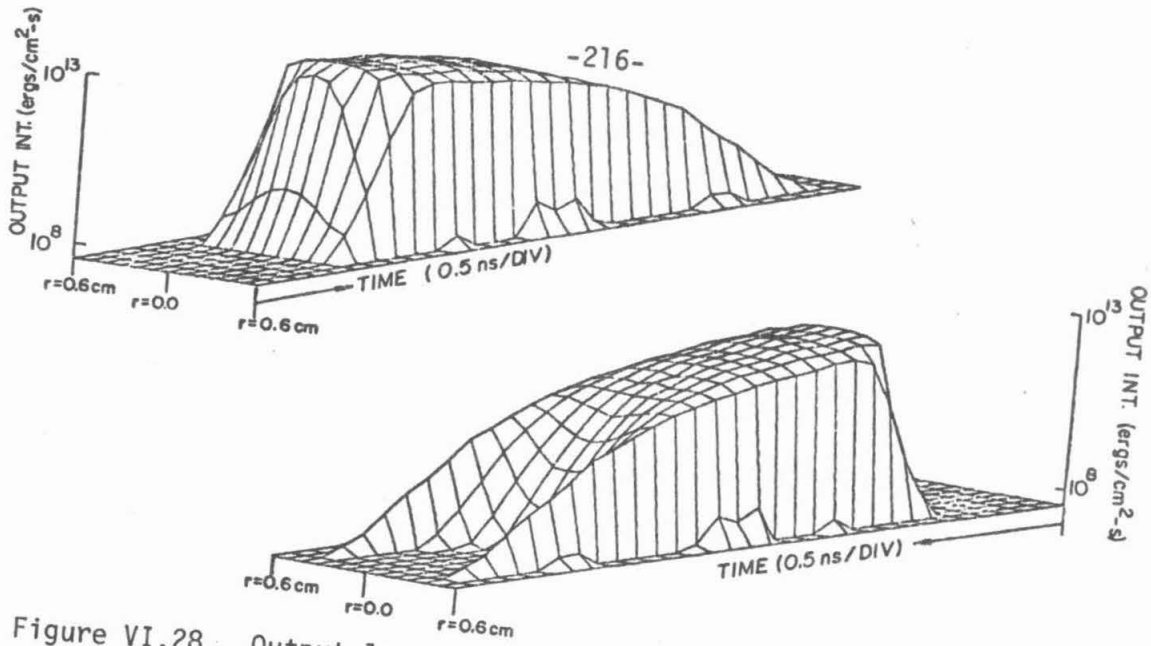

Figure VI.28. Output laser pulse intensity as a function of time and radius (R_f = 0.5).

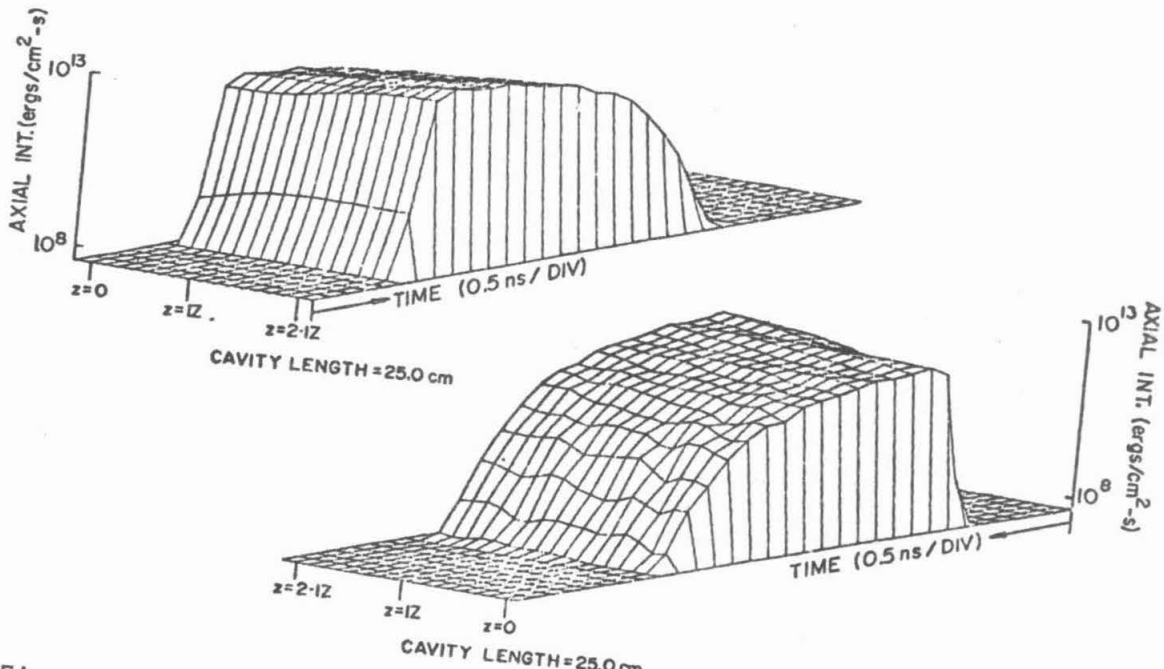

Figure VI.29. Cavity intensity as a function of time and axial position at the center of the tube (R_f = 0.5).

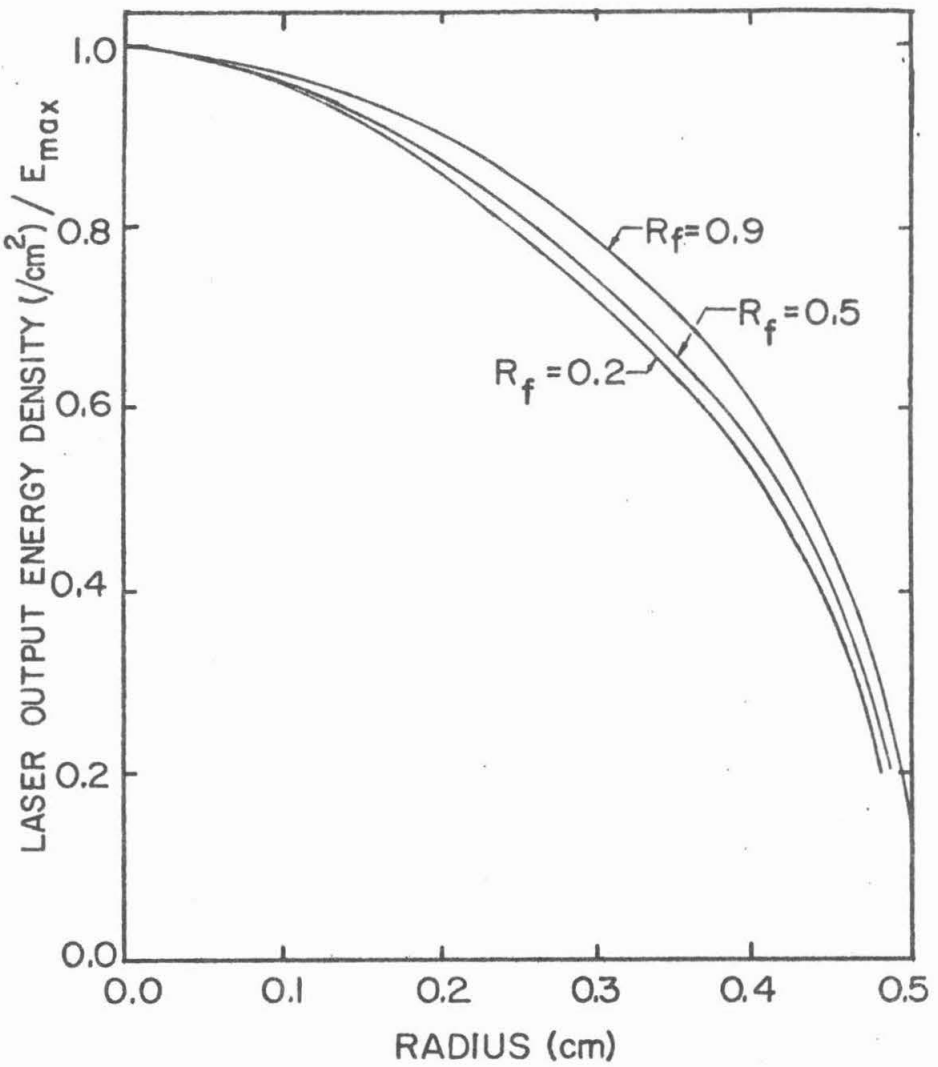

Figure VI.30. Laser pulse energy density as a Function of Radius and Output Mirror Field Reflectance (R_f).

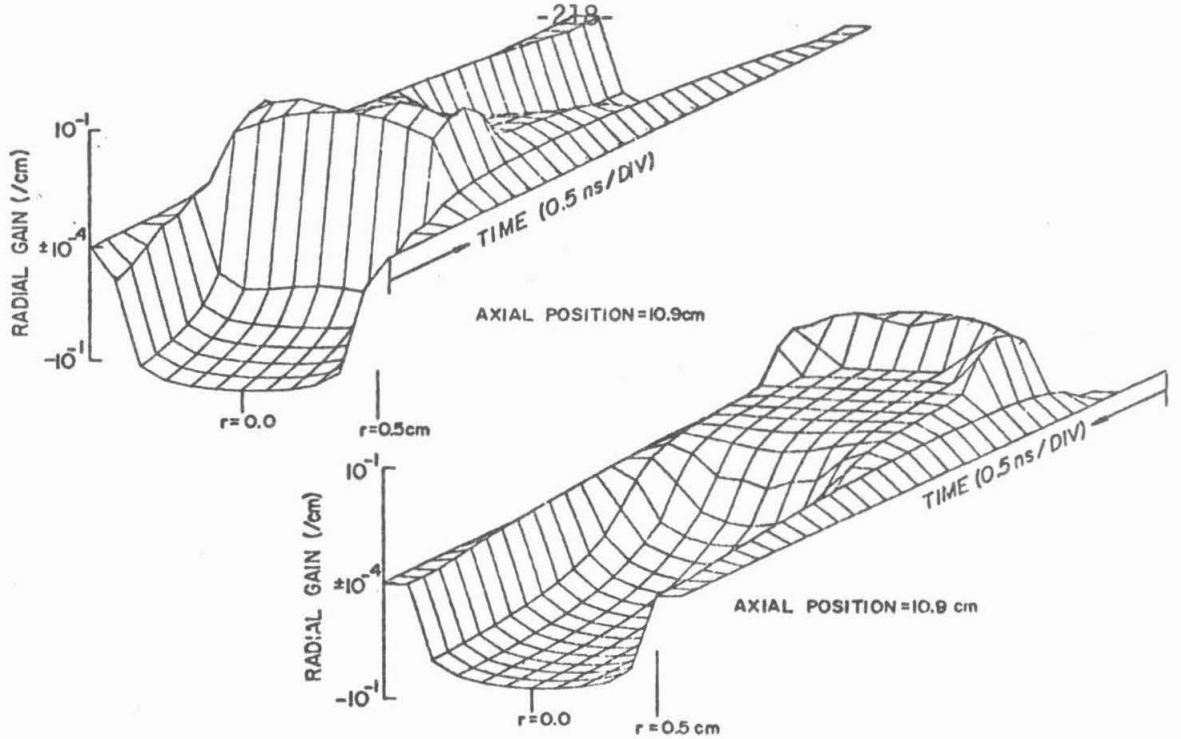

Figure VI.31. Gain as a function of time and radius at the middle of the laser. Plotted above the midplane is log (positive gain). Plotted below the midplane is log (-negative gain) (R_f=0.5).

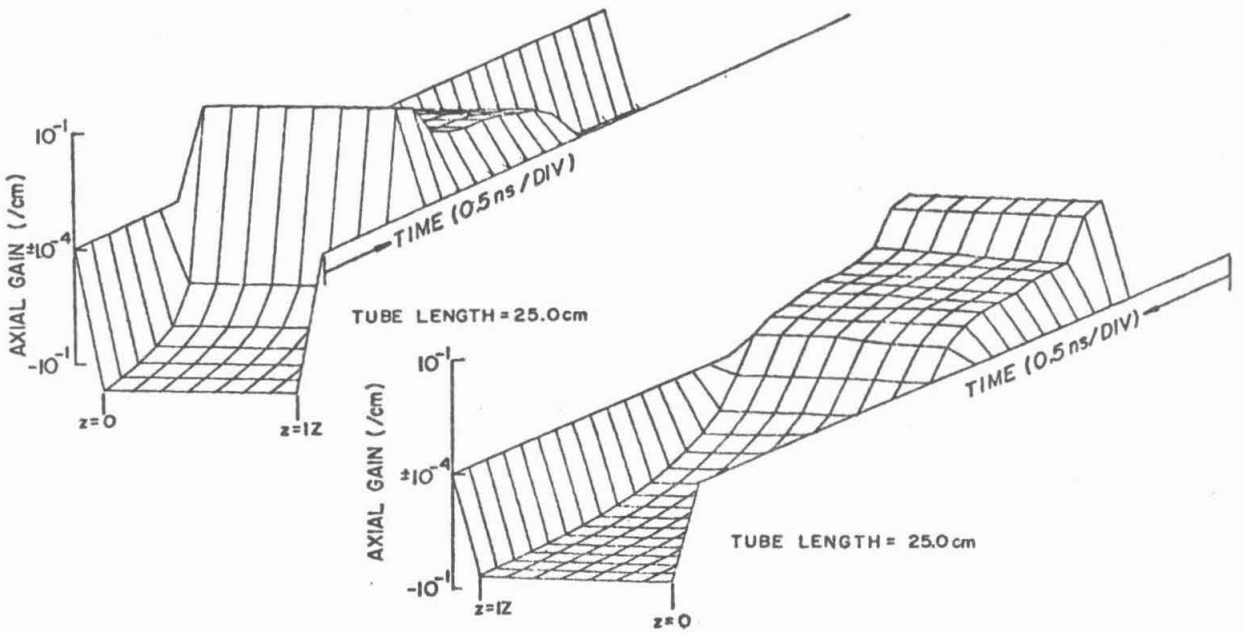

Figure VI.32. Gain as a function of time and axial position at the center of the tube (R_f = 0.5).

point, the upper level "dumps" to the lower level. As seen in Figure VI-31, this gain switching occurs first at the center of the tube where gain was the highest and spreads to the edges as long as 2ns later. This is reflected in Figure VI-28 where the center of the pulse reaches its maximum value a nanosecond or more earlier than at the edge of the pulse. Gain remains positive until 8ns, but then falls quickly negative at all points except those adjacent to the wall of the tube. The transition to negative gain is due to depletion of the ground state, and a large metastable copper density. The "hollow" appearance of the laser pulse is due to absorption. The decay of the pulse envelope is due to output coupling.

The axial and radial differentiation in gain can be coupled to the intensity distribution. Axially, the positive gain is always largest near the rear mirror, and smallest near the output mirror (see Figure VI-32). The difference is as much as 50% at the time just after gain is maximum. The axial intensity displays the opposite behavior. For periods of positive gain, the sum of the intensities of the right and left moving waves is in general largest at the output mirror and smallest at the rear mirror. Clearly the higher intensity at the output mirror saturates the gain, preventing it from becoming large, while the larger gain at the opposite end of the cavity feeds the small but growing field amplitude.

VI.D.3b Laser Pulses and Mirror Reflectivity

In Section III.E, experimental and numerical data concerning

the insensitivity of laser pulse energy to output mirror reflectivity were discussed. This phenomenon was again investigated here with the results shown in Figure VI-33. The laser pulse energy remains nearly constant over a wide range of reflectivity. The pulse length increases with increasing mirror reflectivity in a manner similar to that shown in Figure III-9.

Output intensity, radial gain and axial gain for mirror field reflectances of 0.2 and 0.9 (reflectivities of .04 and .81) are shown in Figures VI-34, 35 and 36. Note that as the mirror reflectance decreases, axial gradients in gain increase sharply. The maximum gain obtained during the laser pulse decreases as the mirror reflectance increases, the change being about 10% for the range .2 to .9. The behavior of the gain at times later than the peak gain is a sensitive function of mirror reflectivity. First note that the axial gain for R_f = 0.2 is as much as an order of magnitude higher at the rear mirror than at the output mirror, while the axial gain for R_f = 0.9 is essentially flat. Also note that the R_f = 0.2 gain is modulated in the plateau region with a period equal to the cavity round trip light travel time. This modulation is 180^o out of phase with the modulation in intensity.

The plateau appearance of the post optimum gain diminishes as the reflectance increases. The time at which the gain falls off this plateau and turns negative decreases as R_f increases. For the low reflectance cases, non-radiative processes contribute heavily to the abrupt decline in gain. For the high reflectance case, radiative

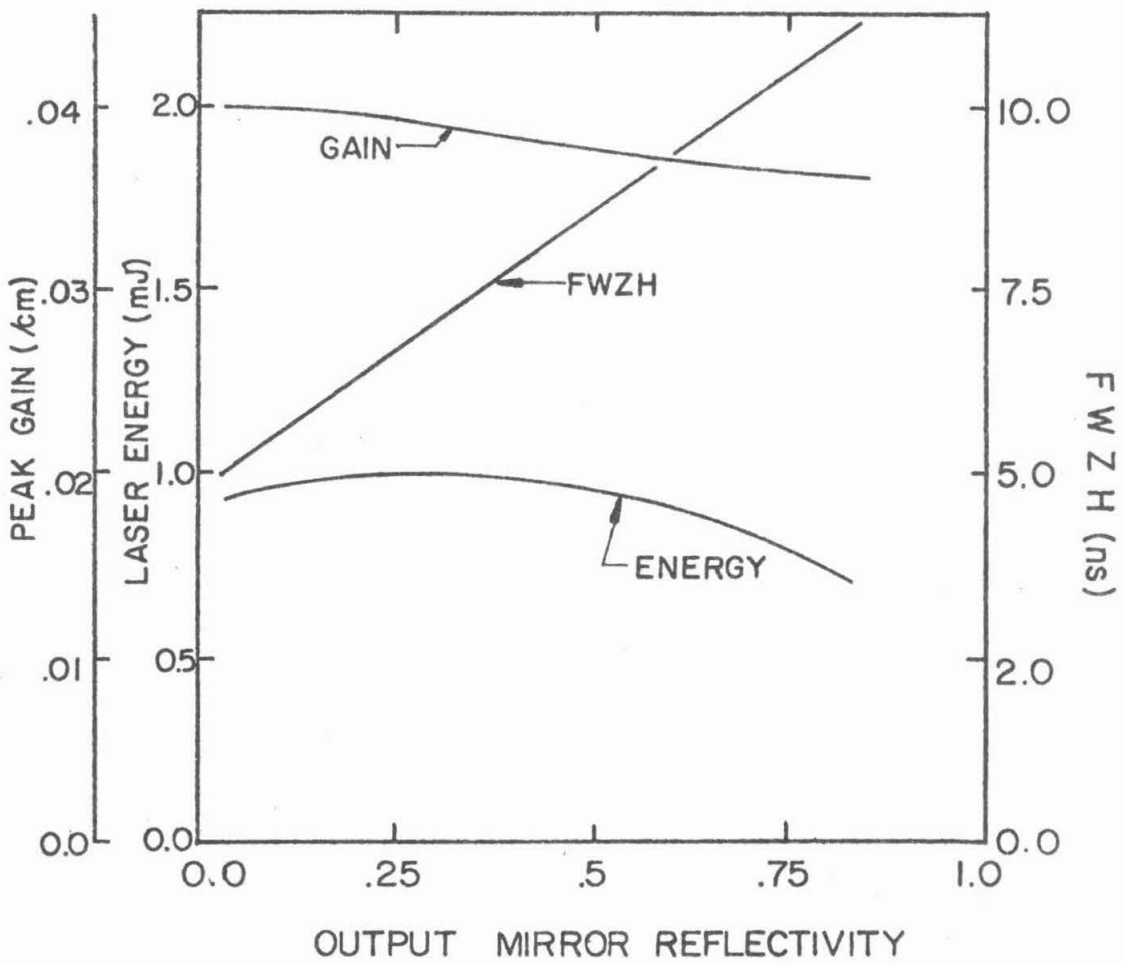

Figure VI.33. Peak gain, laser pulse energy and full width at zero height (FWZH) as a function of output mirror reflectivity. The output mirror reflectivity is the square of the field reflectance R_f.

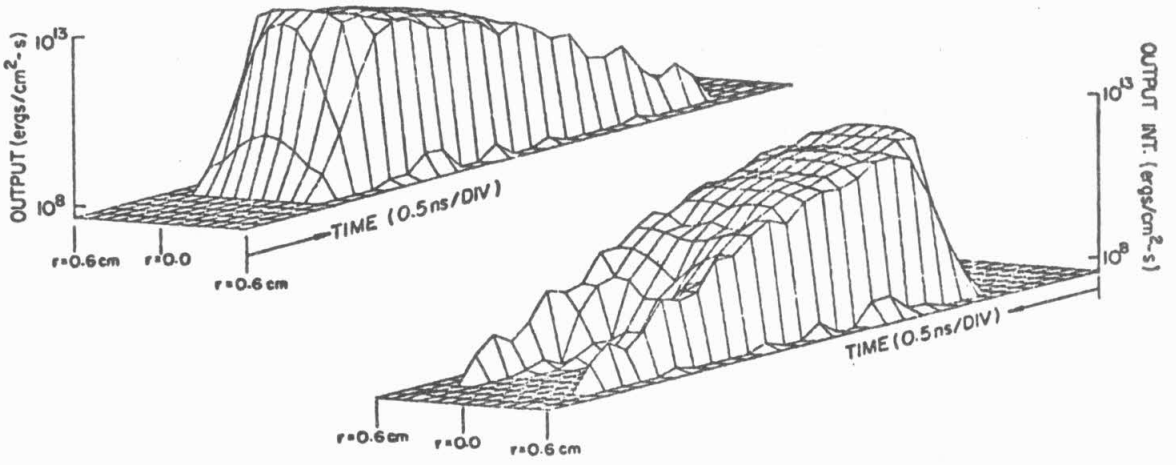

a) $R_f = 0.2$

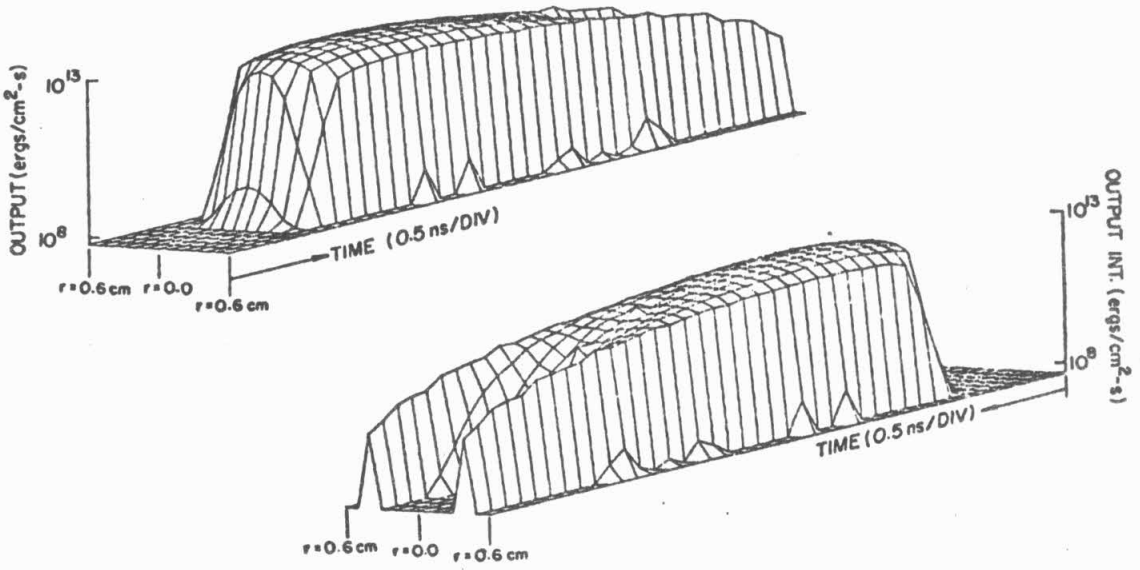

b) $R_f = 0.9$

Figure VI.34. Output laser pulse intensity as a function of time and radius.

Figure VI.35. Gain as a function of time and radius at the middle of the laser. Plotted above the midplane is log (positive gain). Plotted below the midplane is log (- negative gain).

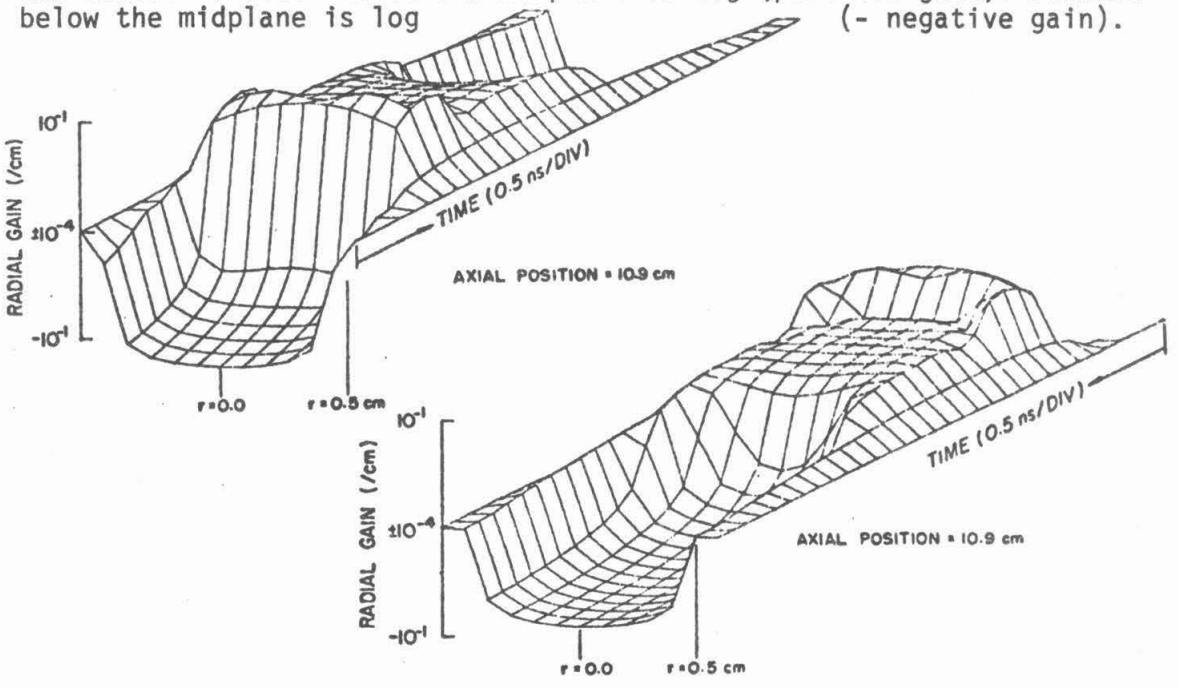

a) $R_f = 0.2$

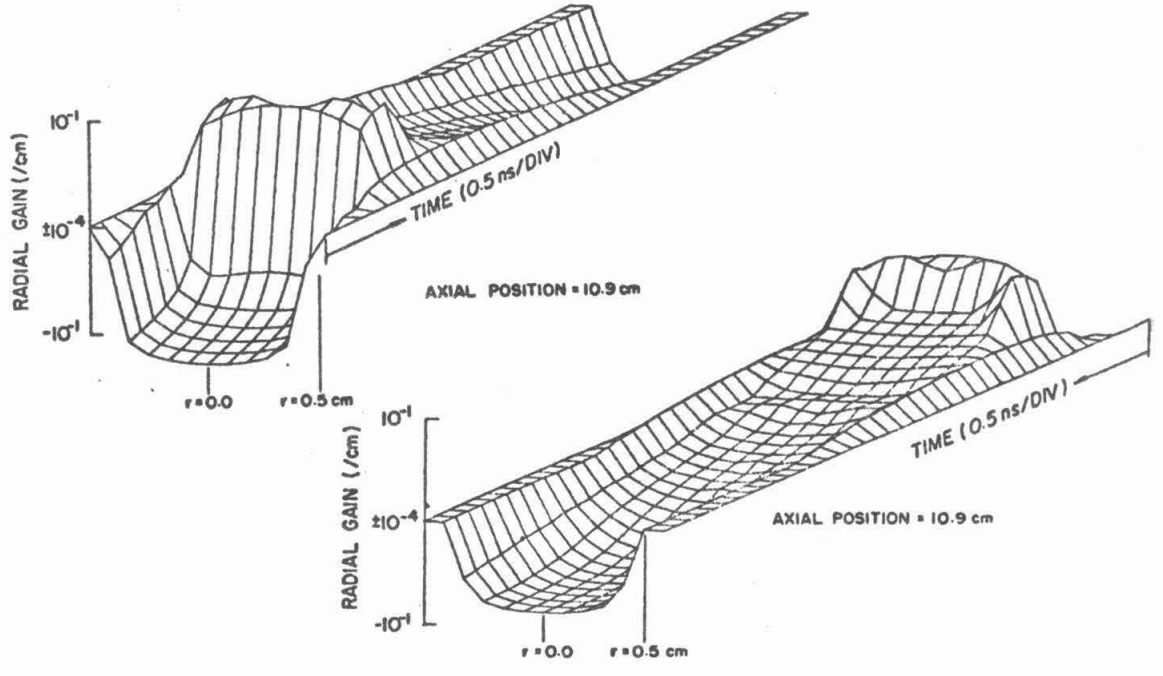

b) $R_f = 0.9$

Figure VI.36. Gain as a function of time and axial position at the center of the tube.

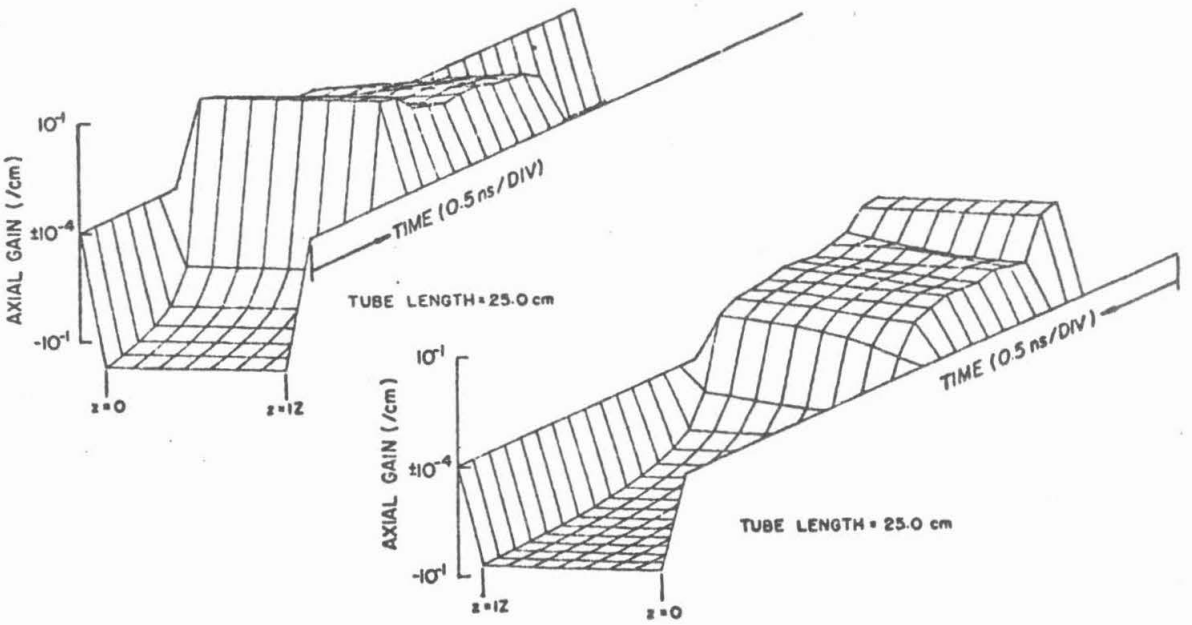

a) $R_f = 0.2$

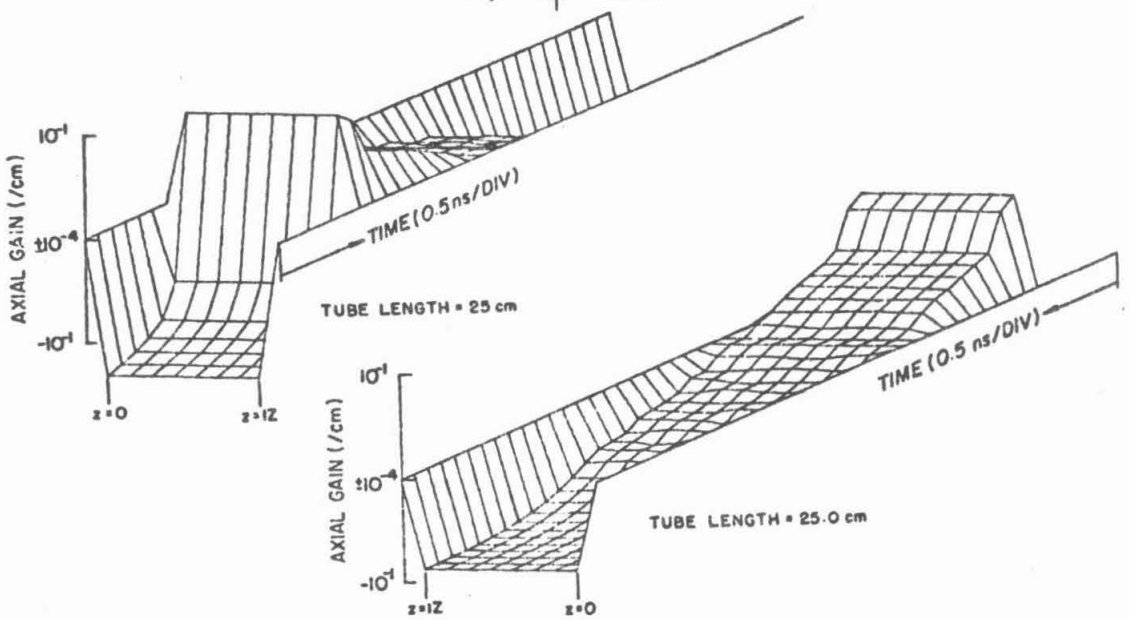

b) $R_f = 0.9$

processes dominate the behavior. Although the average intensity is lower for the high reflectance case, the pulse length is longer so that the field continues to feed on the inversion, reducing it until nonradiative factors become dominant.

As the output mirror reflectance is increased from .2 to .9, the spatial radial FWHM of the laser spot increases by 10% (see Figure VI-30). This behavior was also observed experimentally. Figure VI-37 shows the measured FWHM of the laser pulse for mirror reflectivities of 0.04 and .20 (field reflectances of .2 and .45) as a function of the time after minimum delay. For all time delays, the FWHM for the higher reflectivity exceeds that of the smaller reflectivity.

Comparing the calculated spot shape obtained here with the experimental spot shape for comparable discharge conditions, one obtains the results of Figure VI-38. The radius at which the energy density extrapolates to zero has been normalized to the experimental value. The agreement with experiment is very good for the earliest delay for which data could be taken. As the delay increases, the match degrades. (Remember that the initial conditions chosen for the calculation are for a near minimum delay.)

VI.D.3c The Influence of Radiation Trapping

The upper laser level in the copper laser is resonant with the ground state. Hence absorption of resonant spontaneous emission ("radiation trapping") can be important in excited copper vapor [VI-36]. The $^2P_{\frac{3}{2}} - {}^2D_{\frac{5}{2}}$ 5106 $\mathring{A}$ laser transition has a spontaneous emission co-

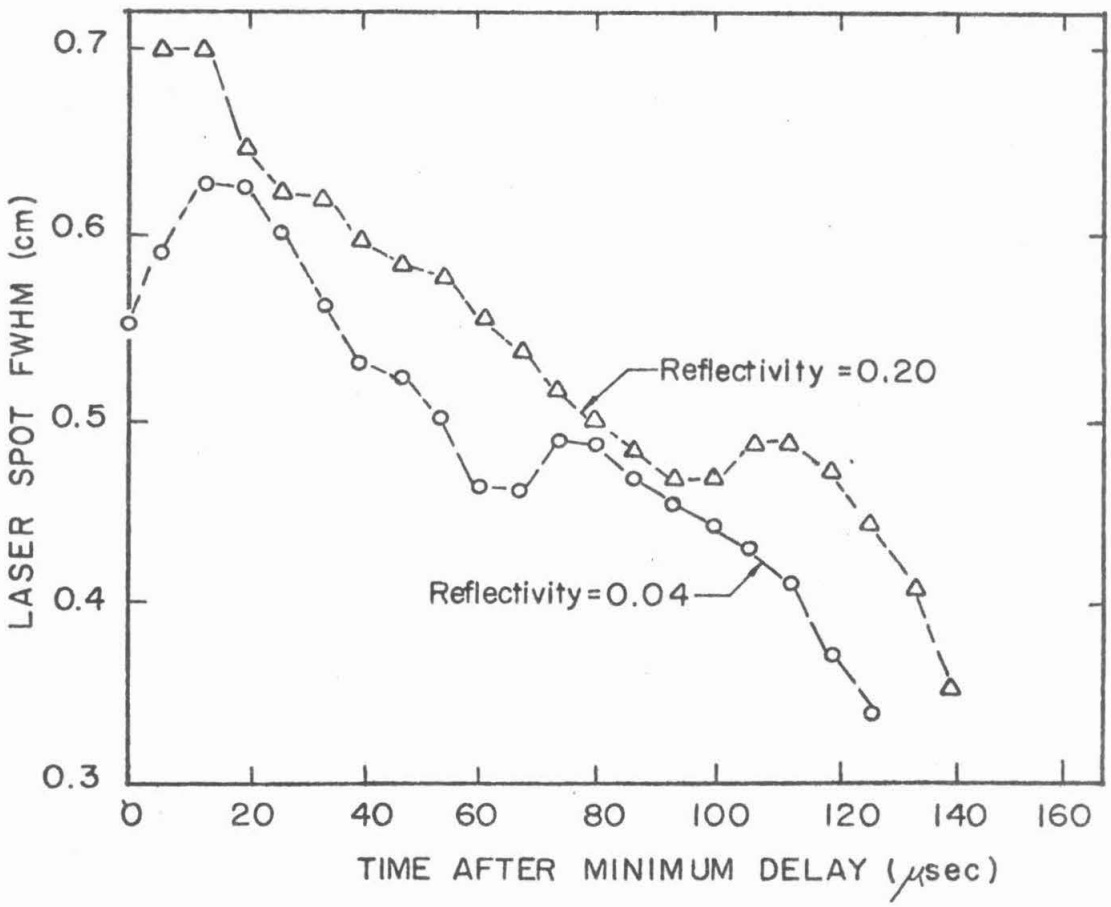

Figure VI.37. Laser spot FWHM as a function of time delay and mirror reflectivity (= R_f^2). The discharge was in 4.75 Torr of helium at 400°C. Note that at every time delay the pulse is wider for the higher reflectivity.

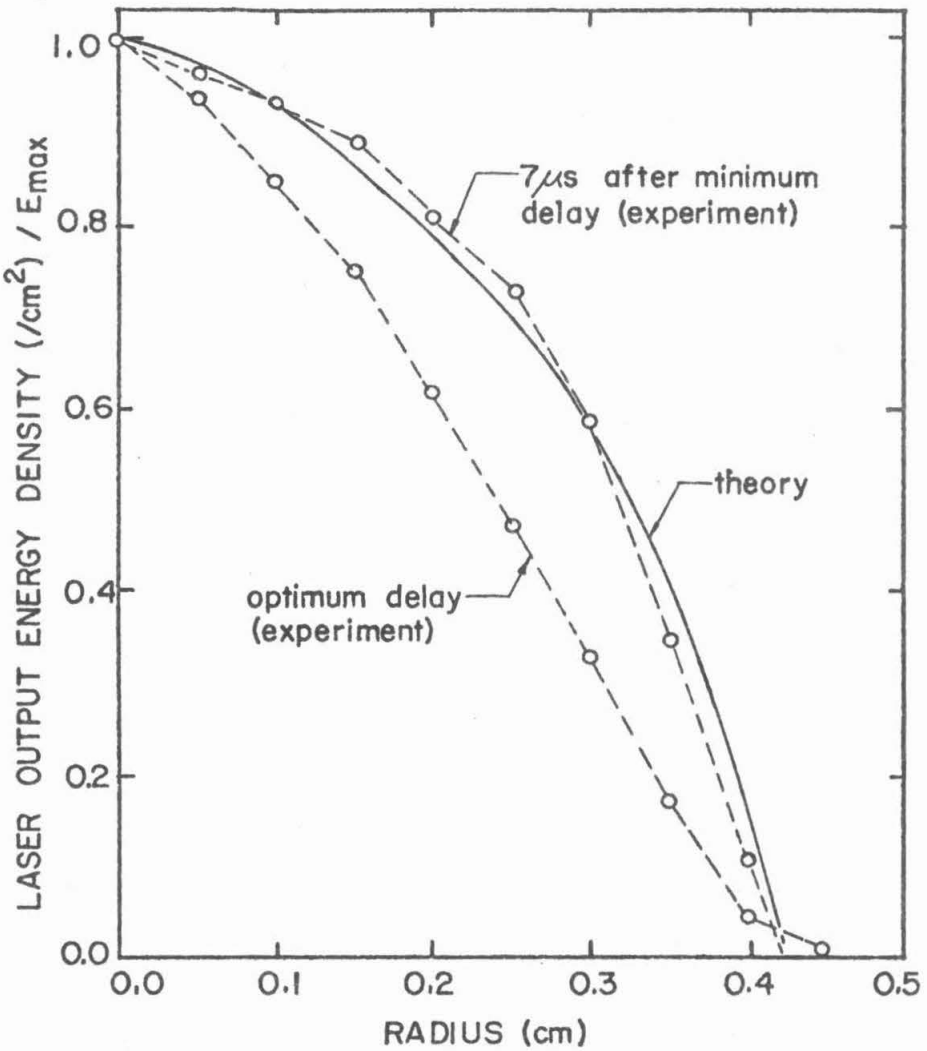

	Experiment	Theory
Buffer Gas	He	He
Pressure	4.75 Torr	5.0 Torr
Temperature	394°C	400°C
Output Mirror Reflectivity	4%	4%

Figure VI.38. The calculated laser spot compared to experiment for a near minimum time delay. The match between the calculation and experiment degrades as the time delay increases.

efficient of 1.275×10^6/sec while the resonant $^2P_{\frac{3}{2}} - {}^2S_{\frac{1}{2}}$ 3248 $\mathring{A}$ transition has a spontaneous emission coefficient of 1.025×10^8/sec [VI-56]. Since the absorption coefficient $B \sim \lambda^3 A$, then exclusive of degeneracy $B_{resonant}/B_{laser} \approx 20$. To one observing the spontaneous decay of the $^2P_{\frac{3}{2}}$ state, the effect of radiation trapping would be to decrease the effective resonant spontaneous emission coefficient. Resonant spontaneous emission from isolated atoms observed to decay as e^{-At} will decay from an ensemble of atoms as e^{-gAt} where g is a function of lineshape, density, and geometry. Values of g as low as a few times 10^{-3} are not unreasonable [VI-37,38].

Although radiation trapping has been observed in the spontaneous decay of an ensemble of excited atoms, its importance during the pumping and laser pulse can be questioned. During the pumping pulse and laser pulse, the density of the upper laser level can be approximated by

$$\frac{d}{dt}C_u = -IB(C_u - \frac{2}{3}C_L) + r_e\, n_e\, C_G - r_I\, n_e\, C_u - (A_1 + A_2)C_u \qquad \text{(VI.D.15)}$$

where

C_u = density of upper laser level (/cm^3)

C_L = density of lower laser level (/cm^3)

C_G = density of ground state (/cm^3)

I = laser pulse intensity (ergs/cm^{2}sec)

r_e = upper level electron impact excitation rate (cm^3/sec)

r_I = upper level ionization rate (cm^3/s)

n_e = electron density ($/cm^3$)

A_1, A_2 = spontaneous emission rates to the lower laser level and ground state (/sec)

Inserting typical values into (VI.D.15)

$$\frac{dC_u}{dt} \approx -1.3\times10^{-3} I(C_u - \tfrac{2}{3}C_L) + 4\times10^{7} C_G - 8\times10^{7} C_u - (A_1+A_2)C_u \qquad \text{(VI.D.16)}$$

Without radiation trapping, an intensity of only 10^{11} ergs/cm^2-sec is required for the electric field to dominate in (VI.D.16). With a "g" factor of only .3, the electron impact terms will dominate in the absence of electric field. Hence radiation trapping, so important in spontaneous decay, probably has little effect during the pumping pulse and laser pulse.

Because radiation trapping has been mentioned in connection with the copper laser, its effect was investigated. Two methods were considered. The first was to calculate explicitly the flux of resonance radiation at each point in the cavity and use this value in conjunction with the resonance radiation absorption cross section to determine the change in ground state and upper level densities. For typical ground state densities of $\approx 10^{14}/cm^3$, and a resonance absorption cross section of $\approx 3\times10^{-13} cm^2$, the photon mean free path is $\approx$ .3mm. Because the cavity grid spacing was greater than this value, no contribution could be recorded from adjacent grid points.

The second method was simply to decrease the resonance spontaneous emission coefficient in accordance with the treatment by Holstein [VI-38]. For a Doppler broadened transition in a tube of radius R,

Holstein showed that the effective spontaneous emission coefficient can be written as

$$A_{2_{effective}} = \frac{1.60A_2}{k_o R(\pi \ell n k_o R)^{1/2}} \qquad \text{(VI.D.17)}$$

where

$$k_o = \frac{\lambda_o^3 C_G}{8\pi^{3/2} V} A_2 \frac{g_u}{g_G}$$

v = atomic thermal velocity (cm/s)

g = level degeneracy

λ_o = resonance wavelength (cm)

For typical conditions, $A_{2_{effective}} \approx 1.6 \times 10^{-3} A_2$.

Using the discharge conditions in Table VI.6 and Figure VI-27, the inclusion of radiation trapping yielded a nominal change. The total laser pulse energy was lower by .1% which must be considered within the numerical roundoff error of the calculation. The peak power increased by .5%, again a small change. The length of the laser pulse (FWHM) increased by 2%.

Based on this analysis, the trapping of resonance radiation in the copper laser is not important for cases in which the cavity intensity becomes large ($\approx$10 kW/cm^2) within nanoseconds of the start of the pumping pulse. For other conditions where the pumping rates are small and the laser pulse does not appear until late into the pumping pulse, radiation trapping may play an important, but temporary role.

REFERENCES

1. A. P. Vitols and H. J. Oskam, "Reaction Rate Constant for $Ne_2^+ + 2Ne \rightarrow Ne_2^+ + Ne$", Phys. Rev. A5, 2618 (1972).

2. J. M. Berlande, R. Cheret, A. Deloche, A. Gonfalone and C. Manus, Phys. Rev. A1, 887 (1970).

3. J. N. Bardsley and M. A. Biondi, "Dissociative Recombination", Advances in Atomic and Molecular Physics 6, 1 (1970).

4. M. A. Biondi, "Recombination" in Principles of Laser Plasmas, ed. George Bekefi, Wiley Interscience, New York, 1976.

5. A. C. G. Mitchell and M. W. Zemansky, Resonance Radiation and Excited Atoms, Cambridge University Press, New York, 1971.

6. J. C. Ingraham and S. C. Brown, "Helium Afterglow and the Decay of the Electron Energy", Phys. Rev. 138, A1015 (1965).

7. I. Ya. Fugol, O. N. Grigorashchenko, and D. A. Myshicis, "Experimental Investigation of the Destruction of Metastable Atoms of Helium in a Plasma at Low Temperature", Sov. Phys. JETP 33, 227 (1971).

8. C. Sol, F. Devos, and J. C. Gauthier, "Elastic Electron-neutral Interaction Measurements in Neon at Ultralow Energies", Phys. Rev. A12, 502 (1975).

9. N. B. Kolokolov, R. I. Lyagushchenko, and P. M. Pramatarov, "Electron Energy Distribution in an Afterglow IV. Rate Constant for the Reaction $He(2^3S_1 + e \rightarrow He\ (1^1S_0) + \vec{e}$", Sov. Phys. Tech. Phys. 22, 1225 (1977).

10. S. C. Brown, Basic Data of Plasma Physics, MIT Press/Wiley, Massachusetts, 1959.

11. M. A. Biondi, "Diffusion Cooling of Electrons in Ionized Gases", Phys. Rev. 93, 1136 (1954).

12. J. O. Hirschfelder, C. F. Curtiss, and R. B. Bird, Molecular Theory of Gases and Liquids, Wiley, New York, 1954.

13. J. Crank, The Mathematics of Diffusion, Clarendon Press, Oxford, 1975.

14. K. Matsumoto, California Institute of Technology Computer Center (unpublished), 1976.

15. J. Tenenbaum, I. Smilanski, S. Gabay, G. Erez, and L. A. Levin, "Time Dependence of Copper-atom Concentration in Ground State and Metastable States in a Pulsed CuCl Laser", J. Appl. Phys. 49, 2662 (1978).

16. L. Brewer, N. L. Lofgren, "The Thermodynamics of Gaseous Cuprous Chloride, Monomer and Trimer", J. Am. Chem. Soc. 72, 3038 (1950).

17. J. Tenenbaum, I. Smilanski, S. Gabay, G. Erez, L. A. Levin, J. Katriel, and Shammai Speiser, "Buffer Gas Effect on Ground and Metastable Populations in a Pulsed CuBr Laser", IEEE J. Quant. Electronics, QE-14, 680 (1978).

18. H. V. Lilenfeld, R. F. Webbink, W. Q. Jeffers, and J. D. Kelley, "Modeling of the CW CO Chemical Laser", IEEE J Quant. Electronics QE-11, 660 (1975).

19. J. H. Kiefer, "The Recombination of O Atoms at High Temperatures

as Measured by Shock Tube Densitometry", Nuclear Science Abstracts 18, Abstract 202 (1964).

20. N. M. Nerheim, "A Parametric Study of the Copper Chloride Laser", J. Appl. Phys. 48, 1186 (1977).

21. C. S. Liu, D. W. Feldman, J. L. Pack, and L. A. Weaver, "Copper Halide Laser Research: Final Report", Westinghouse R & D Center, Pittsburgh, Pennsylvania, December, 1977.

22. A. G. Gridnev, T. M. Gorbunova, V. F. Elaev, G. S. Evtushenko, N. V. Osipova, and A. N. Soldatov, "Spectroscopic Investigation of a Gas Discharge Pulse Plasma of a Cu + Ne Laser", Sov. J. Quant. Electronics 8, 656 (1978).

23. M. Brandt and J. A. Piper, "Improved Dissociation Efficiency in TE Pulsed Copper Halide Lasers", Proc. SPIE Lasers '78, Orlando, Florida, 1978.

24. L. B. Loeb, Basic Properties of Gaseous Electronics, University of California Press, Berkeley, 1960.

25. J. W. Cooper and J. B. Martin, "Electron Photodetachment from Ions and Elastic Collision Cross Sections for O, C, Cl and F", Phys. Rev. 126, 1482 (1962).

26. E. W. McDaniel, Collision Phenomena in Ionized Gases, Wiley, New York, 1964.

27. H. D. Hagstrun and J. T. Tate, "Ionization and Dissociation of Diatomic Molecules by Electron Impact", Phys. Rev. 59 354 (1941).

28. G. J. Shulz, "Cross Sections and Electron Affinity for O^- Ions

from O_2, CO and CO_2 by Electron Impact", Phys. Rev. 128, 178 (1962).

29. A. N. Prasad and J. D. Craggs, "Attachment and Ionization Coefficients", in Atomic and Molecular Processes, ed. D. R. Bates, Academic Press, New York, 1962.

30. J. D. Craggs and B. A. Tozer, "The Attachment of Slow Electrons in Carbon Monoxide", Proc. Roy. Soc. A247, 337 (1958).

31. B. H. Mahan, College Chemistry, Addison-Wesley, Reading, Massachusetts, 1966.

32. G. C. Tiscone and L. M. Branscomb, "Detachment from H^- and O^- by Electron Impact", Phys. Rev. 170, 169 (1968).

33. E. E. Ferguson, F. C. Fehsenfeld, and A. L. Schmeltekopf, Advances in Chemistry Series 80, 83 (1969).

34. E. W. McDaniel, V. Cermak, A. Dalgarno, E. E. Ferguson, and L. Friedman, Ion Molecule Reactions, Wiley-Interscience, New York, 1970.

35. S. Gabay, I. Smilanski, L. A. Levin, and G. Erez, "Comparison of CuCl, CuBr, and CuI as Lasants for Copper-vapor Lasers", IEEE J. Quant. Electronics QE-13, 364 (1977).

36. C. S. Liu, E. W. Sucov, and L. A. Weaver, "Copper Superradiant Emission from Pulsed Discharges in Copper Iodide Vapor", Appl. Phys. Letters 23, 92 (1973).

37. T. Holstein, "Imprisonment of Resonance Radiation in Gases", Phys. Rev. 72, 1212 (1947).

38. T. Holstein, "Imprisonment of Resonance Radiation in Gases II", Phys. Rev. 83, 1159 (1951).

39. C. Deutsch, "Excitation and Ionization of Neutral Atoms in a Dense Discharge", J. Appl. Phys. 44, 1142 (1973).

40. S. Trajmar, W. Williams, and S. K. Srivastava, "Electron-impact Cross Sections for Cu Atoms", J. Phys. B10, 3323 (1977).

41. W. L. Borst, "Excitation of Metastable Argon and Helium Atoms by Electron Impact", Phys. Rev. A9, 1195 (1974).

42. D. R. Bates and A. Dalgarno, "Electronic Recombination" in Atomic and Molecular Processes, D. R. Bates, ed., Academic, New York, 1962.

43. P. L. Herman, J. Seguier, and R. Herman, "Processus D'Emission Daus La Phosphorecescene de L'Argon", Le Journal de Physic et le Radium 19, 463 (1958).

44. N. M. Nerheim, "Measurements of Copper Ground State and Metastable Level Populations in a Copper-chloride Laser", J. Appl. Phys. 48, 3244 (1977).

45. G. J. Collins, R. C. Jensen, and W. R. Bennet, "Charge-exchange Excitation in the He-Cd Laser", Appl. Phys. Letters 19, 125 (1971).

46. T. Shay, H. Kano, and G. J. Collins, "Excitation Mechanism of the He-I^+ Laser", Appl. Phys. Letters 26, 531 (1975).

47. H. Kano, T. Shay, and G. J. Collins, "A Second Look at the Excitation Mechanism of the He-Hg^+ Laser", Appl. Phys. Letters 27, 610 (1975).

48. D. J. Dyson, "Mechanisms of Population Inversion in the Mercury Ion Laser" Nature 207, 361 (1965).

49. E. L. Duman and B. M. Smirnov, "Tables of Cross Sections for Ion-Atom Resonant Charge Exchange", High Temperature 12, 431 (1974).

50. A. G. Fox and T. Li, "Resonant Modes in a Maser Interferometer", BSTJ 40, 453 (1961).

51. R. Shuker, Y. Binur, and A. Szohe, "Studies of Afterglows in Noble-Gas Mixtures: A Model for Energy Transfer in He/Xe^+", Phys. Rev. A12, 515 (1975).

52. F. C. Fehsenfeld, A. L. Schmeltekopf, P. D. Goldan, H. I. Schiff, and E. E. Ferguson, "Thermal Energy Ion-Neutral Reaction Rates I, Some Reactions of Helium Ions", J. Chem. Phys. 44, 4087 (1966).

53. L. Friedman and T. F. Moran, "Small-Cross-Section Exothermic Ion-Molecule Reactions He^+-H_2, Ne^+-H_2", J. Chem. Phys. 42, 2624 (1965).

54. M. A. Biondi and L. M. Chanin, "Mobilities of Atomic and Molecular Ions", Phys. Rev. 94, 910 (1954).

55. M. A. Biondi, "Diffusion, De-excitation and Ionization Cross Sections for Metastable Atoms I", Phys. Rev. 88, 660 (1952).

56. C. H. Corliss and W. R. Bozman, Experimental Transition Probabilities for Spectral Lines of Seventy Elements, U.S. Dept. of Commerce, NBS Monograph 53, 1962.

VII. CONCLUDING REMARKS

The Cu/CuCl double pulse laser was investigated experimentally and numerically. Because of the short duration of the laser pulse, and because the laser pulse appears at the leading edge of the pumping pulse, processes which occur at thermal speeds cannot significantly effect laser energy during the pumping pulse. For a given density of ground state and metastable copper present at the beginning of the pumping pulse, laser pulse energy is determined by how rapidly the upper level can be populated before the cavity intensity dumps the upper laser level. This gain switching explains the dependence of laser pulse energy on the rate at which pumping pulse current rises, and the relative independence of laser pulse energy on mirror reflectivity. This behavior also helps to explain the difficulty encountered in trying to scale the copper laser to larger dimensions. Small inhomogeneities in the discharge and dimensions becoming large in directions other than the optical axis will trigger this gain switching prematurely. As a result, an oscillator amplifier arrangement is probably the only practical means of obtaining more than a few millijoules per pulse from the copper laser.

The characteristics of the pumping pulse (e.g., peak current, rate of current rise) are a sensitive function of time delay. This behavior is believed to be due to the initial conditions (principally ambient electron density) provided by the interpulse afterglow. The numerical model, which incorporated this assumption, reproduced the experimentally observed relationships between the laser pulse, time

delay and pumping pulse.

The interpulse afterglow not only provides initial conditions for the pumping pulse but also determines the ratio of ground state copper to metastable state copper. Therefore "conditioning" this period for optimum initial conditions and copper density ratios is the key to more efficient laser performance. The necessity to provide optimum initial conditions is emphasized by the fact that peak power is obtained at a shorter time delay than optimum energy; a delay when pumping rates are larger. From the numerical model, we have seen that the ground state copper density is often maximum at times prior to the optimum delay, and that metastable copper densities as small as 5% can prevent laser oscillation. Hence to improve efficiency, one must increase the rate at which metastable copper relaxes, or decrease the rate at which the metastables are created. The latter can be accomplished by maintaining the interpulse afterglow so that contributions to the metastable state from collisional radiative recombination are eliminated. A second alternative is to minimize the energy excess in the dissociation of CuCl by tailoring the dissociation pulse to be long and low energy. The smaller electron energy excess during a dissociation will result in a lower rate of forming metastable copper. The ideal dissociation pulse would have a long tail lasting tens or hundreds of microseconds. By using a hollow cathode or a set of closely spaced transverse electrodes, the Faraday dark space and the negative glow will dominate the quasi-cw discharge. Average electron energy is low, and the electron density (negative charge

carrier) is high, providing suitable initial conditions for the pumping pulse.

The results of the computer models confirmed that processes which directly effect the density of metastable copper (e.g., collisional relaxation) have a greater effect on laser energy than indirect processes such as the reassociation of CuCl. As a result, Penning ionization and charge exchange reactions during the afterglow may be beneficial. We have already seen that cross sections for the dissociative Penning and charge exchange reactions are large. Let r_1 be the Penning or charge exchange rate for a reaction with atomic copper, and let r_2 be the rate for the reaction with CuCl. Assume that on the average, half of the reactions with CuCl ionize a copper atom. If α_1 is the fraction of metastable atoms obtained from a CuCl electron impact dissociation and α_2 the fraction obtained from a Penning or charge exchange reaction, then the noble gas reactions are beneficial provided that

$$\frac{r_2}{2r_1}(1-\alpha_2) > \frac{N_{Cu}}{N_{CuCl}}\frac{\alpha_2}{\alpha_1}$$

During the time that the densities of noble gas ions and metastables are large $N_{Cu}/N_{CuCl} < 1$.

The presence of the negative ion is beneficial in that neutralizing collisions can consume a positive copper ion which would otherwise recombine and contribute to the metastable state. It is detrimental in that the electron density is reduced and the initial condi-

tions for the pumping pulse are less favorable. Because the negative ion is lost primarily by diffusion, its presence is not beneficial.

The experimental work, and in particular the numerical results must be considered generic for metallic halide systems. Rate constants and cross sections are not known well so that differentiating between CuCl and CuBr on the basis of dissociation energy is not justified. The fact that many experimental results were reproduced with the model assures us that the appropriate processes were included. For more definitive results, the rate constants must be known more accurately.

APPENDIX A. THE DOUBLE-PULSE POWER SUPPLY

A schematic of the double pulse power supply is shown in Figure A-1. The power supply consists of two identical circuits (with the possible exception of component values). Each circuit can operate independently, thereby allowing an arbitrary time delay between pulses. Note the use of two thyratrons in each circuit. The hold-off thyratron isolates the second discharge circuit from the broken down laser tube, preventing the switching thyratron from firing. The charging resistance R_{C1} is typically .9 - 1.0 MΩ, while R_{C3} is typically .1 MΩ. The resistance R_{C2} is nominal (30Ω). The bias capacitor is 500 pF while the discharge capacitors C1 and C2 are typically 1-20 nF.

Examining the first pulse, the high voltage power supply charges C1 to a preselected voltage (10 - 20 kV). A trigger signal is sent to the thyratron trigger power supply thereby firing the switching thyratron S1. C1 begins to discharge through the nominal resistance R_{C2} and the grid bias capacitor. The voltage drop across R_{C2} is seen by the hold-off thyratron grid thereby firing the thyratron. The voltage on C1 is now seen by the laser tube, initiating breakdown. A preselected time later, the process is repeated for the second pulse.

The optional inductance L1 is sometimes required to slow the charging of C1, thereby enabling the hold off thyratron to shut off.

Repetition rates of 200 Hz are conveniently handled by this circuit.

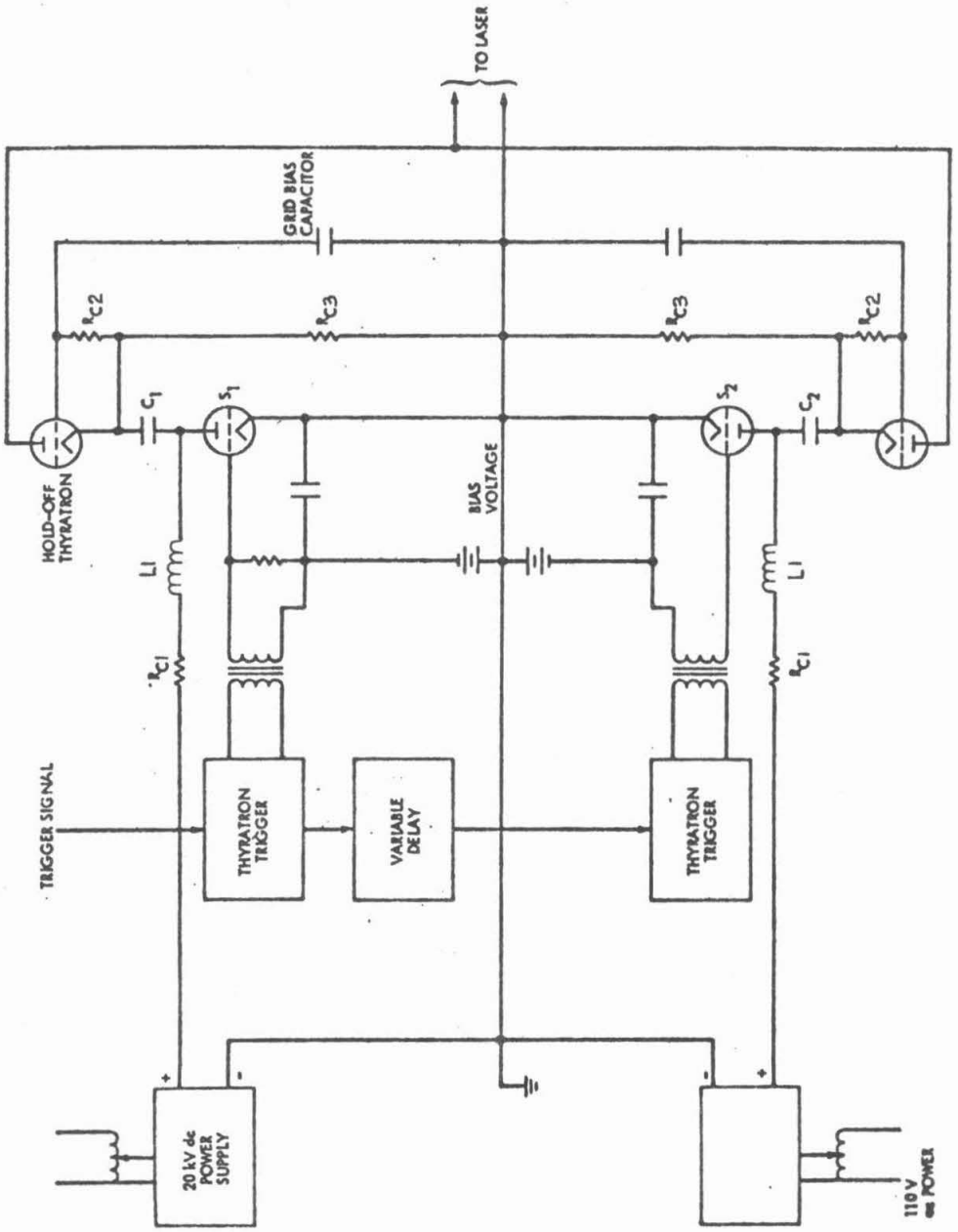

Figure A.1. Schematic of the double pulse power supply. The thyratons were EG&G #7322/1802.

APPENDIX B. THE CO_2 LASER INTERFEROMETER

In this appendix the testing criteria for the CO_2 laser interferometer will be derived. It was shown in Section II.B that the number of cycles of modulation experienced by the CO_2 laser signal for a change in effective discharge cavity length of Δd in a time $\Delta t = t - t_o$ is

$$\chi = \Delta d \frac{2s}{\lambda} \tag{B.1}$$

Consider a disc rotating at angular speed ω of thickness b, and index of refraction n placed in the discharge cavity. The CO_2 laser beam is incident off axis. (See Figure B-1). The rate at which the laser beam path length through the disc changes as the disc rotates is

$$\frac{d\ell}{dt} = \frac{d}{dt}\left(\frac{b}{\cos\alpha}\right) = \frac{b \sin\alpha}{\cos^2\alpha} \frac{d\alpha}{dt} \tag{B.2}$$

where the instantaneous path length

$$\ell = \frac{b}{\cos\alpha} \tag{B.3}$$

From Snell's law $\sin\alpha = \sin\theta/n$ so that (B.2) becomes

$$\frac{d\ell}{dt} = \frac{\omega b n \sin 2\theta}{2(n^2 - \sin^2\theta)^{3/2}} \tag{B.4}$$

where

$$\frac{d\alpha}{dt} = \frac{d\theta}{dt} \frac{\cos\theta}{n\cos\alpha} = \frac{\omega\cos\theta}{n\cos\alpha} \tag{B.5}$$

For a rotation from $-\theta_o$ to θ_o, the effective cavity length will change by an amount

$$\Delta d = \int_0^{\theta_o} \frac{bns\sin 2\theta}{(n^2-\sin^2\theta)^{3/2}}\, d\theta - \int_0^{\theta_o} \frac{bs\sin 2\theta}{(1-\sin^2\theta)^{3/2}}\, d\theta \qquad \text{(B.6)}$$

where the second term in (B.6) is the "empty cavity" contribution. For 10.6 μm radiation in NaCl, $n \simeq 1.5$ [B-1]. For $b = .64$ cm, $s = 4$, and $\theta_o = \frac{\pi}{4}$, from (A.6)

$$\Delta d \simeq .01 \text{ cm}$$

so that

$$\chi \simeq 80$$

For an angular speed of $\omega \simeq 10\pi$/sec, "fringes" should be produced at the rate of 400/s. This was the approximate rate observed when a NaCl flat was rotated in the discharge cavity of the CO_2 laser interferometer.

REFERENCES

B-1. A. Smakula, C. F. Swinehart, G. Whitaker, E. W. O'Dell, and R. W. Johnson, Harshaw Optical Crystals, Harshaw Chemical Company, Crystal and Electronic Products Department, Los Angeles, 1967.

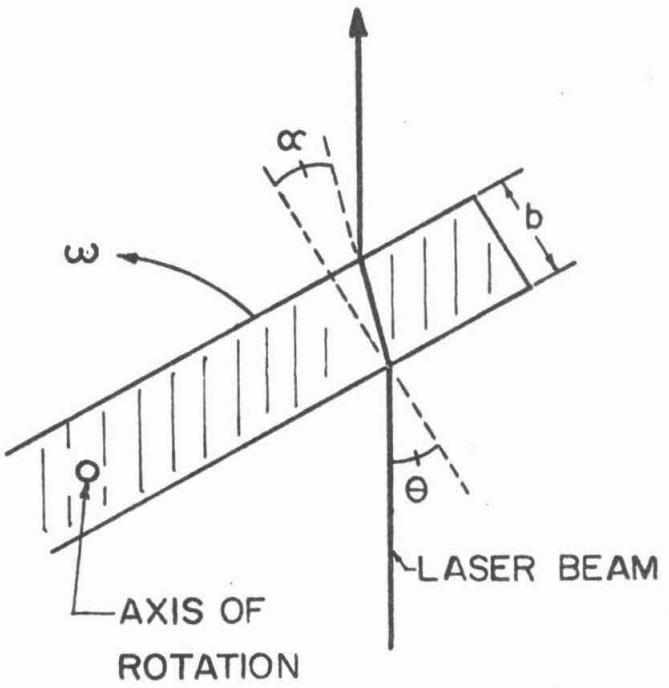

Figure B.1. A disc of thickness b and index of refraction n is rotated in the discharge cavity at angular frequency ω. The CO_2 laser beam is incident off-axis.

APPENDIX C. JUSTIFICATION OF THE ASSUMPTION THAT THE DISCHARGE TUBE IS IN QUASI-EQUILIBRIUM DURING HEATING AND COOLING

In this appendix we will show that during the interferometer electron density measurements, the discharge tube was in thermal equilibrium. Electron density measurements were made periodically while the discharge tube slowly heated up and cooled down. The tube temperature was measured with a thermocouple on the exterior surface of the discharge tube and was assumed to be the instantaneous value. This assumption is justified as follows.

The thermocouple was placed in a length of quartz tubing which was in contact with the discharge tube itself. The thickness of the two tubes were comparable, so the temperature indicated by the thermocouple can be assumed to be nearly equal to that on the inside surface of the discharge tube. The initial radial temperature profile of the discharge tube was uniform at room temperature and can arbitrarily be set equal to zero. The temperature in the discharge tube (diameter d) at a given radius r and time t is given by [C-1]

$$T - c(t - \frac{((\frac{d}{2})^2 - r^2)}{4\kappa} + \frac{4c}{d\kappa} \sum_{n=1}^{\infty} e^{-\kappa\alpha_n^2 t} \frac{J_o(r\alpha_n)}{\alpha_n^3 J_i(\frac{d}{2}\alpha_n)} \qquad (C.1)$$

where κ = thermal diffusivity of the gas (cm^2/sec)

J_i = Bessel function of order i

$\alpha_n = \frac{2\gamma_n}{d}$

γ_n = nth zero of the J_o Bessel function

The tube temperature at the inner tube surface is assumed to vary as ct. Since there is no net gas flow through the tube (see Section II.C.3) a purely conductive approximation has been made. Constant thermal conductivity has also been assumed. For neon at 400°C and 5.0 Torr, $\kappa \approx 240$ cm^2/sec [C-2,3]. The discharge tube heats up 400°K in an hour so that $c \approx .1$°K/sec. Hence for a tube diameter of 2.54 cm, (C.1) becomes

$$T = .1(t-1.68\text{x}10^{-3} + \frac{r^2}{960}) + 1.6\text{x}10^{-4} \sum_{n=1}^{\infty} \exp(-240\alpha_n^2 t) \frac{J_o(r\alpha_n)}{\alpha_n^3 J_1(\frac{d}{2}\alpha_n)} \qquad (C.2)$$

Clearly for times greater than a few seconds, the temperature is independent of r and (C.2) can be written as

$$T = .1t \approx ct \qquad (C.3)$$

Hence a quasi-equilibrium approximation is justified.

REFERENCES

1. H. S. Carslow and J. C. Jaeger, "Conduction of Heat in Solids", Clarendon Press, Oxford, 1959.
2. A. C. Jenkins and G. A. Cook, "Gas Phase Properties" in Argon, Helium, and the Rare Gases, G. A. Cook, ed., Interscience Publishers, New York, 1961.
3. J. O. Hirschfelder, C. F. Curtiss, and R. B. Bird, Molecular Theory of Gases and Liquids, Wiley, New York, 1954.

APPENDIX D. DIFFUSION COOLING

In this appendix, an expression for the time rate of change in electron temperature due to ambipolar diffusion will be derived.

Let $n = n(\varepsilon,r)$ be the density of electrons with energy in $(\varepsilon,\varepsilon+d\varepsilon)$ with radius in $(r,r+dr)$. Let $n_T \equiv n_T(r)$ be the total electron density with radius in $(r,r+dr)$. Let $D \equiv D(\bar{\varepsilon},r)$ be the energy dependent diffusion constant at r for the average electron energy $\bar{\varepsilon}$. The time rate of change in n due to diffusion (assuming azimuthal symmetry) is

$$\frac{\partial n}{\partial t} = \nabla\cdot(D\nabla n) = \frac{D}{r}\frac{\partial n}{\partial r} + D\frac{\partial^2 n}{\partial r^2} + \frac{\partial D}{\partial r}\frac{\partial n}{\partial r} \tag{D.1}$$

Let

$$n(\varepsilon,r) = f(\varepsilon,r)\ n_T(r) \tag{D.2}$$

where $f(\varepsilon,r)$ is the electron distribution function so that (D.1) becomes

$$\frac{\partial n}{\partial t} = n_T\frac{\partial f}{\partial t} + \frac{\partial n_T}{\partial t}\ f = (n_T\frac{\partial f}{\partial r} + \frac{\partial n_T}{\partial r}\ f)(\frac{D}{r} + \frac{\partial D}{\partial r})$$

$$+ D(2\ \frac{\partial n_T}{\partial r}\ \frac{\partial f}{\partial r} + n_T\frac{\partial^2 f}{\partial r^2} + f\ \frac{\partial^2 n_T}{\partial r^2}) \tag{D.3}$$

Solving (D.3) for $\frac{\partial f}{\partial t}$,

$$\frac{\partial f}{\partial t} = -\frac{f}{n_T}\frac{\partial n_T}{\partial t} + (\frac{\partial f}{\partial r} + \frac{f}{n_T}\frac{\partial n_T}{\partial r})(\frac{D}{r} + \frac{\partial D}{\partial r})$$

$$+ \frac{D}{n_T}(2\ \frac{\partial n_T}{\partial r}\ \frac{\partial f}{\partial r} + n_T\ \frac{\partial^2 f}{\partial r^2} + f\ \frac{\partial^2 n_T}{\partial r^2}) \tag{D.4}$$

The electron distribution function is assumed to be Maxwellian at all times. Expressing energy ε and temperature T_e in eV,

$$f(\varepsilon) = \alpha \frac{\varepsilon^{1/2}}{T_e^{3/2}} e^{-\varepsilon/T_e} \quad , \tag{D.5}$$

where $\alpha = \frac{2}{\pi^{1/2}}$

For constant ε, differentiating (D.5) yields

$$\frac{\partial f}{\partial r} = f \frac{\partial T_e}{\partial r}\left(\frac{\varepsilon}{T_e^2} - \frac{3}{2T_e}\right) \tag{D.6}$$

$$\frac{\partial^2 f}{\partial r^2} = f\left[\left(\frac{\partial T_e}{\partial r}\right)^2 \left(\frac{\varepsilon^2}{T_e^4} - \frac{5\varepsilon}{T_e^3} + \frac{15}{4T_e^2}\right) + \frac{\partial^2 T_e}{\partial r^2}\left(\frac{\varepsilon}{T_e^2} - \frac{3}{2T_e}\right)\right] \tag{D.7}$$

The average energy at r is defined as

$$\bar{\varepsilon}(r) = \int_0^\infty \varepsilon f(\varepsilon, r)\, d\varepsilon \tag{D.8}$$

so that

$$\frac{\partial \bar{\varepsilon}(r)}{\partial t} = \int_0^\infty \varepsilon \frac{\partial f}{\partial t}(\varepsilon, r)\, d\varepsilon \tag{D.9}$$

Therefore using (D.6) and (D.7) in (D.4), multiplying by ε, and integrating from 0 to ∞,

$$\frac{\partial \bar{\varepsilon}}{\partial t} = \bar{\varepsilon}\Big[\frac{1}{n_T}\Big(D \frac{\partial^2 n_T}{\partial r^2} - \frac{\partial n_T}{\partial t} + \frac{\partial n_T}{\partial r}\Big(\frac{D}{r} + \frac{\partial D}{\partial r}\Big)$$

$$- \frac{3}{2T_e} \frac{\partial T_e}{\partial r}\Big(\frac{2D}{n_T} \frac{\partial n}{\partial r} + \frac{D}{r} + \frac{\partial D}{\partial r}\Big) - \frac{3D}{2T_e} \frac{\partial^2 T_e}{\partial r^2} + \frac{15D}{4T_e^2}\Big(\frac{\partial T_e}{\partial r}\Big)^2\Big]$$

$$+ \frac{\alpha \partial T_e}{\partial r}\left(\frac{2D}{n_T}\frac{\partial n}{\partial r} + \frac{D}{r} + \frac{\partial D}{\partial r}\right) \int_o^\infty \frac{\varepsilon^{5/2}}{T_e^{7/2}} e^{-\varepsilon/T_e}\, d\varepsilon$$

$$+ D\alpha\left[\left(\frac{\partial T_e}{\partial r}\right)^2 \int_o^\infty \left(\frac{\varepsilon^{7/2}}{T_e^{11/2}} - \frac{5\varepsilon^{5/2}}{T_e^{9/2}}\right) e^{-\varepsilon/T_e}\, d\varepsilon\right.$$

$$\left. + \frac{\partial^2 T_e}{\partial r^2} \int_o^\infty \frac{\varepsilon^{5/2}}{T_e^{7/2}} e^{-\varepsilon/T_e}\, d\varepsilon\right] \qquad (D.10)$$

Remembering that $\bar{\varepsilon} = \frac{3}{2} T_e$ and $\int_o^\infty \varepsilon^{P-\frac{1}{2}} e^{-\varepsilon/T_e}\, d\varepsilon = \frac{(2p-1)\cdot\cdot 5\cdot 3\cdot 1\sqrt{\pi}}{2^P} T_e^{P+\frac{1}{2}}$

(D.10) becomes

$$\frac{\partial T_e}{\partial t} = \frac{\partial T_e}{\partial r}\left(\frac{2D}{n_T}\frac{\partial n_T}{\partial r} + \frac{D}{r} + \frac{\partial D}{\partial r}\right) + D\frac{\partial^2 T_e}{\partial r^2}$$

$$+ \frac{T_e}{n_T}\left(D\frac{\partial^2 n_T}{\partial r^2} \frac{\partial n_T}{\partial t} + \frac{\partial n_T}{\partial r}\left(\frac{D}{r} + \frac{\partial D}{\partial r}\right)\right) \qquad (D.11)$$

The diffusion constant $D = \frac{D_a}{2}\left(1 + \frac{T_e}{T_{gas}}\right)$ where D_a is the ambipolar diffusion constant at thermal equilibrium. Assume a constant gas temperature so that $\frac{\partial D}{\partial r} = \frac{D_a}{2T_g}\frac{\partial T_e}{\partial r}$. The final expression now becomes

$$\frac{\partial T_e}{\partial t} = \frac{D_a}{2}\left[\left(1 + \frac{T_e}{T_g}\right)\left[\frac{\partial T_e}{\partial r}\left(\frac{2}{n_T}\frac{\partial n_T}{\partial r} + \frac{1}{r}\right) + \frac{T_e}{n_T}\frac{\partial^2 n_T}{\partial r^2} + \frac{\partial^2 T_e}{\partial r^2}\right.\right.$$

$$\left.\left. + \frac{T_e}{r n_T}\frac{\partial n_T}{\partial r}\right] + \frac{1}{T_g}\frac{\partial T_e}{\partial r}\left(\frac{\partial T_e}{\partial r} + \frac{T_e}{n_T}\frac{\partial n_T}{\partial r}\right)\right] - \frac{T_e}{n_T}\frac{\partial n_T}{\partial t} \qquad \text{(D.12)}$$

With the spatial derivatives expressed in finite difference form, (D.12) can be placed in equation VI.B.10 to represent the change in electron temperature due to diffusion.

APPENDIX E. OBTAINING CONSISTENT ELECTRON TEMPERATURES FOR THE DISSOCIATION PULSE

In this appendix, consistent electron temperatures for the dissociation pulse will be derived for a given change in buffer gas pressure. This will be done by considering a discharge through the pure buffer gas.

We have the setup depicted in Figure E-1. A capacitor of capacitance C, initially charged to voltage V, discharges through a noble gas in a discharge tube of length ℓ and radius R. The gas is at a pressure P and temperature T. Assume that breakdown is instantaneous. The voltage across the discharge tube will obey

$$\frac{dV}{dt} = - \frac{I}{C} \tag{E.1}$$

where I is the current. Assuming negligible thyratron resistance,

$$I = \frac{V}{R} = \frac{V\sigma A}{\ell}$$

where

$$\sigma = \frac{ne^2}{m\nu_c} = \text{gas conductivity}$$

n = electron density

e = electron charge

m = electron mass

ν_c = electron collision frequency

For an average electric field $E = \frac{V}{\ell}$, (E.1) becomes

$$\frac{dE}{dt} = \frac{-EAne^2}{c\ell m\nu_c} \tag{E.3}$$

At low electron temperatures, the collision frequency in a noble gas is often a function only of gas number density [E.1]. Therefore, writing $\nu_c = \delta \frac{P}{T}$, (E.3) can be written as

$$\frac{dE}{dt} = \frac{-EAne^2T}{c\ell m\delta P} \tag{E.4}$$

The ionization coefficient α is defined as

$$\frac{dn}{dx} = \alpha n \tag{E.5}$$

For the range of E/N of interest, α can be written as [E.1]

$$\alpha = \frac{P}{T}\, a\, \exp(-\frac{BP}{TE}) \quad . \tag{E.6}$$

where a and B are constants. Therefore

$$dn = \alpha n dx = \frac{P}{T} a\, \exp(-\frac{BP}{TE}) dx \tag{E.7}$$

writing

$$dx = \frac{dx}{dt}\frac{dt}{dE}\, dE = V_d \frac{dt}{dE}\, dE \tag{E.8}$$

where V_d is the drift velocity and is a function of E/N, (E.7) becomes

$$dn = \frac{aP^2 c\ell V_d \delta m}{e^2 AET^2} \exp\,(-\frac{BP}{E})\, dE \tag{E.9}$$

To include losses due to diffusion note that

$$dn_{\substack{\text{DIFFUSION}\\ \text{LOSS}}} = \frac{-D_a n}{\Omega^2}\, dt = \frac{D_a n}{\Omega^2}\left(\frac{dt}{dE}\right) dE = \frac{cP\ell D_a \delta m}{e^2 TEA\Omega^2}\, dE \qquad (E.10)$$

where

D_a = ambipolar diffusion coefficient

Ω = diffusion length

To a first approximation, the ambipolar diffusion coefficient [E.1,2]

$$D_a = \gamma\frac{T\varepsilon}{P} \qquad (E.11)$$

where the average electron energy $\varepsilon = \varepsilon(\frac{E}{N})$. Therefore integrating from an initial field E_o, to some arbitrarily small final field E_f, the maximum electron density r_m can be written as

$$n_m - n_o = \int_{E_f}^{E_o} \left[\frac{aP^2 c\ell V_d \delta m}{T^2 AEe^2} \exp\left(\frac{-BP}{ET}\right) - \frac{c\ell\gamma\varepsilon\delta}{Ee^2A\Omega^2}\right] dE \qquad (E.12)$$

Assume that the fractional ion population remains small so that the neutral atom density, N, is approximately constant during the discharge pulse. The time rate of change of electron density can be written as

$$\frac{dn}{dt} = r_I nN \quad , \quad n(t) = n_o e^{r_I Nt} \qquad (E.13)$$

where r_I is the ionization rate constant. If we ignore diffusion losses, then (E.12) and (E.13) can be combined to yield

$$n_o(e^{r_I Nt} - 1) = \int_{E_f}^{E_o} \frac{aP^2 c\lambda V_d \delta m}{T^2 AEe^2} \exp\left(\frac{-BP}{ET}\right) dE \qquad (E.14)$$

The ionization rate constant can be written as a function of electron temperature and ionization potential (see Table VI.3). By solving (E.14) for r_I,

$$r_I(T_e) = \frac{1}{Nt}\,\ell n\left[\frac{1}{n_o}\int_{E_f}^{E_o}\frac{aP^2c\ell V_d\delta m}{T^2AEe^2}\exp\left(\frac{-BP}{ET}\right)\,dE + 1\right] \quad , \qquad (E.15)$$

one has an expression for T_e in terms of discharge parameters. T_e is solved for by iteration of (E.15).

EXAMPLE: For helium, and the standard discharge conditions used in Section VI.C,

$a = 3/\text{cm-Torr}$ $\quad \ell = 50\ \text{cm}$ $\quad \delta = 7.11\text{x}10^{11}\ \frac{^oK}{\text{Torr sec}}$

$A = 1\ \text{cm}^2$ $\quad B = 10200\frac{V\ ^oK}{\text{Torr-cm}}$ $\quad E_o = 300\ \frac{V}{\text{cm}}$

$C = 5\text{nF}$ $\quad V_d = \zeta\frac{ET}{P}$ $\quad T = 400^oC$

$t = 250\ \text{ns}$

The constant ζ in V_d is left as a parameter for appropriate normalization. The normalization chosen was $T_e = 5$ eV at $P = 5$ Torr. The results are shown in Figure E-2.

REFERENCES

1. S. C. Brown, Basic Data of Plasma Physics, MIT Press/Wiley, Massachusetts, 1959.
2. J. M. Hammer and B. B. Aubrey, "Ion Beam Measurements of Cesium Recombination Cross Sections", Phys. Rev. 141, 146 (1966).

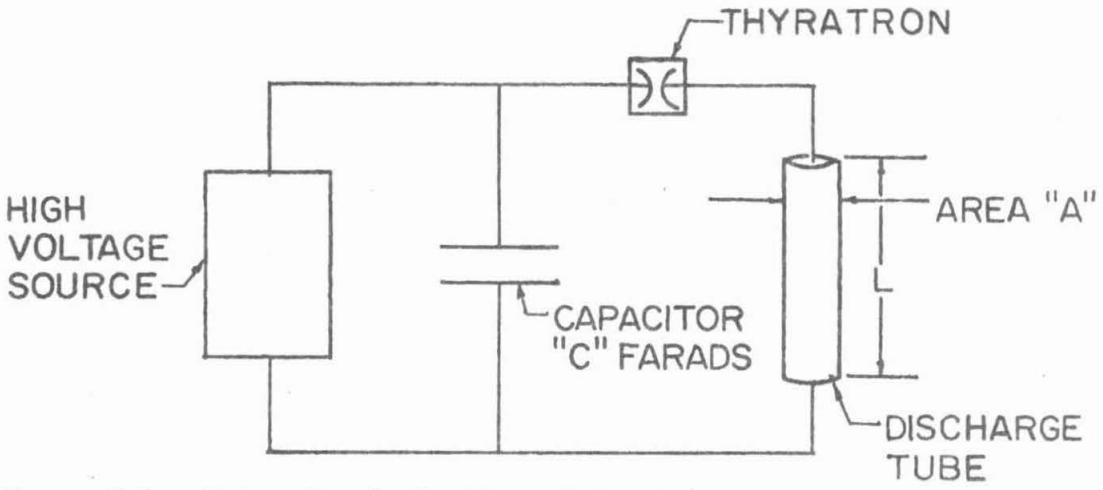

Figure E.1. Setup for derivation of electron temperatures during the dissociation pulse.

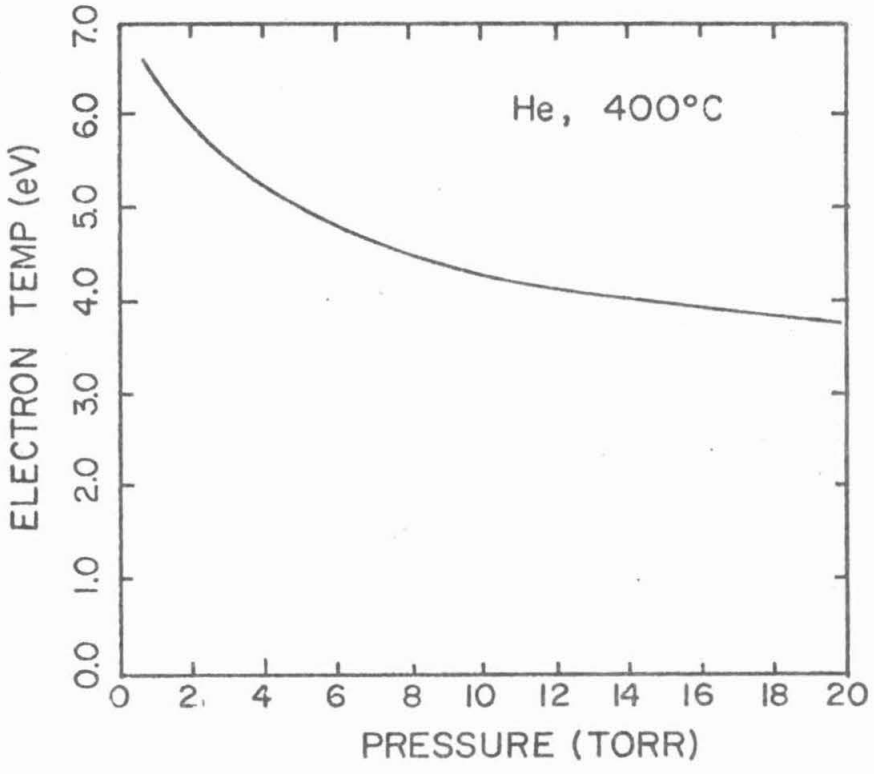

Figure E.2. Electron temperature during the dissociation pulse as a function of helium buffer gas pressure using (E.15).